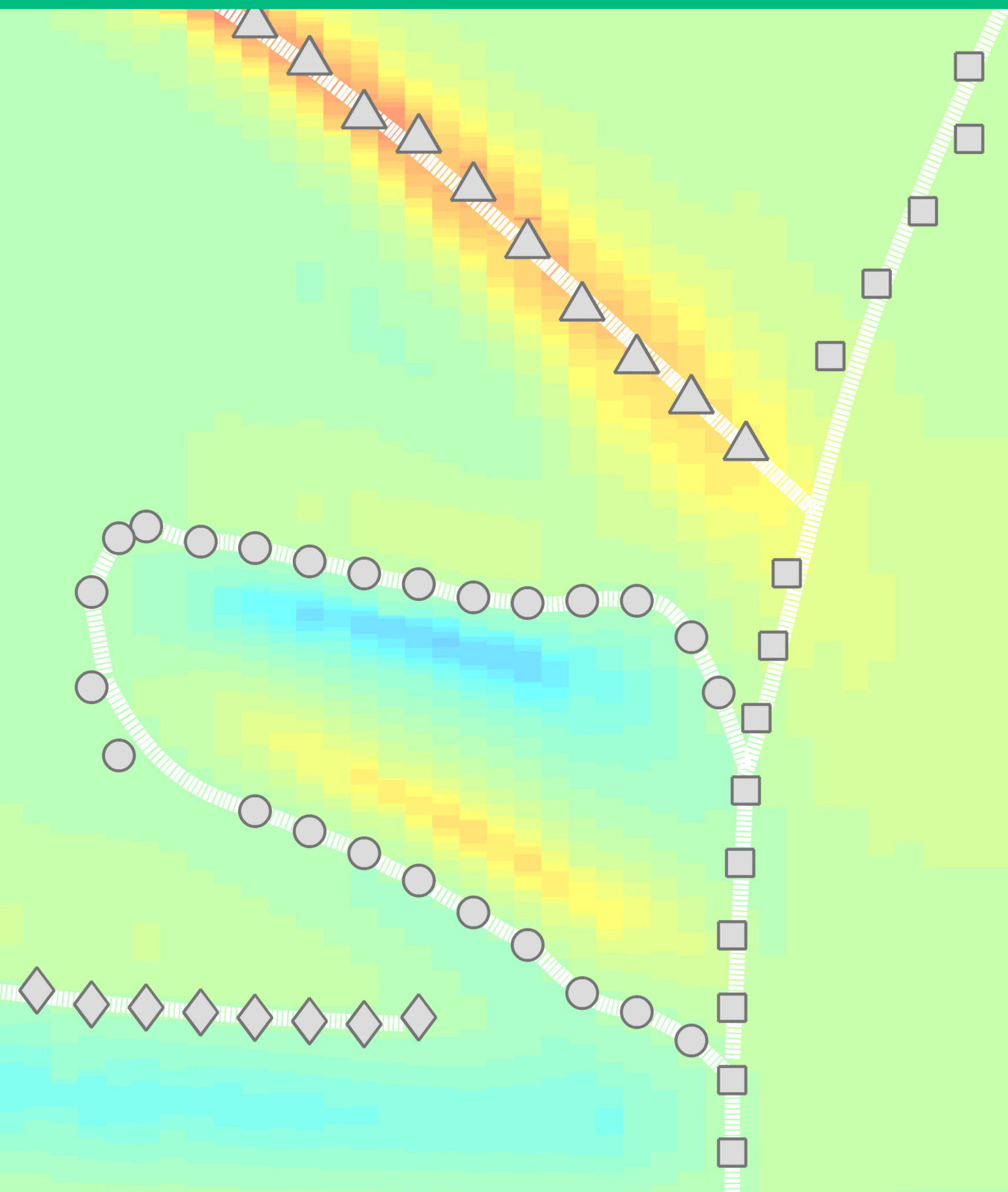


Optically probed order and dynamics in the chiral cluster magnet Cu_2OSeO_3

Rolf Baldwin Versteeg



Optically probed order and
dynamics in the chiral cluster
magnet Cu_2OSeO_3

Inaugural-Dissertation
zur
Erlangung des Doktorgrades
der Mathematisch-Naturwissenschaftlichen Fakultät
der Universität zu Köln

vorgelegt von

Rolf Baldwin Versteeg

aus Zwolle, Niederlande

Köln
März 2019

Gutachter: Prof. Dr. Ir. P.H.M. van Loosdrecht
Gutachter: Prof. Dr. M. Grüninger
Gutachter: Prof. Dr. Rer. Nat. C.H. Back

Vorsitzender der Prüfungskommission: Prof. Dr. Rer. Nat. A. Rosch

Tag der mündlichen Prüfung:

03. Mai 2019

*opgedragen aan
Dini Versteeg-van der Berg en
Willy Schilt-Wierstra*

“Wat is mijn kathedraal? Ik werk aan een kathedraal die ik niet ken en als hij voltooid is, zal ik er niet meer zijn en niemand zal weten dat ik eraan heb gewerkt.”

uit *Nooit meer slapen*, Willem Frederik Hermans, 1966

Contents

1 Introduction	1
1.1 Magnetic order and disorder, magnetization dynamics, and light-matter interaction	1
1.2 Thesis overview	6
1.3 Bibliography	8
2 Magnetic order in non-centrosymmetric materials & the chiral magnet Cu_2OSeO_3	11
2.1 Introduction	11
2.2 Magnetic order in non-centrosymmetric magnetic materials	12
2.2.1 Interactions and energy scales	12
2.2.2 Magnetic phases	13
2.2.3 Topology	17
2.3 Cu_2OSeO_3	20
2.3.1 Structural properties	20
2.3.2 Electronic properties and excitations	21
2.3.3 Magnetic order and magnetic excitations	23
2.3.4 Magneto-electricity	31
2.4 Acknowledgements and own contributions	32
2.5 Bibliography	32
3 Crystal optics and polarization spectroscopy	37
3.1 Introduction	37
3.2 Polarized light	38
3.2.1 The electromagnetic wave	38
3.2.2 Linear and circular polarization	39
3.2.3 Elliptical polarization	40
3.3 Fundamental equation of crystal optics	42
3.4 Dielectric tensor and optical anisotropies	44
3.4.1 The dielectric tensor	44
3.4.2 The zero'th order tensor ϵ_{ij}^0	47
3.4.3 Spatial dispersion effects	48
3.4.4 Magnetization related anisotropies	49

3.4.5	Magneto-spatial anisotropies	51
3.5	Linear polarization rotation	52
3.5.1	Polarization rotation in transmission	52
3.5.2	Polarization rotation in reflection	54
3.6	Polarization spectroscopy setup	55
3.6.1	Overview and schematics	55
3.6.2	Measurement theory	57
3.6.3	Sensitivity of the polarization spectrometer	62
3.7	Kerr spectroscopy of single crystalline SrRuO ₃	63
3.8	Acknowledgements and own contributions	65
3.9	Bibliography	65
4 Optically probed symmetry breaking in the chiral magnet Cu₂OSeO₃		
4.1	Introduction	69
4.2	Structure and magnetism	70
4.3	Experimental methods	72
4.4	Zero-field optical properties	72
4.4.1	Optical excitations	72
4.4.2	Natural optical activity	75
4.5	Magneto-optical properties	76
4.5.1	Phase transitions	76
4.5.2	Field-even rotation and directional dichroism	80
4.5.3	Magnitude of the magneto-optical effect	81
4.6	Conclusions	83
4.7	Appendix	83
4.7.1	Temperature dependence of ellipsometry data	83
4.7.2	Kerr spectroscopy	83
4.7.3	Interference of Faraday and Kerr rotated electromagnetic waves	84
4.8	Own contributions and acknowledgements	90
4.9	Bibliography	90
5 Inelastic light scattering from spin cluster excitations in Cu₂OSeO₃		
5.1	Introduction	95
5.2	The Cu ₄ spin cluster model	96
5.2.1	Exchange interactions	96
5.2.2	The isolated cluster model	96
5.2.3	The interacting cluster model	100
5.2.4	Γ-point excitations: the electron spin resonance spectrum	103
5.2.5	Cluster excitation dispersion: the inelastic neutron scattering spectrum	104

5.3	Magnetic Raman scattering	107
5.3.1	Introduction	107
5.3.2	Classical light-matter interaction	108
5.3.3	Quantum description of light-matter interaction	109
5.3.4	An example: magnetic scattering in fluorides	113
5.4	Magnetic Raman scattering from spin	
	cluster excitations	115
5.4.1	Experimental details	115
5.4.2	Results and discussion	115
5.5	Conclusions	125
5.6	Own contributions and acknowledgements	126
5.7	Bibliography	126
6	A tunable time-resolved spontaneous Raman spectroscopy	
	setup for probing ultrafast collective excitation and	
	quasiparticle dynamics in quantum materials	129
6.1	Introduction	129
6.2	The time-resolved spontaneous Raman	
	spectroscopy setup	132
6.2.1	Design considerations	132
6.2.2	System overview	134
6.2.3	Detection scheme of choice	139
6.3	Experimental results	139
6.3.1	Optical phonon population and hole continuum	
	dynamics in silicon	139
6.3.2	Time- and momentum resolved scattering	
	in silicon	143
6.3.3	Photoinduced melting of helimagnetic order	
	in the chiral magnet Cu_2OSeO_3	146
6.4	Conclusions and outlook	148
6.5	Own contributions and acknowledgements	149
6.6	Bibliography	150
7	Dynamical resonance quench and Fano interference in spon-	
	aneous Raman scattering from quasiparticle and collective	
	excitations	155
7.1	Introduction	155
7.2	Experimental details	156
7.3	Results and discussion	156
7.4	Conclusions	162
7.5	Appendix	163
7.5.1	Carrier density calibration by laser parameters and	
	Fano interference	163
7.5.2	Transient reflectivity	164

7.5.3 Dynamics at 410 nm probe wavelength	165
7.6 Own contributions	166
7.7 Bibliography	166
8 Coupled dynamics of long-range and internal spin cluster	
order in Cu_2OSeO_3	171
8.1 Introduction	171
8.2 High-energy spin cluster excitations	173
8.3 Photoinduced long-range and internal cluster	
order dynamics	174
8.4 Conclusions and outlook	179
8.5 Appendix	180
8.5.1 Transient spectra at 15 K, 38 K, and 60 K	180
8.5.2 Supporting data of transient magnetic scattering	
at $T=5\text{K}$	183
8.5.3 Temperature increase estimated	
from heat capacity	185
8.5.4 Different phonons at $T = 5\text{K}$ and $F \approx 2\text{mJ/cm}^2$	186
8.5.5 Fluence dependence at $T = 5\text{K}$	188
8.5.6 Three-temperature model	189
8.5.7 Temperature dependent time constants	190
8.5.8 Transient absorption spectroscopy measurement	191
8.6 Own contributions and acknowledgements	192
8.7 Bibliography	193
Summary	197
Zusammenfassung	199
Samenvatting	201
List of publications	211
Offizielle Erklärung	213
Lebenslauf	215

Chapter 1

Introduction

1.1 Magnetic order and disorder, magnetization dynamics, and light-matter interaction

Magnetism has fascinated mankind over multiple millenia. The study of magnetism can be traced back as far as to the ancient Greek world, when Thales of Milete observed an attractive force originating from $\mu\alpha\gamma\nu\eta\tau\iota\varsigma$ $\lambda\acute{\iota}\theta\omicron\varsigma$ (“magnesian stone”), a material which we nowadays know as magnetite, or Fe_3O_4 . Thales of Milete had the idea that magnetite contains a soul which can attract iron.^[1] It would take until the 20th century, - where humankind landed in the era of quantum mechanics -, to realize that this attractive force actually ultimately originates in a cooperative spinning of $\sim 10^{23}$ electrons.^[2] The quest to understand how complex phenomena such as magnetic order and disorder, - but also superconductivity, multiferroicity, optical properties, or in general the physical properties of matter -, arise from the cooperative interaction between electrons and the atomic nuclei in a solid, is the domain of condensed matter physics. Obviously, this endeavour to answer fundamental questions on the quantum nature of materials runs parallel with an everlasting drive to develop novel technological applications which can exploit these emergent physical phenomena.^[3]

One of the most fundamental concepts related to magnetism is *order* and *disorder*. We know that the interaction energy between two electrons depends on it’s charge, but also on the spin of the electrons. Whether two spins “want” to align parallel ($\uparrow\uparrow$) or antiparallel ($\uparrow\downarrow$), depends on the sign of the exchange integral J .^[4] When for $\sim 10^{23}$ electron spins it becomes energetically favourable to all align collinearly with the spins pointing in the same direction, we call this ferromagnetic order. Thermal fluctuations may overcome the exchange energy at temperatures of the order $T \sim J/k_{\text{B}}$ (with k_{B} being the Boltzmann constant), and the spins become randomly oriented, in which case we have paramagnetic *disorder*. This order-to-disorder crossover is a phase transition, which we can “quantify” by an increase in en-

trophy S . Phase transitions mostly go hand in hand with a symmetry change, for instance, the paramagnet has a higher symmetry than the magnetically ordered phase. Symmetry thus provides us with another good handle to describe the “amount” of order and disorder, or more formally, the state of matter.

Over the course of the 20th century a wide range of more complicated ordering types have been added to the magnetic ordering palette, examples of which include spin helices and spin cycloids. Such phases stabilize due to a competition between Heisenberg and Dzyaloshinski-Moriya exchange in magnets with broken spatial inversion symmetry.^[5] This type of magnetism will, among others, be central to this thesis work. Interestingly enough, such type of *noncollinear* ordering can also be observed in deceptively “simple” elemental rare-earth metals like dysprosium, where $4f$ -moments couple through the conduction electron mediated RKKY-interaction (Ruderman–Kittel–Kasuya–Yosida).^[6]

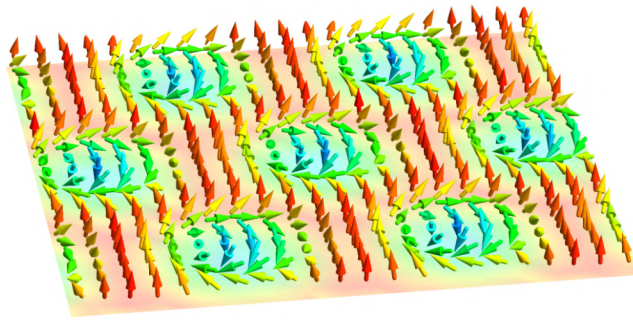


Figure 1.1: The here shown skyrmion lattice phase appears as a hexagonal lattice of spin vortices. The figure has been adapted from Ref. [7] (published under a Creative Commons CC BY-NC-ND 2.5 license).

The above mentioned examples of magnetic order can perhaps by now be regarded as “classical” magnetic states of matter. However, the 2008 experimental discovery of skyrmion lattice order^[8] is just one out of many recent examples which show that today’s magnetism research is as interesting, - if not more -, as it was before. Figure [1.1] provides a beautiful illustration of a so-called skyrmion lattice.^[7] This ordering corresponds to a hexagonal lattice of topologically protected spin vortices, known as skyrmions. This type of magnetic order can be stabilized in, among others, chiral magnets. There are numerous other types of “exotic” magnetic order, but also types of disorder which go beyond simple paramagnetism or diamagnetism, which are studied nowadays.

The devil is in the detail when it comes down to the question whether magnetic moments can order, or whether they stay disordered. The first situation where we may expect to encounter nontrivial magnetic disorder are low-dimensional systems, i.e. 1-dimensional and 2-dimensional magnets.

For magnetic systems with an isotropic Heisenberg exchange, the number of thermally excited magnons should diverge at finite temperature, and 1-dimensional and 2-dimensional magnetic order should not exist. At $T = 0$ K, where there are no thermal fluctuations, but nevertheless still quantum fluctuations, 2-dimensional order can exist, but 1-dimensional order still cannot exist. This is the essence of the so-called Mermin-Wagner-Berezinskii theorem.^[2] That low dimensional (partial) long-range order however has been observed, for instance spin chains in CsCoCl_3 ,^[2] ferromagnetic layers in hybrid organic-inorganic materials,^[9] or antiferromagnetic layers in perovskite materials,^[2] is due to the fact that the disorder restriction imposed by the Mermin-Wagner-Berezinskii theorem gets lifted by competing exchange interactions, magnetic anisotropy, and weak inter-layer or inter-chain interactions.^[2]

Competing interactions can also lead to highly correlated forms of disorder. The dominant symmetric Heisenberg coupling between spin-orbit entangled $j = \frac{1}{2}$ moments on a honeycomb lattice exactly cancel out, and leave higher-order exchange processes, like bond-directional exchange, the relevant exchange interaction. One such a type of coupling, the Kitaev-exchange interaction, cannot be simultaneously satisfied along all bonds on a hexagonal lattice, i.e. the spins are *exchange frustrated*.^[10] In this case a highly nontrivial phase with short-range spin correlations emerges, known as the *Kitaev spin liquid*. One prime candidate for this material with novel fermionic Majorana excitations is $\alpha\text{-RuCl}_3$.^[11]

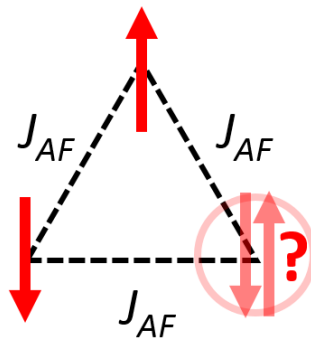


Figure 1.2: Geometric frustration: for antiferromagnetically (J_{AF}) coupled Ising (up or down) spins on a triangle the third spin cannot align.

Frustration can also appear for simpler cases where only the symmetric Heisenberg exchange is relevant. For triangular, hexagonal and kagome lattice geometries there are cases where spins cannot uniquely order for certain spin dimensionalities (Ising, XY, or Heisenberg spin) and interactions. For instance, for antiferromagnetically coupled Ising spins (spins which can only point up or down) on a triangle there is no unique magnetic ordering possible, as illustrated in Fig. 1.2. In this case we can say that the

spins are *geometrically frustrated*, with as a result that the spins stay disordered.^[12] But again, because the spins couple, we still have a correlated type of disorder, known as a *spin liquid phase*. Spins on a three dimensional pyrochlore lattice which are ferromagnetically coupled through the Heisenberg exchange interaction are also frustrated. This situation is drawn in Fig. 1.3a. Each exchange path (grey) has an equal strength. Even though at low temperatures the magnetic moments (light blue) can order, there is no unique magnetic ground state. This “ordered disorder” is named *spin ice*.^[12] Small distortions in the tetrahedra of the pyrochlore lattice lead to a whole different physical picture, where strong (full lines) and weak (dashed lines) exchange paths can be identified, as seen in Fig. 1.3b. In this situation the frustration is lifted and the spins may form a unique long-range ordering pattern consisting of long-range ordered tetrahedral triplet spin clusters (cluster spins indicated in grey), as shown in Fig. 1.3c. We will see that this type of ordering occurs in the central material of this thesis, namely the Mott insulator Cu_2OSeO_3 .^[13] In this thesis work it will be discussed that this type of magnetic order can be regarded as a solid-state spin-analog of a molecular crystal.^[14] From the aforementioned examples we see the importance of the crystallographic structure for magnetic (dis)order. We can thus safely say that complex lattice geometries and low dimensionality are a recipe for highly rich physics.

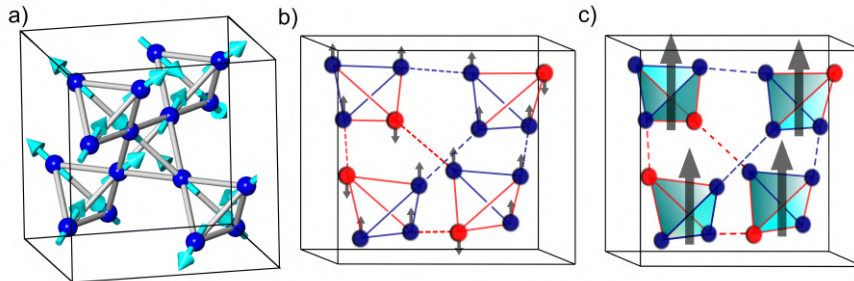


Figure 1.3: a) Spins (light blue) on a pyrochlore lattice. Each exchange path (grey) has an equal strength. In this case magnetic order can exist, but there is no unique spin configuration possible. This is called *spin ice*. Figure adapted from Ref. [15]. Published under a Creative Commons Attribution-ShareAlike 4.0 International (CC BY-SA 4.0) licence. b) The distorted pyrochlore lattice, with spins in grey. In this case strong (full lines) and weak (dashed lines) exchange paths of predominantly ferromagnetic (blue) and antiferromagnetic (red) character can be identified. The strong exchange leads to spin cluster formation. c) The spin clusters are indicated in light blue. We can regard this magnetic ground state as a solid-state analog of a molecular crystal. Such a ground state is observed in the main studied material of this thesis, the Mott insulator Cu_2OSeO_3 .

Light-matter interaction is particularly sensitive to symmetry breaking.^[16] Optical spectroscopy therefore is an ideal tool to study magnetic

order and disorder. Time-reversal symmetry is broken when a material is magnetically ordered (or placed inside a magnetic field). In the case of finite magnetization, such as ferromagnetic or conical spin ordering, we can observe a light polarization rotation proportional to the magnetization upon transmission through a sample, known as Faraday rotation.^[17] This can be used as a sensitive optical probe for magnetic order and disorder, and it even allows to detect the skyrmion lattice phase in Cu_2OSeO_3 , as shown in this thesis work. Chiral molecules and crystals allow for a polarization rotation known as natural optical activity.^[16] We can use this optical phenomenon to determine crystallographic chirality. These optical phenomena are well-known for more than over a century. However, in modern times new “exotic” optical phenomena were discovered, which for instance result from the combined broken spatial inversion and time-reversal symmetry. We will see that such an exotic magneto-optical phenomenon, known as magnetochiral dichroism, can serve as a probe of magnetic chirality.^[18]

At finite temperatures the magnetic order is not a static, frozen collection of spins, but instead thermal fluctuations of the spin order exist, namely *spin waves*, or *magnons*. These spin waves are “magnetic dynamics at thermodynamic equilibrium”. Inelastic scattering techniques like inelastic neutron scattering and spontaneous Raman spectroscopy may give us insight into magnetic equilibrium dynamics. However, we can also use strong external perturbations like magnetic and electric field pulses to perturb the thermodynamic equilibrium, and drive the (magnetic) system into an out-of-equilibrium state. After such a strong disturbance the magnetic system eventually will relax back into its thermodynamic equilibrium within a characteristic timescale. These relaxation timescales are governed by the coupling between lattice, electronic, orbital and magnetic degrees of freedom, and measuring these timescales provides us insight into relaxation channels between the different degrees of freedom in a solid. In this case we speak of nonequilibrium magnetization dynamics.

The fastest perturbation at our disposal to study nonequilibrium dynamics is an ultrashort light pulse. Pulsed lasers have opened the possibility to probe magnetization dynamics and even control magnetic order on femtosecond timescales. The research field studying these ultrafast phenomena has been dubbed femtomagnetism and is a highly active part of condensed matter physics.^[19] Examples on a fundamental level include the electron-spin scattering induced ultrafast melting of ferromagnetic order in nickel,^[20] and optical control of the antiferromagnetic helical pitch through injection of photoinduced carriers in dysprosium.^[6] Recent scientific advances with a truly high potential towards applications include all-optical magnetization switching,^[21] and picosecond optical writing and read-out of magnetic bits.^[22] In the case of melting of ferromagnetic order in nickel, or modulating the helical pitch in dysprosium we change or reduce the magnetic order parameter, but the nature of the magnetic order remains the same. However, optical

excitation also allows to truly alter the nature of the magnetic phase. An example is the femtosecond activation of magnetoelectricity in CuB_2O_4 .^[23] Here, an additional type of ferroic order, in this case ferroelectricity, is transiently stabilized besides magnetic order. In the case of CuB_2O_4 the magnetoelectric phase can also be stabilized through the static control parameters of magnetic field and temperature. However, photoexcitation even allows to create metastable phases not accessible under equilibrium conditions.^[24] As such, a new dimension in the phase space of a material can be uncovered. Again symmetry changes play a role here, but now in a nonequilibrium way. In this thesis it will be discussed that the strong symmetry sensitivity of the spontaneous Raman scattering process can be exploited in the time-resolved variant of the technique in order to elucidate symmetry changes across photoinduced phase transitions.^{[25][26]}

1.2 Thesis overview

The Mott insulator Cu_2OSeO_3 has a “solid-state spin molecular”-like helical ground state, and a rich set of metamagnetic phases. The optically probed order and dynamics of this chiral cluster magnet is the central topic of this thesis.

In **chapter 2** the ground state magnetic order and field induced metamagnetic phases of non-centrosymmetric magnetic materials is discussed. These magnetic phases result from a competition between Heisenberg exchange, Dzyaloshinskii-Moriya-exchange, magnetic anisotropy, and the Zeeman-coupling when a magnetic field is applied. The chiral magnet Cu_2OSeO_3 is introduced. We will see that Cu_4 triplet clusters form the relevant spin entity for the formation of long-range magnetic order in this Mott insulator. Under an applied field different metamagnetic phases form, among others a topologically protected skyrmion lattice phase. The cluster formation and long-range order leads to a complex spin wave spectrum. Furthermore, the lattice and electronic properties of Cu_2OSeO_3 are discussed.

Broken spatial inversion symmetry, time-reversal symmetry, and their combined presence in chiral magnets leads to a rich set of linear optical phenomena, as is discussed in **chapter 3**. The fundamental equation of crystal optics is derived, and it is argued why in the optical range of the electromagnetic spectrum one can describe the light-matter interaction in terms of an effective dielectric constant dependent on magnetization and the wave vector. The for this thesis work constructed polarization spectroscopy setup is described, as well as the measurement theory behind the technique. The working of the setup is illustrated with magneto-optical Kerr effect measurements of the ferromagnetic $4d$ -metal oxide SrRuO_3 .

Chapter 4 focuses on the linear optical properties of Cu_2OSeO_3 . It is shown that the broken spatial inversion symmetry leads to strong dipole ac-

tive crystal field excitations below the charge transfer gap, and in addition, to natural optical activity. The natural optical activity may be used as a probe for structural chirality, and shows sensitivity to magnetic ordering, evidencing a finite magneto-electric coupling. A strong Faraday-rotation is observed, which is discussed to originate from spin cluster formation and the relative ease of domain reorientation. The strong magneto-optical response is used to probe the metamagnetic phase transitions. This allowed to all-optically map the metamagnetic phase diagram, including the skyrmion lattice phase.

Previous work has shown that the long-range spin cluster ordering results in a characteristic spin wave spectrum, which can be divided into low-energy external and high-energy internal spin cluster excitations. In **chapter 5** these works are summarized. For this thesis work spontaneous Raman spectroscopy was used to probe spin cluster transitions at the Brillouin zone center. The Raman-scattering activity of the spin cluster transitions is discussed to originate from the Elliot-Loudon light scattering mechanism. The temperature dependent scattering response of the high-energy internal cluster modes shows a crossover from broad continuum scattering above the critical temperature T_C into well-defined magnetic modes below T_C , which is discussed to originate from a change of the character of the high-energy cluster modes. Above T_C the high-energy spin cluster excitations correspond to localized internal cluster excitations, while in the long-range ordered phase the high-energy modes acquire dispersion, and correspond to optical magnons.

For this thesis work an ultrafast time-resolved spontaneous Raman spectroscopy setup (TiReRa) was designed and constructed. In **chapter 6** the possibilities of the technique are discussed, such as measuring photoinduced quasiparticle and collective excitation population dynamics, and detecting symmetry changes across photoinduced phase transitions. Additionally, the relevant design parameters to optimize the setup for probing nonequilibrium dynamics of quantum materials are discussed. The TiReRa laser system, table optics, Raman-microscopy interface, and spectrometer are presented. Three case studies illustrate the working of the setup. The first focuses on longitudinal-optical phonon population, Raman tensor, and hole dynamics in silicon. The second study focuses on time-and momentum resolved phonon scattering in silicon. A short appetizer to the results of the last chapter is given, in which the photoinduced nonequilibrium dynamics of Cu_2OSeO_3 is presented.

When discussing time-resolved Raman spectroscopy one may be tempted to solely focus on population dynamics, and neglect the role of the Raman tensor in the time-domain. In our test experiments on silicon presented in **chapter 6** we observed a Raman tensor quench, demonstrating that Raman tensor dynamics however is an important factor in correctly interpreting the time-resolved spontaneous Raman scattering response of a photoexcited

material. In chapter **chapter 7** it is discussed in greater detail how simultaneous detection of both anti-Stokes and Stokes scattering permits to disentangle the Raman tensor and genuine population dynamics. The Raman tensor quench in silicon is discussed to originate from the photoinduced hole carrier population. A second effect of the optically excited carriers is an enhancement of the longitudinal optical phonon Fano asymmetry.

The steady-state Raman scattering study described in **chapter 5** established that the high-energy spin cluster excitations can be used as an optical probe of long-range and internal spin cluster order. In **chapter 8** we use the newly constructed time-resolved Raman spectroscopy setup TiReRa to probe the photoinduced near-equilibrium spin and lattice dynamics of the helimagnetic phase in Cu_2OSeO_3 . Multiple ps-decade spin-lattice relaxation dynamics is observed, evidencing a separation of the order parameter dynamics into disordering of long-range and internal spin cluster order. The observations of the steady-state and time-resolved Raman study exemplify that Cu_2OSeO_3 can be regarded as a solid-state molecular crystal of spin nature.

1.3 Bibliography

- [1] N. Ida, *Engineering electromagnetics*, 3rd ed. (Springer, 2015).
- [2] S. Blundell, *Magnetism In Condensed Matter*, (Oxford University Press, 2001).
- [3] D. N. Basov, R. D. Averitt, and D. Hsieh, Towards properties on demand in quantum materials, *Nat. Mater.* **16**, 1077 (2017).
- [4] P. Fazekas, *Lecture notes on electron correlation and magnetism, volume 5* (World scientific, 1999).
- [5] P. Bak and M. H. Jensen, Theory of helical magnetic structures and phase transitions in MnSi and FeGe, *J. Phys. C: Solid St. Phys.* **13**, L881 (1980).
- [6] M. C. Langner, S. Roy, A. F. Kemper, Y.-D. Chuang, S. K. Mishra, R. B. Versteeg, Y. Zhu, M. P. Hertlein, T. E. Glover, K. Dumesnil, and R. W. Schoenlein, Scattering bottleneck for spin dynamics in metallic helical antiferromagnetic dysprosium, *Phys. Rev. B* **92**, 184423 (2015).
- [7] K. Everschor, *Current-induced dynamics of chiral magnetic structures: skyrmions, emergent electrostatics and spin-transfer torques*, PhD thesis, Universität zu Köln, 2012.
- [8] S. Mühlbauer, B. Binz, F. Jonietz, C. Pfleiderer, A. Rosch, A. Neubauer, R. Georgii, and P. Böni, Skyrmion lattice in a chiral magnet, *Science*, **323**, 915 (2009).
- [9] L. J. de Jongh and A. R. Miedema, Experiments on simple magnetic model systems, *Adv. Phys.* **23**, 1 (1974).
- [10] S. Trebst, Kitaev materials, e-print arXiv:1701.07056 [cond-mat.mtrlsci] (2017).
- [11] A. Banerjee, C. A. Bridges, J.-Q. Yan, A. A. Aczel, L. Li, M. B. Stone, G. E. Granroth, M. D. Lumsden, Y. Yiu, J. Knolle, S. Bhattacharjee, D. L. Kovrizhin, R. Moessner, D. A. Tennant, D. G. Mandrus and S. E. Nagler, Proximate kitaev quantum spin liquid behaviour in a honeycomb magnet, *Nat. Mater.* **15**, 733 (2016).

- [12] L. Balents, Spin liquids in frustrated magnets, *Nature* **464**, 199 (2010).
- [13] O. Janson, I. Rousochatzakis, A. A. Tsirlin, M. Belesi, A. A. Leonov, U. K. Rößler, J. Van den Brink, and H. Rosner, The quantum nature of skyrmions and half-skyrmions in Cu_2OSeO_3 , *Nat. Commun.* **5**, 5376 (2014).
- [14] S. V. Streltsov and D. I. Khomskii, Orbital physics in transition metal compounds: new trends, *Phys. Usp.* **60**, 1121-1146 (2017).
- [15] https://commons.wikimedia.org/wiki/File:Fragment_of_pyrochlore_lattice_in_spin_ice_state.png, figure released under a Creative Commons Attribution-ShareAlike 4.0 International (CC BY-SA 4.0) licence.
- [16] A. Glazer and K. G. Cox, *Classical linear crystal optics* in *International Tables for Crystallography, Vol. D*, (John Wiley & Sons, Ltd., 2006), Chapter 1.1.6.
- [17] P. S. Pershan, Magneto-Optical Effects, *J. Appl. Phys.* **38**, 1482 (1967).
- [18] G. L. J. A. Rikken and E. Raupach, Observation of magneto-chiral dichroism, *Nature* **390**, 493 (1997).
- [19] A. Kirilyuk, A. V. Kimel, and T. Rasing, Ultrafast optical manipulation of magnetic order, *Rev. Mod. Phys.* **82**, 2731 (2010).
- [20] E. Beaurepaire, J. -C. Merle, A. Daunois, and J. -Y. Bigot, Ultrafast spin dynamics in ferromagnetic nickel, *Phys. Rev. Lett.* **76**, 4250 (1996).
- [21] M. Savoini, R. Medapalli, B. Koene, A. R. Khorsand, L. Le Guyader, L. Duò, M. Finazzi, A. Tsukamoto, A. Itoh, F. Nolting, A. Kirilyuk, A. V. Kimel, and T. Rasing, Highly efficient all-optical switching of magnetization in GdFeCo microstructures by interference-enhanced absorption of light, *Phys. Rev. B* **86**, 140404 (2012).
- [22] A. Stupakiewicz, K. Szerenos, D. Afanasiev, A. Kirilyuk, and A. V. Kimel, Ultrafast nonthermal photo-magnetic recording in a transparent medium, *Nature* **542**, 71 (2017).
- [23] D. Bossini, K. Konishi, S. Toyoda, T. Arima, J. Yumoto and M. Kuwata-Gonokami, Femtosecond activation of magnetoelectricity, *Nat. Phys.* **14**, 370 (2018).
- [24] D. Fausti, R. I. Tobey, N. Dean, S. Kaiser, A. Dienst, M. C. Hoffmann, S. Pyon, T. Takayama, H. Takagi, and A. Cavalleri, Light-induced superconductivity in a stripe-ordered cuprate, *Science* **331**, 189 (2011).
- [25] D. Fausti, O. V. Misochko, and P. H. M. van Loosdrecht, Ultrafast photoinduced structure phase transition in antimony single crystals, *Phys. Rev. B* **80**, 161207 (2009).
- [26] D. Fausti and P. H. M. van Loosdrecht, in Chapter 14: *Time-resolved Raman scattering* of *Optical Techniques for Solid-State Materials Characterization*, edited by R. P. Prasankumar and A. J. Taylor, (CRC Press, Boca Raton London New York, 2012).

Chapter 2

Magnetic order in non-centrosymmetric materials & the chiral magnet Cu_2OSeO_3

2.1 Introduction

Non-centrosymmetric materials show a variety of magnetic ground states and metamagnetic phases due to the competition of Heisenberg-exchange, Dzyaloshinskii-Moriya-exchange, magnetic anisotropy, and the Zeeman coupling when a magnetic field is applied.^[1,2] In this chapter an overview of the relevant magnetic interactions and resulting metamagnetic phases will be given. A magnetic phase of special interest is the skyrmion lattice phase. This phase consists of vortex-like topologically stable nanometric spin structures,^[3,4] which in a range of different bulk magnetic materials “crystallize” in a lattice consisting of tubes of magnetic skyrmions.^[5] The wave-like interpretation of the skyrmion lattice is presented, as well as an intuitive description of the nontrivial topology of the skyrmion phase.

This chapter furthermore provides an introduction to the central material of this thesis, namely the chiral magnet Cu_2OSeO_3 , which was the first insulating material to be discovered to host a skyrmion lattice under an applied field. The insulating character leads to the possibility of electric field control of the skyrmion phase through magnetoelectric coupling, i.e. a type of control which cannot be realized in metallic and semiconducting skyrmion host counterparts like MnSi and FeGe,^[3] even though these materials possess similar magnetic phase diagrams. Possibly more surprising is that, unlike other skyrmion hosts such as MnSi and FeGe, the long-range magnetic order in Cu_2OSeO_3 is composed of localized spin clusters, as opposed to localized single spins.^[6] This formation of long-range ordered clusters results from the

strong and weak exchange energy scales present in Cu_2OSeO_3 , as discussed in this chapter. Furthermore, an overview of the resulting spin cluster excitations and low-energy chiral excitations will be given.

2.2 Magnetic order in non-centrosymmetric magnetic materials

2.2.1 Interactions and energy scales

In magnets with broken inversion symmetry the symmetric Heisenberg-exchange term $J_{ij} \vec{S}_i \cdot \vec{S}_j$ typically is the strongest energy scale after which the anti-symmetric Dzyaloshinskii-Moriya-exchange (DM-exchange) $\vec{D}_{ij} \cdot \vec{S}_i \times \vec{S}_j$ follows.^[2] (Anti-)symmetry refers to whether the terms change sign when the spins are exchanged. The Heisenberg-exchange leads to parallel or anti-parallel spin alignment depending on the sign of J_{ij} . The case of parallel spin alignment is illustrated in Fig. 2.1a.

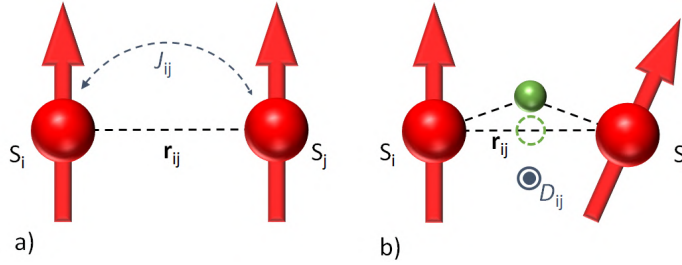


Figure 2.1: a) Illustration of ferromagnetic spin alignment through the symmetric Heisenberg exchange interaction. Here the interaction J_{ij} between the spins \vec{S}_i and \vec{S}_j is of negative sign, which leads to a ferromagnetic spin alignment. b) Illustration of anti-symmetric Dzyaloshinski-Moriya exchange, which leads to a canted spin alignment. The green ion is a ligand ion which breaks inversion symmetry between the spins \vec{S}_i and \vec{S}_j . The direction of the DM-vector in the cartoon points out-of-plane, which leads to spin canting along the bond \vec{r}_{ij} .

The DM-exchange favours a canted spin alignment as illustrated in Fig. 2.1b. The DM-interaction is present when there is no inversion symmetry between the spin sites and is thus present in non-centrosymmetric magnets.^[7] Spin-orbit coupling is a second prerequisite for the DM-exchange interaction. The DM-vector \vec{D}_{ij} can have a component parallel and perpendicular to the connecting vector \vec{r}_{ij} between the spins. The specific form of the DM-interaction depends on the crystallographic symmetry.^[1,2] Magnetocrystalline and shape anisotropy also influence the pointing direction.^[8] The DM-interaction energy is minimized when the spins \vec{S}_i and \vec{S}_j cant at right angles in the plane perpendicular to \vec{D}_{ij} . For the case $\vec{D}_{ij} \perp \vec{r}_{ij}$, as depicted in Fig. 2.1b, spins cant along the connecting vector \vec{r}_{ij} whereas for

the parallel case $\vec{D}_{ij} \parallel \vec{r}_{ij}$ the spins cant perpendicular to \vec{r}_{ij} . Generally, the DM-interaction energy is an order $\mathcal{O} \sim 10^{-2}$ smaller than the Heisenberg exchange.^{9,10} A material with an exceptionally large DM-interaction is the main investigated materials of this thesis work, namely Cu_2OSeO_3 . For some exchange paths the DM-exchange to Heisenberg exchange ratio can be as large as $\mathcal{O} \sim 10^{-1}$ (Refs. [10](#), [11](#)).

A smaller energy scale relevant for the magnetic order in non-centrosymmetric materials results from magnetocrystalline anisotropy (or crystal field anisotropy). This interaction describes the coupling of spins to the crystal lattice through spin-orbit interaction, where it should be understood that the orbital orientation is dictated by Coulomb interaction with the surrounding ligand field. The magnetocrystalline anisotropy thus dictates the orientation of the magnetic moment with respect to the crystal surrounding, or more formally stated it breaks the rotational symmetry.^{7,12} This energy scale is again an order $\mathcal{O} \sim 10^{-2}$ smaller than the Dzyaloshinskii-Moriya-exchange.

The potential energy of a magnetic moment in a magnetic field is given by the Zeeman coupling term $-\boldsymbol{\mu} \cdot \mathbf{B}$. The energy scale is $g\mu_B B$, where g is the g -factor of the magnetic moment, and B gives the magnetic field strength.⁷ The last term of importance is the thermal energy $k_B T$, with k_B being the Boltzmann constant, and T being the temperature. Table [2.1](#) provides a summary of all relevant energy scales.

Table 2.1: Energy scales relevant to the formation of magnetic order in non-centrosymmetric materials. The left column gives the interaction type. The right column gives the order of magnitude with respect to the Heisenberg exchange, which is the dominant contribution.

energy	order of magnitude (compared to J_{ij})
Heisenberg exchange J_{ij}	1
DM-exchange \vec{D}_{ij}	10^{-2}
magnetocrystalline anisotropy	10^{-4}
Zeeman potential $g\mu_B B$	10^{-4}
thermal energy $k_B T$	1

2.2.2 Magnetic phases

Under the presence of an external magnetic field different metamagnetic phases are stabilized in a non-centrosymmetric magnet.¹³ Which types of magnetic order are thermodynamically stable can be inferred by minimizing the Free energy functional $\mathcal{F}(\mathbf{M})$, which is the sum of the different interac-

tion energies integrated over a macroscopic volume. Here \mathbf{M} indicates the magnetization.^[7] For a chiral magnet in a magnetic field \mathbf{B} the Free energy $\mathcal{F}(\mathbf{M})$ is given in a continuum approximation^{[12],[14]} form as:

$$\begin{aligned} \mathcal{F}(\mathbf{M}) \approx & \int d^3r [r_0 \mathbf{M}^2 + J(\nabla \mathbf{M})^2 + U \mathbf{M}^4 + 2D \nabla \mathbf{M} \cdot (\nabla \mathbf{M} \times \mathbf{M}) - \mathbf{M} \cdot \mathbf{B}] \\ & + \mathcal{F}_{\text{anisotropy}} \end{aligned} \quad (2.1)$$

The $r_0 \mathbf{M}^2$, $U \mathbf{M}^4$ and $J(\nabla \mathbf{M})^2$ terms are the Heisenberg exchange terms. Here r_0 , U , and J are phenomenological parameters which depend on microscopic parameters such as the spin length S , the distance a between spins, the amount of nearest-neighbours and the Heisenberg exchange integral.^[7] The Free energy is minimized for a spontaneous magnetization $+\mathbf{M}$ or $-\mathbf{M}$ when only these first three terms are present with the right sign and magnitude for the phenomenological parameters. This can describe ferromagnetic order.^[7]

The term $2D \nabla \mathbf{M} \cdot (\nabla \mathbf{M} \times \mathbf{M})$ term gives the DM-energy contribution. Microscopically this term depends on parameters such as the spin-orbit coupling strength, the DM-exchange integral, the distance between spins, the spin lengths and the amount of nearest-neighbours. The DM-exchange allows for the formation of cycloidal or helical order. The crystallographic point group dictates the form of the DM-interaction and thus whether spins preferentially cant parallel or perpendicular to the connecting vector \mathbf{r} between spins. In the first case spin cycloids form (point group C_{nv} with $n=1, 2, 3, 4, 6$ and T_d), such as in GaV₄S₈ (C_{3v}).^[15] In the second case spin helices form (point groups T and O), such as in Cu₂OSeO₃,^[16] FeGe,^[14] Fe_{1-x}Co_xSi,^[17] and MnSi (point group T).^{[14],[18]}

In chiral magnets the magnetic ground state is a helix,^[2] with continuum approximation solution:

$$\mathbf{M}(\mathbf{r}) = M_0 [\vec{e}_x \cos(\mathbf{q} \cdot \mathbf{r}) + \vec{e}_y \cos(\mathbf{q} \cdot \mathbf{r})] \quad (2.2)$$

The helix only has a transversal spin component. $\mathbf{q} = \frac{2\pi}{\lambda}$ is the helix' wave vector, where λ is the length of the helix, which is dictated by the ratio $|D_{ij}/J_{ij}|$. (Ref. [14] and Ref. [2]) A depiction of helical spin ordering is given in Fig. 2.2a.

The spin cycloid both has a transversal and longitudinal spin component, and is given by:

$$\mathbf{M}(\mathbf{r}) = M_0 [\vec{e}_y \cos(\mathbf{q} \cdot \mathbf{r}) + \vec{e}_z \cos(\mathbf{q} \cdot \mathbf{r})] \quad (2.3)$$

A depiction of spin cycloid ordering is shown in Fig. 2.2b. The functional $\mathcal{F}(\mathbf{M})$ up till this point was described to be isotropic. The helix and cycloid

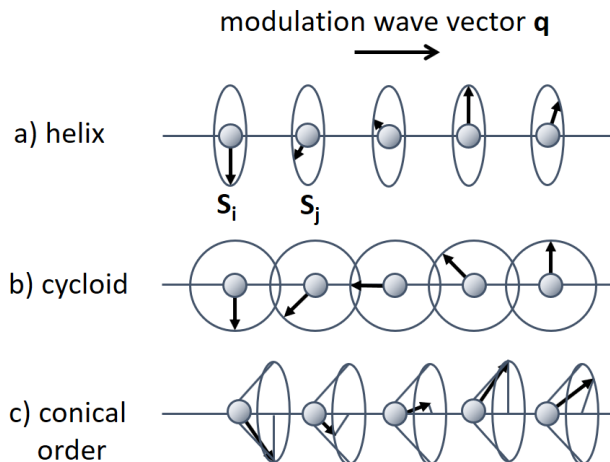


Figure 2.2: a) Helimagnetic spin order. b) Cycloid spin order. c) Conical spin order.

\mathbf{q} -vector, or direction of spontaneous magnetization can thus point in an arbitrary direction \mathbf{r} in real space. The Zeeman term $-\mathbf{M}\cdot\mathbf{B}$ describes the coupling to the magnetic field \mathbf{B} , and breaks the rotational isotropy. The Zeeman term microscopically depends on the g -factor, as discussed in the previous paragraph. A conical type of spin ordering is stabilized when a magnetic field is applied parallel to the helimagnetic wavevector \mathbf{q} , as depicted in Fig. 2.2c. For sufficiently strong external fields the Free energy $\mathcal{F}(\mathbf{M})$ is minimized for field-polarized ferromagnetic or ferrimagnetic order with magnetization $\mathbf{M}(\mathbf{r}) = M_0 \mathbf{z}$ pointing along the magnetic field direction.

For a small temperature range just below T_C , and small field range, the skyrmion lattice phase is stabilized.¹⁹ The skyrmion lattice (SkL) phase forms as a triple- \mathbf{q} hybridized state,^{3,20} consisting of tubes of skyrmions,⁵ where the magnetization in the continuum approximation is given as:

$$\mathbf{M}(\mathbf{r}) \approx \mathbf{M}_0 + \sum_i^3 \mathbf{M}_{\mathbf{q}_i}(\mathbf{r} + \Delta\mathbf{r}) \quad (2.4)$$

The \mathbf{M}_0 term is a uniform magnetization component induced by the Zeeman-term. The second term is a superposition of three helices (or cycloids), with a phase shift with respect to each other. For the condition

$$\sum_i^3 \mathbf{q}_i = 0 \quad (2.5)$$

the Free energy $\mathcal{F}(\mathbf{M})$ is minimized. This is when three helices (or cycloids) have a 120° phase shift with respect to each other. The interference between the helices (or cycloids) results in a lattice of tubes of spin knots,

where the knots are known as skyrmions. These skyrmions have a typical diameter of 1 to 100 nm.³ This description interprets the skyrmion lattice as a 3D wave-like object,^{21,22} however Skyrmions may also form as truly 2-dimensional objects in atomically thin films.²³ The skyrmion lattice order in bulk crystals leads to a characteristic hexagonal diffraction pattern in reciprocal space,^{15,24,25} as seen in Fig. 2.3b (the image is adapted from Ref. 24). Skyrmions may not necessarily crystallize into a lattice, but can also be observed as single objects. In such a case we can regard the skyrmion as a particle.²¹

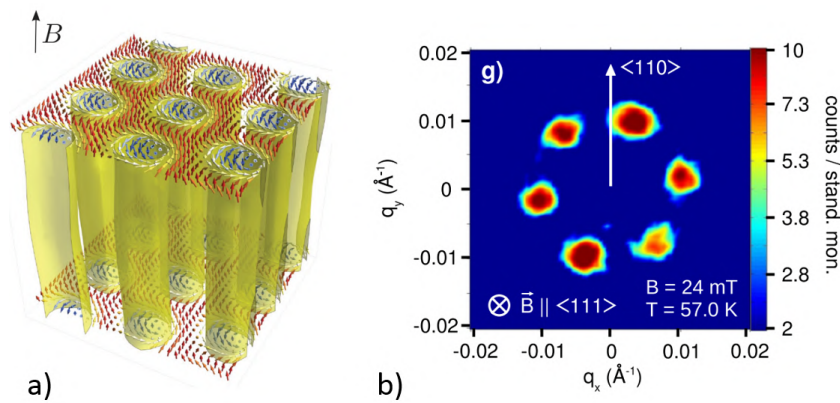


Figure 2.3: a) A lattice of Bloch-type skyrmion tubes. The image is adapted from Ref. 5. Reprinted figure with permission from L. Buhardt and L. Fritz, , Phys. Rev. B **88**, 195137 (2013), <https://doi.org/10.1103/PhysRevB.88.195137>, © Copyright 2013 by the American Physical Society. b) Neutron diffraction of the skyrmion lattice in Cu_2OSeO_3 for a magnetic field applied along the crystallographic [111] direction. The diffraction pattern has a characteristic hexagonal symmetry. The figure is adapted from Ref. 24. Reprinted figure with permission from T. Adams, A. Chacon, M. Wagner, A. Bauer, G. Brandl, B. Pedersen, H. Berger, P. Lemmens, and C. Pfleiderer, Phys. Rev. Lett. **108**, 237204 (2012), <https://doi.org/10.1103/PhysRevLett.108.237204>, © Copyright 2012 by the American Physical Society.

The types of skyrmions observed in bulk materials are in many cases the Bloch- or Néel-type skyrmion. However other skyrmion types are, - both theoretically and experimentally -, known to exist.²⁶ Materials belonging to point group T host Bloch-type skyrmions and skyrmion lattices. A Bloch skyrmion lattice is depicted in Fig. 2.3a. For the C_{nv} point group materials the Néel-type skyrmion and skyrmion lattice stabilizes. The Bloch and Néel-type Skyrmion¹⁵ are shown in Fig. 2.4. Both types have in common that the center spin points anti-parallel to the spins at the periphery. However, for the Néel-type the spins between center and periphery only rotate in radial planes, whereas for the Bloch-type the spins have an additional twist, which leads to a “whirlpool”-like spin configuration. This makes the Bloch-

skyrmion a chiral skyrmion whereas the Néel-skyrmion is achiral.^[15]

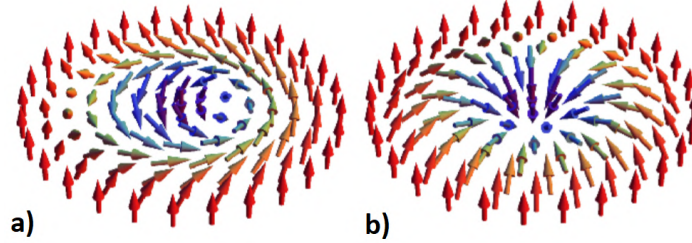


Figure 2.4: a) A Bloch-type skyrmion b) A Néel-type skyrmion. Figures have been adapted from Ref. [15]. Adapted by permission from Springer Nature: Springer Nature, Nature Materials, Néel-type skyrmion lattice with confined orientation in the polar magnetic semiconductor GaV₄S₈, I. Kézsmárki, S. Bordács, P. Milde, E. Neuber, L. M. Eng, J. S. White, H. M. Rønnow, C. D. Dewhurst, M. Mochizuki, K. Yanai, H. Nakamura, D. Ehlers, V. Tsurkan, and A. Loidl, Nat. Mater. **14**, 1116 (2015), © 2015 Macmillan Publishers Limited, <https://www.nature.com/nmat/>

Real-space imaging of skyrmions can be realized by means of Lorentz Transmission Electron Microscopy (LTEM). This technique allows to map the in-plane magnetization component of a skyrmion. In order to image skyrmions by means of LTEM one typically needs to thin down the sample to a few tens of nanometers. In Fig. 2.5 the in-plane spin component of a lattice of Bloch-skyrmions in Fe_{0.5}Co_{0.5}Si as seen by LTEM is shown. Here a 50 mT magnetic field was applied perpendicular to the sample surface with sample temperature at ~ 40 K. A skyrmion lattice spacing of about 90 nm was observed. The color coding gives the lateral direction of the spin. The change in color shows that the spins rotate in-plane and form a chiral magnetic structure.^[17]

The magnetic anisotropy interaction $\mathcal{F}_{\text{anisotropy}}$ (cf. Eq. 2.1) breaks the ground state rotational symmetry and dictates along which crystallographic directions the noncollinear magnetic order spontaneously orients. Even though small, this term can have drastic impact on the extent of the skyrmion phase. For instance, in the lacunar spinel GaV₄Se₈ the Néel-type skyrmion lattice extends from $T_C \approx 15$ K down to 0 K ($\Delta T/T_C \approx 1$) due to the strong orientational confinement induced by the competition between the large magnetocrystalline anisotropy and the C_{nv} DM-interaction.^[15,27,28] In GaV₄Se₈ the skyrmion lattice therefore remains strongly pinned along the rhombohedral axis even for oblique magnetic field orientations. This should be compared and contrasted to materials with minimal anisotropy such as noncentrosymmetric cubic Cu₂OSeO₃ ($\Delta T/T_C \approx 0.03$).

2.2.3 Topology

Topology is the branch of mathematics concerned with the properties and classifications of geometrical objects (or more general, space) that remain

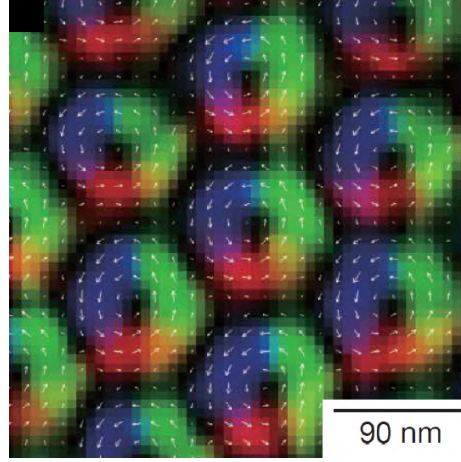


Figure 2.5: a) A real-space image of a Bloch-type skyrmion lattice with lattice constant of 90 nm in $\text{Fe}_{0.5}\text{Co}_{0.5}\text{Si}$ obtained by Lorentz transmission electron microscopy. This imaging technique is sensitive to the in-plane magnetization component of the skyrmion. The figure has been adapted from Ref. [17]. Adapted by permission from Springer Nature: Springer Nature, Nature, Real-space observation of a two-dimensional skyrmion crystal, X. Z. Yu, Y. Onose, N. Kanazawa, J. H. Park, J. H. Han, Y. Matsui, N. Nagaosa, and Y. Tokura, Nature **465**, 901 (2010), © 2010 Macmillan Publishers Limited, <https://www.nature.com/>

preserved with continuous deformations such as bending or stretching. Topology can be invoked to explain the stability of single skyrmions and the skyrmion lattice. The skyrmion belongs to a topologically nontrivial class, whereas the helimagnetic and ferromagnetic phases are topologically trivial.^[3]

In a physically intuitive way the topological protection can be understood as follows: Fig. 2.3a shows a hexagonal skyrmion lattice, consisting of tubes of Bloch skyrmions surrounded by a ferromagnetic continuum. A continuous deformation of the spin configuration, such as “ironing out” the skyrmion into the ferromagnetic continuum, will only make the skyrmion radius increase, but the knot stays. In a more physical scenario the stability means that low-energy excitations such as phonons and magnons cannot annihilate the skyrmion knot. The skyrmion can only be annihilated by adding/removing enough thermal energy $k_B T$ (thermal energy) to cross the critical temperature or changing Zeeman potential energy $-\boldsymbol{\mu} \cdot \mathbf{B}$ to cross the critical field. In this way a phase transition is made from the skyrmion phase to topologically trivial magnetic order. The change of topology goes accompanied by the creation of hedgehog-like point defects which can be interpreted as emergent magnetic monopoles.^[22]

The topology of a spin structure is characterized by the *winding number*:

$$N = \frac{1}{4\pi} \int \left(\frac{\partial \mathbf{n}}{\partial x} \times \frac{\partial \mathbf{n}}{\partial y} \right) \cdot \mathbf{n} \, dx \, dy \quad (2.6)$$

Here $\mathbf{n}(x,y)=\mathbf{m}/|\mathbf{m}|$ is a unit vector parallel to the local magnetic moment $\mathbf{m}(x,y)$. For one-dimensional spin ordering this formula simplifies to:^[29]

$$N_{1D} = \frac{1}{2\pi} \int \frac{\partial\theta}{\partial x} dx \quad (2.7)$$

Here θ is the angle between neighbouring spins. Figure 2.6a shows a ferromagnetic chain. In this topologically trivial case the winding number is $N_{\text{FM}}=0$. One can now add a ferromagnetic domain of opposite magnetization into the ferromagnetic chain. This results in two domain walls with opposite rotational sense as illustrated in Fig.2.6b. The domain walls are drawn in orange. For this situation one again finds $N=0$. In the case of a radial cut-through of a Néel-type skyrmion (Sk) the winding number is $N_{\text{Sk}}=-1$ (Fig.2.6c). For the two-dimensional Bloch-type and Néel-type skyrmion the winding numbers according to Eq. 2.6 are $N_{\text{Sk}}=-1$.

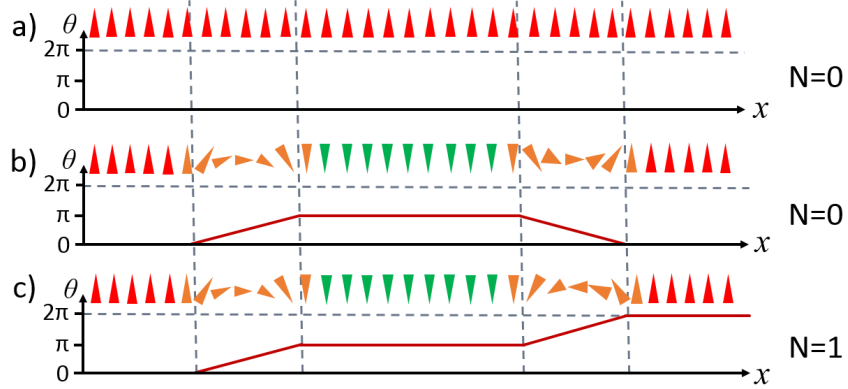


Figure 2.6: a) A ferromagnetic chain with winding number $N_{\text{FM}}=0$. b) Two domain walls (orange coloured) with opposite sense of rotation have $N=0$. c) A radial cut-through of a Néel-type Skyrmion. In this case $N_{\text{Néel}}=1$. The figure is inspired by the work from Ref. [29].

The interplay between conduction electrons and the skyrmion spin configuration leads to a variety of topological transport phenomena. These phenomena are described in terms of the emergent electromagnetic field associated with the skyrmion spin structure, which leads to observable phenomena such as the topological Hall effect and the skyrmion Hall effect.^[4] Moreover, the topological stability makes skyrmions of direct interest for spintronics applications.^[3,30]

2.3 Cu_2OSeO_3

2.3.1 Structural properties

Cu_2OSeO_3 belongs to the noncentrosymmetric cubic space group $P2_13$ (point group T). The tetartoidal point group T (or 23) contains the following symmetry elements: the identity i , a 2_1 -screw rotation about the $[100]$ axes, and a 3-proper rotation along the $[111]$ axes, as illustrated in Fig. 2.7a. The crystal symmetry is reflected in the crystal morphology. Figure 2.8a shows a Cu_2OSeO_3 crystal. The threefold symmetry of the naturally occurring facet shows that this is a $[111]$ -type facet. Materials belonging to space group $P2_13$ crystallize in a left- and right-handed enantiomer.³¹ One way to determine the (relative) handedness of a Cu_2OSeO_3 crystal is determining the sign of the natural optical activity, as discussed in chapter 4. No structural phase transitions have been reported in Cu_2OSeO_3 .^{32,33}

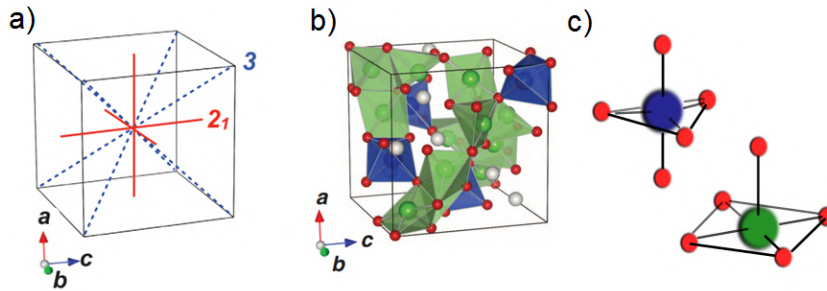


Figure 2.7: a) Symmetry elements for the noncentrosymmetric cubic space group $P2_13$. The 2_1 -screw rotation about the $[100]$ axes, and the 3-proper rotations around the $[111]$ axes are indicated with the red lines and blue dashed lines respectively. The picture is adapted from Ref. 16. From S. Seki, X. Z. Yu, S. Ishiwata, and Y. Tokura, Observation of skyrmions in a multiferroic material, *Science* **336**, 198 (2012), Reprinted with permission from AAAS. b) Structural unit cell of Cu_2OSeO_3 . The figure has been adapted from Ref. 16. From S. Seki, X. Z. Yu, S. Ishiwata, and Y. Tokura, Observation of skyrmions in a multiferroic material, *Science* **336**, 198 (2012), Reprinted with permission from AAAS. c) An illustration of the Cu-I trigonal bipyramid and the Cu-II square pyramid.

The unit cell of Cu_2OSeO_3 is shown in Fig. 2.7b (figure taken from Ref. 16). There are sixteen (magnetic) Cu^{2+} ($3d^9$) ions within the unit cell. The Cu-ions are located on the vertices of corned-shared tetrahedra. Each tetrahedron consists of one Cu ion in a trigonal bipyramid (site symmetry D_{3h}) and three square pyramid Cu ions (site symmetry C_{4v}) with oxygen ligands as illustrated in Fig. 2.7c. The real site symmetries are slightly lower, and given by C_{3v} for the Cu-I site and C_1 for the Cu-II site.³² There are $Z=8$ chemical formula units in the structural unit cell (16 Cu^{2+} -atoms in total). This gives a total of $7 \times 8 \times 4 = 168$ phonons. The phonon spectrum

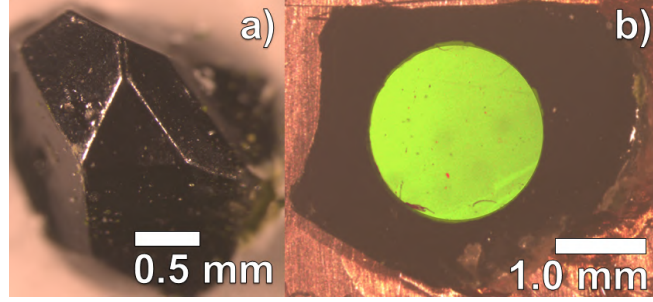


Figure 2.8: a) A Cu_2OSeO_3 crystal. The triangular facet, with sides of about 0.7 mm length, is a naturally occurring $[111]$ facet. b) The double-polished Cu_2OSeO_3 crystal used for the study described in chapter 4. Cu_2OSeO_3 crystals have a green colour.

is briefly discussed in chapter 5.

2.3.2 Electronic properties and excitations

Crystal field theory describes the degeneracy breaking of electron orbital states in a (magnetic) ion due to the static electric field from the neighbouring ligand ion charge density. The degeneracy breaking is dictated by the point symmetry of the magnetic ion.^[7] Figure 2.9 shows the crystal field splittings for the five $3d$ orbitals in a trigonal bipyramidal ligand field (the Cu-I ion) and a square pyramidal ligand field (the Cu-II ion).^[34] The ground state occupation of the 9 electrons in the Cu^{2+} ions are indicated by up and down pointing arrows. In the ground state the $3d_{z^2}$ orbital in the Cu-I ion is occupied by one electron (and one hole). The Cu-II ion has a hole in the $3d_{x^2-y^2}$ orbital.

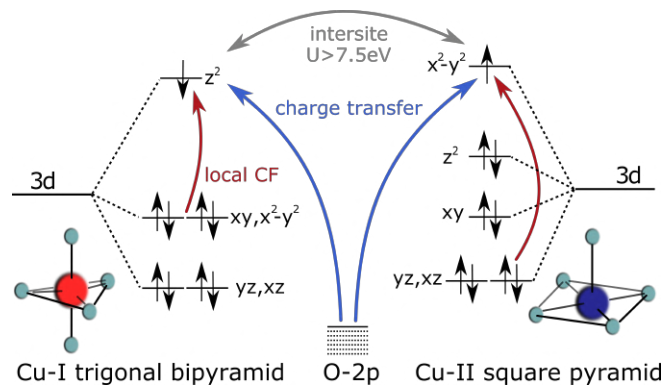


Figure 2.9: The $3d$ crystal-field splittings for the Cu-I (trigonal bipyramid) and Cu-II (square pyramid) ions. The dipole-active local crystal-field (CF) excitations are indicated with red arrows, and the charge-transfer excitations with blue arrows. Inter-site excitations between the Cu ions are indicated with the grey double arrow.

The electronic density of states of Cu₂OSeO₃ was calculated by Hubbard-augmented density functional theory (DFT+*U*) by Yang *et al.*,^[10] showing that Cu₂OSeO₃ is an insulator with a band gap of about $E_g \sim 2.1$ eV. This is in good agreement with the experimental value of $E_g \sim 2.4$ eV (see chapter 4). In Fig. 2.10 the total electronic density of states (DOS) is shown for spin-up and down polarization. The conduction band primarily has a Cu-3*d* orbital character, whereas the valence band primarily has a O-2*p* orbital character. PDOS refers to partial density of states. The conduction band of the Cu-I ion primarily originates in the unoccupied 3*d*_{z²} orbital and the valence band of the Cu-II ion in the unoccupied 3*d*_{x²-y²} orbital. The conduction band however does not have the indicated pure orbital character since the Cu-I 3*d*_{z²} and Cu-II 3*d*_{x²-y²} orbitals mix with other Cu²⁺-3*d* orbitals. The Cu²⁺-3*d* orbitals additionally mix with O²⁻-2*p*-orbitals. In the DFT+*U* calculation result of Fig. 2.10 this is reflected by that the Cu-I and Cu-II PDOS only partially makes up the total electronic DOS for both spin polarizations.

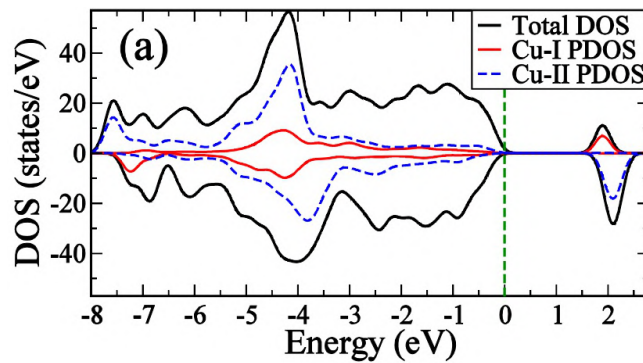


Figure 2.10: Spin-resolved electronic density of states (DOS) for Cu₂OSeO₃. Whether the DOS is positive or negative refers to the (arbitrary) opposite spin polarization. Black lines give the total density of states, whereas the red line and blue dashed line give the partial density of states for the Cu-I and Cu-II ion respectively. The conduction band primarily has a Cu-3*d* orbital character. The valence band has a mixed Cu-3*d* orbital and O-2*p* orbital character. Figure adapted from Ref. [10]. Reprinted figure with permission from J. H. Yang, Z. L. Li, X. Z. Lu, M. -H. Whangbo, Su-Huai Wei, X. G. Gong, and H. J. Xiang, Phys. Rev. Lett. **109**, 107203 (2012), <https://doi.org/10.1103/PhysRevLett.109.107203>, © Copyright 2012 by the American Physical Society.

The lowest hopping-type of electronic excitation in Cu₂OSeO₃ is from the O²⁻ 2*p*-levels to the Cu²⁺ 3*d*-levels, meaning that Cu₂OSeO₃ is a charge-transfer insulator in the Zaanen-Sawatsky-Allen classification of transition metal oxides.^[35] This excitation is indicated in Fig. 2.9 with blue arrows. The Hubbard-hopping excitation between Cu²⁺ sites is indicated with a grey double arrow, and has a large energy cost on the order of the Coulomb repulsion term *U*, which is on the order of $U \sim 7.5$ eV in Cu₂OSeO₃.^[11] On-

site electronic excitations within the crystal-field manifold, known as crystal-field transitions, are possible in the dipole approximation in Cu₂OSeO₃ since the trigonal bipyramid and square pyramid are inversion asymmetric. These excitations are indicated with the red arrows. In chapter 4 the dipole active electronic excitations in the visible range are discussed in more detail.

2.3.3 Magnetic order and magnetic excitations

Interactions and energy scales

Table 2.2 provides the representative energy scales for the magnetic interactions in Cu₂OSeO₃. The first column indicates the energy type and the second and third columns give the energy scale in kelvin and meV. The Heisenberg and Dzyaloshinski-Moriya exchange coupling paths in Cu₂OSeO₃ can be subdivided in stronger and weaker couplings. For some couplings the DM-exchange can have a relatively large contribution $|\vec{D}_{ij}|/|J_{ij}| \sim 0.6$ with respect to the Heisenberg exchange.

Table 2.2: Representative energy scales in Cu₂OSeO₃. The first column indicates the energy type. The Dzyaloshinskii-Moriya-exchange is abbreviated as DM-exchange. The exchange paths in Cu₂OSeO₃ can be subdivided in comparatively strong and weak paths. The second and third column give the energy order of magnitude in kelvin and meV for the respective energy types.

Energy type	$E(\text{K})$	$E(\text{meV})$	comment	Ref.
Heisenberg exchange J_{ij} , strong paths	130 - 170	11 - 15		11
Heisenberg exchange J_{ij} , weak paths	25 - 45	2 - 4		11
DM-exchange $ \vec{D}_{ij} $, strong paths	7 - 15	0.6 - 1.2	$ \vec{D}_{ij} / J_{ij} \sim 0.05 - 0.08$	11
DM-exchange $ \vec{D}_{ij} $, weak paths	5 - 15	0.4 - 1.2	$ \vec{D}_{ij} / J_{ij} \sim 0.1 - 0.6$	11
anisotropy energy E_{ani}	0.15	0.012		36
Zeeman-energy $g\mu_B B$	0.08	0.006	with $g_{\text{eff}} \approx 2.1$ and $B = 50 \text{ mT}$	6
thermal energy $k_B T$	57	5	inside skyrmion lattice phase	16

Cu_4 spin cluster formation and spin cluster excitations

The subdivision of the exchange energy scales into a strong and weak exchange coupling leads to the formation of long-range ordered spin clusters. This can be understood by considering the magnetic unit cell of Cu_2OSeO_3 , as shown in Fig. 2.11a. Both the Cu-I (red spheres) and Cu-II Cu^{2+} -ions (blue spheres) have 9 electrons, giving a $S = 1/2$ ground state. The electrons are localized, which makes Cu_2OSeO_3 an insulator. The $S = 1/2$ spins are located on the vertices of corner-shared distorted tetrahedra. DFT+ U calculations^[11] reveal that these tetrahedra can be separated into tetrahedra of “stronger” and “weaker” exchange energy scales.^[6,11] The blue lines are predominantly ferromagnetic exchange couplings and the red lines predominantly antiferromagnetic exchange couplings. The full lines represent strong exchange couplings and the dashed lines weak exchange couplings. A subset of exchange paths are indicated in Fig. 2.11a as $J_{F,s}$, $J_{AF,s}$, $J_{F,w}$, and $J_{AF,w}$ where the subscripts refer to (anti)ferromagnetic and strong or weak exchange. The DM-interaction isn’t indicated in the illustration for the sake of clarity. However, also for this interaction the separation into strong and weak exchange paths is valid (see Table 2.2).

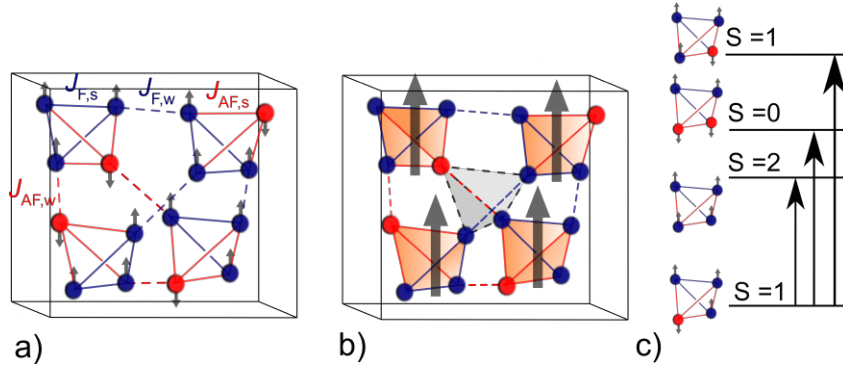


Figure 2.11: a) The magnetic unit cell in Cu_2OSeO_3 . The blue lines are predominantly ferromagnetic and the red line predominantly antiferromagnetic exchange paths. The full lines are strong, and the dashed lines weak exchange paths. A subset of exchange interaction paths are indicated as $J_{F,s}$, $J_{AF,s}$, $J_{F,w}$, and $J_{AF,w}$ where the subscripts refer to (anti)ferromagnetic and strong or weak exchange. The strong exchange paths lead to effective $S = 1$ spin clusters. DM-interaction also contributes to the exchange paths (the DM-contribution is however not indicated) b) The orange shaded tetrahedra are the strongly coupled $S = 1$ tetrahedra. The spin clusters are coupled through the weaker inter-cluster exchange paths (dashed lines), which form a weakly coupled cluster (the grey shaded tetrahedron) c) The spin cluster ground state in the non-interacting cluster model is $|g\rangle = |1, S^z\rangle_{A_1}$. The excitations within the spin cluster can be understood as spin flip excitations into a singlet $|0, S^z\rangle_{A_1}$ state, a quintet $|2, S^z\rangle_{A_1}$ state and an excited $|1, S^z\rangle_{A_1}$ triplet state. The illustrated states are “classical” states. However, in reality the states are a quantum superposition of states. The figures are made with inspiration drawn from Ref. [11]

The stronger Heisenberg and Dzyaloshinskii-Moriya (DM) exchange interactions couples four localized $S = 1/2$ spins into a three-up-one-down $S = 1$ entity as depicted by orange shaded tetrahedra in Fig. 2.11b. Here the Cu-II ions couple predominantly ferromagnetically through $J_{F,s}$ and the Cu-I couples predominantly antiferromagnetically to the Cu-II ions through $J_{AF,s}$. Predominantly means that it should be understood that even inside the cluster a small spin canting is present through the (strong) DM-interaction. The strongly coupled $S = 1$ clusters form a magnetic trillium lattice, where these clusters are coupled through the weaker exchange paths $J_{F,w}$ and $J_{AF,w}$, which form the “weakly coupled” grey shaded tetrahedron (see Fig. 2.11b).³⁷ The $S = 1$ spin clusters form far above the macroscopic ordering temperature $T_C \approx 58$ K. This is evidenced in the magnetic susceptibility, which shows a gradual crossover from a $S = 1/2$ to a $S = 1$ Curie-Weiss constant, as is shown in Fig. 2.12 (Ref. 38). More conclusive verification of the spin cluster formation came from spin wave dispersion studies,^{38,39} terahertz-transmission studies,^{6,40} and quantum calculations.^{11,41}

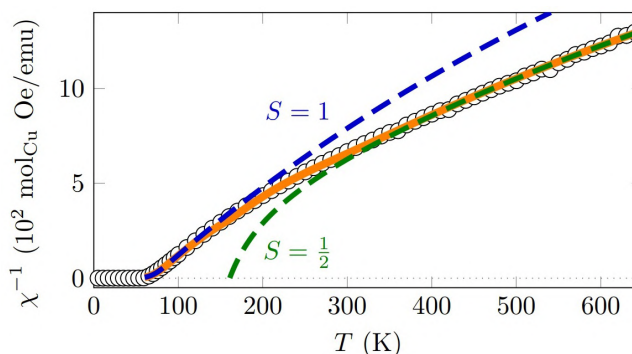


Figure 2.12: Inverse magnetic susceptibility $1/\chi$ for helimagnetic Cu_2OSeO_3 . The circles give the measured inverse susceptibility, and the orange line the Curie-Weiss-fit in the paramagnetic phase. At high temperatures the susceptibility is best fitted with a Curie “constant” for a $S = 1/2$ paramagnet (green dashed line). At lower temperatures in the paramagnetic phase the spin system gradually changes into a system which has a Curie “constant” for a $S = 1$ paramagnet (blue dashed line). The crossover in Curie constant is an indication for spin cluster formation in Cu_2OSeO_3 . Below $T_C \approx 58$ K Cu_2OSeO_3 is helimagnetically ordered. Figure adapted from Ref. 38. Reprinted figure with permission from G. S. Tucker, J. S. White, J. Romhányi, D. Szaller, I. Kézsmárki, B. Roessli, U. Stuhr, A. Margrez, F. Groitl, P. Babkevich, P. Huang, I. Živković, and H. M. Rønnow, Phys. Rev. B **93**, 054401 (2016). © Copyright 2016 by the American Physical Society.

The excited cluster states can be obtained by symmetry principles. The point symmetry of a single cluster (only considering the magnetic Cu^{2+} ions) is given by C_{3v} . Under this symmetry, the $2^4 = 16$ -dimensional Hilbert space of a single tetrahedron splits up in the ground state A_1 -triplet $|g\rangle = |1, S^z\rangle_{A_1}$, and into A_1 -singlet $|0, S^z\rangle_{A_1}$, A_1 -quintet $|2, S^z\rangle_{A_1}$, and E-triplet $|1, S^z\rangle_{A_1}$

excited states, as indicated in Fig. 2.11c. In the state notation $|S, S^z\rangle_R$ the spin quantum number is given by S , and the secondary spin quantum number by S_z . The label R refers to the irreducible representations of the cluster's C_{3v} point group. A classical picture for the single cluster states is shown in Fig. 2.11c. In the ground state $|g\rangle = |1, S^z\rangle_{A_1}$ the minority spin-1/2 is located on the Cu-I site, whereas in the excited state $|1, S^z\rangle_E$ the minority spin is located on the Cu-II site. For the $|0, S^z\rangle_{A_1}$ and A_1 -quintet $|2, S^z\rangle_{A_1}$ a spin-1/2 on the Cu-II, or Cu-I site respectively is flipped with respect to the ground state order. It should be noted that in reality the cluster states are *not* described by these classical states, but by a quantum superposition of the classical states.^[11,41]

The interaction between clusters has important consequences for the magnetic states in the cluster. The degeneracy in the secondary spin quantum number S_z for the different states is partially raised,^[41] and the quintet state mixes into the triplet ground state. This ground state mixing is shown to be of key importance in explaining, for instance, the reduced magnetic moment of Cu₂OSeO₃, the helimagnetic wavelength, and the Curie temperature.^[32,41] The refinement of the cluster model is discussed in more detail in chapter 5.

The long-range cluster formation leads to distinctly different types of spin excitations with long-range and internal Cu₄ cluster character. Figure 5.5 shows the spin wave excitation spectrum of Cu₂OSeO₃ in the helimagnetic phase. A clear division into high-energy and low-energy excitation spin wave branches can be observed. The high-energy *internal* cluster modes were introduced in the previous paragraph as spin flip excitations of the triplet tetrahedron, as illustrated in Fig. 2.11c. This picture applies well in the paramagnetic phase when local clusters have already formed. However, as seen in the neutron spectrum, this simple picture is not fully valid anymore in the long-range ordered phase, since the internal modes now show dispersion. The low-energy *external* spin excitations contain, among others, the magnetic Goldstone mode. The Goldstone mode corresponds to the collective motion of long-range ordered spin clusters.^[6,39,41] Such a separation into external and internal modes is also discussed in the context of molecular crystals, which shows low-energy (acoustic) phonon excitations characteristic of the crystalline nature, but also high-energy molecular vibration-like excitations characteristic of the individual molecular constituents.^[42] As such, we can regard Cu₂OSeO₃ as a generalized solid-state molecular crystal of spin nature.^[43]

The spin excitation spectrum is discussed in more detail in chapter 5. Special emphasis will be given to the Raman-activity of the high-energy internal cluster modes, as well as their characteristic temperature dependence. In chapter 8 the Raman-active $\Delta S^z = \pm 1$ internal cluster excitations are used as a probe of photoinduced long-range and internal cluster order parameter dynamics.

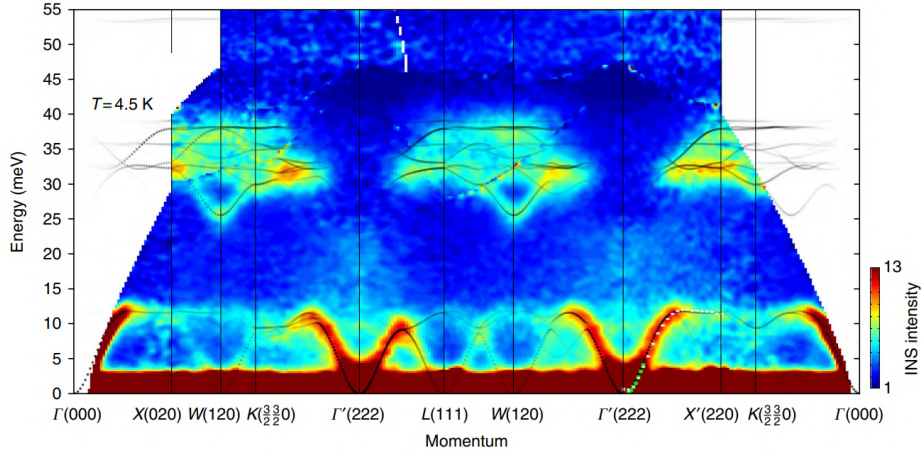


Figure 2.13: The inelastic neutron spectrum in the helimagnetic phase at $T = 4.5$ K. The spin wave excitation spectrum shows a clear separation into high-energy *internal* cluster modes, and low-energy *external* cluster modes. Figure adapted from Ref. [39] (published under Creative Commons Attribution 4.0 International License, CC BY 4.0).

Long-range order and collective excitations

Different metamagnetic phases stabilize under the presence of an external magnetic field. The critical fields for which the metamagnetic phase transitions are induced strongly depend on temperature, as seen in the phase diagram of Fig. 4.6 (field applied along the [111] crystallographic axis). Below $T_C \approx 58$ K the $S = 1$ spin clusters form long-range helimagnetic order up to a critical field of about 50 mT. The helix' wavelength is $\lambda_h \approx 62$ nm.^[24]

Applied magnetic fields of a few tenths of mT are enough to fully lift the degeneracy of the helical domains, giving a conical type of order with the propagation vector \mathbf{q} along the applied field. Above a second critical field of 50-200 mT the system is driven into the field-polarized ferrimagnetic phase, where all tetrahedral $S = 1$ entities are aligned to the magnetic field. The skyrmion lattice phase (SkL) is located within a narrow field-temperature window just below $T_C \approx 58$ K for moderate applied fields of the order of 20-50 mT.^[16,24] Just above $T_C \approx 58$ K, within a window of $\Delta T \approx 1$ K the fluctuating regime is observed.^[44] The phase diagram appears slightly different for fields applied along different crystallographic directions due to the small magnetic anisotropy.^[24] In chapter 4 the phase diagram and phase transitions for bulk Cu_2OSeO_3 with a field applied along the crystallographic [111] axis is discussed in more detail.

In literature there is a spread of critical field values reported for the metamagnetic phase transitions. This is because of the sample dependent demagnetization factor.^[45] A thin plate (thickness $\approx 221 \mu\text{m}$), with large de-

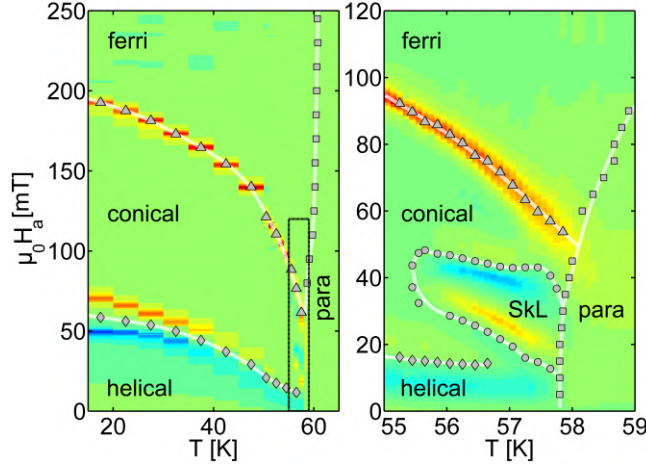


Figure 2.14: The magnetic phase diagram of Cu_2OSeO_3 . $\mu_0 H_a$ is the applied magnetic field along the crystallographic (111) direction given in mT. The left panel shows the magnetic phase diagram for a large $(\mu_0 H_a, T)$ range, whereas the right panel gives a zoom-in around the skyrmion lattice phase (SkL). The triangles indicate the conical-ferrimagnetic phase boundary. Diamonds give the helical-conical phase boundary. The SkL phase boundary is indicated by the circles. The phase boundary between ordered phases and the paramagnetic phase is indicated by the squares.

magnetization factor, was used to map the metamagnetic phase diagram shown in Fig. 4.6. Stronger external fields are necessary to magnetize a thin plate, in comparison to, for instance, cubic shaped samples. The skyrmion phase can greatly extend in temperature and applied fields when a bulk sample is made ultrathin (a thickness on the 100 nm scale).¹⁷ The extended skyrmion phase stability in milled-down samples results from an enhanced uniaxial anisotropy, which suppresses the conical phase.⁴⁶

The long-range metamagnetic order results in various low-energy ($\sim \mu\text{eV}$) spin-wave excitations.^{47,48} In the ferrimagnetic phase one mode exists: a uniform spin precession known as the ferromagnetic resonance mode or Kittel mode. Two low-energy modes can be excited in the helical and conical phase. These collective excitations are a periodic spin compression parallel ($+\mathbf{Q}$) or anti-parallel ($-\mathbf{Q}$) along the helix \mathbf{q} -vector, as depicted in Fig. 2.15a. Lastly, in the skyrmion lattice phase three collective modes exist. These are a clockwise (CW), and counterclockwise (CCW) rotation of Skyrmions, and a breathing mode, as depicted in Figs. 2.15b,c, and d. Here individual skyrmions inside the skyrmion lattice all rotate or breathe in-phase with respect to each other.⁴⁷ An illustration of the spin precession within a single skyrmion for these modes is shown in Fig. 2.15. The CW and CCW modes lead to an in-plane magnetization modulation, whereas the breathing mode leads to an out-of-plane magnetization modulation.

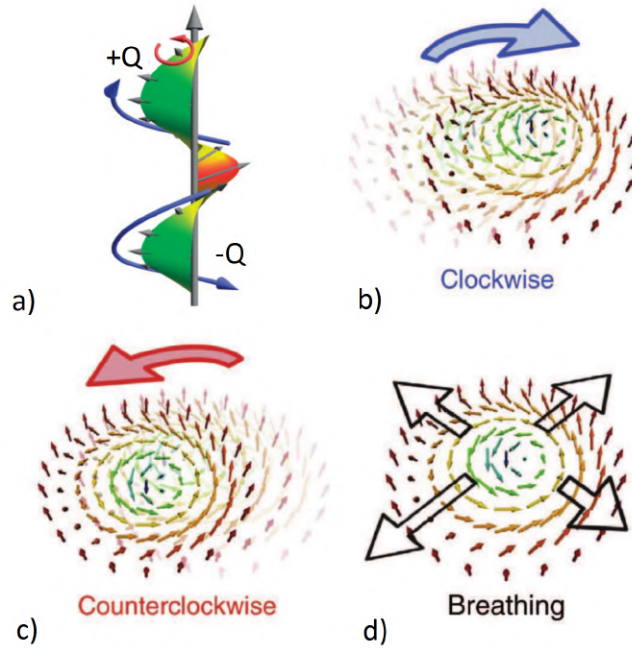


Figure 2.15: a) The helimagnon is a uniform spin precession parallel or anti-parallel to the helical ordering vector (grey arrow). Figure adapted from Ref. [48] Adapted by permission from Springer Nature: Springer Nature, Nature Materials, Universal helimagnon and skyrmion excitations in metallic, semiconducting and insulating chiral magnets, T. Schwarze, J. Waizner, M. Garst, A. Bauer, I. Stasinopoulos, H. Berger, C. Pfleiderer and D. Grundler, Nat. Mater. **14**, 478 (2015), © 2015 Macmillan Publishers Limited, <https://www.nature.com/nmat/> b) Clockwise rotation of a single skyrmion. This mode leads to an in-plane magnetization modulation. c) The counterclockwise skyrmion rotation. d) The skyrmion breathing mode. This mode leads to an out-of-plane magnetization modulation. Figures b, c, and d adapted from Ref. [49] Adapted by permission from Springer Nature: Springer Nature, Nature Communications, Microwave magnetoelectric effect via skyrmion resonance modes in a helimagnetic multiferroic, Y. Okamura, F. Kagawa, M. Mochizuki, M. Kubota, S. Seki, S. Ishiwata, M. Kawasaki, Y. Onose, and Y. Tokura, Nat. Comm. **4**, 2391 (2013), © 2013 Macmillan Publishers Limited, <https://www.nature.com/ncomms/>

The most commonly used technique to measure these low-energy spin wave excitations is microwave spectroscopy, [49,50] This technique has been applied successfully in determining the eigenfrequencies for a large set of skyrmion materials. [51] Another technique, more of interest to this thesis work is pump-probe magneto-optical spectroscopy. In the case of transparent samples such as Cu_2OSeO_3 , the ultrafast excitation of magnetic modes can be realized through the inverse Faraday effect. [52] Here, ultrafast circularly polarized pump pulses act as a transient magnetic field, which dynamically magnetizes a sample (anti-)parallel to the wave vector \mathbf{k} of the light,

depending on the light helicity. This effective field can act as an impulsive trigger to dynamically drive magnetic resonances.⁵³ The strength of the inverse Faraday effect is dictated by the magneto-optical susceptibility χ_{MO} . An efficient ultrafast driving of skyrmion modes can be expected based on the strong χ_{MO} in the visible range in Cu_2OSeO_3 (see chapter 4). Indeed, in the study of Ogawa *et al.* (Ref. 52), circularly polarized IR-pulses are used to dynamically drive the CW, CCW, and breathing modes in Cu_2OSeO_3 . The experimental geometry is shown in Fig. 2.16a. An external field is applied along the crystallographic $[\bar{1}10]$ direction. The orange tubes represent tubes of skyrmions. The polarization rotation is probed in Voight-geometry with 2.2 eV photon energy. A circularly polarized IR-probe of 0.95 eV is used, which falls in the transparency region below the crystal-field absorption region. In Fig. 2.16b it is seen that oppositely circularly polarized pump pulses dynamically trigger the CCW and CW mode, which have a frequency of about 1.1 GHz and 1.3 GHz respectively. The polar geometry, shown in Fig. 2.16c, allows to observe the out-of-plane breathing mode, with a characteristic frequency of $f \sim 1.7$ GHz.

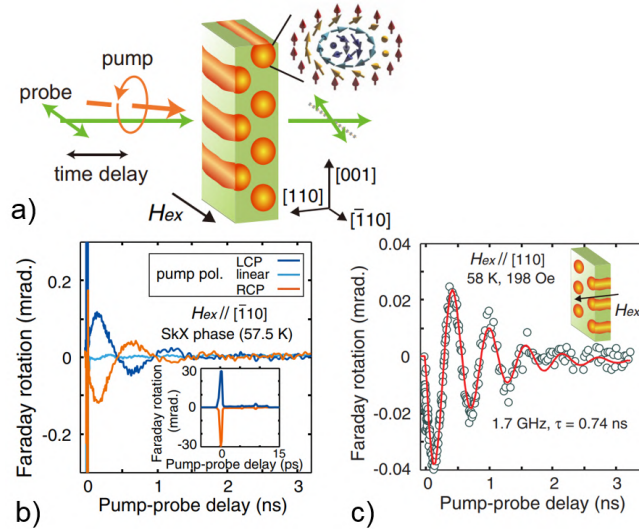


Figure 2.16: The inverse Faraday experiment of Ogawa *et al.* (Ref. 52): a) Probing is performed with 2.2 eV probe pulses in a Voigt-geometry with the external magnetic field applied along $\mathbf{H}_a \parallel [\bar{1}10]$. Pumping is performed via the inverse Faraday effect with circularly polarized 0.95 eV pump pulses. b) The CW and CCW modes are excited by the inverse Faraday effect. A magnetization modulation is visible in the Voigt geometry. It can be seen that the modes have an opposite phase. c) In the polar Faraday geometry the breathing mode is visible. Figures adapted from Ref. 52 (published under Creative Commons Attribution 4.0 International License, CC BY 4.0).

2.3.4 Magneto-electricity

Cu_2OSeO_3 is a unique skyrmion host material owing to its magneto-electric nature.^[16] This implies that under an externally applied magnetic field a macroscopic electric polarization is established. Through the magneto-electric coupling the Skyrmion lattice also carries a finite polarization. This makes the skyrmion lattice in Cu_2OSeO_3 electric-field controllable, and thus of interest for skyrmion manipulation.^[54]

The microscopic magneto-electric coupling mechanism in Cu_2OSeO_3 is *pd-hybridization*.^[55] The principle is illustrated in Fig. 2.17. On a single magnetic site Cu^{2+} site, with neighboring O^{2-} ligand, a spin-direction dependent hybridization arising from the spin-orbit coupling establishes a local polarization along the bond direction. When the local polarizations \mathbf{p} due to the field-induced spin alignment do not cancel out, as is the case for specific space groups, a macroscopic electric polarization is established. The magneto-electricity in Cu_2OSeO_3 thus is anisotropic in nature. Only for a field applied along $\mathbf{H}_a \parallel [110]$ and $\mathbf{H}_a \parallel [111]$ an electric polarization \mathbf{P} is established.^[16] This directional anisotropy is a fingerprint of the *pd-hybridization* microscopic origin of the magneto-electric effect in Cu_2OSeO_3 .^[56] The enhanced natural optical activity in the helimagnetic phase is a strong indication of magneto-electric coupling, as discussed in chapter 4.

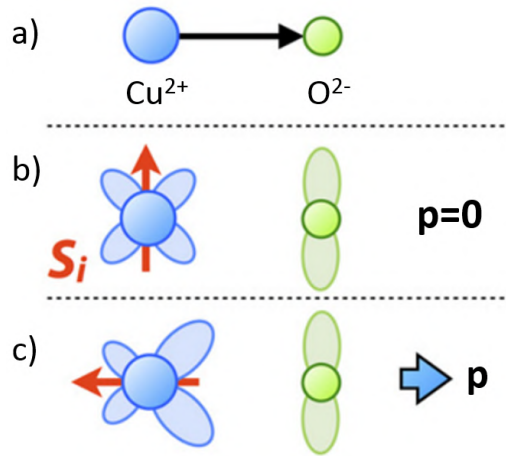


Figure 2.17: Illustration of the magneto-electric *pd*-hybridization principle. On a single magnetic site Cu^{2+} site, with neighboring O^{2-} ion (Fig. a), a spin-direction dependent hybridization (Fig. b) arising from the spin-orbit coupling establishes a local polarization along the bond direction (Fig. c). Figure adapted from Ref. [55] Y. Tokura, S. Seki, and N. Nagaosa, Multiferroics of spin origin, Rep. Prog. Phys. **77**, 076501 (2014). Reproduced with permission of IOP Publishing.

2.4 Acknowledgements and own contributions

I would like to thank Aisha Aqeel from the University of Groningen (Groningen, The Netherlands) for providing the Cu₂OSeO₃ crystals, shown in the photographs of Fig. 2.8. The major part of this chapter is written by myself, and comprises a literature overview on magnetic order in noncentrosymmetric materials and the material properties of Cu₂OSeO₃. The text on the electronic properties and long-range magnetic order of Cu₂OSeO₃ contains parts of research described in chapter 4. These parts of chapter 2 have been written by myself, with contributions by P. H. M. van Loosdrecht, M. Grüninger, and Ignacio Vergara.

2.5 Bibliography

- [1] A. Bogdanov and A. Hubert, Thermodynamically stable magnetic vortex states in magnetic crystals, *J. Magn. Magn. Mater.* **138**, 255 (1994).
- [2] U. K. Röbber, A. A. Leonov, and A. N. Bogdanov, Chiral skyrmionic matter in non-centrosymmetric magnets, *J. Phys.: Conf. Ser.* **303**, 012105 (2011).
- [3] N. Nagaosa and Y. Tokura, Topological properties and dynamics of magnetic skyrmions, *Nat. Nanotechnol.* **8**, 899 (2013).
- [4] N. Kanazawa, S. Seki, and Y. Tokura, Noncentrosymmetric magnets hosting magnetic skyrmions, *Adv. Mater.* **29**, 1603227 (2017).
- [5] S. Buhrandt and L. Fritz, Skyrmion lattice phase in three-dimensional chiral magnets from Monte Carlo simulations, *Phys. Rev. B* **88**, 195137 (2013).
- [6] M. Ozerov, J. Romhányi, M. Belesi, H. Berger, J.-Ph. Ansermet, J. van den Brink, J. Wosnitza, S. A. Zvyagin, and I. Rousochatzakis, Establishing the fundamental magnetic interactions in the chiral skyrmionic mott insulator Cu₂OSeO₃ by terahertz electron spin resonance, *Phys. Rev. Lett.*, **113**, 157205 (2014).
- [7] S. Blundell, *Magnetism In Condensed Matter*, (Oxford University Press, 2001).
- [8] B. Schweflinghaus, B. Zimmermann, M. Heide, G. Bihlmayer, and S. Blügel. Role of Dzyaloshinskii-Moriya interaction for magnetism in transition-metal chains at Pt step edges, *Phys. Rev. B* **94**, 024403 (2016).
- [9] T. Moriya, Superexchange interaction and weak ferromagnetism, *Phys. Rev.* **120**, 91 (1960).
- [10] J. H. Yang, Z. L. Li, X. Z. Lu, M.-H. Whangbo, S.-H. Wei, X. G. Gong, and H. J. Xiang, Strong Dzyaloshinskii-Moriya interaction and origin of ferroelectricity in Cu₂OSeO₃, *Phys. Rev. Lett.* **109**, 107203 (2012).
- [11] O. Janson, I. Rousochatzakis, A. A. Tsirlin, M. Belesi, A. A. Leonov, U. K. Röbber, J. Van den Brink, and H. Rosner, The quantum nature of skyrmions and half-skyrmions in Cu₂OSeO₃, *Nat. Commun.* **5**, 5376 (2014).
- [12] K. Everschor, *Current-induced dynamics of chiral magnetic structures: skyrmions, emergent electrodynamics and spin-transfer torques*, PhD thesis, Universität zu Köln, 2012.
- [13] S. Mühlbauer, B. Binz, F. Jonietz, C. Pfleiderer, A. Rosch, A. Neubauer, R. Georgii, and P. Böni, Skyrmion lattice in a chiral magnet, *Science*, **323**, 915 (2009).

- [14] P. Bak and M. H. Jensen, Theory of helical magnetic structures and phase transitions in MnSi and FeGe, *J. Phys. C: Solid St. Phys.* **13**, L881 (1980).
- [15] I. Kézsmárki, S. Bordács, P. Milde, E. Neuber, L. M. Eng, J. S. White, H. M. Rønnow, C. D. Dewhurst, M. Mochizuki, K. Yanai, H. Nakamura, D. Ehlers, V. Tsurkan, and A. Loidl, Néel-type skyrmion lattice with confined orientation in the polar magnetic semiconductor GaV₄S₈, *Nat. Mater.* **14**, 1116 (2015).
- [16] S. Seki, X. Z. Yu, S. Ishiwata, and Y. Tokura, Observation of skyrmions in a multi-ferroic material, *Science* **336**, 198 (2012).
- [17] X. Z. Yu, Y. Onose, N. Kanazawa, J. H. Park, J. H. Han, Y. Matsui, N. Nagaosa, and Y. Tokura, Real-space observation of a two-dimensional Skyrmion crystal, *Nature* **465**, 901 (2010).
- [18] A. Bauer, A. Chacon, M. Wagner, M. Halder, R. Georgii, A. Rosch, C. Pfleiderer, and M. Garst. Symmetry breaking, slow relaxation dynamics, and topological defects at the field-induced helix reorientation in MnSi, *Phys. Rev. B* **95**, 024429 (2017).
- [19] A correction in the form of thermal fluctuations needs to be added to the mean-field solution $\mathcal{F}(\mathbf{M})$ to stabilize the Skyrmion phase, as discussed in Refs. [12](#) and [13](#).
- [20] J. Zaanen, Fast electrons tie quantum knots, *Science* **323**, 888 (2009).
- [21] A. Rosch, Magnetic skyrmions: Particles or waves, *Nat. Mater.* **15**, 1231 (2016).
- [22] P. Milde, D. Köhler, J. Seidel, L. M. Eng, A. Bauer, A. Chacon, J. Kindervater, S. Mühlbauer, C. Pfleiderer, S. Buhbrandt, C. Schütte, and A. Rosch, Unwinding of a skyrmion lattice by magnetic monopoles, *Science* **340**, 1076 (2013).
- [23] S. Heinze, K. Von Bergmann, M. Menzel, J. Brede, A. Kubetzka, R. Wiesendanger, G. Bihlmayer, and S. Blügel, Spontaneous atomic-scale magnetic skyrmion lattice in two dimensions, *Nat. Phys.* **7**, 713 (2011).
- [24] T. Adams, A. Chacon, M. Wagner, A. Bauer, G. Brandl, B. Pedersen, H. Berger, P. Lemmens, and C. Pfleiderer, Long-wavelength helimagnetic order and skyrmion lattice phase in Cu₂OSeO₃, *Phys. Rev. Lett.* **108**, 237204 (2012).
- [25] M. C. Langner, S. Roy, S. K. Mishra, J. C. T. Lee, X. W. Shi, M. A. Hossain, Y.-D. Chuang, S. Seki, Y. Tokura, S. D. Kevan, and R. W. Schoenlein, Coupled skyrmion sublattices in Cu₂OSeO₃, *Phys. Rev. Lett.* **112**, 167202 (2014).
- [26] K. Everschor-Sitte, J. Masell, R. M. Reeve, and M. Kläui, Perspective: Magnetic skyrmions - overview of recent progress in an active research field, *J. Appl. Phys.* **124**, 240901 (2018).
- [27] S. Bordács, A. Butykai, B. G. Szigeti, J. S. White, R. Cubitt, A. O. Leonov, S. Widmann, D. Ehlers, H.-A. Krug von Nidda, V. Tsurkan, A. Loidl, and I. Kézsmárki, Equilibrium Skyrmion lattice ground state in a polar easy-plane magnet, *Sci. Rep.* **7**, 7584 (2017).
- [28] A. O. Leonov and I. Kézsmárki, Skyrmion robustness in noncentrosymmetric magnets with axial symmetry: The role of anisotropy and tilted magnetic fields, *Phys. Rev. B* **96**, 214413 (2017).
- [29] M. Menzel, *Non-collinear magnetic ground states observed in iron nanostructures on iridium surfaces*, PhD thesis, University of Hamburg, 2011.
- [30] J. Müller, Magnetic skyrmions on a two-lane racetrack, *New. J. Phys.* **19**, 025002 (2017).
- [31] V. Dyadkin, K. Prša, S. V. Grigoriev, J. S. White, P. Huang, H. M. Rønnow, A. Magrez, C. D. Dewhurst, and D. Chernyshov, Chirality of structure and magnetism in the magnetoelectric compound Cu₂OSeO₃. *Phys. Rev. B* **89**, 140409 (2014).

- [32] J.-W. G. Bos, C. V. Colin, and T. T. M. Palstra, Magnetoelectric coupling in the cubic ferrimagnet Cu_2OSeO_3 , *Phys. Rev. B* **78**, 094416 (2008).
- [33] V. P. Gnezdilov, K. V. Lamonova, Y. G. Pashkevich, P. Lemmens, H. Berger, F. Bussy, and S. L. Gnatchenko, Magnetoelectricity in the ferrimagnetic Cu_2OSeO_3 : symmetry analysis and Raman scattering study, *Low Temp. Phys.* **36**, 550 (2010).
- [34] M. I. Aroyo, A. Kirov, C. Capillas, J. M. Perez-Mato, and H. Wondratschek, *Bilbao Crystallographic Server. II. Representations of crystallographic point groups and space groups*, *Acta Crystallogr. Sect. A* **62**, 115 (2006).
- [35] J. Zaanen, G. A. Sawatzky, and J. W. Allen, Band gaps and electronic structure of transition-metal compounds, *Phys. Rev. Lett.* **55**, 418 (1985).
- [36] M. I. Kobets, K. G. Dergachev, E. N. Khatsko, A. I. Rykova, P. Lemmens, D. Wulferding, and H. Berger, Microwave absorption in the frustrated ferrimagnet Cu_2OSeO_3 , *J. Low Temp. Phys.* **36**, 176 (2010).
- [37] J. M. Hopkinson, and H.-Y. Kee, Geometric frustration inherent to the trillium lattice, a sublattice of the B20 structure, *Phys. Rev. B* **74**, 224441 (2006).
- [38] G. S. Tucker, J. S. White, J. Romhányi, D. Szaller, I. Kézsmárki, B. Roessli, U. Stuhr, A. Magrez, F. Groitl, P. Babkevich, P. Huang, I. Živković, and H. M. Rønnow, Spin excitations in the skyrmion host Cu_2OSeO_3 , *Phys. Rev. B* **93**, 054401 (2016).
- [39] P. Y. Portnichenko, J. Romhányi, Y. A. Onykiienko, A. Henschel, M. Schmidt, A. S. Cameron, M. A. Surmach, J. A. Lim, J. T. Park, A. Schneidewind, D. L. Abernathy, H. Rosner, J. van den Brink, and D. Inosov, Magnon spectrum of the helimagnetic insulator Cu_2OSeO_3 , *Nat. Commun.* **7**, 10725 (2016).
- [40] N. J. Laurita, G. G. Marcus, B. A. Trump, J. Kindervater, M. B. Stone, T. M. McQueen, C. L. Broholm, and N. P. Armitage, Low-energy magnon dynamics and magneto-optics of the skyrmionic Mott insulator Cu_2OSeO_3 , *Phys. Rev. B* **95**, 235155 (2017).
- [41] J. Romhányi, J. van den Brink, and I. Rousochatzakis, Entangled tetrahedron ground state and excitations of the magnetoelectric skyrmion material Cu_2OSeO_3 , *Phys. Rev. B* **90**, 140404 (2014).
- [42] G. Venkataraman and V. C. Sanhi, External vibrations in complex crystals. *Rev. Mod. Phys.* **42**, 409 (1970).
- [43] S. V. Streltsov and D. I. Khomskii, Orbital physics in transition metal compounds: new trends, *Phys. Usp.* **60**, 1121-1146 (2017).
- [44] M. Janoschek, M. Garst, A. Bauer, P. Krautscheid, R. Georgii, P. Böni, and C. Pfleiderer, Fluctuation-induced first-order phase transition in dzyaloshinskii-moriya helimagnets, *Phys. Rev. B* **87**, 134407 (2013).
- [45] A. Bauer and C. Pfleiderer, in *Topological Structures in Ferroic Materials: Domain Walls, Vortices and Skyrmions*, chapter *Generic Aspects of Skyrmion Lattices in Chiral Magnets*, (Springer International Publishing, 2016).
- [46] A. B. Butenko, A. A. Leonov, U. K. Röbner, and A. N. Bogdanov. Stabilization of skyrmion textures by uniaxial distortions in noncentrosymmetric cubic helimagnets, *Phys. Rev. B* **82**, 052403 (2010).
- [47] M. Mochizuki, Spin-wave modes and their intense excitation effects in skyrmion crystals, *Phys. Rev. Lett.* **108**, 017601 (2012).
- [48] T. Schwarze, J. Waizner, M. Garst, A. Bauer, I. Stasinopoulos, H. Berger, C. Pfleiderer, and D. Grundler, Universal helimagnon and skyrmion excitations in metallic, semiconducting and insulating chiral magnets, *Nat. Mater.* **14**, 478 (2015).

-
- [49] Y. Okamura, F. Kagawa, M. Mochizuki, M. Kubota, S. Seki, S. Ishiwata, M. Kawasaki, Y. Onose, and Y. Tokura, Microwave magnetoelectric effect via skyrmion resonance modes in a helimagnetic multiferroic, *Nat. Comm.* **4**, 2391 (2013).
 - [50] Y. Onose, Y. Okamura, S. Seki, S. Ishiwata, and Y. Tokura, Observation of magnetic excitations of skyrmion crystal in a helimagnetic insulator Cu_2OSeO_3 . *Phys. Rev. Lett.* **109**, 037603 (2012).
 - [51] M. Garst, J. Waizner, and D. Grundler, Collective spin excitations of helices and magnetic skyrmions: review and perspectives of magnonics in non-centrosymmetric magnets, *J. Phys. D Appl. Phys.* **50**, 293002 (2017).
 - [52] N. Ogawa, S. Seki, and Y. Tokura, Ultrafast optical excitation of magnetic skyrmions, *Sci. Rep.* **5**, 9552 (2015).
 - [53] A. V. Kimel, A. Kirilyuk, P. A. Usachev, R. V. Pisarev, A. M Balbashov, and T. Rasing, Ultrafast non-thermal control of magnetization by instantaneous photomagnetic pulses, *Nature* **435**, 655 (2005).
 - [54] J. S. White, K. Prša, P. Huang, A. A. Omrani, I. Živković, M. Bartkowiak, H. Berger, A. Magrez, J. L. Gavilano, G. Nagy, J. Zang, and H. M. Rønnow, Electric-field-induced skyrmion distortion and giant lattice rotation in the magnetoelectric insulator Cu_2OSeO_3 , *Phys. Rev. Lett.* **113**, 107203 (2014).
 - [55] Y. Tokura, S. Seki, and N. Nagaosa, Multiferroics of spin origin, *Rep. Prog. Phys.* **77**, 076501 (2014).
 - [56] P. Milde, E. Neuber, A. Bauer, C. Pfleiderer, H. Berger, and L. M. Eng, Heuristic description of magnetoelectricity of Cu_2OSeO_3 , *Nano Lett.* **16**, 5612 (2016).

Chapter 3

Crystal optics and polarization spectroscopy

3.1 Introduction

In this chapter an introduction to linear crystal optics, and polarization modulation spectroscopy is given. First, the linear, circular and elliptical polarization states of light are defined in the Jones-formalism. From the Maxwell equations and the constitutive equations the fundamental equation of crystal optics is derived. This equation relates the dielectric tensor to the four electromagnetic propagation modes in matter. Crystal symmetry and time-reversal symmetry dictate the form of the dielectric tensor, and which optical anisotropies can be observed. A non-exhaustive overview of linear crystal optics phenomena is given, and categorized according to whether inversion symmetry, time-reversal symmetry, and their combined operation are broken. The relation between the dielectric tensor, and linear polarization rotation in the case of materials with circular eigenmodes are derived. The constructed polarization spectroscopy setup is described, and accompanied with the measurement theory and principles. A magneto-optical Kerr effect study of single crystalline SrRuO₃ is described as test measurement.

3.2 Polarized light

3.2.1 The electromagnetic wave

In vacuum the (microscopic) Maxwell equations are given by:

$$\nabla \times \mathbf{B} = \frac{1}{c} \frac{\partial \mathbf{E}}{\partial t} \quad (3.1a)$$

$$\nabla \times \mathbf{E} = -\frac{1}{c} \frac{\partial \mathbf{B}}{\partial t} \quad (3.1b)$$

$$\nabla \cdot \mathbf{E} = 0 \quad (3.1c)$$

$$\nabla \cdot \mathbf{B} = 0 \quad (3.1d)$$

Here \mathbf{E} is the electric field, \mathbf{B} the magnetic induction, and c the speed of light. From these equations the following wave equations are derived:

$$\nabla^2 \mathbf{E}(\mathbf{r}, t) - \frac{1}{c^2} \frac{\partial^2}{\partial t^2} \mathbf{E}(\mathbf{r}, t) = 0 \quad (3.2a)$$

$$\nabla^2 \mathbf{B}(\mathbf{r}, t) - \frac{1}{c^2} \frac{\partial^2}{\partial t^2} \mathbf{B}(\mathbf{r}, t) = 0 \quad (3.2b)$$

For a monochromatic wave (in frequency ω and wave vector \mathbf{k}) the solutions are:

$$\mathbf{E}(\mathbf{r}, t) = \mathbf{E}_0 e^{i(\mathbf{k} \cdot \mathbf{r} - \omega t)} \quad \text{and} \quad \mathbf{B}(\mathbf{r}, t) = \mathbf{B}_0 e^{i(\mathbf{k} \cdot \mathbf{r} - \omega t)} \quad (3.3)$$

As such, it is understood that electromagnetic radiation is a wave, consisting of a synchronously oscillating electric field $\mathbf{E}(\mathbf{r}, t)$ and magnetic induction $\mathbf{B}(\mathbf{r}, t)$ with frequency ω , propagating at the speed of light c , with wave vector \mathbf{k} . The electromagnetic wave (EM-wave) however can be fully described with the electric field, since the electric field amplitude \mathbf{E}_0 , and magnetic induction amplitude \mathbf{B}_0 are related by:

$$\omega \mathbf{B}_0 = c \mathbf{k} \times \mathbf{E}_0 \quad (3.4)$$

Furthermore:

$$\mathbf{k} \cdot \mathbf{E}_0 = 0 \quad \text{and} \quad \mathbf{k} \cdot \mathbf{B}_0 = 0 \quad (3.5)$$

The electric field and magnetic induction components are thus orthogonal to each other and orthogonal to the wave vector. As such, the electromagnetic wave is a transverse wave, and carries a distinct polarization. For linearly polarized light the polarization plane is fixed, as illustrated in Fig. 3.1. The electric field vector traces out a circle or an ellipse in time in the case of circular or elliptical polarization respectively.

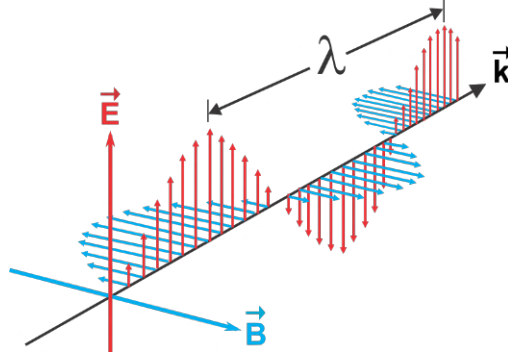


Figure 3.1: A linearly polarized electromagnetic wave. The electric field \mathbf{E} oscillates in the vertical plane. The magnetic induction component \mathbf{B} is orthogonal to the electric field. The wave propagates in the direction $\mathbf{k} \parallel \mathbf{E} \times \mathbf{B}$. Figure adapted from Ref. [1] (figure released in public domain).

3.2.2 Linear and circular polarization

The different polarization states of an electromagnetic wave, and the action of optical elements on a polarized electromagnetic wave, can be described in vector and matrix form in the so-called Jones-calculus formalism.^[2] This formalism is a simplification of the Müller-matrix and Stokes-vector formalism, which in addition to the fully polarized wave also allows to describe the partially polarized and unpolarized electromagnetic wave.^[3] In the Jones-formalism a normalized EM-wave propagating in the positive z -direction is described by:

$$\begin{aligned}
 \vec{E}(\omega, t) &= \frac{1}{\sqrt{E_{0,x}^2 + E_{0,y}^2}} \begin{pmatrix} E_{0,x} e^{i(kz - \omega t)} \\ E_{0,y} e^{i(kz - \omega t + \delta)} \end{pmatrix} \\
 &= \frac{1}{\sqrt{E_{0,x}^2 + E_{0,y}^2}} \begin{pmatrix} E_{0,x} \\ E_{0,y} e^{i\delta} \end{pmatrix} e^{i(kz - \omega t)} \\
 &\equiv \frac{1}{\sqrt{E_{0,x}^2 + E_{0,y}^2}} \cdot \mathcal{J} \cdot e^{i(kz - \omega t)}
 \end{aligned} \tag{3.6}$$

The vector \mathcal{J} is known as the Jones-vector for the electric field, and describes the polarization state of the light. The basis vectors below span the polarization plane and correspond to linearly polarized light along the x and y direction respectively:

$$\hat{e}_x = \begin{pmatrix} 1 \\ 0 \end{pmatrix} \qquad \hat{e}_y = \begin{pmatrix} 0 \\ 1 \end{pmatrix} \tag{3.7}$$

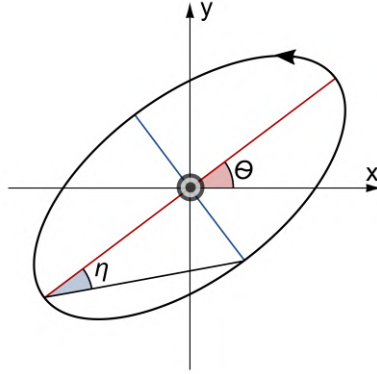


Figure 3.2: Elliptically polarized light: The polarization plane is rotated over an angle $+\theta$. The ellipticity angle is given by η . The z-axis points out of the paper. Note that in this two dimensional depiction the angle *appears* to be counterclockwise. It is however a positive rotation for a right-handed system.

A phase shift of $\delta = \pm\frac{\pi}{2}$ between the \hat{e}_x and \hat{e}_y components leads to circularly polarized light. From here on it is important to make a decision on how to label the $\delta = +\frac{\pi}{2}$ and $\delta = -\frac{\pi}{2}$ vectors. This is done either as seen from the source or as seen from the observer. The connection between right circularly polarized light and right-handed quantum mechanical photon helicity is readily made when we define the polarization states as seen from the source.^[2] In this case the right (RCP) and left (LCP) circularly polarized light basis vectors are:

$$\text{RCP} : \hat{e}_+ = \frac{1}{\sqrt{2}} \begin{pmatrix} 1 \\ +i \end{pmatrix} \quad \text{LCP} : \hat{e}_- = \frac{1}{\sqrt{2}} \begin{pmatrix} 1 \\ -i \end{pmatrix} \quad (3.8)$$

Switching from linear to circular polarization basis is realized by the following transformation matrix \vec{F} :

$$\begin{pmatrix} \hat{e}_+ \\ \hat{e}_- \end{pmatrix} = \frac{1}{\sqrt{2}} \begin{pmatrix} 1 & i \\ 1 & -i \end{pmatrix} \begin{pmatrix} \hat{e}_x \\ \hat{e}_y \end{pmatrix} \equiv \vec{F} \cdot \begin{pmatrix} \hat{e}_x \\ \hat{e}_y \end{pmatrix} \quad (3.9)$$

Switching from circular to linear polarization basis is realized by the inverse transformation matrix \vec{F}^{-1} :

$$\begin{pmatrix} \hat{e}_x \\ \hat{e}_y \end{pmatrix} = \frac{1}{\sqrt{2}} \begin{pmatrix} 1 & 1 \\ -i & i \end{pmatrix} \begin{pmatrix} \hat{e}_+ \\ \hat{e}_- \end{pmatrix} = \vec{F}^{-1} \cdot \begin{pmatrix} \hat{e}_+ \\ \hat{e}_- \end{pmatrix} \quad (3.10)$$

3.2.3 Elliptical polarization

The generalization of circular into elliptical light proceeds in the following way: start with RCP light in the Cartesian basis, as given by Eq. [3.8](#). The

polarization circle is turned into an ellipse by multiplying the x and y components by $A \cos \eta$, and $A \sin \eta$ respectively. The ellipticity ratio is defined by $\epsilon = \frac{l_{\text{minor}}}{l_{\text{major}}} \equiv \tan(\eta) \equiv \frac{A \sin \eta}{A \cos \eta}$, where η is the ellipticity angle. So:

$$\hat{e}_+ = \frac{1}{\sqrt{2}} \begin{pmatrix} 1 \\ +i \end{pmatrix} \rightarrow \frac{1}{\sqrt{2}} \begin{pmatrix} A \cos \eta \\ +iA \sin \eta \end{pmatrix} \rightarrow \dots \quad (3.11)$$

After this step the ellipse is clockwise (right-handed) rotated over the angle $+\theta$, as illustrated in Fig. 3.2.

$$\dots \rightarrow \frac{1}{\sqrt{2}} \begin{pmatrix} A \cos \eta \\ +iA \sin \eta \end{pmatrix} \rightarrow \frac{1}{\sqrt{2}} \begin{pmatrix} \cos \theta & -\sin \theta \\ \sin \theta & \cos \theta \end{pmatrix} \cdot \begin{pmatrix} A \cos \eta \\ +iA \sin \eta \end{pmatrix} = \hat{E}_{\text{ell.}} \quad (3.12)$$

Moving to the circular basis representation by multiplying $\hat{E}_{\text{elliptical}}$ by \vec{F} according to Eq. 3.9 allows to extract the circular components of the elliptically polarized wave:

$$\begin{pmatrix} \hat{E}_{\text{ell.}+} \\ \hat{E}_{\text{ell.}-} \end{pmatrix} = \frac{A}{2} \begin{pmatrix} (\cos \eta - \sin \eta)e^{+i\theta} \\ (\cos \eta + \sin \eta)e^{-i\theta} \end{pmatrix} \quad (3.13)$$

The complex *polarization variable* $\zeta_{\text{ell.}}$ is now defined as the ratio of the circular components:

$$\zeta_{\text{ell.}} \equiv \frac{\hat{E}_{\text{ell.}+}}{\hat{E}_{\text{ell.}-}} = \frac{1 - \tan \eta}{1 + \tan \eta} e^{i2\theta} \approx 1 + 2(i\theta - \eta) \quad (3.14)$$

The approximation holds for an appropriately small polarization rotation θ and ellipticity angle η . In this case the ellipticity ratio $\epsilon = \tan(\eta) \approx \eta$ is equal to the ellipticity angle.

The exact rotation θ , and ellipticity ratio $\epsilon = \tan(\eta)$ as a function of the complex polarization variable $\zeta_{\text{ell.}}$ are:

$$\theta = \frac{1}{2} \arg(\zeta_{\text{ell.}}) \quad \epsilon = \tan(\eta) = \frac{1 - |\zeta_{\text{ell.}}|}{1 + |\zeta_{\text{ell.}}|} \quad (3.15)$$

The exact ellipticity angle is:

$$\eta = \tan^{-1} \left(\frac{1 - |\zeta_{\text{ell.}}|}{1 + |\zeta_{\text{ell.}}|} \right) \quad (3.16)$$

3.3 Fundamental equation of crystal optics

The propagation of an electromagnetic wave through a material fulfills the (macroscopic) Maxwell equations. These are given by:

$$\nabla \times \mathbf{H} = \frac{1}{c} \frac{\partial \mathbf{D}}{\partial t} + \frac{\mathbf{j}}{c} \quad (3.17a)$$

$$\nabla \times \mathbf{E} = -\frac{1}{c} \frac{\partial \mathbf{B}}{\partial t} \quad (3.17b)$$

$$\nabla \cdot \mathbf{D} = \rho \quad (3.17c)$$

$$\nabla \cdot \mathbf{B} = 0 \quad (3.17d)$$

Here

$$\begin{aligned} \mathbf{E} & \text{ is the EM-wave's electric field} \\ \mathbf{D} & \text{ is the electric induction} \\ \mathbf{H} & \text{ is the EM-wave's magnetic field} \\ \mathbf{B} & \text{ is the magnetic induction} \\ \mathbf{j} & \text{ is the current density} \\ \rho & \text{ is the charge density} \\ c & \text{ is the light speed} \end{aligned} \quad (3.18)$$

Furthermore, three constitutive equations hold for the propagation of an electromagnetic wave through matter:

$$\mathbf{D} = \boldsymbol{\epsilon} \mathbf{E} \quad (3.19a)$$

$$\mathbf{B} = \boldsymbol{\mu} \mathbf{H} \quad (3.19b)$$

$$\mathbf{j} = \boldsymbol{\sigma} \mathbf{E} \quad (3.19c)$$

Here $\boldsymbol{\epsilon}$ and $\boldsymbol{\mu}$ are the dielectric permittivity and magnetic permeability tensors respectively,^[4] and $\boldsymbol{\sigma}$ is the specific conductivity tensor. These equations describe the response of matter to an electric and magnetic field. The constitutive relation $\mathbf{D} = \boldsymbol{\epsilon} \mathbf{E}$ is alternatively written as $\mathbf{D} = \epsilon_0(\mathbf{1} + \boldsymbol{\chi}) \mathbf{E}$, with $\boldsymbol{\chi}$ being the electric susceptibility tensor and ϵ_0 the vacuum permittivity. Here $\mathbf{P} = \boldsymbol{\chi} \mathbf{E}$ is the electric polarization. The constitutive relation $\mathbf{B} = \boldsymbol{\mu} \mathbf{H}$ is alternatively written as $\mathbf{B} = \mu_0(\mathbf{1} + \boldsymbol{\chi}_m) \mathbf{H}$, with $\boldsymbol{\chi}_m$ being the magnetic susceptibility tensor and μ_0 the vacuum permeability. Here $\mathbf{M} = \boldsymbol{\chi}_m \mathbf{H}$ is the magnetization field.

The material response to an electromagnetic wave at optical frequencies can be described by an effective $\boldsymbol{\epsilon}$ tensor.^{[5][6]} The constitutive equation

$\mathbf{j} = \boldsymbol{\sigma}\mathbf{E}$ describes that the electric field of light can induce a current density \mathbf{j} . This however can be taken into account by defining a complex dielectric permittivity tensor, and a renormalized electric induction. In this case the Maxwell equation can be used with $\mathbf{j} = 0$, and $\rho = 0$, and an effective electric induction \mathbf{D} .^[5] The magnetization of a material cannot follow the rapid oscillation of near infrared/visible electromagnetic radiation since there are no magnetic resonances at the corresponding light frequencies ω . Thus the magnetic susceptibility $\chi_m(\omega) = 0$ in crystal optics, and the magnetic permeability $\boldsymbol{\mu}$ can be taken equal to the unit tensor $\mathbf{1}$. This means that for light-matter response at optical frequencies only the constitutive equation $\mathbf{D} = \boldsymbol{\epsilon}\mathbf{E}$ plays a role.^[8] Magneto-optical effects in the optical frequency range can thus always be described solely by an effective dielectric tensor $\boldsymbol{\epsilon}$.^[6]

Electromagnetic waves are plane waves of the form (cf. Eq. 3.3):

$$\mathbf{G}(\mathbf{r}, t) = \mathbf{G}_0 e^{i(\mathbf{k}\cdot\mathbf{r} - \omega t)} \quad (3.20)$$

and fulfill the Maxwell equations and constitutive equations. Here \mathbf{G}_0 is the amplitude of the electric (\mathbf{E}_0) or magnetic induction (\mathbf{B}_0), ω is the circular frequency, and \mathbf{k} is the wave vector, which is expressed as:

$$\mathbf{k} = \frac{\omega n}{c} \hat{\mathbf{s}} \quad (3.21)$$

in terms of the (complex) refractive index n , and the light speed c . Here $\hat{\mathbf{s}}$ is a unit vector in the direction of the wave normal. It is also helpful to define:

$$\mathbf{s} = \frac{c}{\omega} \mathbf{k} = n \hat{\mathbf{s}} \quad (3.22)$$

Mind here the difference between the unit vector $\hat{\mathbf{s}}$, and the non-unit vector \mathbf{s} . For a plane wave, as expressed in Eq. 3.20, the identity $\nabla \times \mathbf{G} = -i\mathbf{G} \times \mathbf{k}$ holds. Using this relation, the first two Maxwell equations give:

$$n\mathbf{H} \times \hat{\mathbf{s}} = \mathbf{D} \quad (3.23a)$$

$$-n\mathbf{E} \times \hat{\mathbf{s}} = \mathbf{B} \quad (3.23b)$$

for a plane wave. With $\boldsymbol{\mu} = \mathbf{1}$, thus $\mathbf{H} = \mathbf{B}$ (cf. Eq. 3.19b), the magnetic field can be eliminated from the above two expressions. This allows to express the displacement field (cf. Eq. 3.19a) as:

$$\mathbf{D} = n^2\mathbf{E} - (\mathbf{s} \cdot \mathbf{E})\mathbf{s} = \boldsymbol{\epsilon}\mathbf{E} \quad (3.24)$$

in terms of the non-unitary vector \mathbf{s} , defined in Eq. 3.22. Rearrangement gives:

$$\boldsymbol{\epsilon}\mathbf{E} + (\mathbf{s} \cdot \mathbf{E})\mathbf{s} = n^2\mathbf{E} \quad (3.25)$$

Referring to Eq. 3.22, it is seen that $\mathbf{s} \cdot \mathbf{s} = \sum_j s_j s_j = n^2$. With $\mathbf{s} \cdot \mathbf{E} = \sum_j s_j E_j$, and $\boldsymbol{\epsilon} \cdot \mathbf{E} = \sum_j \epsilon_{ihj} E_j$, in summation form, expression 3.24 is rewritten as:

$$\sum_j (\epsilon_{ihj} + s_i s_j) E_j = n^2 I E_i \quad (3.26)$$

These last two equations (either in vector form in Eq. 3.25 or summation form in Eq. 3.26) are referred to as the *fundamental equation of crystal optics*. This equation is the relevant starting point to derive how light propagates through anisotropic matter described by an effective dielectric tensor ϵ_{ij} . The solutions are four proper electromagnetic waves with polarizations \mathbf{E}_0 , refractive indices n , and wave vector $\mathbf{k} = \frac{\omega n}{c} \hat{\mathbf{s}}$. The polarization states \mathbf{E}_0 of the waves are either linear, circular or elliptical depending on the dielectric tensor symmetry. The electromagnetic waves are “proper” waves in the sense that they do not alter their polarization state when they propagate through a medium. Two proper waves have the wave vector $+\mathbf{k}$, and two proper waves have the wave vector $-\mathbf{k}$. When the solutions for $+\mathbf{k}$, and $-\mathbf{k}$ are equal, the light propagation is *reciprocal*. When the solutions for $+\mathbf{k}$, and $-\mathbf{k}$ are different the light propagation is *non-reciprocal*.

3.4 Dielectric tensor and optical anisotropies

3.4.1 The dielectric tensor

The response of matter to an electromagnetic wave in the optical range can be fully described by an effective dielectric tensor $\boldsymbol{\epsilon}$ as discussed in the previous paragraph. The dependence of $\boldsymbol{\epsilon}$ on the frequency ω is called *frequency dispersion*. Spatial inhomogeneity, as is the case in for instance a chiral crystal, leads to a wave vector \mathbf{k} dependent dielectric tensor. 10, 11 This dependence is named *spatial dispersion*.

In addition, $\boldsymbol{\epsilon}$ can depend on a magnetic field, either expressed as \mathbf{H} (“field”) or \mathbf{B} (“induction”), and the magnetization field \mathbf{M} . 6 It depends on the material’s characteristics whether the \mathbf{M} field is relevant, or the \mathbf{H} field (alternatively \mathbf{B} field). We should furthermore think about internal and external fields. 12 For materials with no finite magnetic moments, so diamagnets, the magneto-optical effect results from the direct action of the magnetic field on the orbital motion of electrons, leading to a Zeeman splitting $\Delta E = g\mu_B B_i$, with B_i being the internal B -field strength. In diamagnets the demagnetization effect is negligible. This means that the internal and external H -field strengths are approximately equal ($H_i \approx H_a$), so $B_i \approx \mu_0 H_i \approx \mu_0 H_a$, 12 and $\Delta E \approx g\mu_B \mu_0 H_a$. Thus for diamagnetic materials $\boldsymbol{\epsilon}$ is best expressed as a function of (external) field $\mathbf{H}_{(a)}$. This diamagnetic contribution to $\boldsymbol{\epsilon}$ is present in any material. In materials with finite mag-

netic momenta, the diamagnetic contribution gets overshadowed by spin-orbit coupling effects. These can, to some extent, be thought of as a field of an order 100 – 1000 times stronger than magnetic fields which can be produced in a lab.^[2,6,7] So for materials with finite magnetic momenta (e.g. a paramagnet or ferromagnet) the dielectric tensor effectively depends on \mathbf{M} ,^[6] and the role of the external magnetic field reduces to a means to magnetize a sample along the applied field direction.^[7]

The dielectric permittivity tensor for a chiral magnetized material thus takes the form $\epsilon(\omega, \mathbf{k}, \mathbf{M})$.^[11] The effects of spatial dispersion and magnetization, can be taken into account by expanding ϵ in first and second order terms of \mathbf{k} and \mathbf{M} .^[4,10,11] This is most easily done in the Einstein summation notation:

$$\epsilon_{ij} = \epsilon_{ij}^0 + i\gamma_{ijl}k_l + \alpha_{ijlm}k_l k_m + f_{ijn}M_n + g_{ijnp}M_n M_p + \eta_{ijln}k_l M_n \quad (3.27)$$

The contributions are in order: the zero'th order dielectric tensor ϵ_{ij}^0 , the first and second order spatial dispersion terms $i\gamma_{ijl}k_l$ and $\alpha_{ijlm}k_l k_m$, first and second order magneto-optical effects $f_{ijn}M_n$ and $g_{ijnp}M_n M_p$, and a magneto-spatial cross term $\eta_{ijln}k_l M_n$. These terms result in many types of optical anisotropies. In the most general form the tensor would have nine different real and imaginary components for a single frequency. Luckily, the crystallographic point group, whether the material is invariant under inversion i , time-reversal t (presence or absence of magnetic order/magnetization), the combined operation $i \cdot t$, and whether the material is *lossless* (non-absorbing) in the optical frequency range, puts restrictions on the form of the material tensor ϵ , and thereby which optical effects can be observed.^[5]

In Table [3.1](#) an overview of linear optical anisotropies is given. A phenomenon can be observed when the indicated operations for inversion i , time-reversal t , and the combined operation $i \cdot t$ aren't (–) a symmetry of the material anymore. The operation indicated with (+) may still be a valid symmetry operation to observe the respective optical phenomenon. The last column indicates from which dielectric tensor expansion term the optical effect originates. In the following paragraphs the anisotropies will be discussed individually. Not every anisotropy will be discussed in as much detail as the other, since some are rather rare or not directly relevant to this thesis work.

Table 3.1: Overview of optical anisotropies in a chiral magnet: An anisotropy can be observed when the indicated operations for inversion i , time-reversal t , and the combined operation $i \cdot t$ aren't $(-)$ a symmetry of the material anymore. The operation indicated with $(+)$ may still be a valid symmetry operation to observe the respective optical phenomenon. The last column indicates from which dielectric tensor expansion term the optical effect originates.

crystal optics phenomenon	i	t	i and t	$i \cdot t$	expansion term
linear birefringence and dichroism	+	+	+	+	ϵ_{ij}^0
natural circular birefringence and dichroism	-	+	-	-	$i\gamma_{ij}k_l$
second-order spatial birefringence and dichroism	+	+	+	+	$\alpha_{ijklm}k_lk_m$
magnetic circular birefringence and dichroism	+	-	-	-	$f_{ijn}M_n$
magnetic linear birefringence and dichroism	+	-	-	-	$g_{ijnp}M_nM_p$
gyrotropic birefringence and dichroism	-	-	-	+	$i\gamma_{ij}k_l$
magneto-chiral birefringence and dichroism	-	-	-	-	$\eta_{ijn}k_lM_n$
optical magnetoelectric birefringence and dichroism	-	-	-	-	$\phi_{ijlmq}k_lM_nP_q$

In magnetoelectric and multiferroic materials a (spontaneous) ferroelectric polarization \mathbf{P} can be induced. The effect of the ferroelectric polarization \mathbf{P} on the dielectric tensor can again be taken into account by expansion in first and second order terms of \mathbf{P} .

$$\Delta\epsilon_{ij} = s_{ijq}P_q + t_{ijqr}P_qP_r + \phi_{ijlnq}k_lM_nP_q \quad (3.28)$$

The first and second term are the linear and quadratic electro-optic effect, which will not be further discussed.^[13] The last term is a combination of spatial, magnetic, and ferroelectric origin, and leads to optical magnetoelectric birefringence and dichroism. This phenomenon is also relevant to chiral magnetic media, and will be briefly touched upon in the context of nonreciprocal dichroism.

3.4.2 The zero'th order tensor ϵ_{ij}^0

The tensor ϵ_{ij}^0 is non-zero for all crystals. When only this tensor element is present, the two proper propagating waves in a crystal are linearly polarized, mutually orthogonal, and reciprocal. In the optical range the tensor $\epsilon_{ij}^0 = \epsilon_{ij}^0 + i\epsilon_{ij}^0$ always has a real symmetric part ϵ_{ij}^0 . The imaginary symmetric part ϵ_{ij}^0 is nonzero when the material is absorptive in the optical range. The crystallographic point group of a crystal imposes constraints on the tensor elements. Three cases are distinguished. In isotropic crystals (cubic point groups) $\epsilon_{xx} = \epsilon_{yy} = \epsilon_{zz} \neq 0$. Alternatively, the principle refractive indices $n_1 = \sqrt{\epsilon_{xx}}$, $n_2 = \sqrt{\epsilon_{yy}}$, and $n_3 = \sqrt{\epsilon_{zz}}$ are all equal. In uniaxial crystals (like tetragonal or hexagonal lattice) $\epsilon_{xx} = \epsilon_{yy} \neq \epsilon_{zz}$, and there is only one direction, the optic axis in z-direction, where the refractive indices for the linear polarization states, - mostly labelled n_o and n_e for ordinary and extraordinary refractive index -, are equal.^[13] In all other propagation directions linear birefringence, or alternatively named double breaking, is observed, for which $n_o \neq n_e$. In biaxial crystals, such as orthorhombic or monoclinic point groups, $\epsilon_{xx} \neq \epsilon_{yy} \neq \epsilon_{zz}$. When light propagates along any of the crystallographic axes, linear birefringence is always observed (under the premise that the size of the effect is measurable). However, there are still two optic axes, along which light can propagate without experiencing linear birefringence. In order to find these special axes in a biaxial crystal, one has to solve the optical indicatrix equation.^[14]

Anisotropy in the imaginary part ϵ_{ij}^0 leads to linear dichroism. The point group again imposes symmetry restrictions. Evidently, the material cannot be lossless in order to observe linear dichroism. Analogous to the case of birefringence there are optical axes along which dichroism is not observed. These axes do not necessarily have to coincide with the optical axes for linear birefringence.

3.4.3 Spatial dispersion effects

Since the light wavelength λ is large with respect to the unit cell length a , the dependence of ϵ on \mathbf{k} can be treated as a perturbation $\Delta\epsilon_{ij} = i\gamma_{ijl}k_l + \alpha_{ijkl}k_lk_m$. The terms scale in magnitude as $\sim(a/\lambda)$ and $\sim(a/\lambda)^2$, where a is the unit cell length and λ the wavelength of the electromagnetic wave. These effects originate in the fact that the displacement field \mathbf{D} at a given point not only depends on the local electric field, but also on the local electric field at neighboring sites. This makes the displacement field, or dielectric tensor, wave vector dependent.^[5,10,15]

The first order expansion term $i\gamma_{ijl}k_l$ leads to off-diagonal elements in the dielectric tensor. This third-rank tensor γ_{ijl} vanishes for crystals with an inversion center.^[10,15,16] The *anti-symmetric* real part of γ_{ijl} leads to natural circular birefringence, and the antisymmetric imaginary part to natural circular dichroism. In order to observe circular dichroism, the material must not be lossless. If one considers a lossless crystal with broken inversion symmetry, the proper waves are left- and right-circularly polarized, with different refractive indices n_{LCP} and n_{RCP} . When linearly polarized light propagates through a crystal with broken inversion symmetry the linear polarization plane is rotated, as illustrated in Figs. 3.3a and b along the lines of Fresnel.^[14] In the illustration the left circularly polarized light (LCP) has a larger phase velocity than the right circularly polarized light (RCP) component, meaning $n_{\text{RCP}} > n_{\text{LCP}}$. This leads to a (left-handed) polarization rotation. This optical phenomenon is referred to as natural optical activity. In Fig. 3.3c the case of circular dichroism is illustrated. In Fig. 3.4a a naturally optically active crystal is shown, represented by a “gyration” vector γ ,^[5] where the light propagates through the sample twice. After traversing the sample for the first time, the linear polarization plane has clockwise rotated over an angle θ_{NOA} . Upon counter-propagation the polarization plane again rotates over a clockwise angle θ_{NOA} (clockwise as seen from the mirror source), by which the total polarization rotation is zero. The natural optical activity rotation sense is the same for $+\mathbf{k}$ and $-\mathbf{k}$ propagation, making the effect reciprocal.

The *symmetric* real part of γ_{ijl} leads to a rather exotic linear birefringence called *gyrotropic birefringence*, or non-reciprocal linear birefringence.^[5,18] The symmetry conditions to observe this phenomenon are broken inversion symmetry i , and broken time-reversal symmetry, while the product of the two, $i\cdot t$ can still be a symmetry of the material.^[5,18] This occurs in some magneto-electric materials. It is evident that it is difficult to separate this contribution from other linear birefringence mechanisms such as magnetic linear birefringence. Gyrotropic birefringence has however been observed in Cr_2O_3 .^[19] The non-reciprocity implies that the refractive indices for $+\mathbf{k}$ and $-\mathbf{k}$ propagating linearly polarized light are different. The absorptive component, *gyrotropic dichroism*, thus leads to a different absorption coefficient

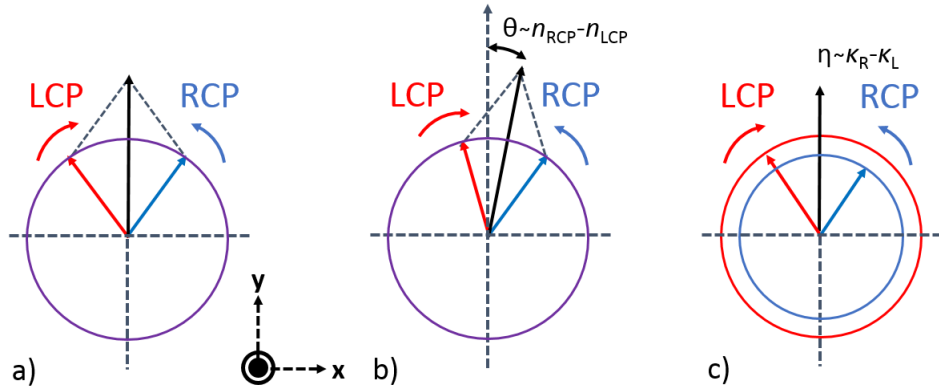


Figure 3.3: a) Fresnel's explanation of optical rotation (Ref. [14]). Linearly polarized light (black arrow) is the equal superposition of left (LCP) and right circular polarization (RCP) states (red and blue arrow respectively). Mind the definition of the right-handed Cartesian system, as in Fig. 3.2. The light thus propagates out of the paper. b) A difference in the refractive indices for the LCP and RCP polarization states, i.e. $n_{\text{RCP}} \neq n_{\text{LCP}}$, results in a phase difference for the two states upon transmission (or reflection). In this case the RCP wave travels slower than the LCP wave, which implies $n_{\text{RCP}} > n_{\text{LCP}}$. This leads to a polarization plane rotation $\theta \sim n_{\text{RCP}} - n_{\text{LCP}}$ of the incident linearly polarized light. In the defined Cartesian coordinate system this corresponds to a left-handed rotation. c) The difference in absorption for the LCP and RCP states leads to circular dichroism. Drawn here is the case where for the imaginary part of the refractive index $\kappa_{\text{RCP}} > \kappa_{\text{LCP}}$ holds.

for linearly polarized light depending on the propagation direction.

The second order spatial perturbation term $\alpha_{ijkl}k_l k_m$ has the interesting consequence that *every* material is in principle linearly birefringent. This linear birefringence for instance was observed in seemingly optically isotropic silicon (centrosymmetric cubic point group O_h).^[15]

3.4.4 Magnetization related anisotropies

In magnetically ordered states, such as ferro-, ferri-, and antiferromagnetic phases, the time-reversal symmetry t is broken. Time-reversal symmetry is additionally broken when a magnetic field is applied to diamagnetic or paramagnetic materials.^[20] In this case the proper modes are circularly polarized, and non-reciprocal. Since the refractive indices n_{LCP} and n_{RCP} are different, a rotation polarization θ is observed when linearly polarized light propagates through a magnetized material, as illustrated in Fig. 3.3. This is the well-known Faraday effect, while in reflection the polarization rotation phenomenon is known as the magneto-optical Kerr effect (MOKE). In Fig. 3.4a a magnetized material with magnetization \mathbf{M} is shown where the light propagates through the sample twice. After traversing the sample for the first time, the linear polarization plane has clockwise rotated over an

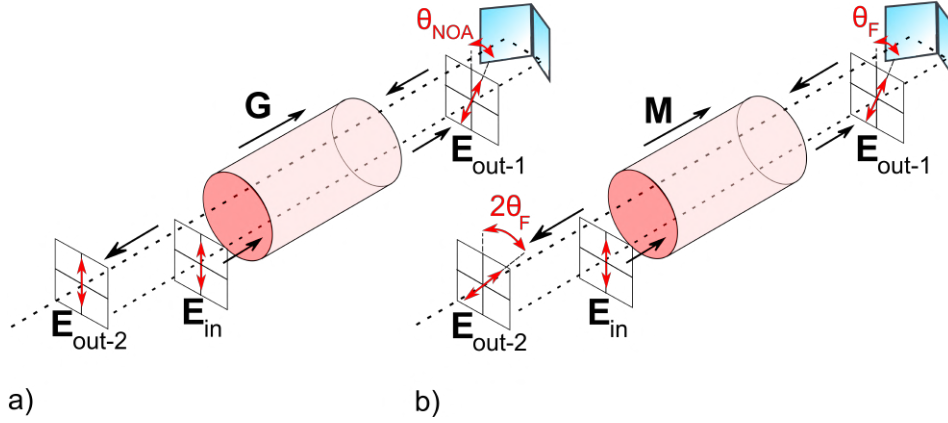


Figure 3.4: Illustration of natural optical activity (NOA). Linearly polarized light makes a clockwise rotation of the polarization plane over an angle θ_{NOA} (clockwise as seen from source) after traversing a chiral sample with “gyration” G . Upon counter-propagation the polarization plane again rotates over a clockwise angle θ_{NOA} (clockwise as seen from the mirror source), by which the total polarization rotation is zero. Natural optical activity thus is a reciprocal effect. b) Illustration of the Faraday effect. Linearly polarized light traverses through a magnetized medium with magnetization M . This leads to a clockwise rotation of the polarization plane over an angle θ_F . Upon counter-propagation the polarization plane rotates over a counter-clockwise angle θ_F (counter-clockwise as seen from the mirror source). Upon back-propagation the linear polarization plane thus has effectively rotated over $2\theta_F$. This makes the Faraday effect non-reciprocal. Illustration adapted from Ref. [17] (figure released in public domain).

angle θ_F . Upon counter-propagation the polarization plane rotates counter-clockwise over an angle $-\theta_F$ (counter-clockwise as seen from the mirror source). The total polarization after passing the sample twice is $2\theta_F$. The rotation sense is different for $+\mathbf{k}$ and $-\mathbf{k}$ propagation, making the Faraday effect (and magneto-optical Kerr effect) non-reciprocal. The polarization rotation is proportional to the off-diagonal component in the dielectric tensor, which itself is proportional to the magnetization $\theta \propto \epsilon_{xy} \propto \mathbf{M}$ in materials with finite magnetic moments, and $\theta \propto \epsilon_{xy} \propto \mathbf{H}_a$ in diamagnets, as discussed above. [6] As such, this optical anisotropy can be used as a sensitive probe for magnetization.

The microscopic magneto-optical interaction depends on the difference in dipole transition strength for the $\sigma_{RCP}(\omega)$ and $\sigma_{LCP}(\omega)$ transitions at a given frequency ω . In the dipole approximation the interaction of photons with spins is mediated through spin-orbit coupling. Therefore, spin-orbit coupling should at least be present in either/both the ground state or/and excited orbital state in the dipole transition. A difference in dipole strength

between the $\sigma_{\text{RCP}}(\omega)$ and $\sigma_{\text{LCP}}(\omega)$ transitions can then result from spin-orbit effects,^[7] different types of energy level splittings such as spin-orbit splitting Δ_{LS} , exchange splitting Δ_{ex} , Zeeman splitting $\Delta E = g\mu_{\text{B}}B$, and spin dependent electronic population differences in the ground and/or excited orbital states.^[6] Which effect is dominant (and relevant) evidently depends on the material's characteristics.

The ionic positions in a magnetic crystal may change as a result of spin alignment. For instance, exchange striction leads to a change in the bond length $\mathbf{r}_{ij} \rightarrow \mathbf{r}_{ij} - \delta\mathbf{r}_{ij}\langle\mathbf{S}_i \cdot \mathbf{S}_j\rangle$.^[21] This leads to a refractive index proportional to $\propto \langle\mathbf{S}_i \cdot \mathbf{S}_j\rangle$. This magneto-optical effect is quadratic in the spin moment, and described by the symmetric part of the dielectric permittivity tensor. For instance, when light travels (not along the optic axis) through antiferromagnetic KNiF₃, it acquires an ellipticity ζ proportional to the difference in magnetic sublattice magnetizations; $\zeta \propto \mathbf{L}^2 \propto (\mathbf{M}_{\uparrow} - \mathbf{M}_{\downarrow})^2$, where \mathbf{L} is the antiferromagnetic vector.^[22]

3.4.5 Magneto-spatial anisotropies

For certain low symmetry (magnetic) space groups time-reversal symmetry t , inversion symmetry i , and their product $i \cdot t$ are simultaneously broken. Along certain crystallographic directions the $\pm\mathbf{k}$ degeneracy for the two orthogonal polarization states can be broken, irrespective of whether the polarization states are circular or linear. Each of the four waves then has a different refractive index, and will be absorbed with a different strength. The two microscopic origins are the *optical magnetoelectric effect* (OME), and *magneto-chiral dichroism* (MChD) and *birefringence* (MChB).^[23] The OME is observed in ferrotoroidal materials,^[24] and the magneto-chiral dichroic effect in chiral magnets, such as Cu₂OSeO₃.

When the four solutions of the Maxwell equations all have a different refractive index, the phenomenon of *quadrochromism* is possible. OME-induced quadrochromism for magnon modes has been observed in a range of multiferroic materials.^[9] Another consequence of four different refractive indices is that counter-propagating ($\pm\mathbf{k}$) light of arbitrary polarization has a different absorption coefficient, called *directional dichroism*. In the case of MChD the effect originates from $\mathbf{k} \cdot \mathbf{M}$ terms in the diagonal of the dielectric tensor expansion in Eq. [3.28](#). When the propagation direction is reversed, the absorption coefficient changes. In the chiral magnet Cu₂OSeO₃ this dichroism has been observed in the microwave range with an external field $\mathbf{H}_a \parallel [111]$ (Ref. [25](#)). The case of OME is slightly more difficult. It can be observed in multiferroic and magnetoelectric materials when the light propagates along the toroidal vector $\mathbf{T} = \mathbf{M} \times \mathbf{P}$, and thus originates from $\mathbf{k} \cdot (\mathbf{M} \times \mathbf{P})$ terms in the dielectric tensor expansion, where \mathbf{P} is the ferroelectric polarization.^[26] Also in the case of OME a different absorption coefficient is observed when the propagation direction is reversed. In the multiferroic material CuB₂O₄

it has been shown that in high magnetic fields the OME leads to the extreme situation of directional dichroism, known as *one-way transparency*, where a material is transparent or non-transparent depending on the propagation direction.^[27] The OME may also be expected in Cu_2OSeO_3 for an external field $\mathbf{H}_a \parallel [110]$, which induces an electric polarization $\mathbf{P} \parallel [001]$ and magnetization $\mathbf{M} \parallel [110]$. In this case OME induced birefringence or dichroism may be observed along $\mathbf{k} \parallel [1\bar{1}0]$.^[28]

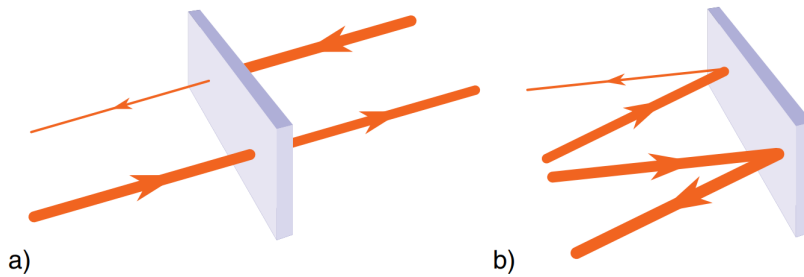


Figure 3.5: a) Directional dichroism: depending on the propagation direction in transmission a different absorption coefficient is experienced. This effect either originates in magnetochiral dichroism or the optical magnetoelectric effect. b) Directional birefringence: depending on the direction of the incident light a different refractive index is experienced. This leads to a directional dependent reflection coefficient. Figures are adapted from Ref.^[23] Reprinted figure with permission from D. Szaller, S. Bordács, and I. Kézsmárki, Phys. Rev. B **87**, 014421 (2013), <https://doi.org/10.1103/PhysRevB.87.014421>, © Copyright 2013 by the American Physical Society.

3.5 Linear polarization rotation

3.5.1 Polarization rotation in transmission

In chiral, or magnetized media, the proper waves are left- and right circularly polarized, with different refractive indices. Therefore, when linearly polarized light propagates through a material, the linear polarization can be thought to be resolved in LCP and RCP light with different phase velocities, and different absorptive indices. After passage through the crystal the light is rotated by an angle θ_T , and has acquired an ellipticity angle η_T . Below the relation between the dielectric tensor:

$$\epsilon_{ij} = \begin{pmatrix} \epsilon_{xx} & \epsilon_{xy} & 0 \\ -\epsilon_{xy} & \epsilon_{xx} & 0 \\ 0 & 0 & \epsilon_{xx} \end{pmatrix} \quad (3.29)$$

and polarization rotation θ_T and ellipticity angle η_T is derived based on the fundamental optics equation.^[29] The above tensor symmetry applies

to a material with a chirality and/or magnetization along the z-direction. Assume that the light travels along the z-axis. In this case only $s_3s_3 = n^2$ is a finite element of the summation $s_i s_j$ in Eq. 3.26. One now gets the eigenvector-eigenvalue equations:

$$\begin{pmatrix} \epsilon_{xx} - n^2 & \epsilon_{xy} & 0 \\ -\epsilon_{xy} & \epsilon_{xx} - n^2 & 0 \\ 0 & 0 & \epsilon_{xx} \end{pmatrix} \begin{pmatrix} E_1 \\ E_2 \\ E_3 \end{pmatrix} = \vec{0} \quad (3.30)$$

The eigenvalues $\tilde{n}_{\pm}^2 = \epsilon_{xx} \pm i\epsilon_{xy}$ are determined by solving the determinant equation. The longitudinal solution is non-physical, as light is a transverse wave, hence $E_3 = 0$. For the eigenvalues $\tilde{n}_{\pm}^2 = \epsilon_{xx} \pm i\epsilon_{xy}$ the corresponding eigenvectors are obtained:

$$\vec{E}_{n_+} = \frac{1}{\sqrt{2}} \begin{pmatrix} 1 \\ +i \\ 0 \end{pmatrix} \quad \vec{E}_{n_-} = \frac{1}{\sqrt{2}} \begin{pmatrix} 1 \\ -i \\ 0 \end{pmatrix} \quad (3.31)$$

By dropping the non-physical longitudinal component, these eigenvectors are indeed readily identified as the *right and left circularly polarized light* in the Jones matrix formalism in Eq. 3.8. The propagation modes in a material with the dielectric tensor of Eq. 3.29 thus are:

$$\vec{E}_{\pm}(\omega, t) = \frac{1}{\sqrt{2}} \begin{pmatrix} 1 \\ \pm i \end{pmatrix} E_0 e^{-i(\omega t - \tilde{n}_{\pm} k z)} \quad (3.32)$$

Linear light is the sum of both $\vec{E}_{\pm}(\omega, t)$ (cf. Eq. 3.8). The polarization variable for linear light after propagation of a sample length $z = d$ is given by:

$$\zeta_{\text{T}} \equiv \frac{\vec{E}_{\text{out},+}}{\vec{E}_{\text{out},-}} = e^{i(\tilde{n}_+ - \tilde{n}_-) \frac{\omega}{c} d} \approx 1 + i(\tilde{n}_+ - \tilde{n}_-) \frac{\omega}{c} d \rightarrow \dots \quad (3.33)$$

Under the case of $\epsilon_{xy} \ll \epsilon_{xx}$ the refractive indices can be approximated as:

$$\tilde{n}_{\pm} = \sqrt{\epsilon_{xx} \pm i\epsilon_{xy}} \approx \sqrt{\epsilon_{xx}} \left(1 \pm \frac{1}{2} \frac{i\epsilon_{xy}}{\epsilon_{xx}} \right) \quad (3.34)$$

This gives for the polarization variable:

$$\dots \rightarrow \zeta_{\text{T}} \approx 1 - \frac{\epsilon_{xy}}{\sqrt{\epsilon_{xx}}} \frac{\omega}{c} d \quad (3.35)$$

Comparing Eq. 3.14 and Eq. 3.35 finally gives:

$$\theta_{\text{T}} + i\eta_{\text{T}} = \frac{\omega d}{2c} (\tilde{n}_+ - \tilde{n}_-) = \frac{\pi d}{\lambda} (\Delta n_{\text{circ}}) = \frac{\omega d}{2c} \frac{i\epsilon_{xy}}{\sqrt{\epsilon_{xx}}} \quad (3.36)$$

Here θ_T gives the linear polarization rotation upon transmission and η_T the ellipticity angle. Since the small angle approximation is used in Eq. 3.14, the expression Eq. 3.36 gives the ellipticity angle η_T , and not the ratio ϵ_T . This expression is valid irrespective of the origin of the off-diagonal dielectric tensor elements. It thus can describe both natural optical activity and the Faraday effect. The Faraday effect in case of diamagnetic materials ϵ_{xy} is proportional to the external field, i.e. $\theta_T \propto \epsilon_{xy} \propto \mathbf{H}$. For paramagnetic and magnetically ordered materials ϵ_{xy} is proportional to the magnetization \mathbf{M} , which by itself generally depends on the external magnetic field.⁶

3.5.2 Polarization rotation in reflection

Below the derivation between the polarization rotation in reflection is derived for a material described by a dielectric tensor of the form in Eq. 3.29. In the derivation the assumption is made that the incident angle is appropriately small enough such that the Fresnel formula for the reflection coefficient $\tilde{\rho}$ is approximated by the normal incidence expression:

$$\tilde{\rho} = \frac{\tilde{n} - 1}{\tilde{n} + 1} \quad (3.37)$$

Here \tilde{n} is the complex refractive index, and $\tilde{\rho}$ the complex reflection coefficient. From the previous paragraph it is understood that the proper waves under the symmetry of ϵ in Eq. 3.29 are left and right circularly polarized, with refractive indices \tilde{n}_+ and \tilde{n}_- , as given in Eq. 3.34. The complex reflectivities for the circular eigenmodes thus are:

$$\tilde{\rho}_{\pm} = \frac{\tilde{n}_{\pm} - 1}{\tilde{n}_{\pm} + 1} \quad (3.38)$$

With the incident light being linearly polarized, i.e. the sum of equal amplitude left and right circularly polarized light, the polarization variable after reflection is:

$$\zeta_R \equiv \frac{\vec{E}_{\text{out},+}}{\vec{E}_{\text{out},-}} = \frac{\vec{E}_{\text{in},+}\tilde{\rho}_+}{\vec{E}_{\text{in},-}\tilde{\rho}_-} = \frac{\tilde{\rho}_+}{\tilde{\rho}_-} \rightarrow \dots \quad (3.39)$$

Using again the approximation $\epsilon_{xy} \ll \epsilon_{xx}$, with refractive indices \tilde{n}_{\pm} approximated as in Eq. 3.34, the polarization variable upon reflection is:

$$\dots \rightarrow \zeta_R = \frac{\tilde{\rho}_+}{\tilde{\rho}_-} \approx \frac{2i\epsilon_{xy}}{\sqrt{\epsilon_{xx}}(\epsilon_{xx} - 1) - i\epsilon_{xy}} + 1 \approx \frac{2i\epsilon_{xy}}{\sqrt{\epsilon_{xx}}(\epsilon_{xx} - 1)} + 1 \quad (3.40)$$

Comparing this polarization variable to Eq. 3.14 the rotation angle, and ellipticity angle upon reflection are:

$$\theta_R + i\eta_R = \frac{\epsilon_{xy}}{\sqrt{\epsilon_{xx}} \cdot (\epsilon_{xx} - 1)} \quad (3.41)$$

The most well known effect where a rotation of linearly polarized light in reflection occurs is the magneto-optical Kerr effect. In principle natural optical activity should also be observable in reflection. This phenomenon of *specular* optical activity is however elusive.^[30] One scarce example is the observation of specular optical activity from the chiral material α -HgS.^[31]

3.6 Polarization spectroscopy setup

A polarization spectroscopy setup based on the double-modulation technique described in Refs. [32] and [33] was constructed for this thesis work. By the double-modulation technique the polarization rotation and ellipticity can be simultaneously measured. First the schematics of the setup are presented. The details of the measurement theory are worked out in the next paragraph. A discussion on the rotation and ellipticity calibration is given based on the measurement theory.

3.6.1 Overview and schematics

A schematics of the polarization spectroscopy setup is shown in Fig. [3.6]. A summary of the system specifications is given in Table [3.2]. The output of a 450 W Xe lamp is monochromatized with a JOBINYVON MICROHR $F = 140$ mm monochromator. The light is subsequently collimated with a parabolic mirror, and s-polarized with a Glan-Taylor prism and focused on the sample with a biconvex lens. When using a $F = 15$ cm lens a spot size of ~ 1 mm² is obtained. A mechanical chopper modulates the incident light in order to determine the reflected or transmitted quasi-DC intensity I_{DC} . Samples can be placed in an OXFORD MAGNETOSTATMO superconducting magnet. The transmitted or reflected light is refocused with a biconvex lens through a photoelastic modulator PEM-100 HINDS INSTRUMENTS and second Glan-Taylor polarizer onto a silicon photodiode. The PEM modulates the light polarization state with a 50 kHz frequency. The phase difference is generally set to $\delta_0 = 150.5^\circ$ to ensure a trade-off in modulation efficiency for the ellipticity and rotation. The ellipticity is proportional to the $f = 50$ kHz signal and the polarization plane rotation is proportional to the $2f = 100$ kHz signal. The second Glan-Taylor prism acts as an analyzer for the polarization state. The intensity components I_{DC} , I_{1f} and I_{2f} are read out by two lock-ins (AMETEK SIGNAL RECOVERY 7230), of which one measures I_{1f} and I_{2f} simultaneously. Rotation spectra can be taken over a wavelength range of 350-1500 nm. The typical spectral resolution is $\Delta\lambda \sim 5$ -10 nm depending on central wavelength, and monochromator slit width. A magnetic field can be applied (and swept) between ± 5 T. The sample temperature can be set (and swept) between 8-300 K. For small rotation θ and ellipticity ϵ the relation between measured intensities, and θ , and ϵ is:

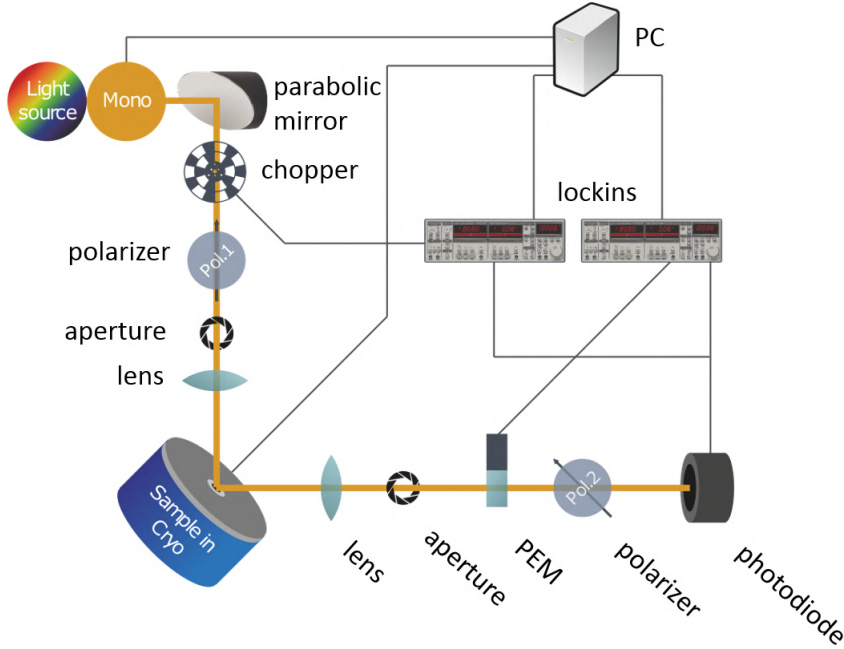


Figure 3.6: The polarization spectroscopy setup in reflection geometry (schematics drawn by Simon Schäfer). In reality the light is incident under an angle of ~ 5 deg. The output of a 450 W Xe lamp is monochromatized with a $F = 140$ mm monochromator. The diverging light is collimated by a parabolic mirror of focal length $F = 25$ mm, subsequently polarized by Pol. 1, and focused on a sample in the cryostat. The reflected light passes the photoelastic modulator, and a second polarizer Pol. 2, which acts as the polarization analyser. A mechanical chopper modulates the light in order to determine the reflected or transmitted quasi-DC intensity I_{DC} . The light intensity is measured with a photodiode detector. The intensity components I_{DC} , I_{1f} and I_{2f} are read out by the lock-ins. The setup in addition allows for a transmission (Faraday) geometry (not drawn).

$$\epsilon \approx C_1 \cdot \frac{I_f}{I_{DC}}, \quad \theta \approx C_2 \cdot \frac{I_{2f}}{I_{DC}} \quad (3.42)$$

The rotation calibration constant C_2 is determined by rotating the incident polarization for a known rotation. The calibration of the ellipticity, and the case of large polarization rotation angles is saved for the measurement theory paragraph.

The rotation sensitivity for $\lambda = 540$ nm (10 nm bandwidth) probe light was experimentally determined by measuring $\theta_K(H_a)$ on a sample with small magnetization. The smallest detectable polarization rotation is about ± 5 mdeg. Details of the measurement are found in Par. [3.6.3](#).

Table 3.2: Properties and specifications of the polarization spectroscopy setup

system property	specification
sample temperature T range	8-300 K
magnetic field $\mu_0 H_a$ range	± 5 T
wavelength λ range	350-1500 nm
spectral resolution $\Delta\lambda$	5-10 nm
polarization rotation sensitivity (at 540 ± 10 nm)	0.005°

3.6.2 Measurement theory

Intensity modulation

The setup response is calculated in the Jones matrix formalism. After the monochromator the light passes a polarizer, which vertically polarizes the incident light:

$$\begin{pmatrix} 0 \\ 1 \end{pmatrix} \quad (3.43)$$

The linearly polarized light is reflected from a sample represented by the reflection matrix:

$$\tilde{\rho}_{\text{circ}} = \begin{pmatrix} \tilde{\rho}_+ & 0 \\ 0 & \tilde{\rho}_- \end{pmatrix} \quad (3.44)$$

given in circular basis.

The complex circular reflection coefficients are:

$$\tilde{\rho}_\pm = r_\pm e^{i\phi_\pm} \quad (3.45)$$

where r_\pm is the amplitude, and ϕ_\pm the phase. When linearly polarized light reflects from the sample, the polarization variable (cf. Eq. 3.40) is:

$$\zeta_m = \frac{\tilde{\rho}_+}{\tilde{\rho}_-} = \frac{r_+}{r_-} e^{i(\phi_+ - \phi_-)} \quad (3.46)$$

The polarization rotation and ellipticity ratio are in this case (cf. Eq. 3.15)

$$\theta_m = \frac{1}{2}(\phi_+ - \phi_-) \quad \epsilon_m = \frac{r_- - r_+}{r_+ + r_-} \quad (3.47)$$

In Cartesian coordinates the sample reflection matrix is:

$$\tilde{\rho}_{\text{lin}} = \vec{F}^{-1} \cdot \tilde{\rho}_{\text{circ}} \cdot \vec{F} = \frac{1}{2} \begin{pmatrix} 1 & 1 \\ -i & i \end{pmatrix} \begin{pmatrix} \tilde{\rho}_+ & 0 \\ 0 & \tilde{\rho}_- \end{pmatrix} \begin{pmatrix} 1 & i \\ 1 & -i \end{pmatrix} \quad (3.48)$$

The light consecutively passes the photoelastic modulator. This element has a periodically modulated linear birefringence, represented^[33] by the matrix :

$$\text{PEM} = \begin{pmatrix} \exp(i\frac{\delta(t)}{2}) & 0 \\ 0 & \exp(-i\frac{\delta(t)}{2}) \end{pmatrix}, \quad \delta(t) = \delta_0 \sin(\omega t) = \sin(2\pi f t) \quad (3.49)$$

The second polarizer, which acts as the polarization state analyzer, is set to 135° (or 45°). The $\pm 45^\circ$ relative angle to the incident polarization yields the highest signal-to-noise.^[33] A vertical analyzer is represented by:

$$A = \begin{pmatrix} 0 & 0 \\ 0 & 1 \end{pmatrix} \quad (3.50)$$

After rotation through an angle of 135° the matrix is:

$$A' = R^{-1}(135^\circ) \cdot A \cdot R(135^\circ) = \frac{1}{2} \begin{pmatrix} 1 & -1 \\ -1 & 1 \end{pmatrix} \quad (3.51)$$

Here R is the rotation matrix and it's inverse is R^{-1} . After passing the analyser A' the electric field thus is:

$$\begin{aligned} \mathbf{E}_{\text{out}} &= A' \cdot \text{PEM} \cdot \vec{F}^{-1} \cdot \tilde{\rho}_{\text{circ}} \cdot \vec{F} \cdot \begin{pmatrix} 0 \\ 1 \end{pmatrix} \\ &= \frac{e^{-i\frac{\delta(t)}{2}}}{4} \cdot [ie^{\delta(t)}(\tilde{\rho}_+ - \tilde{\rho}_-) - (\tilde{\rho}_+ + \tilde{\rho}_-)] \cdot \begin{pmatrix} 1 \\ -1 \end{pmatrix} \end{aligned} \quad (3.52)$$

The signal intensity at the detector thus is:

$$I_{\text{out}} = \mathbf{E}_{\text{out}}^* \mathbf{E}_{\text{out}} = \frac{1}{8} [ie^{\delta(t)}(\tilde{\rho}_+ - \tilde{\rho}_-) - (\tilde{\rho}_+ + \tilde{\rho}_-)]^* [ie^{\delta(t)}(\tilde{\rho}_+ - \tilde{\rho}_-) - (\tilde{\rho}_+ + \tilde{\rho}_-)] \quad (3.53)$$

After reworking this expression, and using the definitions of Eq.^[3.47] the expression below is obtained:

$$I_{\text{out}} = \frac{1}{\sqrt{2}} [(r_+^2 + r_-^2) + (r_+^2 - r_-^2) \sin(\delta(t)) + 2r_+ r_- \sin(2\theta_m) \cos(\delta(t))] \quad (3.54)$$

Since $r_+ \approx r_-$ the following two approximations can be made:

$$\frac{r_+ r_-}{r_+^2 + r_-^2} \approx \frac{1}{2} \quad \text{and} \quad \frac{r_+^2 - r_-^2}{r_+^2 + r_-^2} \approx 2 \frac{r_+ - r_-}{r_+ + r_-} = -2\epsilon_m \quad (3.55)$$

In addition, the shorthand notation $R = \frac{1}{2}(r_+^2 + r_-^2)$ is introduced, to write the expression as:

$$I_{\text{out}} = \sqrt{2}R \cdot [1 - 2\epsilon_m \sin(\delta(t)) + \sin(2\theta_m) \cos(\delta(t))] \quad (3.56)$$

The above intensity expression contains the terms of interest: the rotation θ_m , and ellipticity ratio ϵ_m , however still superimposed. The PEM modulates the intensity by $\delta(t) = \delta_0 \sin(\omega t) = \delta_0 \sin(2\pi f t)$. The sine and cosine function terms are expanded in Bessel function terms \mathcal{J} as:³²

$$\begin{aligned} \cos(\delta_0 \sin(\omega t)) &= \mathcal{J}_0(\delta_0) + 2 \sum_{n=1}^{\infty} \mathcal{J}_{2n}(\delta_0) \cos(2n\omega t) \\ &= \mathcal{J}_0(\delta_0) + 2\mathcal{J}_2(\delta_0) \cos(4\pi f t) + \text{higher order even } f \text{ terms} \end{aligned} \quad (3.57)$$

$$\begin{aligned} \sin(\delta_0 \sin(\omega t)) &= 2 \sum_{n=0}^{\infty} \mathcal{J}_{2n+1}(\delta_0) \sin((2n+1)\omega t) \\ &= 2\mathcal{J}_1(\delta_0) \sin(2\pi f t) + \text{higher order uneven } f \text{ terms} \end{aligned} \quad (3.58)$$

The modulated intensity arriving at the detector thus is of the form:

$$I = I_0 + I_{1f} \sin(2\pi f t) + I_{2f} \sin(4\pi f t) + \text{higher order } f \text{ terms} \quad (3.59)$$

with:

$$I_0 = \sqrt{2}R [1 + \mathcal{J}_0(\delta_0) \sin(2\theta_m)] \quad (3.60a)$$

$$I_{1f} = -4\sqrt{2}R \mathcal{J}_1(\delta_0) \epsilon_m \quad (3.60b)$$

$$I_{2f} = 2\sqrt{2}R \mathcal{J}_2(\delta_0) \sin(2\theta_m) \quad (3.60c)$$

The intensity contributions I_0 , I_{1f} and I_{2f} are separated by lock-in detection technique. The f and $2f$ frequencies correspond to the fundamental PEM-driving frequency and its second harmonic. The I_0 intensity is determined by mechanically chopping the incident light at a frequency $f_{\text{chopper}} \ll f_{\text{PEM}}$ depend on the retardation amplitude δ_0 through the zero'th, first and second order Bessel functions $\mathcal{J}_0(\delta_0)$, $\mathcal{J}_1(\delta_0)$, and $\mathcal{J}_2(\delta_0)$ respectively. These functions take their maximum values at angles 0° , 105.5° , and 175° respectively. A retardation amplitude $\delta_0 = 150.7^\circ$ is chosen in order to optimize the detection sensitivity of both the rotation and ellipticity.

The detector and lock-in amplifiers have different gains sensitivities to low frequency and high frequency signals. This dependency is captured with

effective constants A_f , B_{2f} , and D_0 for the different frequency components. The ratio of the detected intensities is then given as:

$$\frac{I_{1f}}{I_0} = \frac{-4A_f \mathcal{J}_1(\delta_0) \epsilon_m}{1 + D_0 \mathcal{J}_0(\delta_0) \sin(2\theta_m)} \approx -4A_f \mathcal{J}_1(\delta_0) \cdot \epsilon_m = C_1 \cdot \epsilon_m \quad (3.61a)$$

$$\frac{I_{2f}}{I_0} = \frac{2B_{2f} \mathcal{J}_2(\delta_0) \sin(2\theta_m)}{1 + D_0 \mathcal{J}_0(\delta_0) \sin(2\theta_m)} \approx 4B_{2f} \mathcal{J}_2(\delta_0) \cdot \theta_m = C_2 \cdot \theta_m \quad (3.61b)$$

Note that Eq. 3.61 is proportional to the ellipticity ratio along the definitions made in Eq. 3.55. The ellipticity angle is: $\eta_m = \tan^{-1}(\epsilon_m)$.

Rotation calibration

For small angles ($\theta < 3^\circ$) the calibration constant for the polarization rotation for wavelength λ is easily determined. To calibrate a rotation spectrum $\theta(\lambda)$ the incident polarization is rotated by a positive and negative angle $\pm\phi$ (in practice $\pm 1^\circ$). This leads to the intensity:

$$\frac{I_{2f}}{I_0}(\lambda) |_{\pm\phi} = C_2(\lambda)(\pm\phi) \quad (3.62)$$

The wavelength dependent calibration curve $C_2(\lambda)$ is accordingly obtained:

$$C_2(\lambda) = \frac{\frac{I_{2f}}{I_0} |_{+\phi} - \frac{I_{2f}}{I_0} |_{-\phi}}{2\phi} \quad (3.63)$$

This allows to calibrate the measured rotation from measured intensity by:

$$\theta(\lambda) = \frac{\frac{I_{2f}}{I_0}(\lambda)}{C_2(\lambda)} \quad (3.64)$$

For a single wavelength measurement (temperature or field sweep) the ratio $\frac{I_{2f}}{I_{DC}}$ is measured for known incident positive and negative incident polarization rotations $\pm\phi$ (normally $\pm 1^\circ$, $\pm 2^\circ$, $\pm 3^\circ$, ...). The measured ratios are then fitted with the function $\frac{I_{2f}}{I_{DC}}(\phi) = C_2 |\phi - \phi_0|$ in order to extract the calibration constant C_2 .

When a material shows large rotations the full (single wavelength) calibration curve should be measured, and fitted according to Eq. 3.61b. The result is shown in Fig. 3.7. It can be seen that the system response has a 180° periodicity. When a H_a -field-sweep measurement (single wavelength) is made and large rotations are measured, the polarization rotation $\theta(H_a)$ is obtained from the measured intensity by the inverted expression:

$$\theta(H_a) = \frac{1}{2} \sin^{-1} \left(\frac{\frac{I_{2f}}{I_{DC}}(H_a)}{2B_{2f}\mathcal{J}_2(\delta_0) - 2D_0\mathcal{J}_0(\delta_0)\frac{I_{2f}}{I_{DC}}(H_a)} \right) \quad (3.65)$$

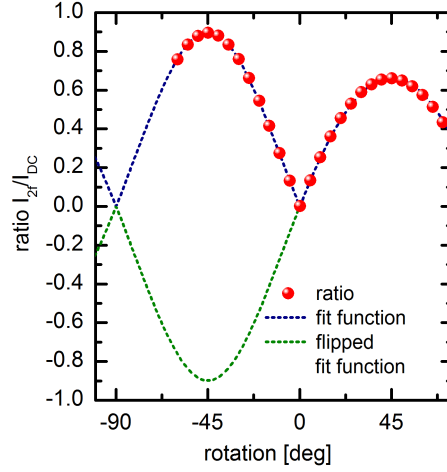


Figure 3.7: For angles θ between $\pm 3^\circ$ degrees an approximately linear relation between θ and $I_{2f}/I_{DC}(\theta)$ holds. For larger rotations the full response function is measured, and fitted with Eq. [3.61](#)b, as seen in the dotted blue lines. The response function has a 180° periodicity.

Ellipticity calibration

In order to calibrate the ellipticity a quarter wave plate is placed between the PEM and the polarization analyser. This leads to an additional phase retardation $\frac{\pi}{2}$ after the PEM. Thus $\delta(t) \rightarrow \delta(t) + \frac{\pi}{2}$ in Eq. [3.56](#), which thereby becomes:

$$I_{out} = \sqrt{2R} \cdot [1 - 2\epsilon_m \cos(\delta(t)) - \sin(2\theta_m) \sin(\delta(t))] \quad (3.66)$$

Using again the Bessel expansions and similar approximations, the following intensity ratio is obtained:

$$\frac{I_{1f}}{I_0} \approx -4A_f \mathcal{J}_1(\delta_0) \cdot \theta_m = C_1 \cdot \theta_m \quad (3.67)$$

The $\frac{I_{1f}}{I_0}$ ratio thus becomes a function of the experimentally controllable incident polarization. The wavelength dependent ellipticity calibration function is thus determined by again measuring the intensity ratio for a small incident angle $\pm\phi$:

$$C_1(\lambda) = \frac{\frac{I_{1f}}{I_0} |_{+\phi} - \frac{I_{1f}}{I_0} |_{-\phi}}{2\phi} \quad (3.68)$$

Broadband optical elements which can be used to introduce the $\pi/4$ shift are the Fresnel rhomb and waveplates. The waveplate (THORLABS SUPER-ACHROMATIC QUARTER-WAVE PLATE SAQWP05M-700) is the preferred choice, since it does not lead to a beam displacement as is the case with the Fresnel rhomb.

3.6.3 Sensitivity of the polarization spectrometer

A field sweep scan of a 5 monolayer (5ML) thick SrRuO₃ film was made with $\lambda = 540 \pm 10$ nm probe wavelength in order to determine the measurement sensitivity of the polarization spectroscopy setup. For this sample thickness the ferromagnetic transition temperature is approximately $T_C \approx 120$ K.^[34] The measurement was carried out at $T = 70$ K, being the highest temperature for which the Kerr rotation θ_K was still resolvable. The lock-in integration time was $\tau = 200$ μ s, with a typical magnetic field-sweep rate of 30 mT/min. The data is shown in Fig. 3.8, where the window Faraday background is already subtracted. A Kerr-angle of about $\theta_K \approx \pm 5$ mdeg, or ± 100 μ rad was still resolvable, which is taken as the sensitivity limit of the setup. This is on the order of the expected sensitivity of ~ 2 mdeg under similar measurement conditions as reported in the seminal setup-paper of Sato *et al.* in Ref. [32]. Note however, that in this study measurements are performed without the hinder of a cryostat window.

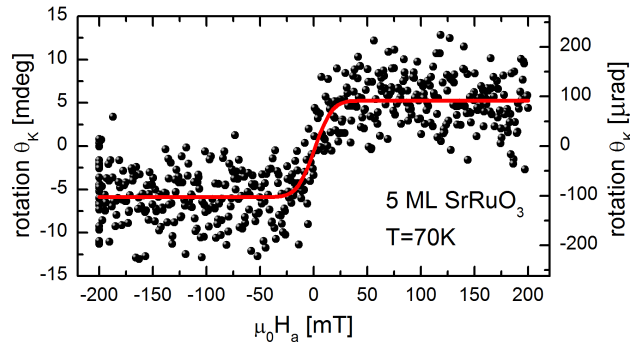


Figure 3.8: Field sweep of the Kerr angle θ_K in mdeg and μ rad units of a 5 atomic layer (5ML) ultrathin film of SrRuO₃. The dots give the data points. The red curve is an erfc-fit to the rotation response. The sample temperature is $T = 70$ K.

Slight improvements upon the ± 5 mdeg sensitivity value can in principle be made. For instance, by making field- or temperature sweeps with a laser as light source. In this case a higher degree of polarization is obtained with respect to the Xe-lamp based setup, since for the Xe-lamp based setup it is

challenging to obtain a nicely collimated light beam. The higher degree of polarization will reduce the background intensity of the measurement. In addition there is a Faraday-rotation contribution from the cryostat window as background in a field-dependent sweep. This background contribution is difficult to avoid when one needs to work at cryogenic temperatures. Lastly, repeated measurements and averaging will improve the signal-to-noise ratio.

Demonstrated solutions for even higher polarization rotation sensitivities are the Sagnac interferometer for dc-magnetization detection (down to the $\sim 1 \mu\text{rad}$ -level),^[35] and simultaneous modulation of the magnetization for ac-magnetization.^[36,37]

3.7 Kerr spectroscopy of single crystalline SrRuO₃

SrRuO₃ is a ferromagnetic metallic oxide which serves as an important building block for complex oxide heterostructures.^[38] An example of such a heterostructure relevant to this thesis work is the epitaxial bilayer system of SrRuO₃-SrIrO₃ on an SrTiO₃ substrate.^[39] In this heterostructure configuration the inversion symmetry in SrRuO₃ is artificially broken since it is situated between two different oxide materials. This artificial breaking of inversion symmetry induces Dzyaloshinskii-Moriya interaction in SrRuO₃, by which it is claimed that Skyrmions form in this system.^[39] Since the volume magnetization of such ultrathin SrRuO₃ heterostructures is small, conventional magnetometry measurements might not always be most fortuitous to measure the magnetization. In this case magneto-optics may form a convenient alternative. Early magneto-optical studies on SrRuO₃ showed large magneto-optical effects.^[40,41] However, these studies were always carried out on thin film SrRuO₃ due to the lack of single crystals. With recent advances in growth, single crystals of SrRuO₃ are now available.^[42] The strong magneto-optical effects observed in epitaxial SrRuO₃, the small coercive fields observed in the single crystal, and the recent claims of complex magnetic order in SrRuO₃-heterostructures make single crystalline SrRuO₃ a good test sample for the constructed setup.

A Kerr spectrum θ_K in polar geometry of a [101] oriented single crystal of SrRuO₃ was taken at $T = 15 \text{ K}$. The magnetic field is first ramped up to $\mu_0 H_a = +3 \text{ T}$, after which the measurement is performed at $\mu_0 H_a = +0.5 \text{ T}$, with $\mathbf{H}_a \parallel [101]$. In this field the magnetization is saturated. The red dots in Fig. 3.9a shows the measured Kerr spectrum θ_K given in degrees. The grey curve is the theoretical Kerr spectrum taken from Ref. [40]. The experimental spectrum can be fitted with two Lorentzian oscillators with peak positions 1.75 eV and 2.85 eV, which is in good quantitative agreement with the theoretical peaks observed at $\sim 1.65 \text{ eV}$ and $\sim 2.65 \text{ eV}$. The theoretical absolute rotation value is a factor 3-4 larger than the observed rotation. The origin of the first peak is assigned to the plasma resonance^[43] in the

diagonal optical conductivity σ_{xx} . The second peak is a magneto-optically active $O(2p) \rightarrow Ru(4d)$ interband transition.^[40,41]

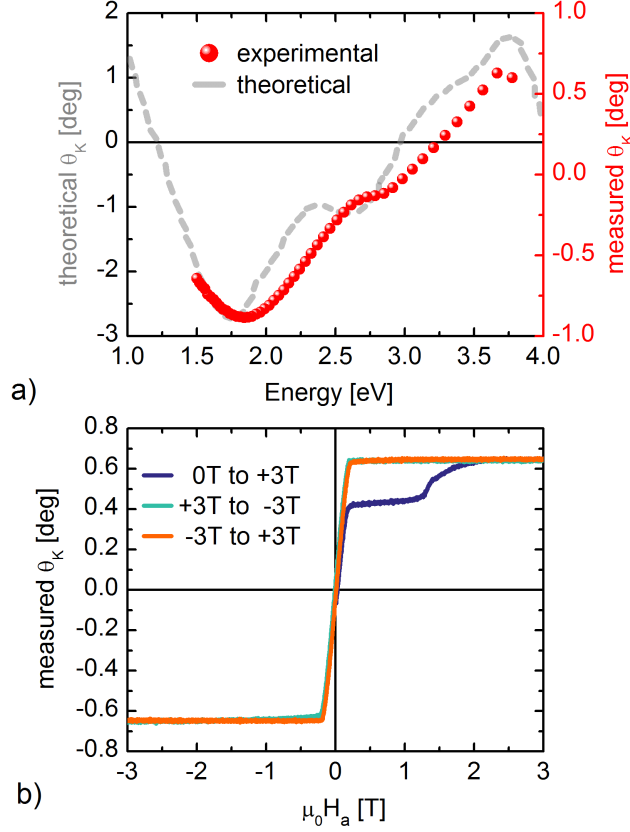


Figure 3.9: a) The gray dashed line gives the theoretical $\theta_K(E)$ spectrum. The red spheres give the measured $\theta_K(E)$ at $\mu_0 H_a = +0.5$ T at $T = 15$ K. Peaks are observed at 1.75 eV and 2.85 eV. b) θ_K for the field sweep sequence $\mu_0 H_a : 0 \text{ T} \rightarrow +3 \text{ T} \rightarrow -3 \text{ T} \rightarrow +3 \text{ T}$. The used probe wavelength is $\lambda_{\text{probe}} = 540 \pm 10$ nm.

In Fig 3.9b a field sweep sequence of θ_K at probe wavelength $\lambda_{\text{probe}} = 540 \pm 10$ nm is shown. The measurement was performed in polar geometry, with $\mathbf{H}_a \parallel [101]$. The sample is zero-field cooled to $T = 15$ K, after which the H_a -field is swept towards +3 T. At a field of $T \sim +0.2$ T in the sweep sequence $0 \text{ T} \rightarrow +3 \text{ T}$ a rapid increase of the rotation to ≈ 0.4 deg is observed. At $\sim +1.2$ T the rotation again increases, after which a saturation rotation value of ~ 0.7 deg is observed when the field reaches $\mu_0 H_{a,\text{sat}} \sim +2$ T. When the field is swept from $+3 \text{ T} \rightarrow -3 \text{ T}$ the saturation rotation ~ 0.7 deg is reversed to ~ -0.7 deg at $\mu_0 H_{a,\text{sat}} \sim -0.2$ T. The opposite field sweep, $-3 \text{ T} \rightarrow +3 \text{ T}$ again shows a fast magnetization reversal with small saturation field. In Ref. [44] the origin of the difference in the virgin curve and subsequent sweeps is discussed. At room temperature, and below $T_C \approx 160$ K

when zero-field cooled, single crystal SrRuO₃ is orthorhombic with six twin domain orientations. One of these twins has the c-axis parallel to the applied field direction [101]. A field of ~ 0.2 T is necessary to align the magnetization of this structural domain. At ~ 1.2 T the other structural domains gradually reorient through magnetostriction. At about 2 T magnetization saturation is reached. In the consecutive field sweeps the sample remains in the structurally single-domain state.

3.8 Acknowledgements and own contributions

The polarization spectroscopy setup was constructed by myself, with significant assistance from Simon Schäfer. The measurement theory calculations for our setup have been performed by myself, with help from Simon Schäfer. Stefan Kunkemöller (group Prof. Dr. M. Braden) has grown the SrRuO₃ crystal. Ionela Vrejoiu and Lena Wysocki have grown the ultrathin SrRuO₃ film. The measurements on the SrRuO₃ crystal and thin film have been carried out by myself, with assistance from Ramil Mirzaaghayev. The text of this chapter has been written by myself.

3.9 Bibliography

- [1] "<https://pixabay.com/de/elektromagnetische-wellen-wellenlänge-1526374/>" figure released in public domain under CC0 Creative Commons license
- [2] P. Fumagalli, *Magneto-Optic Spectroscopy of Magnetic Thin Films: Influence of Structural Properties on Magnetic Ordering, Exchange, and Coercivity*, Habilitation thesis, RWTH Aachen, Germany (1997).
- [3] M. Born and E. Wolf, *Principles of Optics, 7th ed.*, (Cambridge University Press, Cambridge, 1999).
- [4] J. Ferré and G. A Gehring, Linear optical birefringence of magnetic crystals, Rep. Prog. Phys. **47**, 513 (1984).
- [5] M. Kremers, *Optical and morphological aspects of incommensurate crystals*, Radboud University Nijmegen, The Netherlands (1995).
- [6] P. S. Pershan, Magneto-Optical Effects, J. Appl. Phys. **38**, 1482 (1967).
- [7] P. N. Argyres, Theory of the Faraday and Kerr effects in ferromagnetics, Phys. Rev. **97**, 334 (1955).
- [8] For magnon absorption (THz range) this assumption *does not* hold. In this case the generalized constitutive relations (cf. Eq. 3.19) need to be used, where \mathbf{D} also depends on \mathbf{H} , and \mathbf{M} also depends on \mathbf{E} . See for instance: I. Kézsmárki *et al.*, One-way transparency of four-coloured spin-wave excitations in multiferroic materials, Nat. Commun. **5**, 3203 (2014).
- [9] I. Kézsmárki, D. Szaller, S. Bordács, V. Kocsis, Y. Tokunaga, Y. Taguchi, H. Murakawa, Y. Tokura, H. Engelkamp, T. Rößm, and U. Nagel, One-way transparency of four-coloured spin-wave excitations in multiferroic materials, Nat. Commun. **5**, 3203 (2014).

- [10] V. L. Ginzburg, On crystal optics with spatial dispersion, *Phys. Rep.* **194**, 245 (1990).
- [11] D. L. Portigal and E. Burstein, Magneto-spatial dispersion effects on the propagation of electro-magnetic radiation in crystals, *J. Phys. Chem. Solids* **32**, 603 (1971).
- [12] S. Blundell, *Magnetism In Condensed Matter*, (Oxford University Press, 2001).
- [13] M. Fox, *Optical Properties of Solids*, (Oxford University Press, 2011).
- [14] A. Glazer and K. G. Cox, *Classical linear crystal optics* in *International Tables for Crystallography, Vol. D*, (John Wiley & Sons, Ltd., 2006), Chapter 1.1.6.
- [15] J. Pastrnak and K. Vedam, Optical anisotropy of silicon single crystals, *Phys. Rev. B* **3**, 2567 (1971).
- [16] P. Y. Yu and M. Cardona, Spatial dispersion in the dielectric constant of GaAs, *Solid State Commun.* **9**, 1421 (1971).
- [17] "<https://de.wikipedia.org/wiki/Faraday-Effekt>", figure released in public domain (2007).
- [18] R. M. Hornreich and S. Shtrikman, Theory of gyrotropic birefringence, *Phys. Rev.* **171**, 1065 (1968).
- [19] R. V. Pisarev, B. B. Krichevtsov, and V. V. Pavlov, Optical study of the antiferromagnetic-paramagnetic phase transition in chromium oxide Cr_2O_3 , *Phase Transit. B* **37**, 63 (1991).
- [20] J. Quintanilla, *Lecture notes on magnetism and superconductivity*, University of Kent, United Kingdom.
- [21] Y. Tokura, S. Seki, and N. Nagaosa, Multiferroics of spin origin, *Rep. Prog. Phys.* **77**, 076501 (2014).
- [22] D. Bossini, A. M. Kalashnikova, R. V. Pisarev, T. Rasing, and A. V. Kimel, Controlling coherent and incoherent spin dynamics by steering the photoinduced energy flow, *Phys. Rev. B* **89**, 060405 (2014).
- [23] D. Szaller, S. Bordács, and I. Kézsmárki, Symmetry conditions for nonreciprocal light propagation in magnetic crystals, *Phys. Rev. B* **87**, 014421 (2013).
- [24] N. A. Spaldin, M. Fiebig, and M. Mostovoy, The toroidal moment in condensed-matter physics and its relation to the magnetoelectric effect, *J. Phys. Condens. Matter* **20**, 434203 (2008).
- [25] Y. Okamura, F. Kagawa, S. Seki, M. Kubota, M. Kawasaki, and Y. Tokura, Microwave magnetochiral dichroism in the chiral-lattice magnet Cu_2OSeO_3 , *Phys. Rev. Lett.* **114**, 197202 (2015).
- [26] S. Bordács, *Exotic magneto-optical effects in solids*, PhD thesis, Budapest University of Technology and Economics, Hungary (2011).
- [27] S. Toyoda, N. Abe, S. Kimura, Y. H. Matsuda, T. Nomura, A. Ikeda, S. Takeyama, and T. Arima, One-way transparency of light in multiferroic CuB_2O_4 , *Phys. Rev. Lett.* **115**, 267207 (2015).
- [28] M. Mochizuki and S. Seki, Dynamical magnetoelectric phenomena of multiferroic skyrmions, *J. Phys. Condens. Matter* **27**, 503001 (2015).
- [29] An interesting example of how to use the fundamental optics equation (see Eq. [3.26](#)) to describe linear birefringence is worked out in Ref. [14](#). A. Glazer and K. G. Cox, *Classical linear crystal optics*
- [30] L. D. Barron, *Molecular Light Scattering and Optical Activity*, (Cambridge University Press, New York, 2009).

-
- [31] A. R. Bungay, Y. P. Svirko, and N. I. Zheludev, Experimental observation of specular optical activity, *Phys. Rev. Lett.* **70**, 3039 (1993).
- [32] K. Sato, Measurement of Magneto-optical Kerr effect using piezo-birefringent modulator, *Jpn. J. Appl. Phys.* **20**, 2403 (1981).
- [33] S. Polisetty, J. Scheffler, S. Sahoo, Y. Wang, T. Mukherjee, X. He, and Ch. Binek, Optimization of magneto-optical kerr setup: Analyzing experimental assemblies using Jones matrix formalism, *Rev. Sci. Instrum.* **79**, 055107 (2008).
- [34] J. Xia, W. Siemons, G. Koster, M. R. Beasley, and A. Kapitulnik, Critical thickness for itinerant ferromagnetism in ultrathin films of SrRuO₃, *Phys. Rev. B* **79**, 140407 (2009).
- [35] J. Xia, P. T. Beyersdorf, M. M. Fejer, and A. Kapitulnik, Modified Sagnac interferometer for high-sensitivity magneto-optic measurements at cryogenic temperatures, *Appl. Phys. Lett.* **89**, 062508 (2006).
- [36] Y. K. Kato, R. C. Myers, A. C. Gossard, and D. D. Awschalom, Observation of the spin hall effect in semiconductors, *Science* **306**, 1910 (2004).
- [37] G. Phelps, J. Abney, M. Broering, and W. Korsch, A sensitive Faraday rotation setup using triple modulation, *Rev. Sci. Instrum.* **86**, 073107 (2015).
- [38] G. Koster, L. Klein, W. Siemons, G. Rijnders, J. S. Dodge, C.-B. Eom, D. H. A. Blank, and M. R. Beasley. Structure, physical properties, and applications of SrRuO₃ thin films, *Rev. Mod. Phys.* **84**, (2012).
- [39] J. Matsuno, N. Ogawa, K. Yasuda, F. Kagawa, W. Koshibae, N. Nagaosa, Y. Tokura, and M. Kawasaki, Interface-driven topological hall effect in SrRuO₃-SrIrO₃ bilayer, *Sci. Adv.* **2**, e1600304 (2016).
- [40] H. Ohta, E. Kulatov, Y. Uspenskii, and S. Halilov, Optics and magneto-optics of SrRuO₃, *J. Magn. Soc. Jpn.* **22**, 185 (1998).
- [41] J. S. Dodge, E. Kulatov, L. Klein, C. H. Ahn, J. W. Reiner, L. Miéville, T. H. Geballe, M. R. Beasley, A. Kapitulnik, H. Ohta, Y. Uspenskii, and S. Halilov, Temperature-dependent local exchange splitting in SrRuO₃, *Phys. Rev. B* **60**, 6987 (1999).
- [42] S. Kunkemöller, F. Sauer, A. A. Nugroho, and M. Braden. Magnetic anisotropy of large floating-zone-grown single-crystals of SrRuO₃, *Cryst. Res. Technol.* **51**, 299 (2016).
- [43] H. Feil and C. Haas. Magneto-optical Kerr effect, enhanced by the plasma resonance of charge carriers, *Phys. Rev. Lett.* **58**, 65 (1987).
- [44] S. Kunkemöller, D. Brüning, A. Stunault, A. A. Nugroho, T. Lorenz, and M. Braden, Magnetic shape-memory effect in SrRuO₃, *Phys. Rev. B* **96**, 220406 (2017).

Chapter 4

Optically probed symmetry breaking in the chiral magnet Cu_2OSeO_3

4.1 Introduction

Materials with low symmetry exhibit a large variety of intriguing optical phenomena. As is well known, the absence of inversion symmetry leads to the occurrence of natural optical activity. In addition to this, inversion symmetry breaking strongly affects the electric dipole selection rule, and thus allows for direct excitation of local crystal-field excitations in linear spectroscopy. In magnetic materials, the breaking of time-reversal symmetry leads to the magneto-optical Kerr and Faraday effect. Many of the optical phenomena originating from a reduced symmetry have technological applications, examples of which include optical isolators and magneto-optical storage devices.^[1]

In recent years, materials lacking both spatial inversion and time-reversal symmetry have been a focal point of condensed matter research. Their combined absence may for instance lead to magneto-electric and multiferroic behavior,^[2-4] the formation of chiral and skyrmion magnetic ground states,^[5] and the occurrence of toroidal order,^[6,7] and excitations.^[8,9] Effects on the optical properties have been studied extensively.^[10-12] One intriguing optical phenomenon originating from the combined absence of time-reversal and space-inversion symmetry is the so-called nonreciprocal directional dichroism.^[13-16]

The high sensitivity of optical properties to symmetry breaking may be used to gain a better understanding of the underlying material properties. Cu_2OSeO_3 belongs to the class of non-centrosymmetric cubic crystal structures. These materials have recently triggered a great deal of research interest owing to the occurrence of topologically protected spin-vortex-like

structures, known as skyrmions.⁵

In these chiral crystal structures, the absence of inversion symmetry between the spin sites leads to a non-vanishing antisymmetric Dzyaloshinskii-Moriya (DM) exchange interaction, which competes with the energetically stronger isotropic Heisenberg exchange. This combination of exchange interactions stabilizes spin helices.¹⁷ In the presence of an external magnetic field, the Zeeman interaction energy stabilizes the formation of a topologically robust hexagonal lattice of nanometer-sized skyrmions.¹⁸

In this chapter we discuss a variety of linear optical properties¹⁹ associated with the broken inversion symmetry, structural chirality, and magnetic order in the chiral magnet Cu_2OSeO_3 .²⁰ The orbital aspect of Cu_2OSeO_3 has only received minimal experimental attention so far.²¹ Local crystal-field excitations are revealed below the charge-transfer gap by means of spectroscopic ellipsometry. These orbital excitations acquire a finite dipole matrix element due to the low crystal-field symmetry. Optical polarization rotation measurements are used to study the structural chirality and to probe the magnetic order. The natural optical activity, resulting from the chiral crystal structure, shows an abrupt change upon magnetic ordering. This observation is evidence of a finite magneto-electric coupling in the phase with helical magnetic order. The large magneto-optical response is quantified by a magneto-optical susceptibility on the order of $\mathcal{V}(540 \text{ nm}) \sim 10^4 \text{ rad/T}\cdot\text{m}$ in the helimagnetic phase, and maximum Faraday rotation of $\sim 170 \text{ deg/mm}$ in the field-polarized ferrimagnetic phase. This strong response serves as an excellent probe for the various magnetic phase transitions. The magneto-optical data allows to derive the phase diagram of Cu_2OSeO_3 as a function of magnetic field and temperature. The optically determined phase diagram is in excellent agreement with results obtained by other techniques.^{20,22,23} Lastly, Kerr-spectroscopy data of Cu_2OSeO_3 , and a rather intriguing optical effect which can be observed in Cu_2OSeO_3 , namely the interference between Faraday rotated and Kerr electromagnetic waves are presented.

4.2 Structure and magnetism

Cu_2OSeO_3 has a complex chiral crystal structure with cubic space group $P2_13$. The unit cell contains 16 Cu ions, all having a 2+ valence state (d^9 configuration). These Cu ions are located within two crystallographically distinct oxygen ligand field geometries,²⁴ which can be approximated by a trigonal bipyramid (D_{3h}) for Cu-I ions and by a square pyramid (C_{4v}) for Cu-II ions, as depicted in Fig. 4.1. The true site symmetries are lower, and are given by C_{3v} for Cu-I and C_1 for the Cu-II ions.²⁴ These ligand fields lead to different crystal-field splittings of the $3d$ orbitals on the Cu-I and Cu-II sites, as shown in Fig. 4.1. For Cu-I the hole is located in the z^2 orbital, whereas for Cu-II the hole is in the $x^2 - y^2$ orbital. Note that these

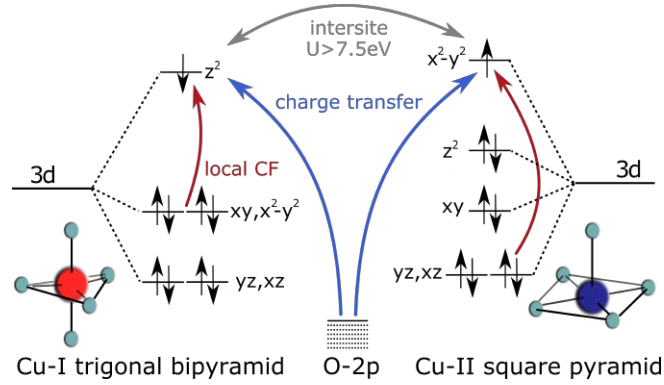


Figure 4.1: The $3d$ crystal-field splittings for the Cu-I (trigonal bipyramid) and Cu-II (square pyramid) ions. The dipole-active local crystal-field (CF) excitations are indicated with red arrows, and the charge-transfer excitations with blue arrows. Intersite excitations between the Cu ions, illustrated with a gray arrow, lie outside the experimentally accessible energy range of this work.

are no pure $3d$ orbitals due to the low site symmetry, i. e., parity is not a good quantum number.

The 16 Cu ions in the unit cell are distributed over 4 Cu-I sites and 12 Cu-II sites and form a network of corner-sharing tetrahedra, where each Cu tetrahedron comprises 1 Cu-I and 3 Cu-II ions. Owing to the different bond lengths between the 16 Cu^{2+} sites in the unit cell, it is possible to make a real space classification of the exchange energy scales into a “strong” and “weak” type.^[25] Through the strong Heisenberg and DM exchange interactions, tetrahedral 3-spin-up-1-down triplet clusters couple far above^[25] the macroscopic ordering temperature $T_C \approx 58$ K. These $S = 1$ spin clusters turn out to be the relevant low-energy spin entities in Cu_2OSeO_3 . The weaker inter-tetrahedral Heisenberg and DM exchange couplings mediate the interactions between the $S = 1$ entities, giving rise to long-range helimagnetic order below T_C . This separation into inter- and intra-tetrahedral energy scales is well supported by the splitting of the magnon spectra in two well separated energy bands.^[26] Finally, weak cubic magnetic anisotropy terms pin the helimagnetic spirals along the six equivalent crystallographic $\langle 100 \rangle$ directions, leading to domain formation.^[22,27,28] In the presence of an external magnetic field, different metamagnetic phases are formed. Applied magnetic fields of a few tenths of mT are enough to fully lift the degeneracy of the helical domains, giving a conical type of order with the propagation vector \mathbf{q} along the applied field. Above a second critical field the system is driven into the field-polarized ferrimagnetic phase, where all tetrahedral $S = 1$ entities are aligned with the magnetic field. The skyrmion lattice phase (SkL) is located within a narrow field-temperature window just below $T_C \approx 58$ K for moderate applied fields of the order of 20 - 50 mT.^[20,22]

4.3 Experimental methods

High-quality single crystals were grown using a standard chemical vapor transport method.^[29] Single crystal x-ray diffraction^[30] measurements and the here described optical polarization rotation measurements show that Cu_2OSeO_3 single crystals are chiral, and that both handednesses can be realized experimentally. The studied crystals were oriented by crystal morphology inspection after which the fine orientation was done by means of a Laue camera. For the ellipsometry study a (100) surface was prepared (sample surface dimensions approximately $2.7 \text{ mm} \times 2.8 \text{ mm}$, thickness 0.8 mm). For the polarimetry study, two (111) oriented samples with opposite crystallographic chirality were used. A levorotatory crystal (as seen from the source) was chosen for the temperature- and field-dependent polarization rotation measurements. The surface area was approximately $3.6 \text{ mm} \times 3.2 \text{ mm}$, with used thicknesses of $d \approx 1.00 \text{ mm}$ and $d \approx 221 \pm 3 \mu\text{m}$. The dextrorotatory crystal, used for a consistency check of the natural optical activity, had a surface area of approximately $2.1 \text{ mm} \times 1.8 \text{ mm}$ and thickness $d \approx 223 \pm 3 \mu\text{m}$. All samples were polished with Al_2O_3 suspension ($\approx 1 \mu\text{m}$ grain size) in order to obtain optically smooth surfaces.

For the optical spectroscopy part, a Woollam VASE spectroscopic ellipsometer with an autoretarder between source and sample was used. Ellipsometry allows to obtain the real and imaginary parts of the complex dielectric function in a self normalizing way. The (100) sample was mounted in a UHV chamber with liquid-He flow cryostat and measured in the range 0.75 to 5 eV at a fixed angle of incidence (70°). For the analysis of the ellipsometric data, the surface roughness was estimated using the knowledge that absorption is small in the transparency windows below 1 eV and around 2.3 eV.

For the polarization rotation measurements a home built optical polarimetry setup based on the polarization modulation technique described in Refs. [31] and [32] was used (also see chapter [3]). Measurements are possible in the energy range of 1.1 eV to 3.5 eV in fields up to 5 T and temperatures down to 10 K. The measurements are performed in Faraday (transmission) geometry, where the light propagates along the crystallographic [111] direction, with the magnetic field also applied along this direction.

4.4 Zero-field optical properties

4.4.1 Optical excitations

In Fig. [4.2] the diagonal component $\sigma_{xx,1}$ of the optical conductivity at 15 K and 300 K is shown. A clear electronic gap with an onset at about 2.5 eV at 15 K, and charge-transfer excitations peaking at 3.2 eV and 4.0 eV with an optical conductivity of about 400 and $1200 \Omega^{-1}\text{cm}^{-1}$ respectively is ob-

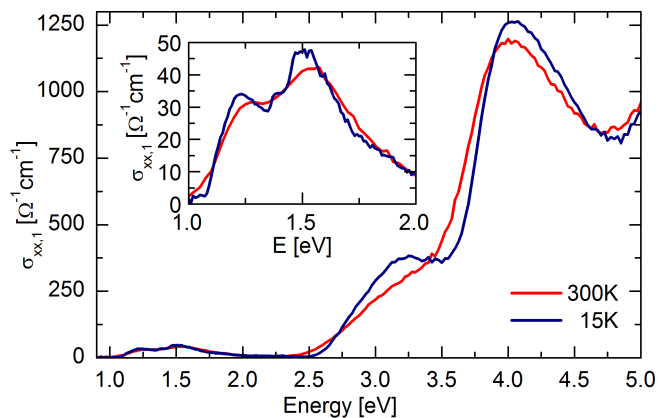


Figure 4.2: Optical conductivity at 15 K and 300 K as obtained by ellipsometry. The onset of charge-transfer excitations is observed at about 2.5 eV at 15 K. Between 1.0 and 2.0 eV local crystal-field excitations are observed with conductivity values not surpassing $50 \Omega^{-1} \text{cm}^{-1}$. At 15 K, pronounced peaks are located at 1.2, 1.4, and 1.5 eV. The features broaden with increasing temperature, obscuring the 1.4 eV peak at 300 K, as seen in the inset.

served. Hubbard-augmented density functional theory (DFT+ U) calculations find narrow Cu hole bands for both Cu sites with an energy difference of about $\Delta E = E_{\text{II}} - E_{\text{I}} = 0.2 \text{ eV}$, while the valence band primarily consists of broad oxygen bands.³³ The structure in the charge-transfer region is tentatively assigned to both the splitting ΔE and the structure in the O2p valence band density of states. With decreasing temperature, the charge-transfer excitations show a blueshift and a sharpening.

The first consequence of the low structural symmetry appears in the optical conductivity. Between 1.0 and 2.0 eV we find a multi-peak absorption feature, with a conductivity maximum of about $50 \Omega^{-1} \text{cm}^{-1}$, i. e., much weaker than the charge-transfer excitations (see inset of Fig. 4.2). At 15 K, pronounced peaks are located at 1.2, 1.4, and 1.5 eV. The peaks broaden with increasing temperature, obscuring the peak at 1.4 eV at 300 K. These features are interpreted as local crystal-field (CF) excitations. Similar excitation energies were observed before for CF excitations of Cu^{2+} ions in a trigonal bipyramidal crystal field.³⁴ For materials with inversion symmetry at the transition-metal site, such crystal-field excitations would be parity forbidden within the dipole approximation. They only become weakly allowed via the simultaneous excitation of an inversion-symmetry-breaking odd-parity phonon. Typical values of $\sigma_1(\omega)$ for such phonon-assisted excitations are below $10 \Omega^{-1} \text{cm}^{-1}$.³⁵ In contrast, the absence of inversion symmetry at the Cu-I and Cu-II sites in Cu_2OSeO_3 allows for dipole-active CF excitations by symmetry, and thus naturally explains the sizable spectral weight below the gap between 1.0 and 2.0 eV.

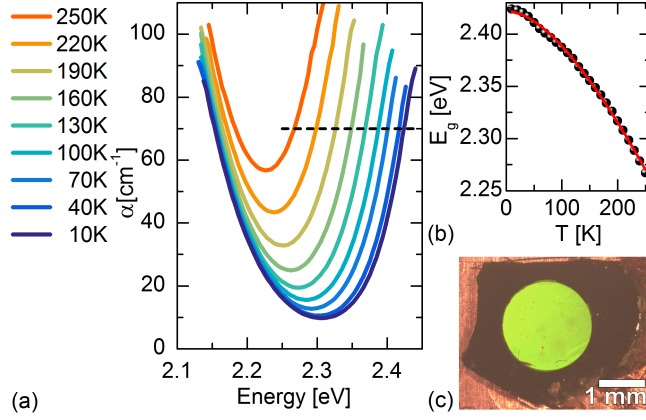


Figure 4.3: (a) Temperature-dependent absorption spectra in the range of the transmission window as measured on the 1 mm thick sample. (b) Temperature dependence of the onset E_g of excitations across the gap, determined at $\alpha = 70 \text{ cm}^{-1}$. The fit (red line) is based on the empirical Varshni equation. (c) Cu_2OSeO_3 is transparent for green light. The (111) sample, with a thickness $d \approx 221 \pm 3 \mu\text{m}$, is glued on a copper sample holder with a 2.0 mm diameter hole.

According to group theory,³⁶ dipole-active excitations are allowed from xy and $x^2 - y^2$ to z^2 for the Cu-I site (assuming D_{3h} symmetry) and from xz and yz to $x^2 - y^2$ for the Cu-II site (assuming C_{4v} symmetry). Both sets of transitions are schematically indicated in Fig. 4.1. The spectral weight in the low-energy region, however, has a richer structure with at least three peaks at 15 K. The above mentioned analysis ignores the fact that the Cu sites show a slight distortion away from the ideal square pyramidal and trigonal bipyramidal symmetries. Considering the correct, lower site symmetries, the remaining crystal-field excitations also are dipole active and will also contribute to the total spectral weight. Note that the two peak energies observed at 300 K *soften* to lower energy with decreasing temperature (see the appendix for a more detailed T dependence). This is opposite to the behavior of the charge-transfer peaks and can be attributed to the asymmetric line shape found in particular at low temperature. Such an asymmetric line shape can be described by the Franck-Condon line shape typical for crystal-field excitations.^{35,37}

The assignment of the onset of charge-transfer excitations to an energy of about 2.5 eV is corroborated by the observation of a narrow transmission window which is situated between the crystal-field excitations and the charge-transfer region. At 10 K the absorption coefficient becomes as low as 10 cm^{-1} at 2.3 eV, see Fig. 4.3. On the low-energy side the absorption decreases with decreasing temperature due to the sharpening of the crystal-field excitations. On the high-energy side a more drastic change of the absorption coefficient is found, reflecting the temperature dependence of the

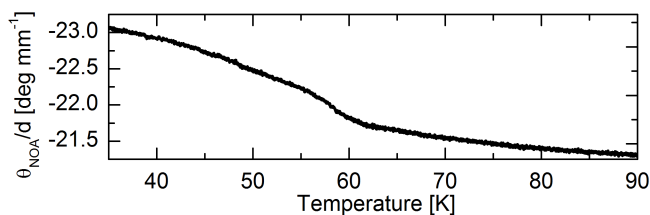


Figure 4.4: The natural optical activity θ_{NOA} per sample thickness d in deg/mm measured along the crystallographic (111) axis with probe photon energy $E_{\text{probe}} = 2.30 \pm 0.03$ eV. The crystal is levorotatory. Above the Curie temperature $T_{\text{C}} \approx 58$ K, the temperature dependence is weak. Below T_{C} an enhancement of θ_{NOA} is observed, which is attributed to the finite magneto-electric coupling in the helimagnetically ordered state.

onset E_{g} of excitations across the gap. This temperature dependence is well described by the empirical Varshni equation,³⁸ as seen in Fig. 4.3b.

Previously, Miller *et al.*³⁹ reported on the optical conductivity of Cu_2OSeO_3 at 300 K based on a Kramers-Kronig analysis of reflectivity data. Above 2.5 eV, the data from Miller *et al.* agrees reasonably well with the results reported above, showing a dominant peak at 4 eV. However, a Kramers-Kronig analysis is not sensitive to weak absorption features, thus the crystal-field excitations between 1.0 and 2.0 eV were not resolved. Additionally, Miller *et al.*³⁹ reported on a transmission window in the frequency range above the phonons and below about 1 eV. This agrees with the onset of crystal-field excitations observed in the ellipsometry data.

4.4.2 Natural optical activity

Due to the chiral crystal structure, Cu_2OSeO_3 is expected to show circular birefringence with a concomitant optical rotation for linearly polarized light, known as natural optical activity with rotation angle θ_{NOA} .^{19,40} The low absorption around 2.3 eV allows to measure the polarization rotation in transmission geometry. As a probe wavelength $\lambda_{\text{probe}} = 540 \pm 5$ nm ($E_{\text{probe}} = 2.30 \pm 0.03$ eV) was used, which corresponds to the transmission maximum at low temperature. At room temperature both, the left- and the right-handed (111) oriented crystals have a rotation magnitude of around 18 deg/mm, but the sign of the polarization rotation changes with crystallographic handedness. When the light propagation direction is reversed, the rotational sense keeps the same for both crystals. The latter two observations are regarded as earmarks for the phenomenon of natural optical activity.⁴¹

The temperature dependence of θ_{NOA} across the paramagnetic-helimagnetic phase transition ($T_{\text{C}} \approx 58$ K) was measured for the levorotatory crystal. The result is given in Fig. 4.4, showing θ_{NOA}/d .

Above T_C a finite θ_{NOA}/d of around -21.5 deg/mm is found. The temperature dependence of θ_{NOA} in the paramagnetic phase hints at an increase of the structural chirality upon lowering temperature, i. e., a displacement of ions at general coordinates within the Cu_2OSeO_3 unit cell, satisfying the threefold rotational symmetry of the structural helix.

In the helimagnetically ordered phase, the temperature dependence of θ_{NOA} is enhanced. Since there is no net magnetization in the helimagnetic phase for $\mu_0 H_a = 0$ mT, [Ref. 27] no Faraday rotation is expected. Different studies suggest that no significant magnetostrictive lattice contraction nor lattice deformations are present in Cu_2OSeO_3 related to the transition into the helimagnetic phase. 24,42 Instead, the increasing θ_{NOA} strongly hints to the presence of a finite magneto-electric coupling in the helimagnetic phase, as suggested in Refs. 23, 24, 27 and 28.

4.5 Magneto-optical properties

4.5.1 Phase transitions

In the presence of a magnetic field $\mathbf{H}_a \parallel [111]$, different metamagnetic phases with a finite magnetization $M(H_a)$ form in Cu_2OSeO_3 . 20 For these phases, the total polarization rotation can be approximated by

$$\theta_{\text{tot}} \approx \theta_{\text{NOA}} + \theta_{\text{F}}(M(H_a)) \quad (4.1)$$

where θ_{F} denotes the Faraday rotation which is proportional to the magnetization $M(H_a)$ in the $[111]$ direction. 43,44 The field-dependent magnetization can be rewritten as $M(H_a) = \chi_m(H_a) \cdot H_a$, where $\chi_m(H_a)$ refers to the magnetic susceptibility. Note that the magnetic susceptibility χ_m itself is a function of the external field strength H_a . The probed Faraday rotation per sample thickness d thus equals:

$$\begin{aligned} \frac{1}{d} \theta_{\text{F}}(\omega, M(H_a)) &= \beta(\omega) \cdot M(H_a) \\ &= \beta(\omega) \cdot \chi_m(H_a) \cdot H_a \end{aligned} \quad (4.2)$$

where $\beta(\omega)$ captures the microscopic magneto-optical properties. 45

Figure 4.5 shows the Faraday rotation per sample thickness, θ_{F}/d , as a function of field strength $\mu_0 H_a$ for temperatures ranging from 15 K to 65 K. At zero applied field, different helimagnetic domains exist. However, there is no net magnetization, even for a single helical domain. In this way, θ_{F} is zero for $\mu_0 H_a = 0$ mT [Ref. 27]. With increasing field the helimagnetic domains acquire a conical contribution, leading to a finite field-induced magnetization $M(H)$, and hence a Faraday rotation. The multi- \mathbf{q} helimagnetic domain structure however still persists. At a critical field of around 60 mT at 15 K, the reorientation transition from the multi- \mathbf{q} helical to the single- \mathbf{q} conical

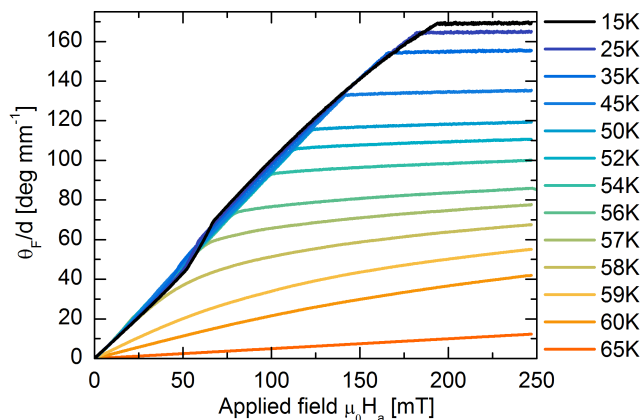


Figure 4.5: The Faraday rotation per sample thickness, θ_F/d , as a function of field for different temperatures. With increasing field, θ_F increases until a plateau is reached, marking the phase transition between conical and ferrimagnetic order. At 15 K this phase transition is induced around an applied field of $\mu_0 H_a \approx 195$ mT. At lower fields, in the 15 K curve around $\mu_0 H_a \approx 60$ mT, the helical-conical phase transition becomes apparent as a kink in the field dependence of θ_F/d .

phase is observed. With increasing field, the spin projection parallel to \mathbf{q} and \mathbf{H}_a increases. It is for this reason that in the conical phase the Faraday rotation still increases with field, until a plateau is reached, marking the phase transition from conical to field-polarized ferrimagnetic order. At 15 K this phase transition is induced around an applied field of $\mu_0 H_a \approx 195$ mT. At the plateau a rotation of around 170 deg/mm is found for 15 K. The Faraday rotation sense was determined to be positive.⁴⁶

The second derivative⁴⁷ of the Faraday rotation allows to construct the phase diagram shown in Fig. 4.6. The right panel gives a zoom-in around T_C . In this way the phase transitions to the skyrmion lattice phase (SkL) become apparent. With a field applied along the $\langle 111 \rangle$ hard axis, the phase transition from conical to ferrimagnetic order (indicated by triangles) is of second order,²⁵ and the phase transition can be identified with a local minimum in the second derivative of the order parameter $M \propto \theta_F$. The phase transitions from helical to conical order (diamonds) and between the conical phase and the SkL phase (indicated by circles) are of first order and can be identified with a zero-crossing in the second derivative of θ_F . The diamonds and circles in Fig. 4.6 indicate these zero crossings, marking the phase boundaries.

The phase transitions from the paramagnetic phase to the ordered phases are best observed in temperature sweeps at constant field. Depending on the field strength, different phase transitions occur. Figure 4.7 shows $\theta_F / (\mu_0 H_a \cdot d)$ across the paramagnetic-helimagnetic phase transition for $|\mu_0 H_a| < 2$ mT. At low temperatures, deep within the helimagnetic phase,

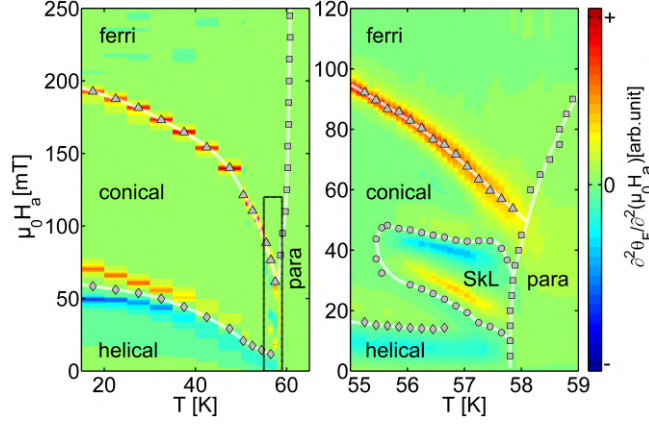


Figure 4.6: The magnetic phase diagram of Cu_2OSeO_3 as obtained from the Faraday rotation. $\mu_0 H_a$ is the applied magnetic field strength along the crystallographic (111) direction. The left panel shows the magnetic phase diagram for a large $(\mu_0 H_a, T)$ range, whereas the right panel gives a zoom-in around the skyrmion lattice phase (SkL). The triangles indicate the conical-ferrimagnetic phase boundary. Diamonds give the helical-conical phase boundary. The SkL phase boundary is indicated by the circles. The phase boundary between ordered phases and the paramagnetic phase is indicated by the squares. The color mapping indicates the second derivative of the Faraday rotation. For a quantitative comparison of the critical fields with results obtained by other techniques, one needs to take into account the demagnetization factor (see main text).

$\theta_F / (\mu_0 H_a \cdot d)$ does not show a significant temperature dependence. However, an anomaly is observed around the paramagnetic-helimagnetic transition. In fact, the anomaly marks T_C . In mean-field approximation this phase transition is expected to be of second order. However, the interaction between chiral fluctuations renormalizes the phase transition into a weak first-order transition,^[48] as seen in the temperature dependence of $\theta_F / (\mu_0 H_a \cdot d)$. The fluctuation-disordered region is observed just above T_C .^[49] In this region the magnetic susceptibility deviates from pure Curie-Weiss behavior. The onset of this region is identified by the inflection point, located about 1 K above T_C (indicated by the red diamonds).

The high-field phase transitions from the paramagnetic to the ordered phases are best seen in the temperature dependence of the first derivative $d\theta_F/dH_a$. The first derivative is defined as a magneto-optical susceptibility:

$$\chi_{\text{MO}} = \frac{1}{d} \frac{d\theta_F}{dH_a} = \beta(\omega) \left[\chi_m(H_a) + \frac{\partial \chi_m}{\partial H_a} H_a \right], \quad (4.3)$$

as shown in Fig. 4.8 in $\text{rad}/\text{T}\cdot\text{m}$ unit, at different values of applied field strength $\mu_0 H_a$. The temperature and field dependence of χ_{MO} show reasonable agreement with the magnetic ac-susceptibility as reported by Živković *et al.*^[50] Small deviations can be attributed to the field dependence of χ_m .

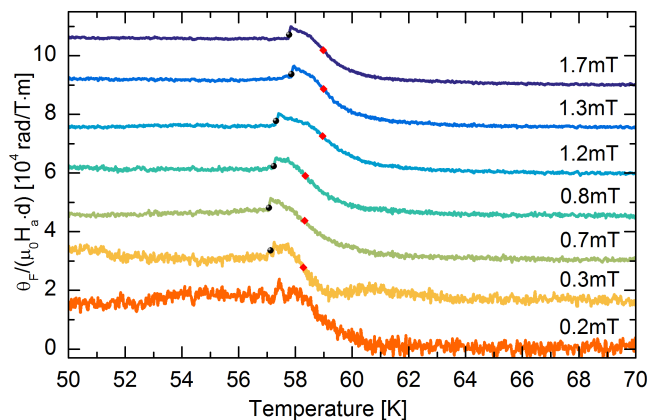


Figure 4.7: Faraday rotation across the paramagnetic-helimagnetic phase transition, normalized by applied field strength $\mu_0 H_a$. The curves are offset by $(\pi/1.8) \cdot 10^5$ rad/T·m with respect to each other. Within the helical phase the scaled rotation attains a value of $\theta_F / (\mu_0 H_a \cdot d) \approx 1.7 \cdot 10^5$ rad/T·m. The weak first-order transition into the helical phase is marked by black circles. The fluctuation-disorder regime is located between the black dot and the red diamond.

For 5 mT the characteristic anomaly for the paramagnetic-helimagnetic transition is visible again. For applied fields of 15, 25, and 45 mT the first-order nature remains for the paramagnetic-SkL and paramagnetic-conical transitions. The broad maximum found at lower temperatures for these applied fields indicates the temperature-induced conical-helical phase transition. At higher fields such as 100, 150, and 225 mT, the paramagnetic-ferrimagnetic phase transition is crossed. The magneto-optical susceptibility for these field values shows that the character of the phase transition changes to second order. For Cu_2OSeO_3 , this change of the phase-transition type has been discussed extensively by Živković *et al.*^[50] The increase in χ_{MO} at lower temperatures for field values between 80 and 190 mT shows where the temperature-induced ferrimagnetic-conical phase transition is crossed. With the first derivative, the phase diagram can be completed. The boundary between the paramagnetic phase and the ordered phases is indicated by squares in the phase diagram. Qualitatively, the optically probed phase diagram is in excellent agreement with previously reported results based on other techniques.^[20,22,23] For a quantitative comparison of the applied field strengths at which the phase transitions are observed, one has to take into account demagnetization effects related to the sample shape. For the Faraday measurements a thin plate of Cu_2OSeO_3 was used, for which demagnetization effects are substantial. The demagnetization factor can be estimated^[51] to lie around $N_z \approx 0.9$. Accordingly, the phase transitions occur at higher applied fields than for instance in a spherical sample with $N_z = 1/3$.

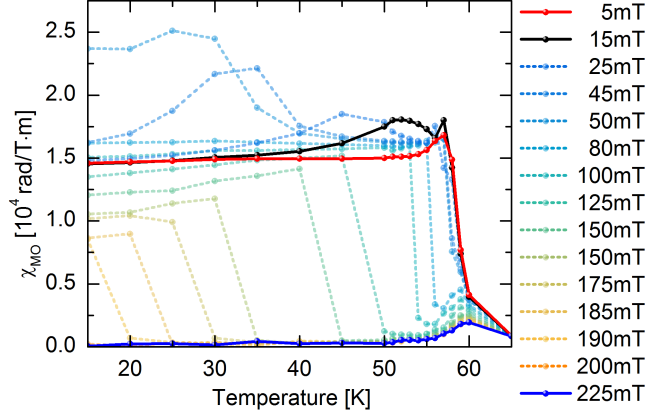


Figure 4.8: The magneto-optical susceptibility χ_{MO} as a function of temperature at different applied field strengths $\mu_0 H_a$. The phase transition from the paramagnetic phase to one of the ordered phases shows a rescaling from first order (for the para to helical/conical/SkL phases) to second order (para-ferri) with increasing field. The changes in χ_{MO} below $T_C \approx 58$ K show the temperature-induced conical-helical and ferrimagnetic-conical phase transitions.

4.5.2 Field-even rotation and directional dichroism

Phenomenologically, the measured polarization rotation $\theta_{\text{tot}}(H_a)$ can be split into odd and even contributions, $\theta_{\text{odd/even}}(H_a) = [\theta_{\text{tot}}(+H_a) \mp \theta_{\text{tot}}(-H_a)]/2$. In systems which simultaneously lack time-reversal and spatial inversion symmetry, one may expect a field-even contribution to the Faraday effect, in addition to the usual field-odd effect.^[1,52,53]

A finite polarization rotation even in H_a is indeed observed, as shown in Fig. 4.9. Besides the Faraday rotation, the natural optical activity of chiral magnets lacking spatial inversion symmetry may show a field-even variation as well.^[54,55] Unfortunately, the present experiments do not allow to discriminate between these contributions. At 15 K, θ_{even} constitutes less than about 2% of the measured field-dependent polarization rotation. With increasing field, θ_{even} increases until the ferrimagnetic phase is reached, where the rotation levels off. At the helical-conical phase transition, a jagged feature appears. This feature reflects hysteretic behavior. Since the sweeps were performed between opposite field polarities, the phase transitions are traversed in opposite direction, i.e. the applied field either decreases or increases. Symmetrization of the hysteretic behavior leads to the jagged feature. Such hysteretic behavior in the field direction has also been observed for phase transitions in other cubic chiral magnets, as for instance in $\text{Fe}_{1-x}\text{Co}_x\text{Si}$.^[56]

The magnetic chiral structure allows for an additional higher-order optical effect, namely non-reciprocal directional dichroism.^[13,14] In Cu_2OSeO_3 this effect has been observed for microwave resonance modes.^[57] This effect was investigated in the optical range (around 2.3 eV) for the various mag-

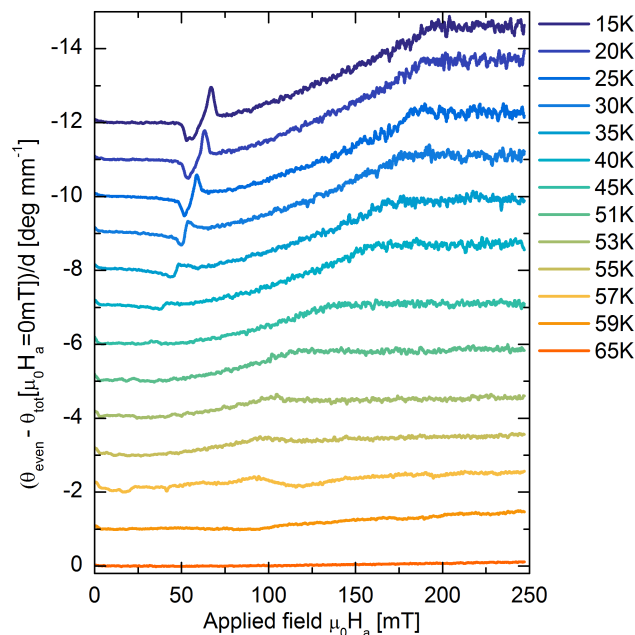


Figure 4.9: The field-even rotation θ_{even} , shown here per sample thickness d for some selected temperatures. The curves are offset by -1 deg/mm for clarity. The phase transition from conical to ferrimagnetic order again becomes apparent. The jagged feature at the helical-conical phase transition is due to hysteresis in θ_F .

netic phases at 15 K, but no conclusive observation could be made. Given the sensitivity of the setup, this limits a possible non-reciprocal directional dichroism to well below 1%.

4.5.3 Magnitude of the magneto-optical effect

The polarization rotation reaches a value of around 170 deg/mm in the field-polarized ferrimagnetic phase above 195 mT at 15 K. At this temperature a magneto-optical susceptibility on the order of 10^4 rad/T·m for smaller magnetic fields is found. Both these values are large, but can be explained by the fact that the spin clusters are fully polarized already for moderate magnetic fields of 195 mT.

For a field-independent magnetic susceptibility, the size of the magneto-optical response can be expressed by the Verdet coefficient $\mathcal{V}(\omega) = \beta(\omega) \cdot \chi_m$ (cf. Equ. 4.3). In the helical phase at low temperatures and small fields the field dependence of χ_m is only small. This is apparent from the magneto-optical susceptibility χ_{MO} , see Fig. 4.8. The helical phase therefore has a Verdet coefficient of around $1.5 \cdot 10^4$ rad/T·m to first approximation. Taking into account the demagnetizing field correction,^[50,51] this means $\mathcal{V}(540 \text{ nm}) \approx 3 \cdot 10^4$ rad/T·m, a value rivaling known strong magneto-optical

rotators such as the paramagnets $\text{Tb}_3\text{Ga}_5\text{O}_{12}$ (with $\mathcal{V}(1053 \text{ nm}) \approx 0.3 \cdot 10^4 \text{ rad/T}\cdot\text{m}$ at 4.2 K)^[58] and $\text{Cd}_{1-x}\text{Mn}_x\text{Te}$ ($\mathcal{V} \lesssim 9 \cdot 10^4 \text{ rad/T}\cdot\text{m}$ at 77 K depending on ω and stoichiometry).^[59] For these paramagnets, the large size of \mathcal{V} solely originates in $\beta(\omega)$.^[43] In contrast, the large magneto-optical response of Cu_2OSeO_3 can be attributed to the large magnetic susceptibility at low fields and the strong magnetization at larger fields.

The magnetization^[24] of Cu_2OSeO_3 shows that the $S = 1$ clusters are fully aligned along the applied field in the ferrimagnetic phase, i. e. already for moderate magnetic fields of 0.2 T. This reflects that the magnetocrystalline anisotropy is weak in this cubic magnet with small spin-orbit coupling. As a result, the helical or conical domains can be easily reoriented,^[60] even when the magnetic field is applied along the $\langle 111 \rangle$ hard axis. This in turn is reflected in a large magnetic susceptibility χ_m , and hence a large magneto-optical susceptibility χ_{MO} .

For the field-polarized ferrimagnetic phase, strong magneto-optical effects are naturally expected. In fact, roughly similar (volume) magnetizations and polarization rotations have been observed in ferromagnetic cuprates such as the 2D compounds K_2CuF_4 [61] and $(\text{CH}_3\text{NH}_3)_2\text{CuCl}_4$ [62], showing rotations of 36 deg/mm and 50 deg/mm, respectively. This shows that the magneto-optical coupling $\beta(\omega)$ in Cu_2OSeO_3 is of equal order of magnitude as in these materials.

The microscopic magneto-optical interaction $\beta(\omega)$ depends on the difference in dipole transition strength for the σ_+ and σ_- transitions at ω , where \pm refers to right/left circularly polarized light, respectively.^[43] A *larger* difference in transition strength leads to a *stronger* rotation. In a ferromagnet with full spin polarization, only one of the transitions σ_{\pm} is preferentially allowed due to angular momentum conservation.

In contrast, a perfect antiferromagnet with zero magnetization shows equal transition strengths and thus no polarization rotation. In Cu_2OSeO_3 , one finds a ferromagnetic alignment of the $S = 1$ clusters but antiferromagnetic alignment between Cu-I and Cu-II sites within a given cluster, see Fig. 4.1. However, the excitation energies are different for Cu-I and Cu-II sites, which holds for both, the crystal-field excitations and charge-transfer excitations. In addition, the Cu-I and Cu-II sites are present in a ratio of 1:3. Accordingly, the cancellation typical for a simple antiferromagnet does not occur in Cu_2OSeO_3 . Moreover, the transition dipole strength of both types of excitations is relatively large, which magnifies the magneto-optical response. Whether the different optical transitions have the same rotational sense or not cannot be answered based on a single-wavelength measurement and remains open for further studies.

4.6 Conclusions

We have discussed how a variety of linear optical properties can be used to probe inversion and time-reversal breaking properties of the chiral magnetic cuprate Cu_2OSeO_3 . The broken inversion symmetry at the two crystallographically inequivalent Cu sites leads to a finite dipole matrix element for local crystal-field excitations. These orbital excitations were observed below the charge-transfer gap, in the energy range from 1.0 to 2.0 eV. The transmission window found between the crystal-field and the charge-transfer absorption regions allowed to measure the optical polarization rotation across the various magnetic phase transitions in Cu_2OSeO_3 . The zero-field optical rotation, corresponding to the natural optical activity of the crystal, is enhanced upon entering the helimagnetically ordered phase. This observation provides evidence for a finite magneto-electric coupling in the helimagnetic phase of Cu_2OSeO_3 .

In the presence of an external magnetic field, the finite magnetization leads to a sizable Faraday rotation. The ease of domain reorientation by the external magnetic field was discussed to be at the origin of the large magneto-optical susceptibility in the helical and conical phases. The large Faraday rotation observed in the field-polarized ferrimagnetic phase agrees with results obtained on ferromagnetic cuprates. The Faraday rotation provides a sensitive tool to conveniently probe the nature of the various magnetic phase transitions in Cu_2OSeO_3 , including the subtle first-order nature of the helimagnetic-paramagnetic phase transition. From the magneto-optical data the phase diagram of Cu_2OSeO_3 as a function of magnetic field and temperature was reconstructed, including the skyrmion lattice phase.

4.7 Appendix

4.7.1 Temperature dependence of ellipsometry data

The temperature dependence of the optical conductivity in the region of the crystal-field excitations is shown in more detail in Fig. 4.10. The inset shows the temperature dependence of the spectral weight of this region, i. e. the integral of $\sigma_1(\omega)$ from 1 to 2 eV. We find a slight increase of the spectral weight with increasing temperature. The onset of magnetic order at 58 K has no significant effect on the spectral weight of the crystal-field excitations.

4.7.2 Kerr spectroscopy

Kerr spectra in polar geometry of a [111] oriented single crystal of Cu_2OSeO_3 were taken at $T = 10$ K. The colored lines give the $\theta_K(E)$ spectra in degrees at the indicated external fields as a function of photon energy E in eV. The grey curve is the optical conductivity at 15 K for reference. In both the

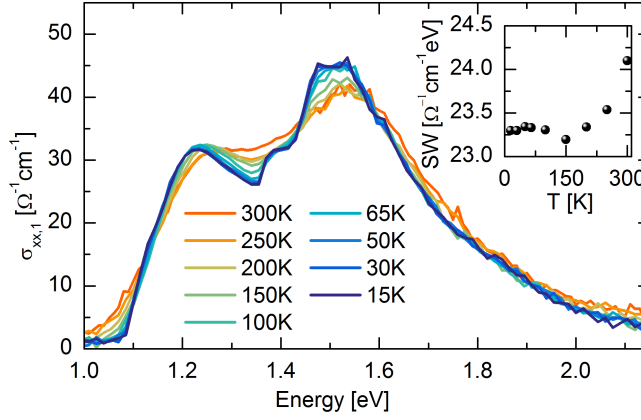


Figure 4.10: Optical conductivity in the region of the crystal-field excitations for different temperatures. The inset depicts the spectral weight (integral of the optical conductivity between 1.0 and 2.0 eV) as a function of temperature.

local crystal field excitation region, and the charge transfer excitation region a Kerr rotation is observed, with a magnitude up to about $|\theta_K| \sim 0.6$ deg. In the energy range 2.1 to 2.5 eV the sample is transparent. In this region an interference between Faraday and Kerr rotated electromagnetic waves is observed. This spectral region isn't plotted since the measured rotation does not correspond to a pure Kerr-rotation. The phenomenon is explained in detail below.

Magnetic field sweeps were performed at 800 nm probe wavelength for various temperatures, as shown in Fig. 4.11. The signal to noise is lower than the Faraday measurements described in Par. 4.5.1, however, the helical to conical, and conical to ferrimagnetic phase transitions can still be clearly resolved. The 60 K curve shows an approximately linear response as expected for the paramagnetic phase.

4.7.3 Interference of Faraday and Kerr rotated electromagnetic waves

Measurements

The transparency and strong Faraday rotation for 540 nm probe wavelength allows for the observation of a rather intriguing optical effect, namely the interference between Faraday and Kerr rotated electromagnetic waves. The experiment was performed on two Cu_2OSeO_3 samples with thicknesses $d \approx 0.38$ mm and $d \approx 1.23$ mm respectively. Figure 4.12a shows field sweeps of the polarization rotation θ_m for the $d \approx 0.38$ mm sample for various temperatures measured in a reflection geometry (polar Kerr geometry with $\mathbf{H}_a \parallel [111]$). For 540 nm probe wavelength the field dependent rotation θ_m significantly deviates from the Kerr rotation θ_K measured at 800 nm probe

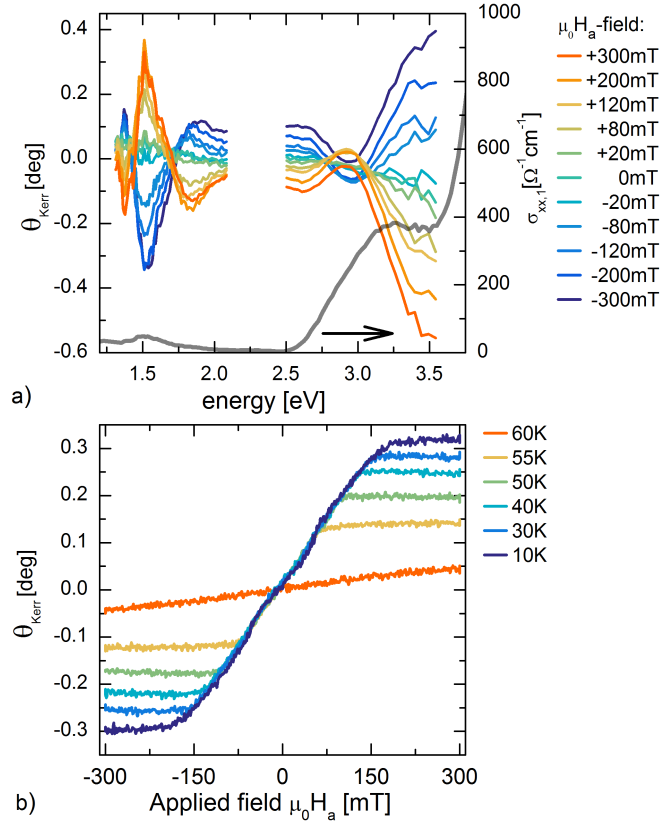


Figure 4.11: a) Kerr spectra for various applied magnetic field strengths $\mu_0 H_a$ (colored curves). The spectra were taken at 10 K. The Kerr rotation θ_K is indicated in deg units. The optical conductivity $\sigma_{xx,1}$ is shown for reference. In both the crystal field excitation region, and the charge transfer region a Kerr rotation is observed. b) Field sweeps were taken at 800 nm probe wavelength for various temperatures. In the 10 K curve the helical-conical and conical-ferrimagnetic phase transition are both clearly resolved. The 60 K curve shows an approximately linear response, as expected for the paramagnetic phase.

wavelength as presented in Fig. 4.11b. For temperatures below $T_C \approx 58$ K a clear sinusoidal-like modulation is observed, where at $T = 10$ K two full periods can be observed. The modulation eventually appears to stop at the conical-ferrimagnetic phase transition. The critical fields for the conical-ferrimagnetic phase transition decrease with increasing temperature. At $T = 60$ K the response is nearly flat, i.e. a paramagnetic response is measured. These observations are in good agreement with the Kerr probing at 800 nm and Faraday probing at 540 nm. For the $d \approx 1.23$ mm thick sample a similar observation is made, however five full periods can now be distinguished. The rotation amplitude $|\theta_m|_{\max}$ has decreased by approximately a factor of $\times 45$ with respect to the thinner sample.

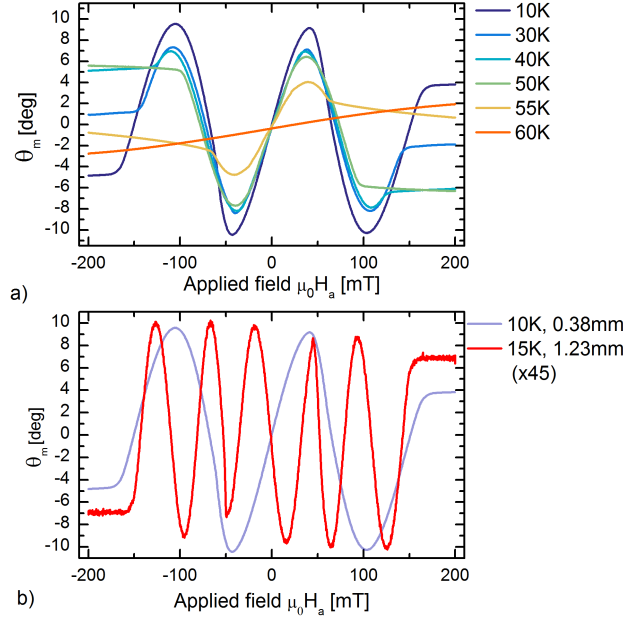


Figure 4.12: a) Temperature dependent rotation in reflection geometry for 540 nm probing wavelength. A $d \approx 0.38$ mm sample was used. The most striking difference with respect to probing at 800 nm is the sinusoidal-like interference. Two full periods are observed. The modulation eventually appears to stop at the conical-ferrimagnetic phase transition. b) Thickness-dependence of the interference. For a 1.23 mm thick sample five full periods are observed, whereas for the 0.38 mm thick sample two full periods are observed. Note that the rotation amplitude for the thicker sample is about $\times 45$ smaller.

Model

The sinusoidal-like modulation is understood in terms of interference between front and back surface reflected light as schematically depicted in Fig. 4.13. Consider a slab of a weakly absorbing magnetic material with thickness $d \gg \lambda$, where λ is the light wavelength. The incident electric field is \mathbf{E}_0 . Part of the wave is reflected from the front surface with a complex reflectivity constant $r \cdot e^{-i\theta_K}$. The reflected electric field component therefore is:

$$\mathbf{E}_r = r \cdot e^{-i\theta_K} \mathbf{E}_0 \quad (4.4)$$

where the polarization plane has rotated over an angle $-\theta_K$. The sign of the Kerr rotation is defined to be negative. The transmission coefficient for the interface is $t = 1 - r$. The electric field strength attenuates by a factor $e^{-\alpha d}$ upon transmission through the slab, where α is the absorption coefficient. In addition the electric field polarization plane rotates over an angle $+\theta_F$ (Faraday rotation). Note that the Faraday and Kerr effect have

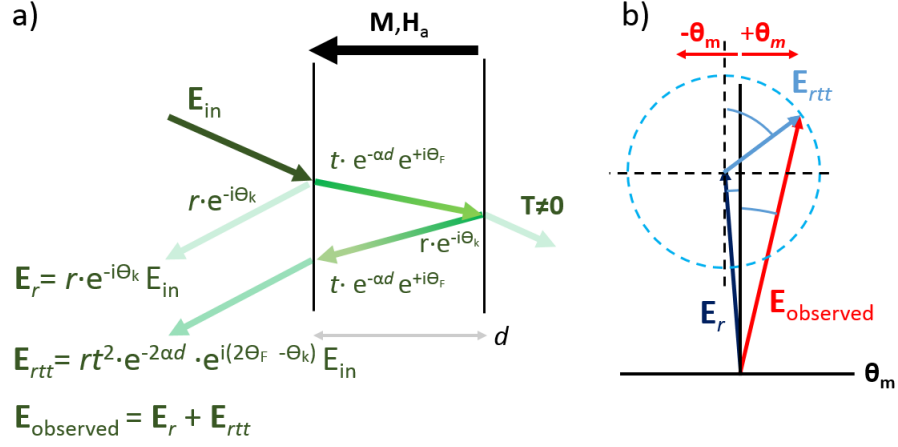


Figure 4.13: a) Interference of front and back reflected electric fields with rotated polarization planes in a magnetic material. The magnetization is indicated with \mathbf{M} . An incident electric field \mathbf{E}_{in} is reflected from the front surface and Kerr rotated over an angle $-\theta_K$, giving the electric field \mathbf{E}_r . The transmitted light acquires a double Faraday rotation $+2\theta_F$ and in addition a Kerr rotation $-\theta_K$ from the back surface, giving the electric field \mathbf{E}_{rtt} . The front and back surface reflected electric fields add to $\mathbf{E}_{observed} = \mathbf{E}_r + \mathbf{E}_{rtt}$, leading to an interference pattern in the observed rotation. b) In the scheme the reflected field \mathbf{E}_r has a small negative Kerr rotation $-\theta_K$. Furthermore it is assumed that $|\theta_K| \ll \frac{\pi}{2}$ and $|\theta_K| \ll |2\theta_F|$. The doubled Faraday rotation $+2\theta_F$ is large and can make multiple 2π rotations. The back surface reflected field \mathbf{E}_{rtt} has acquired a total polarization rotation angle of $+2\theta_F - \theta_K$. The fields \mathbf{E}_r and \mathbf{E}_{rtt} add up to $\mathbf{E}_{observed}$. For approximately $2n\pi \lesssim 2\theta_F - \theta_K \lesssim (2n+1)\pi$, where $n \in \mathbb{Z}$ the observed polarization rotation is *positive* ($\mathbf{E}_{observed}$ lies in the right plane). For $(2n+1)\pi \lesssim 2\theta_F - \theta_K \lesssim (2n+2)\pi$, where $n \in \mathbb{Z}$ the observed polarization rotation is *negative* ($\mathbf{E}_{observed}$ lies in the left plane).

an opposite sense of rotation.^[44] Upon reflection from the back surface, the electric field acquires an additional rotation $-\theta_K$. The back surface reflected beam acquires an additional Faraday rotation $+\theta_F$ upon transmission. The back reflected electric field thereby is:

$$\mathbf{E}_{rtt} = r t^2 \cdot e^{-2\alpha d} \cdot e^{i(2\theta_F - \theta_K)} \mathbf{E}_0 \quad (4.5)$$

The total electric field at the detector side is:

$$\mathbf{E}_{observed} = \mathbf{E}_r + \mathbf{E}_{rtt} = r \cdot e^{-i\theta_K} \mathbf{E}_0 + r t^2 \cdot e^{-2\alpha d} \cdot e^{i(2\theta_F - \theta_K)} \mathbf{E}_0 \quad (4.6)$$

with an amplitude and phase component:

$$\mathbf{E}_{observed} = |\mathbf{E}_{observed}| e^{i \cdot \text{Arg}(\mathbf{E}_{observed})} \quad (4.7)$$

The interference of the front and back reflected electric fields mixes the pure Faraday and Kerr rotation. The measured polarization rotation in

reflection geometry equals:

$$\theta_m = \text{Arg}(\mathbf{E}_{\text{observed}}) = \text{Arg}(r \cdot e^{-i\theta_K} \mathbf{E}_0 + rt^2 \cdot e^{-2\alpha d} \cdot e^{i(2\theta_F - \theta_K)} \mathbf{E}_0) \quad (4.8)$$

The Kerr rotation is generally $|\theta_K|_{\text{max}} \ll \frac{\pi}{2}$. Furthermore $|\theta_K|_{\text{max}} \ll |\theta_F|_{\text{max}}$. In that case, for approximately $2n\pi \lesssim 2\theta_F - \theta_K \lesssim (2n+1)\pi$, where $n \in \mathbb{Z}$, the measured polarization rotation is *positive*. In the sketch in Fig. 4.13b the vector $\mathbf{E}_{\text{observed}}$ lies in the right plane. For $(2n+1)\pi \lesssim 2\theta_F - \theta_K \lesssim (2n+2)\pi$ the observed polarization rotation is *negative*, with the vector $\mathbf{E}_{\text{observed}}$ in the left plane. Equation 4.8 reduces to the Kerr rotation $-\theta_K$ in case of $r = 1$, or $d \rightarrow \infty$.

Discussion

The polarization rotation θ_m is measured as a function of external field strength H_a . However, the Faraday and Kerr rotation are proportional to the magnetization M instead, where the magnetization is again a function of external field H_a (see Par. 4.5.1):

$$\theta_F = d \cdot \beta \cdot M(H_a) \quad (4.9a)$$

$$\theta_K = \zeta \cdot M(H_a) \quad (4.9b)$$

Here β and ζ are magneto-optical constants. The field dependent Kerr rotation $\theta_K(H_a)$ for 800 nm can be used to map the external field H_a onto magnetization M by Eq. 4.9b. In Fig. 4.14a the rotation $\theta_m(H_a)$ measured at 540 nm is plotted versus the rotation $\theta_K(H_a)$ at 800 nm. As such, θ_m is now plotted as function of a “magnetization” given in deg units, leaving only the sinusoidal-like modulation. The mapping works good up till the conical-ferrimagnetic phase transition. A fit to the interference angle θ_m in Eq. 4.8 is plotted.

The rotation amplitude $|\theta_m|_{\text{max}}$ for the thick sample is approximately $\times 45$ smaller than the thin sample. We see that the amplitude of the Faraday rotated electric field \mathbf{E}_{rtt} scales with $e^{-2\alpha d}$. When $d \gg \frac{1}{\alpha(\lambda)}$ the interference thus disappears. This is in qualitative agreement with the observation of the reduced $|\theta_m|_{\text{max}}$ for the thicker sample.

For the thin sample 2 full periodicities in θ_m are observed at $T = 10$ K, and for the thick sample at least 5 full periodicities. For the thick sample this means that $2\theta_F \approx 5 \cdot 2\pi$ rad, or in other words, the back reflected phase front has Faraday rotated over $\approx 1800^\circ$ degrees! This large Faraday rotation underlines why we took the effort to prepare a thin Cu_2OSeO_3 sample in the study of the main part of the chapter. For thick Cu_2OSeO_3 samples measured Faraday rotation will multiple times pass $\pm 45^\circ$, the angle around

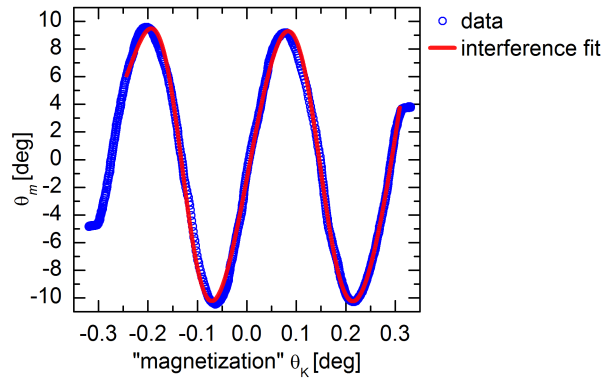


Figure 4.14: The blue data points are the rotation at 540 nm versus the pure Kerr-rotation measured at 800 nm. Fit to the polarization rotation interference function from Eq. 4.8.

which the polarization detection response flattens out with the used double modulation technique (see chapter 3). Popularly speaking, the above described interference allows to compress a *pure* $\theta_F \approx 1800^\circ$ Faraday rotation into a $\theta_m \approx 0.25^\circ$ *measurable* polarization rotation.

The interference effect is expected to be observable in other magnetic materials under the condition of a small absorption ($\frac{1}{\alpha(\lambda)} \sim d \gg \lambda$). The sample has to be thick enough to allow for multiple 2π Faraday rotations. Furthermore a large magnetic susceptibility χ_m is necessary over a wide field range. This can, for instance, be found in materials with similar meta-magnetic phase transitions as in Cu_2OSeO_3 (think of cycloidal order) or materials with strongly pinned ferromagnetic domains.

Interference effects in magneto-optical spectroscopy have been discussed in quite detail in literature. Internal reflections influence the measured Faraday rotation (transmission geometry).⁶³ One very interesting application is the simultaneous detection of Kerr and Faraday rotation by terahertz time-domain spectroscopy,⁶⁴ as was also demonstrated in Cu_2OSeO_3 .⁶⁵ Transparent/absorptive multilayers can be created to amplify the Kerr angle through interference in highly absorbing films.^{44,66} The here observed interference effect does not appear to be described by either one of these effects.

4.8 Own contributions and acknowledgements

The main part of this chapter is published in:

R. B. Versteeg, I. Vergara, S. D. Schäfer, D. Bischoff, A. Aqeel,
T. T. M. Palstra, M. Grüninger, and P. H. M. van Loosdrecht,
Optically probed symmetry breaking in the chiral magnet Cu_2OSeO_3 ,
Phys. Rev. B **94**, 094409 (2016)
© 2016 “American Physical Society”

The for this chapter used polarization spectroscopy setup was constructed by me and Simon Schäfer. The absorption, natural optical activity, and magneto-optical measurements described in the main part of the chapter and the appendix, have been carried out and analysed by myself, with assistance from Simon Schäfer and Dario Bischof. Ignacio Vergara performed the ellipsometry measurements and analysed the ellipsometry data. Aisha Aqeel (University of Groningen, The Netherlands) grew the single crystals used in the work of this chapter. The main part of this chapter was written by myself, with contributions made by P. H. M. van Loosdrecht, M. Grüninger, and Ignacio Vergara. The appendix part was written by myself.

I am grateful to M. Garst, A. Rosch, P. Becker, L. Bohatý, T. Lorenz, and G. R. Blake for insightful discussions. I would also like to thank Prashant Padmanabhan for critical reading of part of this chapter.

4.9 Bibliography

- [1] A. K. Zvezdin and V. A. Kotov, *Modern Magneto-optics and Magneto-optical Materials*, (Institute of Physics Publishing, London, 1997).
- [2] Y. Tokura, S. Seki, and N. Nagaosa, Multiferroics of spin origin, Rep. Prog. Phys. **77**, 076501 (2014).
- [3] D. I. Khomskii, Trend: Classifying multiferroics: Mechanisms and effects, Physics **2**, 20 (2009).
- [4] D. I. Khomskii, Multiferroics: Different ways to combine magnetism and ferroelectricity, J. Magn. Magn. Mater. **306**, 1 (2006).
- [5] N. Nagaosa and Y. Tokura, Topological properties and dynamics of magnetic skyrmions, Nat. Nanotechnol. **8**, 899 (2013).
- [6] N. A. Spaldin, M. Fiebig, and M. Mostovoy, The toroidal moment in condensed-matter physics and its relation to the magnetoelectric effect, J. Phys. Condens. Matter **20**, 434203 (2008).
- [7] A. S. Zimmermann, D. Meier, and M. Fiebig, Ferroic nature of magnetic toroidal order, Nat. Commun. **5**, 4796 (2014).
- [8] T. Kaelberer, V. A. Fedotov, N. Papasimakis, D. P. Tsai, and N. I. Zheludev, Toroidal dipolar response in a metamaterial, Science **330**, 1510 (2010).
- [9] N. Papasimakis, V. Fedotov, V. Savinov, T. Raybould, and N. I. Zheludev, Electromagnetic toroidal excitations in matter and free space, Nat. Mater. **15**, 263 (2016).

- [10] B. B. Krichevtsov, V. V. Pavlov, R. V. Pisarev, and V. N. Gridnev, Spontaneous non-reciprocal reflection of light from antiferromagnetic Cr_2O_3 , *J. Phys. Condens. Matter* **5**, 8233 (1993).
- [11] A. Pimenov, A. A. Mukhin, V. Yu. Ivanov, V. D. Travkin, A. M. Balbashov, and A. Loidl, Possible evidence for electromagnons in multiferroic manganites, *Nat. Phys.* **2**, 97 (2006).
- [12] P. Rovillain, J. Liu, M. Cazayous, Y. Gallais, M-A. Measson, H. Sakata, and A. Sauter, Electromagnon and phonon excitations in multiferroic TbMnO_3 , *Phys. Rev. B* **86**, 014437 (2012).
- [13] G. L. J. A. Rikken and E. Raupach, Pure and cascaded magnetochiral anisotropy in optical absorption, *Phys. Rev. E* **58**, 5081 (1998).
- [14] D. Szaller, S. Bordács, and I. Kézsmárki, Symmetry conditions for nonreciprocal light propagation in magnetic crystals, *Phys. Rev. B* **87**, 014421 (2013).
- [15] I. Kézsmárki, D. Szaller, S. Bordács, V. Kocsis, Y. Tokunaga, Y. Taguchi, H. Murakawa, Y. Tokura, H. Engelkamp, T. Rõöm, and U. Nagel, One-way transparency of four-coloured spin-wave excitations in multiferroic materials, *Nat. Commun.* **5**, 3203 (2014).
- [16] S. Toyoda, N. Abe, S. Kimura, Y. H. Matsuda, T. Nomura, A. Ikeda, S. Takeyama, and T. Arima, One-way transparency of light in multiferroic CuB_2O_4 , *Phys. Rev. Lett.* **115**, 267207 (2015).
- [17] P. Bak and M. H. Jensen, Theory of helical magnetic structures and phase transitions in MnSi and FeGe , *J. Phys. C: Solid St. Phys.* **13**, L881 (1980).
- [18] U. K. Röbller, A. A. Leonov, and A. N. Bogdanov, Chiral skyrmionic matter in non-centrosymmetric magnets, *J. Phys.: Conf. Ser.* **303**, 012105 (2011).
- [19] A. Glazer and K. G. Cox, *Classical linear crystal optics* in *International Tables for Crystallography, Vol. D*, (John Wiley & Sons, Ltd., 2006), Chapter 1.1.6.
- [20] S. Seki, X. Z. Yu, S. Ishiwata, and Y. Tokura, Observation of skyrmions in a multiferroic material, *Science* **336**, 198 (2012).
- [21] M. C. Langner, S. Roy, S. K. Mishra, J. C. T. Lee, X. W. Shi, M. A. Hossain, Y.-D. Chuang, S. Seki, Y. Tokura, S. D. Kevan, and R. W. Schoenlein, Coupled skyrmion sublattices in Cu_2OSeO_3 , *Phys. Rev. Lett.* **112**, 167202 (2014).
- [22] T. Adams, A. Chacon, M. Wagner, A. Bauer, G. Brandl, B. Pedersen, H. Berger, P. Lemmens, and C. Pfleiderer, Long-wavelength helimagnetic order and skyrmion lattice phase in Cu_2OSeO_3 , *Phys. Rev. Lett.* **108**, 237204 (2012).
- [23] E. Ruff, P. Lunkenheimer, V. V. Tsapenko, A. Loidl, H. Berger, and S. Krohns, Magnetoelectric effects in the skyrmion host material Cu_2OSeO_3 , *Sci. Rep.* **5**, 15025 (2015).
- [24] J.-W. G. Bos, C. V. Colin, and T. T. M. Palstra, Magnetoelectric coupling in the cubic ferrimagnet Cu_2OSeO_3 , *Phys. Rev. B* **78**, 094416 (2008).
- [25] O. Janson, I. Rousochatzakis, A. A. Tsirlin, M. Belesi, A. A. Leonov, U. K. Röbller, J. Van den Brink, and H. Rosner, The quantum nature of skyrmions and half-skyrmions in Cu_2OSeO_3 , *Nat. Commun.* **5**, 5376 (2014).
- [26] P. Y. Portnichenko, J. Romhányi, Y. A. Onykiienko, A. Henschel, M. Schmidt, A. S. Cameron, M. A. Surmach, J. A. Lim, J. T. Park, A. Schneidewind, D. L. Abernathy, H. Rosner, J. van den Brink, and D. Inosov, Magnon spectrum of the helimagnetic insulator Cu_2OSeO_3 , *Nat. Commun.* **7**, 10725 (2016).

- [27] M. Belesi, I. Rousochatzakis, M. Abid, U. K. Röbber, H. Berger, and J.-Ph. Ansermet, Magnetolectric effects in single crystals of the cubic ferrimagnetic helimagnet Cu_2OSeO_3 , *Phys. Rev. B* **85**, 224413 (2012).
- [28] S. Seki, S. Ishiwata, and Y. Tokura, Magnetolectric nature of skyrmions in a chiral magnetic insulator Cu_2OSeO_3 , *Phys. Rev. B* **86**, 060403 (2012).
- [29] M. Belesi, I. Rousochatzakis, H. C. Wu, H. Berger, I. V. Shvets, F. Mila, and J. Ph. Ansermet, Ferrimagnetism of the magnetoelectric compound Cu_2OSeO_3 probed by ^{77}Se NMR, *Phys. Rev. B* **82**, 094422 (2010).
- [30] A. Aqeel, J. Baas, G. R. Blake, and T. T. M. Palstra, *unpublished* (2016).
- [31] K. Sato, Measurement of Magneto-optical Kerr effect using piezo-birefringent modulator, *Jpn. J. Appl. Phys.* **20**, 2403 (1981).
- [32] S. Polisetty, J. Scheffler, S. Sahoo, Y. Wang, T. Mukherjee, X. He, and Ch. Binek, Optimization of magneto-optical kerr setup: Analyzing experimental assemblies using Jones matrix formalism, *Rev. Sci. Instrum.* **79**, 055107 (2008).
- [33] J. H. Yang, Z. L. Li, X. Z. Lu, M.-H. Whangbo, S.-H. Wei, X. G. Gong, and H. J. Xiang, Strong Dzyaloshinskii-Moriya interaction and origin of ferroelectricity in Cu_2OSeO_3 , *Phys. Rev. Lett.* **109**, 107203 (2012).
- [34] R. Kuroda, S. F. Mason, T. Prosperi, S. Savage, and G. E. Tranter, Solid-state absorption and circular-dichroism spectra of five-co-ordinated trigonal copper(II) complexes: anisotropic contributions to the $d-d$ transition probabilities, *J. Chem. Soc., Dalton Trans.* **12**, 2565 (1981).
- [35] R. Rückamp, E. Benckiser, M. W. Haverkort, H. Roth, T. Lorenz, A. Freimuth, L. Jongen, A. Möller, G. Meyer, P. Reutler, B. Büchner, A. Revcolevschi, S.-W. Cheong, C. Sekar, G. Krabbes, and M. Grüninger, Optical study of orbital excitations in transition-metal oxides, *New J. Phys.* **7**, 144 (2005).
- [36] M. I. Aroyo, A. Kirov, C. Capillas, J. M. Perez-Mato, and H. Wondratschek, *Bilbao Crystallographic Server. II. Representations of crystallographic point groups and space groups*, *Acta Crystallogr. Sect. A* **62**, 115 (2006).
- [37] B. N. Figgis and M. A. Hitchman, *Ligand field theory and its applications*, (Wiley-VCH, 2000).
- [38] Y. P. Varshni, Temperature dependence of the energy gap in semiconductors, *Physica* **34**, 149 (1967).
- [39] K. H. Miller, X. S. Xu, H. Berger, E. S. Knowles, D. J. Arenas, M. W. Meisel, and D. B. Tanner, Magnetodielectric coupling of infrared phonons in single-crystal Cu_2OSeO_3 , *Phys. Rev. B* **82**, 144107 (2010).
- [40] L. D. Barron, *Molecular Light Scattering and Optical Activity*, (Cambridge University Press, New York, 2009).
- [41] R. E. Newnham. *Properties of Materials: Anisotropy, Symmetry, Structure*, (Oxford University Press, USA, 2008).
- [42] V. S. Kurnosov, V. P. Gnezdilov, V. V. Tsapenko, P. Lemmens, and H. Berger, Analysis of the low-frequency spectrum of the cubic noncentrosymmetric ferrimagnet Cu_2OSeO_3 , *Low Temp. Phys.* **38**, 489 (2012).
- [43] P. S. Pershan, Magneto-Optical Effects, *J. Appl. Phys.* **38**, 1482 (1967).
- [44] M. J. Freiser, A survey of magneto-optic effects, *IEEE Trans. Magn.* **4**, 152 (1968).
- [45] The effect of internal reflections on the measured Faraday rotation is neglected since the reflection coefficient $R \approx 0.12$ at 540 nm. This means that only $\mathcal{O}(R^2) \sim 1\%$ of the transmitted intensity originates from the first back reflection.

- [46] J.-M. Liu, *Photonic Devices*, (Cambridge University Press, Cambridge, 2005).
- [47] R. Chartrand, Numerical differentiation of noisy, nonsmooth data, *ISRN Appl. Math.* **2011**, 164564 (2011).
- [48] M. Janoschek, M. Garst, A. Bauer, P. Krautscheid, R. Georgii, P. Böni, and C. Pfleiderer, Fluctuation-induced first-order phase transition in Dzyaloshinskii-Moriya helimagnets, *Phys. Rev. B* **87**, 134407 (2013).
- [49] A. Bauer and C. Pfleiderer, in *Topological Structures in Ferroic Materials: Domain Walls, Vortices and Skyrmions*, chapter *Generic Aspects of Skyrmion Lattices in Chiral Magnets*, (Springer International Publishing, 2016).
- [50] I. Živković, J. S. White, H. M. Rønnow, K. Prša, and H. Berger, Critical scaling in the cubic helimagnet Cu_2OSeO_3 , *Phys. Rev. B* **89**, 060401 (2014).
- [51] M. Sato and Y. Ishii, Simple and approximate expressions of demagnetizing factors of uniformly magnetized rectangular rod and cylinder, *J. Appl. Phys.* **66**, 983 (1989).
- [52] N. F. Kharchenko, A. V. Bibik, and V. V. Eremenko, Quadratic magnetic rotation of the polarization plane of light in the antiferromagnet CoF_2 , *Zh. Eksp. Teor. Fiz.* **42**, 447 (1985).
- [53] N. F. Kharchenko, A. V. Bibik, D. M. Desvignes, and H. Le Gall, Quadratic magnetic rotation of polarization plane of light in antiferromagnetic CaMnGe garnet, *Low Temp. Phys.* **20**, 296 (1994).
- [54] M. Surma, Magneto-optical circular birefringence of a chiral medium in high magnetic field, *Mol. Phys.* **90**, 993 (1997).
- [55] R. Zawodny, S. Woźniak, and G. Wagnière, On quadratic dc magnetic field-induced circular birefringence and dichroism in isotropic chiral media, *Mol. Phys.* **91**, 165 (1997).
- [56] A. Bauer, M. Garst, and C. Pfleiderer, History dependence of the magnetic properties of single-crystal $\text{Fe}_{1-x}\text{Co}_x\text{Si}$, *Phys. Rev. B* **93**, 235144 (2016).
- [57] Y. Okamura, F. Kagawa, S. Seki, M. Kubota, M. Kawasaki, and Y. Tokura, Microwave magnetochiral dichroism in the chiral-lattice magnet Cu_2OSeO_3 , *Phys. Rev. Lett.* **114**, 197202 (2015).
- [58] R. Yasuhara, S. Tokita, J. Kawanaka, T. Kawashima, H. Kan, H. Yagi, H. Nozawa, T. Yanagitani, Y. Fujimoto, H. Yoshida, and M. Nakatsuka, Cryogenic temperature characteristics of verdet constant on terbium gallium garnet ceramics, *Opt. Express* **15**, 11255 (2007).
- [59] J.A. Gaj, R.R. Gałazka, and M. Nawrocki, Giant exciton faraday rotation in $\text{Cd}_{1-x}\text{Mn}_x\text{Te}$ mixed crystals, *Solid State Commun.* **25**, 193 (1978).
- [60] V. A. Chizhikov and V. E. Dmitrienko, Microscopic description of twisted magnet Cu_2OSeO_3 , *J. Magn. Magn. Mater.* **382**, 142 (2015).
- [61] R. Laiho and T. Levola, Dispersions of the optical faraday rotation and of the refractive index in K_2CuF_4 , *Solid State Commun.* **18**, 1619 (1976).
- [62] H. Arend, J. Schoenes, and P. Wachter, Magneto-optical investigations of the two-dimensional ferromagnet $(\text{CH}_3\text{NH}_3)_2\text{CuCl}_4$, *Phys. Status Solidi B* **69**, 105 (1975).
- [63] H. Piller, Effect of internal reflection on optical Faraday rotation, *J. Appl. Phys.* **37**, 763 (1966).
- [64] R. Valdés Aguilar, A. V. Stier, W. Liu, L. S. Bilbro, D. K. George, N. Bansal, L. Wu, and J. Cerne, A. G. Markelz, S. Oh, and N. P. Armitage, Terahertz Response and Colossal Kerr Rotation from the Surface States of the Topological Insulator Bi_2Se_3 .

- [65] N. J. Laurita, G. G. Marcus, B. A. Trump, J. Kindervater, M. B. Stone, T. M. McQueen, C. L. Broholm, and N. P. Armitage, Low-energy magnon dynamics and magneto-optics of the skyrmionic Mott insulator Cu_2OSeO_3 , *Phys. Rev. B* **95**, (2017).
- [66] G. A. N. Connell, Interference enhanced Kerr spectroscopy for very thin absorbing films, *Appl. Phys. Lett.* **40**, 212 (1982).

Chapter 5

Inelastic light scattering from spin cluster excitations in Cu_2OSeO_3

5.1 Introduction

This chapter discusses Cu_2OSeO_3 's spin cluster physics in greater detail and reports on spontaneous Raman scattering from spin cluster excitations. The exchange interactions in Cu_2OSeO_3 are repeated and the spin cluster Hamiltonian with resulting spin cluster states is discussed. The results of an electron spin resonance study and an inelastic neutron scattering study of the spin cluster excitation spectrum are summarized. Particularly interesting is that the long-range order of spin clusters leads to a clear division of the spin wave spectrum into low-energy *external* spin cluster excitations, and high-energy *internal* spin cluster excitations, showing that Cu_2OSeO_3 can be regarded as a solid-state molecular crystal of spin nature. In order to understand the Raman-activity of the spin cluster excitations, an introduction to magnetic Raman scattering is provided. Temperature dependent steady-state Raman spectra of Cu_2OSeO_3 are presented. Different high-energy spin cluster excitations are observed besides a multitude of phonons. The Raman scattering mechanism of the spin cluster modes is discussed. The temperature dependence of the scattering of a subset of spin cluster excitations and phonons is furthermore presented. The high-energy spin excitations are shown to soften and broaden below the long-range ordering temperature T_C , while a broad magnetic scattering continuum persists above T_C . Such behaviour is discussed to be characteristic of internal spin cluster excitations in solid-state molecular crystals of spin nature.

5.2 The Cu_4 spin cluster model

5.2.1 Exchange interactions

Figure 5.1a shows the magnetic unit cell of Cu_2OSeO_3 . The localized Cu^{2+} $S = 1/2$ spins reside on the vertices of corner-shared tetrahedra in a distorted pyrochlore lattice.^[1] DFT+ U calculations reveal that these tetrahedra can be divided into tetrahedra of “stronger” and “weaker” exchange energy scales.^[1,2] A few exchange couplings are indicated in Fig. 5.1a as $J_{\text{F},\text{s}}$, $J_{\text{AF},\text{s}}$, $J_{\text{F},\text{w}}$, and $J_{\text{AF},\text{w}}$, where the subscripts refer to (anti)ferromagnetic (AF/F) and strong or weak exchange (s/w). The blue lines are predominantly ferromagnetic, and the red lines predominantly antiferromagnetic exchange couplings. The full lines represent strong intra-cluster exchange couplings and the dashed lines weak inter-cluster exchange couplings. An additional antiferromagnetic exchange $J_{\text{AF},\text{OO}}$ couples spins across a hexagon of alternating Cu-I and Cu-II sites, as indicated with the green hexagon in Fig. 5.1b. Dzyaloshinskii–Moriya (DM) interactions are also present along all bondings. The DM-interaction is especially strong (relative to the Heisenberg exchange) along the inter-cluster path ways.^[1] The DM-contribution is however not taken into account in the cluster calculations presented in Ref. [1] and [3], of which the results are summarized in this chapter. Evidently, the DM-interaction will have effect on the cluster states and spin wave spectrum. This matter is only briefly addressed, as it is beyond the scope of this thesis work.

The strong Heisenberg (and Dzyaloshinskii-Moriya exchange) interactions couple four localized $S = 1/2$ spins into a three-up-one-down $S = 1$ entity (grey arrow) as depicted by orange shaded tetrahedra in Fig. 5.1c. Here the Cu-II ions couple ferromagnetically through $J_{\text{F},\text{s}}$, while the Cu-I couples antiferromagnetically to the Cu-II ions through $J_{\text{AF},\text{s}}$. These strongly coupled $S = 1$ clusters form a magnetic trillium lattice,^[4] where the clusters are coupled through the weaker exchange paths $J_{\text{F},\text{w}}$ and $J_{\text{AF},\text{w}}$. The weak exchange couplings can be thought to form a “weakly coupled” tetrahedron (grey shaded tetrahedron in Fig. 5.1c).

5.2.2 The isolated cluster model

For the single isolated cluster the relevant exchange paths are the strong paths $J_{\text{F},\text{s}}$ and $J_{\text{AF},\text{s}}$. The eigenenergies of the isolated cluster can be calculated by means of the single-tetrahedron Hamiltonian:

$$\begin{aligned} \hat{\mathcal{H}}_0 &= J_{\text{AF},\text{s}} \hat{S}_1 \cdot \hat{S}_{234} + J_{\text{FM},\text{s}} (\hat{S}_2 \cdot \hat{S}_3 + \hat{S}_3 \cdot \hat{S}_4 + \hat{S}_4 \cdot \hat{S}_2) \\ &= \frac{J_{\text{AF},\text{s}}}{2} \hat{S}^2 + \frac{J_{\text{FM},\text{s}} - J_{\text{AF},\text{s}}}{2} \hat{S}_{234}^2 - \frac{3}{8} (J_{\text{AF},\text{s}} + 3J_{\text{FM},\text{s}}) \end{aligned} \quad (5.1)$$

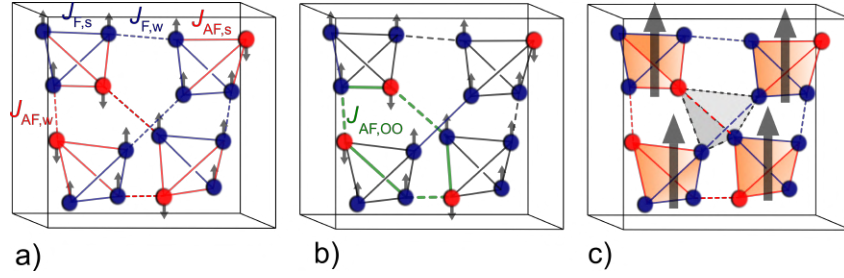


Figure 5.1: a) The magnetic unit cell of Cu₂OSeO₃. A few exchange interactions are indicated as $J_{F,s}$, $J_{AF,s}$, $J_{F,w}$, and $J_{AF,w}$ where the subscripts refer to (anti)ferromagnetic (AF/F) and strong or weak exchange (s/w). The blue lines are predominantly ferromagnetic exchange couplings and the red lines predominantly antiferromagnetic exchange couplings. The full lines are strong exchange couplings and the dashed lines weak exchange couplings. b) The exchange interaction $J_{AF,OO}$ antiferromagnetically couples spins along a hexagon of alternating Cu-I and Cu-II sites. c) The strong exchange interaction leads to effective $S = 1$ spin clusters (orange shaded tetrahedra). The spin clusters are coupled through the weaker inter-cluster exchange interactions (dashed lines), which form a weakly coupled cluster (the grey shaded tetrahedron). Dzyaloshinskii-Moriya exchange is also present along all interaction path ways. The DM-interaction is however not taken into account in the calculations. For clarity the DM-interaction also isn't indicated in the figures. The figures are inspired by the work from Refs. [1] and [3].

as discussed in Ref. [3]. Here \hat{S}_1 is the spin angular momentum operator for the spin on the Cu-I ion, and \hat{S}_2 , \hat{S}_3 , and \hat{S}_4 for the Cu-II ions. Then $\hat{S}_{23} = \hat{S}_2 + \hat{S}_3$, $\hat{S}_{234} = \hat{S}_2 + \hat{S}_3 + \hat{S}_4$, and $\hat{S} = \hat{S}_1 + \hat{S}_{234}$ are the sum of spin angular momentum operators of the three Cu-II sites and the whole cluster respectively. In the first line the exchange interactions between the single cluster spins are readily identified. However, the eigenenergies are more conveniently calculated in the reorganized form of $\hat{\mathcal{H}}_0$ in the second line.

The eigenstates are notated as $|S_{23}, S_{234}, S, S^z\rangle_R$. Here S_{23} , S_{234} and S indicate the spin quantum numbers. The secondary spin quantum number (the spin momentum projection along the z-axis) is indicated by S^z . The symmetry label R refers to the irreducible representations of the single cluster's C_{3v} point group (this is the cluster symmetry when only the magnetic Cu²⁺ ions are considered). Under the symmetry C_{3v} the $2^4 = 16$ -dimensional Hilbert space of a single tetrahedron splits into the ground state A₁-triplet $|g_0\rangle = |1, \frac{3}{2}, 1, S^z\rangle_{A_1}$, and two E₁ and E₂ singlets, one A₁ quintet, and two E₁ and E₂ triplets excited states as indicated in Table 5.1. Here $|S, S^z\rangle_R$ refers to the shortened state notation. The level degeneracy is indicated with D.

The expectation values for the angular momentum operators are:

$$\hat{S}^2 |S_{23}, S_{234}, S, S^z\rangle = S(S + 1) |S_{23}, S_{234}, S, S^z\rangle \quad (5.2)$$

and

$$\hat{S}_{234}^2 |S_{23}, S_{234}, S, S^z\rangle = S_{234}(S_{234} + 1) |S_{23}, S_{234}, S, S^z\rangle \quad (5.3)$$

This allows to calculate the eigenenergies E_N for the isolated cluster, as indicated in Table 5.1. The excitation energies, measured from the ground state energy $E_0 = \frac{1}{4}(-5J_{F,s} + 3J_{AF,s})$, are indicated by $\Delta E_N = E_N - E_0$. The excitation energies are obtained from Density Functional Theory, and are indicated in wavenumbers cm^{-1} and equivalent temperature in kelvin in the last column.[□] The energy diagram in Fig. 5.2a shows the excitation spectrum in cm^{-1} . For each isolated cluster state the irreducible representations R and the spin quantum number S is indicated. The single cluster state degeneracy is indicated in between brackets. Note that the states indicated by E_1 and E_2 are degenerate in energy, and labeled by the irrep E in Fig. 5.2a. The corresponding isolated spin cluster wave functions are indicated in Table 5.2. From the form of the wave functions it becomes apparent that the cluster wave functions are highly entangled.

Table 5.1: Isolated single cluster states and eigenenergies. In total there are 16 states for the isolated cluster. The state notations are given in full notation $|S_{23}, S_{234}, S, S^z\rangle_R$ and shortened notation $|S, S^z\rangle_R$. The state $|1, S^z\rangle_{A_1}$ gives the single cluster ground state. The degeneracy is indicated with D. E_N gives the energy of the degenerate states. ΔE_N gives the energy measured with respect to the ground state energy E_0 . The last two columns give the calculated transition energies in wavenumbers cm^{-1} and temperature K, as obtained from Density Functional Theory in Ref. [I](#)

N	$ S_{23}, S_{234}, S, S^z\rangle_R$	$ S, S^z\rangle_R$	D	E_N	$\Delta E_N = E_N - E_0$	$\Delta E_N [\text{cm}^{-1}]$	$\Delta E_N [\text{K}]$
0	$ 1, \frac{3}{2}, 1, S^z\rangle_{A_1}$	$ 1, S^z\rangle_{A_1}$	3	$\frac{1}{4}(-5J_{AF,s} + 3J_{FM,s})$	0	0	0
1	$ 1, \frac{1}{2}, 0, S^z\rangle_{E_1}$	$ 0, S^z\rangle_{E_1}$	1	$-\frac{3}{4}(J_{AF,s} + J_{FM,s})$	$\frac{1}{2}(J_{AF,s} - 3J_{FM,s})$	191	275
	$ 0, \frac{1}{2}, 0, S^z\rangle_{E_2}$	$ 0, S^z\rangle_{E_2}$	1				
2	$ 1, \frac{3}{2}, 2, S^z\rangle_{A_1}$	$ 2, S^z\rangle_{A_1}$	5	$\frac{3}{4}(J_{AF,s} + J_{FM,s})$	$2J_{AF,s}$	236	340
3	$ 1, \frac{1}{2}, 1, S^z\rangle_{E_1}$	$ 1, S^z\rangle_{E_1}$	3	$\frac{1}{4}(J_{AF,s} - 3J_{FM,s})$	$\frac{3}{2}(J_{AF,s} - J_{FM,s})$	309	445
	$ 0, \frac{1}{2}, 1, S^z\rangle_{E_2}$	$ 1, S^z\rangle_{E_2}$	3				

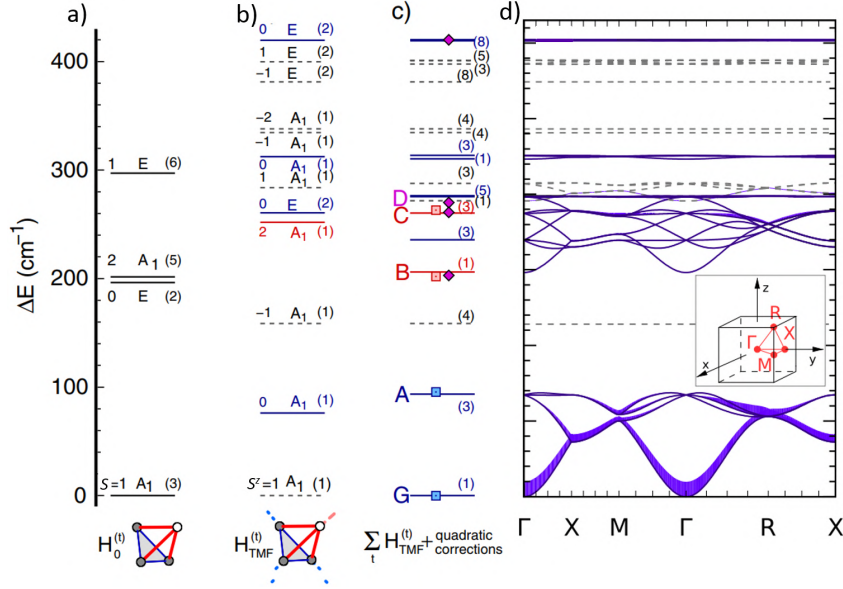


Figure 5.2: a) Energy spectrum of an isolated spin cluster. In total there are 16 states, however divided over a subset of degenerate energy levels. The ground state is $|S, S^z\rangle_{A_1} = |1, S^z\rangle_{A_1}$. There are three excited states. The respective symmetries, spin quantum number S , and degeneracies are indicated. b) The spin cluster energy spectrum in the interacting tetrahedral mean field model. Under the mean field the isolated cluster states lower their degeneracy. The respective symmetries and degeneracies (number in between brackets) are again indicated. The left number gives the secondary spin quantum number S^z of the respective n 'th state. c) Γ -point energies under the multiboson correction. d) The dispersive spin cluster spectrum is obtained in second quantization. The strongly dispersing low-energy branches are *external* cluster excitations. At higher energies the dispersion progressively flattens out. At the higher energy end of the spectrum the excitations have an *internal* cluster excitation character. Figures a to c are adapted from Ref. [2]. Reprinted figure with permission from M. Ozerov, J. Romhányi, M. Belesi, H. Berger, J.-Ph. Ansermet, Jeroen van den Brink, J. Wosnitza, S. A. Zvyagin, and I. Rousochatzakis, Phys. Rev. Lett. **113**, 157205 (2014), <https://doi.org/10.1103/PhysRevLett.113.157205>, © Copyright 2014 by the American Physical Society. Fig. d is adapted from Ref. [3]. Reprinted figure with permission from J. Romhányi, J. van den Brink, and I. Rousochatzakis, Phys. Rev. B **90**, 140404 (2014), <https://doi.org/10.1103/PhysRevB.90.140404>, © Copyright 2014 by the American Physical Society.

5.2.3 The interacting cluster model

The interaction between clusters is to first approximation captured by the tetrahedral mean field (TMF) Hamiltonian:

$$\hat{\mathcal{H}}_{\text{TMF}} = \hat{\mathcal{H}}_0 + J_{\text{AF},s}(\delta\hat{S}_1^z + \Delta\hat{S}_{234}^z) \quad (5.4)$$

Table 5.2: The 16 isolated single cluster wave functions. The state notation is indicated by $|S, S^z\rangle_{\text{R}}$. The superposition for the different cluster wave functions are fully written out. $|1, 1\rangle_{\text{A}_1}$ gives the single cluster ground state. The ground state in the interacting cluster model is a superposition of the states $|1, 1\rangle_{\text{A}_1}$ and $|2, 1\rangle_{\text{A}_1}$.

N	$ n\rangle$	$ S, S^z\rangle$	full wavefunction
0	1⟩	$ 1, 1\rangle_{\text{A}_1}$	$\frac{1}{2\sqrt{3}}(3 \downarrow\uparrow\uparrow\uparrow\rangle - \uparrow\downarrow\uparrow\uparrow\rangle - \uparrow\uparrow\downarrow\uparrow\rangle - \uparrow\uparrow\uparrow\downarrow\rangle)$
	2⟩	$ 1, 0\rangle_{\text{A}_1}$	$\frac{1}{\sqrt{6}}(\downarrow\downarrow\uparrow\uparrow\rangle + \downarrow\uparrow\downarrow\uparrow\rangle + \downarrow\uparrow\uparrow\downarrow\rangle - \uparrow\downarrow\downarrow\uparrow\rangle - \uparrow\downarrow\uparrow\downarrow\rangle - \uparrow\uparrow\downarrow\downarrow\rangle)$
	3⟩	$ 1, \bar{1}\rangle_{\text{A}_1}$	$\frac{1}{2\sqrt{3}}(\downarrow\downarrow\downarrow\uparrow\rangle + \downarrow\downarrow\uparrow\downarrow\rangle + \downarrow\uparrow\downarrow\downarrow\rangle - 3 \uparrow\downarrow\downarrow\downarrow\rangle)$
1	4⟩	$ 0, 0\rangle_{\text{E}_1}$	$\frac{1}{2\sqrt{3}}(2 \downarrow\downarrow\uparrow\uparrow\rangle - \downarrow\uparrow\downarrow\uparrow\rangle - \downarrow\uparrow\uparrow\downarrow\rangle - \uparrow\downarrow\downarrow\uparrow\rangle - \uparrow\downarrow\uparrow\downarrow\rangle + 2 \uparrow\uparrow\downarrow\downarrow\rangle)$
	5⟩	$ 0, 0\rangle_{\text{E}_2}$	$\frac{1}{2}(\downarrow\uparrow\downarrow\uparrow\rangle - \downarrow\uparrow\uparrow\downarrow\rangle - \uparrow\downarrow\downarrow\uparrow\rangle + \uparrow\downarrow\uparrow\downarrow\rangle)$
2	6⟩	$ 2, \bar{2}\rangle_{\text{A}_1}$	$ \downarrow\downarrow\downarrow\downarrow\rangle$
	7⟩	$ 2, \bar{1}\rangle_{\text{A}_1}$	$\frac{1}{2}(\downarrow\downarrow\downarrow\uparrow\rangle + \downarrow\downarrow\uparrow\downarrow\rangle + \downarrow\uparrow\downarrow\downarrow\rangle + \uparrow\downarrow\downarrow\downarrow\rangle)$
	8⟩	$ 2, 0\rangle_{\text{A}_1}$	$\frac{1}{\sqrt{6}}(\downarrow\downarrow\uparrow\uparrow\rangle + \downarrow\downarrow\uparrow\downarrow\rangle + \downarrow\uparrow\downarrow\uparrow\rangle + \uparrow\downarrow\downarrow\uparrow\rangle + \uparrow\downarrow\uparrow\downarrow\rangle + \uparrow\uparrow\downarrow\downarrow\rangle)$
	9⟩	$ 2, 1\rangle_{\text{A}_1}$	$\frac{1}{2}(\downarrow\uparrow\uparrow\uparrow\rangle + \uparrow\downarrow\uparrow\uparrow\rangle + \uparrow\uparrow\downarrow\uparrow\rangle + \uparrow\uparrow\uparrow\downarrow\rangle)$
	10⟩	$ 2, 2\rangle_{\text{A}_1}$	$ \uparrow\uparrow\uparrow\uparrow\rangle$
3	11⟩	$ 1, \bar{1}\rangle_{\text{E}_1}$	$\frac{1}{\sqrt{6}}(\downarrow\downarrow\downarrow\uparrow\rangle + \downarrow\downarrow\uparrow\downarrow\rangle - 2 \downarrow\uparrow\downarrow\downarrow\rangle)$
	12⟩	$ 1, \bar{1}\rangle_{\text{E}_2}$	$\frac{1}{2}(\downarrow\downarrow\downarrow\uparrow\rangle - \downarrow\downarrow\uparrow\downarrow\rangle)$
	13⟩	$ 1, 0\rangle_{\text{E}_1}$	$\frac{1}{2\sqrt{3}}(-2 \downarrow\downarrow\uparrow\uparrow\rangle + \downarrow\uparrow\downarrow\uparrow\rangle + \downarrow\uparrow\uparrow\downarrow\rangle - \uparrow\downarrow\downarrow\uparrow\rangle - \uparrow\downarrow\uparrow\downarrow\rangle + 2 \uparrow\uparrow\downarrow\downarrow\rangle)$
	14⟩	$ 1, 0\rangle_{\text{E}_2}$	$\frac{1}{2}(\downarrow\uparrow\downarrow\uparrow\rangle - \downarrow\uparrow\uparrow\downarrow\rangle + \uparrow\downarrow\downarrow\uparrow\rangle - \uparrow\downarrow\uparrow\downarrow\rangle)$
	15⟩	$ 1, 1\rangle_{\text{E}_1}$	$\frac{1}{\sqrt{6}}(-2 \uparrow\downarrow\uparrow\uparrow\rangle + \uparrow\uparrow\uparrow\downarrow\rangle + \uparrow\uparrow\uparrow\downarrow\rangle)$
	16⟩	$ 1, 1\rangle_{\text{E}_2}$	$\frac{1}{\sqrt{2}}(\uparrow\uparrow\downarrow\uparrow\rangle - \uparrow\uparrow\uparrow\downarrow\rangle)$

where δ and Δ are proportional to the Weiss molecular field strengths exerted by the neighboring tetrahedra. These values depend on the cluster exchange integrals, and single Cu-I and Cu-II sites magnetic moments $\langle S_{\text{I}}^z \rangle = \langle S_{\text{I}}^z \rangle$ and $\langle S_{\text{II}}^z \rangle = \langle S_{\text{II}}^z \rangle = \langle S_{\text{III}}^z \rangle = \langle S_{\text{IV}}^z \rangle$ by:

$$\delta = 3\langle S_{\text{I}}^z \rangle (J_{\text{AF,w}} + J_{\text{AF,OO}}) / J_{\text{AF,s}} > 0 \quad (5.5)$$

and

$$\Delta = [\langle S_{\text{I}}^z \rangle (J_{\text{AF,w}} + J_{\text{AF,OO}}) + 2\langle S_{\text{II}}^z \rangle J_{\text{F,w}}] / J_{\text{AF,s}} < 0 \quad (5.6)$$

where the factors 1, 2, and 3 indicate the number of inter-tetrahedral couplings between the Cu-I and Cu-II sites. In the tetrahedral mean field model the cluster states lower their degeneracy, as seen in the energy diagram of Fig. 5.2b (given in wavenumber cm^{-1}). The states are labeled by the spin quantum numbers S and S^z , and an irrep label. The state degeneracy is indicated in between brackets. The excited state quintet furthermore mixes into the $|g_0\rangle = |1, 1\rangle_{\text{A}_1}$ ground state of the isolated cluster model:

$$|g_{\text{TMF}}\rangle = \cos \frac{\alpha}{2} |1, 1\rangle_{A_1} + \sin \frac{\alpha}{2} |2, 1\rangle_{A_1} \quad (5.7)$$

Here $S^z = +1$ has been chosen as the ground state. Note that in the interacting model the total spin quantum number S isn't a good quantum number anymore. The factor α gives the amount of quintet mixing.^[3] A possible perturbation of the excited state wave functions by the inter-tetrahedral interaction is not discussed in the aforementioned papers. In the later discussion of our Raman spectra we therefore use the perturbed ground state $|g_{\text{TMF}}\rangle$ instead of $|1\rangle$, but use the unperturbed single cluster wave functions $|2\rangle$ to $|16\rangle$ for the excited states.

The magnetizations on the Cu-I and Cu-II sites are:

$$\langle S_{\text{I}}^z \rangle = -\frac{\cos \alpha - \sqrt{3} \sin \alpha}{4} \quad \langle S_{\text{II}}^z \rangle = \frac{1 - \langle S_{\text{I}}^z \rangle}{3} \quad (5.8)$$

The total magnetic moment in the cluster has the value $\langle S_{\text{tot}}^z \rangle = +1$ independent of the mixing parameter. The mixing parameter α depends in a self-consistent way on the Weiss molecular field parameters δ and Δ given in expressions Eqs. 5.5 and 5.6 (Ref. [3]). This value is calculated as $\alpha \approx 0.38$ rad. The spin magnetic moments are $\langle S_{\text{I}}^z \rangle \approx -0.38$ and $\langle S_{\text{II}}^z \rangle \approx 0.46$. This is slightly smaller than the classical $\langle S^z \rangle = \mp \frac{1}{2}$, which explains the measured reduced magnetic moment.^[5]

It should be noted that the tetrahedral mean field model only calculates the zone-center cluster excitation spectrum (the excitations at the Γ -point), i.e. the model does not include dispersion. This can be done in second quantization by a “multi-boson approach” as described in the Supplementary Material of Romhányi *et al.* (Ref. [3]). The resulting dispersion is shown in Fig. 5.2d. The spectrum shows strongly dispersing low-energy branches. At higher energy the dispersion becomes progressively weaker, until at the highest modes the dispersion nearly vanishes. This reflects the energetic difference between the weak inter-cluster exchange couplings $J_{\text{F,w}}$, $J_{\text{AF,w}}$, and $J_{\text{AF,OO}}$, and the stronger intra-cluster exchange couplings $J_{\text{F,s}}$ and $J_{\text{AF,s}}$. The thickness of the branches indicates the magnetic dipole transition strength of the corresponding ground state to excited cluster state transition.^[3]

An interesting analogy can be made here to molecular crystals.^[6,7] In molecular crystals, weakly dispersing to essentially non-dispersing high-energy *internal vibrations* exist, which are essentially weakly perturbed single molecular vibrations. The low-energy excitations originate from the translational symmetry of the crystallized molecules. These *external vibrations* thus have a phononic character. As such, it is also understood that we can regard Cu_2OSeO_3 as being a “generalized molecular crystal of spin nature”.

The Γ -point energies under the “multiboson” correction are indicated in Fig. 5.2c. With 4 clusters in the unit cell, and each cluster having 15 excited states, this gives rise to 60 partially degenerate excitations. The degeneracies are indicated in between brackets. The $|1, 0\rangle_{A_1}$ excitation splits into a 1-fold degenerate G-mode, and a threefold degenerate A-mode. The G-mode is a zero-energy excitation, and thereby describes the long-wavelength magnetic Goldstone boson of the cluster spectrum. The diamonds are previously observed Raman modes,⁸ while the letter-labeled modes were observed in an electron spin resonance study summarized below.²

As stated before, the DM-interactions are neglected in the calculations of Ref. 1 and 3. The DM-interaction is however particularly strong for the inter-cluster bondings, and will thus have a non-negligible effect on the low-energy part of the spin excitation spectrum. Some spin wave branches will become non-degenerate, with a splitting up to ~ 2 meV.⁹ It is recently claimed that this degeneracy breaking might even be a strong indication of the presence of topologically nontrivial *magnonic Weyl modes* in Cu₂OSeO₃.¹⁰ The DM-perturbation of the spin cluster wave functions has not been discussed in literature. We therefore have to work with the 16 single cluster wave functions presented in Table 5.2

5.2.4 Γ -point excitations: the electron spin resonance spectrum

An electron spin resonance (ESR) study of spin cluster excitations in Cu₂OSeO₃ was performed by Ozerov *et al.* (Ref. 2). In the study, a tunable (monochromatic) Terahertz free electron laser source was used to measure the THz-transmittance as a function of external field strength at different THz-frequencies. The frequencies are chosen in regions of low phonon absorption. Figure 5.3a shows the transmittance as a function of magnetic field for various THz-frequencies as indicated in wavenumbers cm⁻¹. A drop in transmittance is observed at certain field strengths. For these fields the electromagnetic radiation is resonant with a transition between the cluster ground state and an excited state.

The ESR data is summarized in Fig. 5.3b. The grey shaded regions correspond to THz-regions of strong phonon absorption. At these frequencies spin cluster excitations cannot be resolved. Within the white regions the phonon absorption is low enough to detect spin cluster transitions. The excitations with a positive applied H-field slope correspond to $\Delta S^z = -1$ spin lowering excitations. These are labeled by G, A, D, and E (the blue squares are data points, and the blue line a linear fit). The excitations with negative B-field slope correspond to $\Delta S^z = +1$ spin raise excitations. These are labeled by B and C (red data points, and red linear fit function). The green measurement points originate from the excitations A ($\Delta S^z = -1$) and B ($\Delta S^z = +1$). All modes can be fitted with a g -factor of $g_{\text{eff}} \approx 2.1 \pm 0.1$, which is as expected

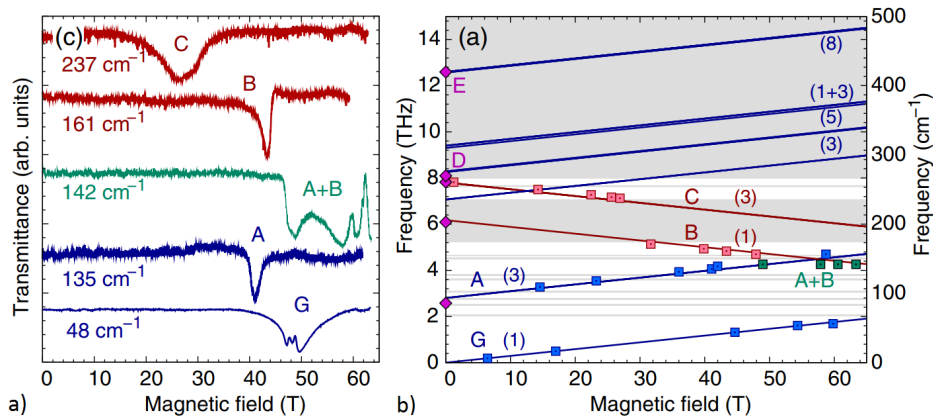


Figure 5.3: a) Thz-transmittance as a function of magnetic field for various Thz-frequencies indicated in wavenumbers cm^{-1} . At certain field strengths a drop in transmittance is observed. At this field strength the electromagnetic radiation is resonant with a transition between the cluster ground state to an excited state. b) Summary of the spin cluster transitions observed in ESR. The grey shaded regions correspond to Thz-regions of strong phonon absorption. At these frequencies spin cluster excitations cannot be resolved. Within the white regions the phonon absorption is low enough to detect spin cluster transitions. The excitations with a positive applied H-field slope correspond to $\Delta S^z = -1$ spin lowering excitations G, A, D, and E (the blue squares are data points, and the blue line a linear fit), and with negative B-field slope to $\Delta S^z = +1$ spin raise excitations B and C (red data points, and red linear fit function). The green measurement points originate from the excitations A ($\Delta S^z = -1$) and B ($\Delta S^z = +1$). Only from fitting the frequency vs. field response it becomes apparent whether the observed excitations in this field and frequency range are a spin raise or lower cluster excitation. Figure adapted from Ref. [2]. Reprinted figure with permission from M. Ozerov, J. Romhányi, M. Belesi, H. Berger, J.-Ph. Ansermet, Jeroen van den Brink, J. Wosnitza, S. A. Zvyagin, and I. Rousochatzakis, Phys. Rev. Lett. **113**, 157205 (2014), <https://doi.org/10.1103/PhysRevLett.113.157205>, © Copyright 2014 by the American Physical Society.

for Cu-ions. Previously observed Raman-active transitions at zero field are indicated with purple diamonds. The Raman-active cluster modes will be discussed in the forthcoming paragraphs.

5.2.5 Cluster excitation dispersion: the inelastic neutron scattering spectrum

In Portnichenko *et al.* [11] an inelastic neutron scattering study of the spin cluster excitations in Cu_2OSeO_3 is presented. By this technique the full spin cluster excitation spectrum including dispersion can be experimentally measured. In order to understand the measured spin excitation dispersion spectrum it is useful to reconsider the lattice and magnetic structure. The

lattice is noncentrosymmetric primitive cubic with crystallographic space group $P2_13$, where P refers to “primitive”. The structural unit cell is shown in Fig. 5.4a. The Cu-II atom is the bigger gold sphere, and the Cu-I atom is the bigger green sphere. The small golden spheres are oxygen atoms, and the small green spheres selenium atoms. The Cu_4 clusters are indicated with dashed black lines. With a being the lattice parameter, a simple cubic Brillouin zone (BZ) with volume $(2\pi/a)^3$ is obtained for the structural reciprocal space. This Brillouin zone is indicated with the grey cube in Fig. 5.4c.

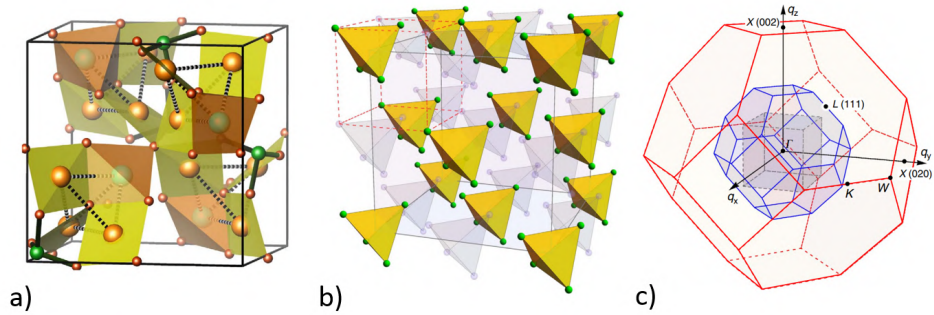


Figure 5.4: a) The structural unit cell of Cu_2OSeO_3 . The large spheres are Cu-I atoms (green) and Cu-II atoms (gold). The small gold spheres are oxygen atoms, and the small green spheres selenium atoms. The simple cubic unit cell has a length a . Figure adapted from Ref. [1]. Adapted by permission from Springer Nature: Springer Nature, Nature Communications, The quantum nature of skyrmions and half-skyrmions in Cu_2OSeO_3 , O. Janson, I. Rousochatzakis, A. A. Tsirlin, M. Belesi, A. A. Leonov, U. K. Rößler, J. Van den Brink, and H. Rosner, Nat. Commun. **5**, 5376 (2014), © 2014 Macmillan Publishers Limited, <https://www.nature.com/ncomms/> b) The copper sublattice can be approximated by an fcc-lattice with length a , with a Cu_4 tetrahedron as basis. This is the grey unit cell. The unit cell can alternatively be described by a half-filled fcc lattice of single Cu-atoms with length $a/2$. This is indicated by the red dashed unit cell. Figure adapted from Ref. [11] (published under Creative Commons Attribution 4.0 International License, CC BY 4.0). c) The different corresponding Brillouin zones (BZ). The grey cubic BZ corresponds to the structural simple cubic unit cell. The blue rhombohedral BZ originates from the fcc-lattice of Cu_4 clusters. The red rhombohedral BZ originates from the half-filled fcc-lattice of Cu-atoms. Figure adapted from Ref. [11] (published under Creative Commons Attribution 4.0 International License, CC BY 4.0).

There are two ways to describe the Cu-sublattice:

- As an fcc-lattice with lattice constant a with the Cu_4 cluster as basis. This is indicated by the grey unit cell in Fig. 5.4b, where the Cu_4 clusters are yellow colored, and form the basis. The orientation and the distortion of the tetrahedron are in this case neglected. The primitive cell of this structure is a rhombohedron with volume $a^3/4$, i.e. four times smaller than the conventional unit cell with volume a^3 (Ref. [12]). This leads to the blue octahedral Brillouin zone with volume

$$4(2\pi/a)^3.$$

- As an half-filled fcc-lattice of Cu-atoms with lattice constant $a/2$. The unit cell is indicated by red dashed lines in Fig. 5.4b. This leads to the red octahedral Brillouin zone with volume $32(2\pi/a)^3$.

The inelastic neutron scattering spectrum shown in Fig. 5.5 appears to be best fitted for the half-filled fcc with lattice constant $a/2$ and the large unfolded octahedral Brillouin zone (red colored). The high symmetry points mentioned in Fig. 5.5 refer to this Brillouin zone, whereas the momentum space coordinates are given in units of $2\pi/a$, i.e. the reciprocal length unit of the simple cubic structural cell. The $\Gamma(000)$ point is the center of the magnetic BZ. Equivalent points in higher BZ's are indicated with a dash. For instance, the $\Gamma'(222)$ is the equivalent point of the first BZ-center.

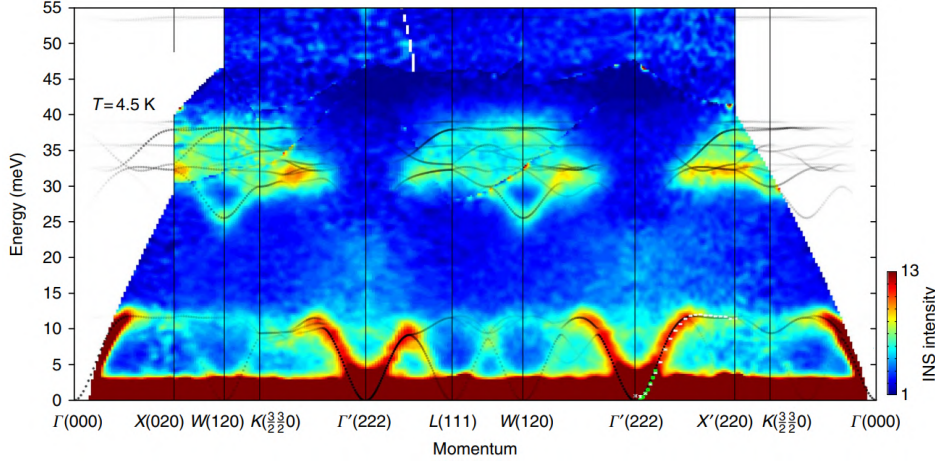


Figure 5.5: The inelastic neutron spectrum in the helimagnetic phase at $T = 4.5$ K. No external field was applied. The $\Gamma(000)$ point is the center of the magnetic Brillouin zone (BZ). Equivalent points in higher BZ's are indicated with a dash, for instance $\Gamma'(222)$. From $\Gamma(000)$ and $\Gamma'(222)$ parabolically dispersing (in the low energy limit) helimagnon bands appear. These modes have an external cluster excitation nature. At high energies a manifold of dispersing bands is observed, which are internal cluster excitations. These modes are separated from the ferromagnon branches by a large energy gap. The continuum below 3 meV, and the significant broadening of the low energy modes originates from the incommensurate helimagnetic ordering as explained in the text. Figure adapted from Ref. 11 (published under Creative Commons Attribution 4.0 International License, CC BY 4.0).

The most striking feature of the spin wave spectrum is the clear subdivision in low and high energy excitations. As discussed before, a division can be made into *external* (up to ~ 12 meV) and *internal* spin cluster excitations (above ~ 25 meV). The low-energy excitations have a strong dispersion. For higher energies the dispersion progressively flattens out, where the mode at

54 meV basically does not even show dispersion anymore. A similar excitation spectrum, of vibrational nature, is also observed in molecular crystals.^[6,7] The spin wave spectrum thus forms a strong evidence of that we can regard Cu_2OSeO_3 as being a realization of a “solid-state molecular crystal of spin nature”.^[13]

In the *external* spin cluster excitation region, parabolically dispersing ferromagnon branches appear from the $\Gamma(000)$ -point and $\Gamma'(222)$ equivalent point towards the other high symmetry points. This ferromagnon mode appears to be gapless due to the experimental resolution (~ 0.14 meV). However, it should be noted that there is a small magnetocrystalline anisotropy gap on the order of ~ 12 μeV .^[14] Between 5 and 10 meV it is seen that the ferromagnon branch is significantly broadened. Below 5 meV the $+\mathbf{q}$ and $-\mathbf{q}$ branch cannot be resolved anymore. This results from the incommensurability of the helimagnetic phase. The helimagnetic Brillouin zone is a factor $(a/2)/\lambda_{helix} \approx 0.007$ smaller than the octahedron of the half-filled fcc-lattice. This leads to Brillouin zone folding and the formation of helimagnon bands periodic in the wave vector $\mathbf{Q} = 2\pi/\lambda_{helix}$. For magnons with a momentum along the helimagnetic wave vector \mathbf{Q} this results in gapless helimagnon bands,^[15] as schematically shown in Fig. 5.6a. An excitation gap opens and flat helimagnon bands appear when the magnon momentum transfer has a component perpendicular to the helical pitch. This is illustrated in Fig. 5.6b. The dispersion bands are approximately quadratic for low momentum transfer \mathbf{k} . A full analytical expression for the helimagnon dispersion is given in Ref. [15]. The Brillouin zone folding due to the helimagnetic incommensurate order in Cu_2OSeO_3 couldn't be resolved in the study of Portnichenko *et al.*^[11] This results in a broadening of the helimagnon branches, and the formation of a magnetic scattering continuum below 3 meV, which originates from unresolved flat helimagnon branches. As a comparison, in MnSi the helimagnon branches were resolved with high-energy resolution inelastic neutron spectroscopy.^[16,17] A part of the Γ -point helimagnon band spectrum in Cu_2OSeO_3 has been observed by GHz-spectroscopy.^[18]

5.3 Magnetic Raman scattering

5.3.1 Introduction

From the 1960's and onwards a lot of work has been devoted to form an understanding of the light-matter interaction in the magnetic Raman scattering process. This has led to a detailed understanding of the magnetic light-scattering excitation spectra in ferromagnets, antiferromagnets, and ferrimagnets.^[19] In the early days a mechanism was coined which treats the magnetic dipole coupling between the magnetic field component of an electromagnetic wave and the spin wave.^[20] It was soon realized that a way stronger mechanism is possible through dipole interaction. Magnons create

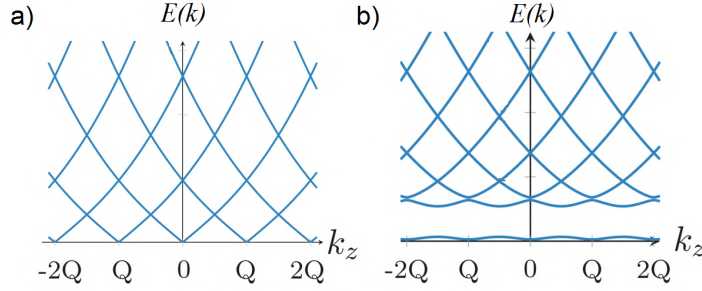


Figure 5.6: a) A picture of the formation of helimagnon bands. The band emerging from $k_z = 0$ is the first helimagnon band. Brillouin zone folding with a periodicity $Q = 2\pi/\lambda_{helix}$ leads to higher order helimagnon bands. The sketched situation is for magnetic excitations with a momentum transfer parallel to \mathbf{Q} . b) A gap opens and flat helimagnon bands appear when the magnetic excitation has a momentum transfer component perpendicular to \mathbf{Q} . Figures adapted from Ref. [15] (published under Creative Commons Attribution 3.0 Unported license (CC BY 3.0)).

a spatial periodic modulation of the dielectric permittivity, from which light can scatter. This is the so-called first order scattering, or *Elliot-Loudon scattering*.^[21] An early-day experimental surprise was the observation of strong two-magnon scattering with scattering cross-sections comparable to the one-magnon scattering in the same material. This two-magnon scattering was explained by second-order *exchange scattering*.^[21] Below, a classical intuitive description of magnetic Raman scattering is given, after which the standard microscopic description of both types of magnetic scattering processes is set out.

5.3.2 Classical light-matter interaction

The light-matter interaction describing magnetic Raman scattering can classically be understood as follows: incident monochromatic light with an electric field $E_j^I(\mathbf{r}, t) = E_{j,0} \cos(\omega_I t)$, and frequency ω_I induces a polarization $\mathbf{P}(\mathbf{r}, t)$ in a magnetic medium:

$$\mathbf{P}_i(\mathbf{r}, t) = \epsilon_0 \sum_j \chi_{ij} E_j^I(\mathbf{r}, t) \quad (5.9)$$

The electric susceptibility χ_{ij} in a magnetic material is modulated by a magnon, or any other collective mode, with excitation frequency Ω .^[22] This modulation can be taken into account by making a first-order expansion of the electric susceptibility in terms of a periodic displacement with normal coordinate Q_k around equilibrium:

$$\chi_{ij}(Q_k) = \chi_{ij}^0 + \left(\frac{\partial \chi_{ijk}}{\partial Q_k} \right)_0 Q_k = \chi_{ij}^0 + R_{ijk,0} \cdot Q_{k,0} \cos(\Omega) \quad (5.10)$$

Here $R_{ijk,0}$ is the Raman tensor, which is a component of the *derived polarizability* tensor. The incident monochromatic light, with electric field $E_j^I(\mathbf{r},t)=E_{j,0} \cos(\omega_I t)$ in turn leads to a fluctuating polarization $\mathbf{P}_i(\mathbf{r}, t)$, with three frequency components:

$$\begin{aligned} \mathbf{P}_i(\mathbf{r}, t) = & \epsilon_0 \sum_j \chi_{ij}^0 E_{j,0} \cos(\omega_I t) + \\ & \epsilon_0 \sum_k \sum_j \frac{1}{2} R_{ijk,0} Q_{k,0} E_{i,0} [\cos((\omega_I + \Omega)t) + \cos((\omega_I - \Omega)t)] \end{aligned} \quad (5.11)$$

This fluctuating electric polarization is the source of electromagnetic waves with frequency components ω_I and $\omega_I \pm \Omega$. The component with frequency ω_I describes elastic scattering. The frequency shifted components $\omega_{AS} = \omega_I + \Omega$ and $\omega_S = \omega_I - \Omega$ correspond to anti-Stokes and Stokes scattering respectively. The measured Raman scattered intensities, or cross sections, are proportional to the square of the Raman tensor $R_{ijk,0}$, and the displacement amplitude $Q_{k,0}$. The Raman tensor can furthermore describe light-scattering selection rules.

Such a phenomenological classical description can only provide us a first insight to Raman scattering. It captures the up-shift and down-shift in scattered light frequency, and links the origin of Raman scattering to a modulation of the electric susceptibility. The quantum-mechanical treatment allows, for instance, to include mode occupation statistics, and obtain the frequency dependence of the scattering efficiency $I_{\text{scatter}} \propto \omega_I \omega_{AS/S}^3$.^[22]

5.3.3 Quantum description of light-matter interaction

Full Hamiltonian

Quantum-mechanically we need to describe a coupling between an incident electric field E^I , a scattered field E^S , and the electric susceptibility tensor χ .^[19] The light-matter interaction is captured by the effective Hamiltonian:

$$\hat{\mathcal{H}} = \sum_{\mathbf{r}} \sum_{ij} E_i^I \chi_{ij}(\mathbf{r}, \hat{\mathbf{S}}) E_j^S \quad (5.12)$$

Here E_I is the incident field with polarization along the crystallographic i direction, and E_S is the scattered electric field with polarization along the crystallographic j direction. The dielectric susceptibility $\chi_{ij}(\mathbf{r}, \hat{\mathbf{S}})$ at the site \mathbf{r} can be expanded in terms of the spin operator $\hat{\mathbf{S}}$ as:

$$\begin{aligned} \chi_{ij}(\mathbf{r}, \hat{\mathbf{S}}) = & \chi_{ij}^0(\mathbf{r}) + \sum_k K_{ijk}(\mathbf{r}) \hat{\mathbf{S}}_{\mathbf{r}}^k + \sum_{kl} G_{ijkl}(\mathbf{r}) \hat{\mathbf{S}}_{\mathbf{r}}^k \hat{\mathbf{S}}_{\mathbf{r}}^l \\ & + \sum_{\delta} \sum_{kl} H_{ijkl}(\mathbf{r}, \delta) \hat{\mathbf{S}}_{\mathbf{r}}^k \hat{\mathbf{S}}_{\mathbf{r}+\delta}^l + \text{higher order terms} \end{aligned} \quad (5.13)$$

The static susceptibility term $\chi_{ij}^0(\mathbf{r})$ leads to elastic scattering. The inelastic terms can be divided into single and double site terms, where the tensors K_{ijk} , G_{ijkl} , and H_{ijkl} describe the strength of the light-matter interaction. The term K leads to first-order Elliot-Loudon scattering (one-magnon). The term G leads to an additional contribution to one-magnon scattering, and second-order Elliot-Loudon scattering. The last sum term involves spins at different ionic sites \mathbf{r} and $\mathbf{r} + \delta$. This term is responsible for *exchange* scattering.

One-magnon or Elliot-Loudon scattering

An efficient one-magnon scattering mechanism is possible by an indirect electric-dipole coupling of light to the spin system. This indirect coupling is enabled by the mixing of spin and orbital angular momentum by spin-orbit coupling ($\lambda \hat{L} \cdot \hat{S}$) in a virtual excited state. One-magnon scattering is described by the second and third term in Eq. 5.13 i.e. the terms which only depend on site \mathbf{r} in Eq. 5.13

In the case of an infinitely extended cubic ferromagnetic system the term linear in spin operator $\hat{\mathbf{S}}_{\mathbf{r}}$ at ionic site \mathbf{r} (cf. Eqs. 5.12 and 5.13) can be rewritten as:

$$\begin{aligned} \hat{\mathcal{H}}_{1M,A} = & \frac{1}{2} K \sum_{\mathbf{r}} [(E_{\mathbf{I}}^z E_{\mathbf{S}}^+ - E_{\mathbf{I}}^+ E_{\mathbf{S}}^z) \hat{S}_{\mathbf{r}}^- - (E_{\mathbf{I}}^z E_{\mathbf{S}}^- - E_{\mathbf{I}}^- E_{\mathbf{S}}^z) \hat{S}_{\mathbf{r}}^+] \\ & - iK \sum_{\mathbf{r}} (E_{\mathbf{I}}^x E_{\mathbf{S}}^y - E_{\mathbf{I}}^y E_{\mathbf{S}}^x) \hat{S}_{\mathbf{r}}^z \end{aligned} \quad (5.14)$$

This “easy” form only applies to a cubic ferromagnet, where at site \mathbf{r} all the tensor elements of K_{ijk} are equal.^[19,21] In the case of antiferromagnets or ferrimagnets this site equivalence already doesn’t hold, by which the expansion for $\hat{\mathcal{H}}_{1M,A}$ gets more involved. In the discussion here it is however important to notice that the terms $\hat{S}_{\mathbf{r}}^+$ and $\hat{S}_{\mathbf{r}}^-$ arise, which correspond to:

$$\hat{S}_{\mathbf{r}}^{\pm} = \hat{S}_{\mathbf{r}}^x \pm i \hat{S}_{\mathbf{r}}^y \quad (5.15)$$

Furthermore the circular incident (I) and scattered (S) light polarizations are given as:

$$E_{\mathbf{I},\mathbf{S}}^{\pm} = E_{\mathbf{I},\mathbf{S}}^x \pm i E_{\mathbf{I},\mathbf{S}}^y \quad (5.16)$$

In the ground state of the ferromagnet all spins are aligned along the S^z axis, while the transverse components are zero, i.e. $S^x = S^y = 0$. A magnon is associated with the creation of a transverse spin component, i.e. the operator $\hat{S}_\mathbf{r}^+$. The annihilation of a magnon then is associated with $\hat{S}_\mathbf{r}^-$ (cf. 5.15). This allows to associate the first term in $\hat{\mathcal{H}}_{1M,A}$ with the annihilation of a magnon, i.e. the one-magnon anti-Stokes process, and the second term with the creation of a magnon, i.e. the one-magnon Stokes process. The third term isn't associated with magnon annihilation or creation, and doesn't alter the spin (ground) state.

A magnon carries angular momentum. The scattered photon thus has to carry away angular momentum in order to conserve the angular momentum in the scattering process. For instance, the term $E_I^z E_S^- \hat{S}_\mathbf{r}^+$ describes a scattering process where incident z -polarized light creates a magnon with a transverse spin component in the xy -plane (cf. Eq. 5.15), and the scattered light is circularly polarized with polarization in the xy -plane, i.e. $E_S^- = E_S^x - iE_S^y$. In order to detect one-magnon scattering a transverse scattering geometry thus is wishful.

For a simple cubic ferromagnet the term quadratic in spin operator $\hat{\mathbf{S}}_\mathbf{r}$ at ionic site \mathbf{r} (cf. Eqs. 5.12 and 5.13) can be rewritten as:

$$\begin{aligned} \hat{\mathcal{H}}_{1M,B} = \frac{1}{2}G \sum_{\mathbf{r}} [& (E_I^z E_S^+ - E_I^+ E_S^z)(\hat{S}_\mathbf{r}^+ \hat{S}_\mathbf{r}^z + \hat{S}_\mathbf{r}^z \hat{S}_\mathbf{r}^+) \\ & + (E_I^z E_S^+ - E_I^+ E_S^z)(\hat{S}_\mathbf{r}^- \hat{S}_\mathbf{r}^z + \hat{S}_\mathbf{r}^z \hat{S}_\mathbf{r}^-)] \end{aligned} \quad (5.17)$$

It should again be understood that this easy form only applies for a simple cubic ferromagnet, and that for an antiferromagnet, ferrimagnet, or a more complicated magnetic material the $\hat{\mathcal{H}}_{1M,B}$ will include more G_{ijkl} expansion terms. Important to notice is, that although this term is quadratic in the single site spin operator $\hat{\mathbf{S}}_\mathbf{r}$, it is *linear* in the magnon creation and annihilation operators $\hat{S}_\mathbf{r}^\pm$. This means that the G -term in Eq. 5.13 only adds another *one-magnon* scattering contribution. The relative values of the one-magnon coupling coefficients K and G are proportional to magnetic circular birefringence and magnetic linear birefringence, respectively.^[19]

Two-magnon scattering

Two-magnon scattering involves the creation or annihilation of a magnon pair. This results in a Stokes or anti-Stokes frequency shift $\Omega_{2M} = \Omega_{\mathbf{k}} + \Omega_{\mathbf{k}'}$, which is the sum of the frequencies of the magnon pair.^[21] Since light only has a small momentum compared to the Brillouin Zone edge, the magnon momenta should be nearly equal and opposite, i.e. $\mathbf{k} \approx -\mathbf{k}'$. The two-magnon process thereby may create high momentum magnon pairs with opposite momenta, as is the case in a whole range of antiferromagnets.^[19] Two-magnon

scattering may, in principle, result from higher order terms of the Elliot-Loudon scattering process, as discussed below. However, a more efficient scattering process is the *exchange scattering* mechanism.

In order to understand the two-magnon scattering processes, we consider two magnon excited states with wave functions of the form $|+\mathbf{k}\uparrow\rangle$, $|-\mathbf{k}\uparrow\rangle$, $|+\mathbf{k}\downarrow\rangle$, and $|+\mathbf{k}\downarrow\rangle$. Here $\pm\mathbf{k}$ gives the momentum of the magnon on either a spin-up magnon branch (\uparrow) or a spin-down (\downarrow) magnon branch. This allows to make 4 excited states:

$$|A\rangle = |+\mathbf{k}\uparrow\rangle|-\mathbf{k}\uparrow\rangle \quad \Delta S^z = +2 \quad (5.18a)$$

$$|B\rangle = \frac{1}{\sqrt{2}}[|+\mathbf{k}\uparrow\rangle|-\mathbf{k}\downarrow\rangle + |+\mathbf{k}\downarrow\rangle|-\mathbf{k}\uparrow\rangle] \quad \Delta S^z = 0 \quad (5.18b)$$

$$|C\rangle = \frac{1}{\sqrt{2}}[|+\mathbf{k}\uparrow\rangle|-\mathbf{k}\downarrow\rangle - |+\mathbf{k}\downarrow\rangle|-\mathbf{k}\uparrow\rangle] \quad \Delta S^z = 0 \quad (5.18c)$$

$$|D\rangle = |+\mathbf{k}\downarrow\rangle|-\mathbf{k}\downarrow\rangle \quad \Delta S^z = -2 \quad (5.18d)$$

Excited states $|A\rangle$ and $|D\rangle$ describe second-order Elliot-Loudon scattering. The scattering efficiency is a factor $(\lambda/E_0)^2$ smaller than first-order scattering, where λ is the spin-orbit coupling constant and E_0 the Raman-excitation energy.^[21] In 3d-transition metal oxides this scattering mechanism thus generally is negligible. Furthermore, second-order Elliot-Loudon scattering will only work in magnets with spin number $S > \frac{1}{2}$, since we evidently cannot flip a spin twice ($\Delta S^z = \pm 2$) in a $S = \frac{1}{2}$ spin system.

The excited state $|C\rangle$ can be reached by exchange scattering. Exchange scattering evidently isn't possible in ferromagnets, where only one magnon branch with a specific spin polarization is present. The highest symmetry which allows exchange scattering thus is a three-dimensional simple cubic antiferromagnet. In this case a magnon pair on branches with opposite spin polarization can be created. For completeness: The even parity state $|B\rangle$ is not relevant to Raman scattering, but to two-magnon absorption.^{[19],[21]}

For the three-dimensional simple cubic antiferromagnet, the H_{ijkl} -term in the Hamiltonian $\hat{\mathcal{H}}$ (cf. Eqs. [5.12](#) and [5.13](#)) can be rewritten as:

$$\begin{aligned} \hat{\mathcal{H}}_{2M} &= \sum_{\mathbf{r},\delta} [(H_1 - \frac{1}{3}H_3)\mathbf{E}_I \cdot \mathbf{E}_S + H_3(\mathbf{E}_I \cdot \hat{\delta})(\mathbf{E}_S \cdot \hat{\delta})] \hat{S}_{\mathbf{r}} \cdot \hat{S}_{\mathbf{r}+\delta} \\ &= \sum_{\mathbf{r},\delta} [(H_1 - \frac{1}{3}H_3)\mathbf{E}_I \cdot \mathbf{E}_S + H_3(\mathbf{E}_I \cdot \hat{\delta})(\mathbf{E}_S \cdot \hat{\delta})] [\frac{1}{2}(\hat{S}_{\mathbf{r}}^+ \hat{S}_{\mathbf{r}+\delta}^- + \hat{S}_{\mathbf{r}}^- \hat{S}_{\mathbf{r}+\delta}^+) + \hat{S}_{\mathbf{r}}^z \hat{S}_{\mathbf{r}+\delta}^z] \end{aligned} \quad (5.19)$$

Here $\hat{\delta}$ is the unit vector of the connecting vector between neighboring spins, and H_1 and H_3 are magneto-optical constants. For lower symmetry materials the expansion will be again lengthier, where the sum will run over different bonds. The term $\hat{S}_{\mathbf{r}}^z \hat{S}_{\mathbf{r}+\delta}^z$ isn't associated with transverse spin

waves, as discussed in Par. 5.3.3. The terms of interest are $\hat{S}_{\mathbf{r}}^+ \hat{S}_{\mathbf{r}+\delta}^-$ and $\hat{S}_{\mathbf{r}}^- \hat{S}_{\mathbf{r}+\delta}^+$. These are the terms which lead to $\Delta S_{tot}^z = 0$ scattering into a two-magnon excited state $|C\rangle$. Physically the exchange scattering correspond to the excitation of magnons on opposite polarization magnon branches. In the case of a simple cubic antiferromagnet one can say that two spin flip excitations are generated on the opposite sublattices. There are no restrictions on the light polarization E_I and E_S as in the Elliot-Loudon process.^[19] Only the scattering geometry relative to the connecting bond vector $\hat{\delta}$ needs to be taken into account as selection rule. Microscopically, this scattering mechanism occurs through an excited-state exchange coupling.^[23]

5.3.4 An example: magnetic scattering in fluorides

Inelastic light scattering in fluoride Heisenberg antiferromagnets, such as MnF_2 , NiF_2 , KNiF_3 , KCoF_3 has been extensively studied from the 1960's and onwards.^[19] This is largely due to the fact that these transition metal fluorides have a weak spin-orbit coupling (so only the spin angular momentum needs to be taken into account), a weak magnetocrystalline anisotropy and an isotropic magnon dispersion. They thereby form ideal “model systems” to study the fundamental aspects of magnetic Raman scattering.

Figure 5.7a shows temperature dependent Raman scattering spectra from NiF_2 , taken from Ref. [24]. NiF_2 has a critical temperature of $T_N \approx 73$ K and spin quantum number $S = 1$ (Ni^{2+}). At low temperatures (upper curves) two clear peaks can be observed, namely a narrow one-magnon peak (1M) and a broad two-magnon peak (2M) at higher energies. The one-magnon scattering vanishes above the critical temperature, while the two-magnon peak persists up to at least a temperature of $\sim 1.5 \times T_N$.

This critical behaviour is understood based on the magnon dispersion of NiF_2 .^[25] In one dimension the magnon dispersion for an antiferromagnet along the momentum coordinate k_x is given by:

$$E_{\text{magnon}}(k_x) = \sqrt{(g\mu_B B_A + JSz)^2 - (JSz \cos(k_x a))^2} \quad (5.20)$$

Here $g\mu_B B_A$ gives the single-ion magnetic anisotropy, with g the g -factor, μ_B the Bohr-magneton, and B_A an effective anisotropy field. J gives the Heisenberg exchange constant, S the spin quantum number, and z the amount of magnetic nearest neighbour ions. In Fig. 5.7b a (normalized) dispersion is plotted. Elliot-Loudon scattering ($\Delta S^z = \pm 1$) allows for the excitation of a zone-center magnon (indicated with 1M). Pairs of $+\mathbf{q}$ and $-\mathbf{q}$ magnons can be excited throughout the whole Brillouin Zone via exchange scattering (2M, with total $\Delta S^z = 0$). Only at \mathbf{q} -points with a high magnon Density of States (DOS) the 2M-excitation shows up clearly in the Raman spectrum. For the drawn antiferromagnetic dispersion this is near the Brillouin Zone boundary, so high momentum-transfer.

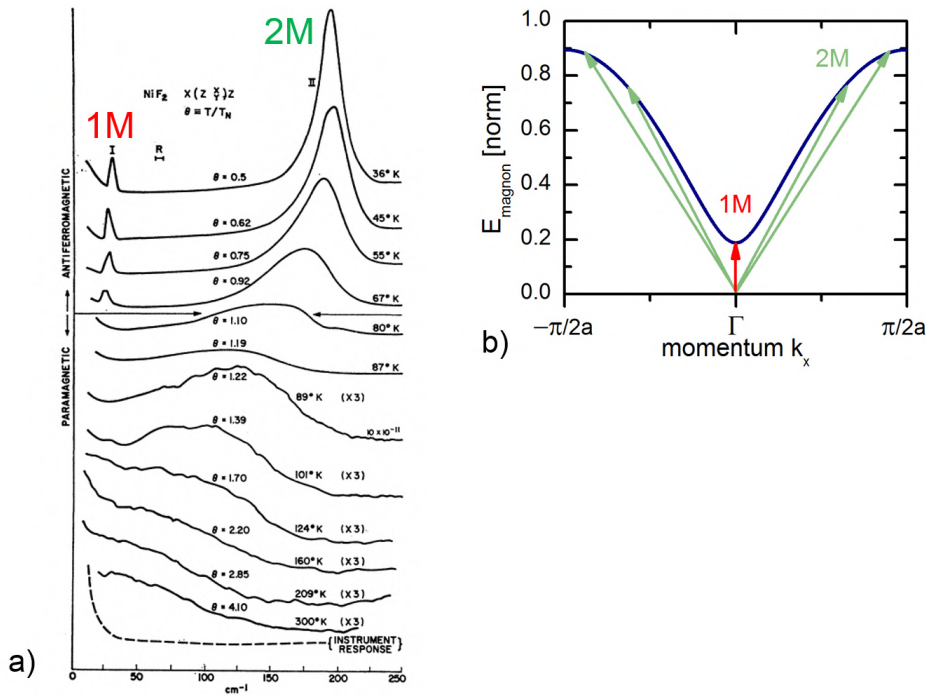


Figure 5.7: a) Temperature dependent one- and two-magnon scattering in NiF_2 . The critical temperature is $T_N \approx 73$ K. A narrow one-magnon (1M) feature is observed at ~ 31 cm^{-1} . The one-magnon peak vanishes above T_N . A broad two-magnon peak is observed around ~ 200 cm^{-1} . The two-magnon scattering persists far above T_N . Figure adapted from Ref. [24]. Reprinted figure with permission from P.A. Fleury, Phys. Rev. **180**, 591 (1969), <https://doi.org/10.1103/PhysRev.180.591>, © Copyright 1969 by the American Physical Society. b) Generalized dispersion for an antiferromagnet. One-magnon Raman scattering corresponds to a magnon excitation at the Γ -point (1M). Pairs of $+\mathbf{q}$ and $-\mathbf{q}$ magnons can be excited throughout the whole Brillouin Zone via exchange scattering (2M), as indicated with the green arrows. Only at \mathbf{q} -points with a high magnon Density of States (DOS) the 2M-excitation shows up clearly in the Raman spectrum. For the drawn antiferromagnetic dispersion this is near the Brillouin Zone boundary, so high momentum-transfer.

At $T_N \approx 73$ K long-range magnetic correlations are strongly suppressed. The one-magnon peak therefore vanishes. However, short-range correlations still persist in the paramagnetic phase. It is therefore still possible to excite pairs of short wavelength (high momentum) magnons in the paramagnetic phase far above T_N in an antiferromagnet. [24]

5.4 Magnetic Raman scattering from spin cluster excitations

5.4.1 Experimental details

A chemical vapor transport grown Cu_2OSeO_3 crystal was used for the Raman study. A (111) oriented plate-shaped sample was prepared with a flat as-grown (111) face and a lapped parallel opposite surface, which was polished with $1\ \mu\text{m}$ grit size diamond paste. The Raman scattering experiments were performed at low temperatures ranging from 7.5 K to 150 K. The sample is placed in a OXFORD MICROSTAT with a temperature stability of 0.1 K. The used excitation light is provided by a frequency doubled Nd:YAG (central wavelength $\lambda_C = 532\ \text{nm}$) laser. The polarization for the excitation light is cleaned with a Glan Taylor polarizer. The scattered light polarization is analyzed with a sheet polarizer. We used a confocal backscattering geometry, with a $\text{NA} = 0.5$ microscope objective which illuminates the sample and collects the scattered light. The excitation density was kept below $500\ \text{W}/\text{cm}^2$. Laser heating effects are minimal since the 532 nm excitation falls within the transmission window of Cu_2OSeO_3 (see Chapter 6). A JOBIN YVON T64000 triple subtractive spectrometer, equipped with a SYMPHONY 1024×256 charge-coupled device, was used to detect the scattered light. The resolution in the studied energy interval lies below $2\ \text{cm}^{-1}$. Throughout this chapter the Porto notation $z(x,y)\bar{z}$ is used to indicate the polarization of the incoming (x) and scattered (y) light, with the light wave vector parallel to z. The x-polarization lies along the crystallographic $[1\bar{1}0]$ axis, and y-polarization along $[\bar{1}10]$.

5.4.2 Results and discussion

Raman-active phonons

The noncentrosymmetric cubic lattice of Cu_2OSeO_3 is described by space group $P2_13$. There are $Z = 8$ chemical formula units in the structural unit cell (16 Cu^{2+} -atoms in total). This gives a total of $7 \times 8 \times 3 = 168$ phonons. There are 5 atoms on a $4a$ Wyckoff-position, and 3 atoms on a $12b$ Wyckoff-position.^{[5],[8]}

The total Γ -point phonon spectrum is decomposed in the following irreducible representations:

$$\Gamma = 14A + 14E_1 + 14E_2 + 42T \quad (5.21)$$

where the acoustic phonons contribute $1T$.^[26]

The Γ -point optical phonon spectrum is decomposed in:

$$\Gamma^{\text{optical}} = 14A^{(\text{R})} + 14E_1^{(\text{R})} + 14E_2^{(\text{R})} + 41T^{(\text{R,IR})} \quad (5.22)$$

The threefold degenerate T-irrep phonons are only infrared active (IR), whereas the one-fold degenerate A, E_1 , and E_2 are both infrared and Raman-active (R). For the (111) oriented sample the A modes will only show up in parallel polarization geometry, while the E_1 , E_2 , and T modes are observable in both parallel and crossed polarization geometry.^[8]

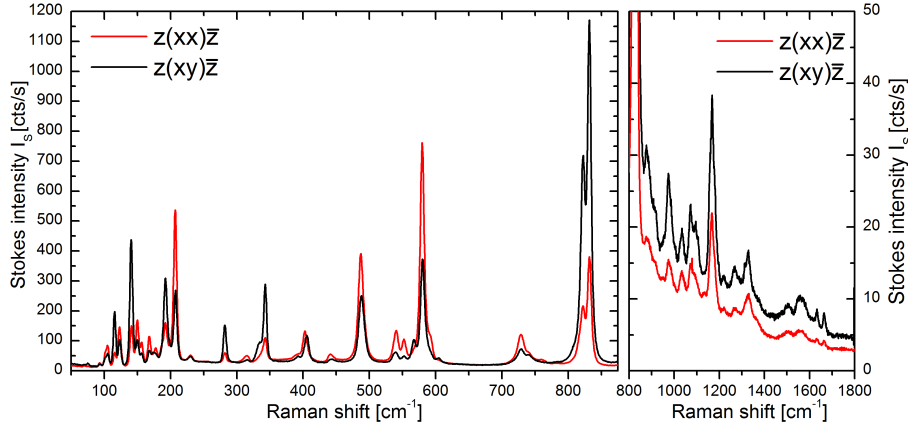


Figure 5.8: Phonon spectrum obtained at $T=80$ K for parallel $z(x,x)\bar{z}$ and perpendicular $z(x,y)\bar{z}$ polarization geometries. Strong phonon modes are observed in the frequency range up to 850cm^{-1} . Between 850cm^{-1} and 1800cm^{-1} weaker phonon modes are observed.

Figure 5.8 shows the phonon spectrum in $z(x,x)\bar{z}$ and $z(x,y)\bar{z}$ polarization configuration at $T=80$ K over the range $50\text{--}1800\text{cm}^{-1}$. The spectra agree with the observations of Gnezdilov *et al.* (Ref. [8]), which reports the observation of 53 strong optical phonons in the frequency range up to 850cm^{-1} and 21 weak optical phonons in the frequency range between $850\text{--}2000\text{cm}^{-1}$. For completeness, 26 T-phonons were detected in the infrared absorption spectrum by Miller *et al.* (Ref. [27]).

Raman-activity of spin cluster excitations

Figure 5.9 shows temperature dependent Raman spectra in the range $220\text{--}460\text{cm}^{-1}$ for the $z(x,x)\bar{z}$ polarization configuration. The spectra have been normalized to the phononic scattering intensity in the region $520\text{--}610\text{cm}^{-1}$. The spectra in Fig. 5.9b are offset for clarity. In this way the presence of the mode M_2 at 273cm^{-1} is better visible. Four modes of magnetic origin are identified: 263cm^{-1} (M_1), 273cm^{-1} (M_2), 300cm^{-1} (M_3), and 425cm^{-1} (M_4). A previous study has identified two weaker modes at 86cm^{-1} (M^*) and 204cm^{-1} (M^{**}) respectively,^[8] but these could not be clearly resolved in our data set. Two phonon modes of interest are indicated with P_1 (231cm^{-1}) and P_2 (444cm^{-1}).

We wish to discuss the possible cluster transitions from the ground state

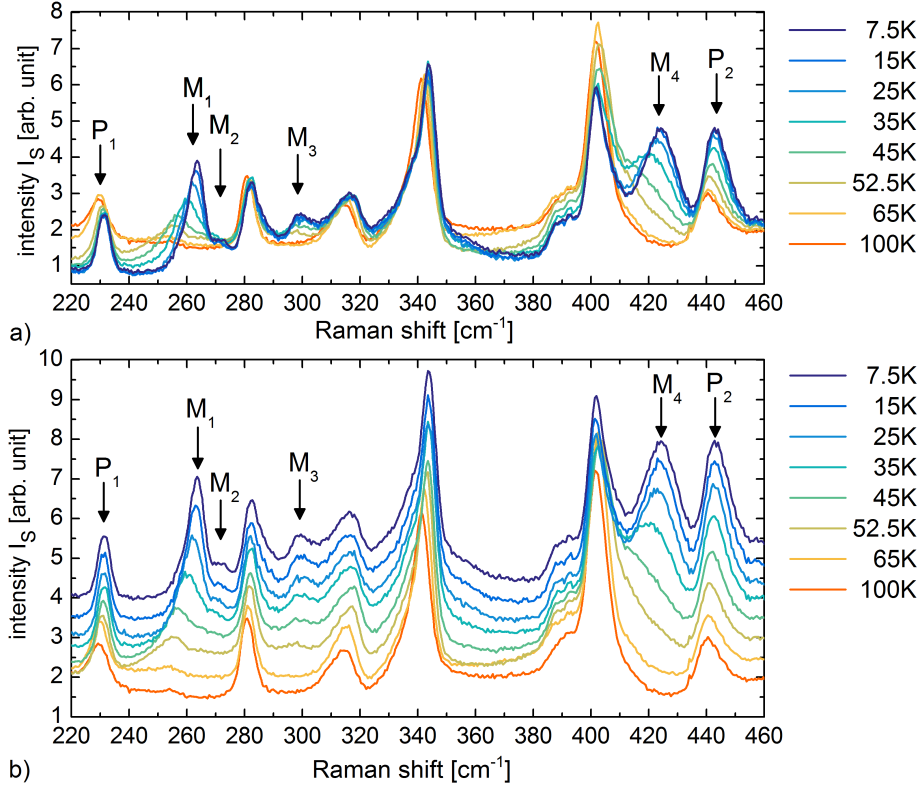


Figure 5.9: a) Normalized temperature dependent Raman spectra for Cu_2OSeO_3 in $z(x,x)\bar{z}$ polarization configuration. Four modes of magnetic origin are identified within this energy range: 263 cm^{-1} (M_1), 273 cm^{-1} (M_2), 300 cm^{-1} (M_3), and 425 cm^{-1} (M_4). Two phonon modes of interest are indicated with P_1 (231 cm^{-1}) and P_2 (444 cm^{-1}). b) The same spectra, but with an offset. In this way the presence of mode M_2 at 273 cm^{-1} is better visible.

$|g_{\text{TMF}}\rangle$ to the excited states $|n\rangle = |2\rangle$ to $|16\rangle$ from Table 5.2, associate the observed high-energy spin excitations with the cluster transitions, and discuss the corresponding scattering mechanism. The following effective Raman scattering Hamiltonian is used:

$$\hat{\mathcal{H}}_{\text{R}} = K \sum_{i=1:4} (\hat{S}_i^+ + \hat{S}_i^-) + 2L \sum_{\substack{i,j=1:4 \\ i \neq j}} \hat{S}_i^+ \hat{S}_j^- \quad (5.23)$$

Here, the four cluster spin sites are labelled by $i=1, 2, 3, 4$. The clusters are helimagnetically oriented, with the helimagnetic wave vector \mathbf{q} pointing along the $[100]$ equivalent crystallographic axes.²⁸ We assume that this ordering leads to a situation where polarization selection rules are always fulfilled for a subset of the spin cluster projections, irrespective of incident and scattered polarization geometry. Thereby, the electric field po-

larization selection rules are ignored,^[21] and we only discuss the linear and quadratic spin operators, as indicated in Eq. 5.23. The linear spin operators \hat{S}_i^\pm ($\Delta S^z = \pm 1$) correspond to Elliot-Loudon scattering. Note that higher order Elliot-Loudon scattering of the form $\hat{S}_i^+ \hat{S}_i^+$ or $\hat{S}_i^- \hat{S}_i^-$ ($\Delta S^z = \pm 2$) isn't allowed in Cu_2OSeO_3 since the spin cluster consists of $S = \frac{1}{2}$ spins. The exchange scattering terms are $\hat{S}_i^+ \hat{S}_j^- + \hat{S}_i^- \hat{S}_j^+$ ($\Delta S^z = 0$),^[21] but since these operators have the same effect on the cluster wave functions we used the notation $2\hat{S}_i^+ \hat{S}_j^-$ in Eq. 5.23 to avoid double counting.

The transition probability P for the three relevant spin operators $\hat{O} = \{\hat{S}_i^+, \hat{S}_i^-, \hat{S}_i^+ \hat{S}_j^-\}$ in $\hat{\mathcal{H}}_R$ is determined as:

$$P = |\langle f | \hat{O} | g_{\text{TMF}} \rangle|^2 \quad (5.24)$$

In Table 5.3 the possible spin cluster transitions and corresponding Raman modes are indicated. Here, $|f\rangle = |S, S^z\rangle_R$ (or $|n\rangle$) gives the excited cluster state, where it should be understood that $|1\rangle$ is the ground state. ΔS^z indicates the necessary change in spin projection number in order to reach the final state $|n\rangle$. When no transition is possible, this is indicated with a hyphen (-). All cluster states with a change $\Delta S^z = \pm 1, 0$ can be reached either by a one-magnon (Elliot-Loudon) or two-magnon (exchange) scattering process. All the linear and quadratic Raman spin operators which allow for a cluster transition are indicated the table. E_A and E_B give the transition energies as calculated by spin wave theory.^[23] The final state degeneracy is indicated in between brackets. The second-last column gives the measured Raman shifts E_R . The modes M_1 to M_4 were observed in both our work and earlier work. The modes M^* and M^{**} are weak Raman modes reported in Ref. 8. The last column gives the cluster excitation energies E_{ESR} observed by electron spin resonance (ESR), as reported in Ref. 2. All energies are indicated in wavenumbers (cm^{-1}).

Based on the Raman spectra shown in Fig. 5.9, and the study from Ref. 8 we can unambiguously identify the 86 cm^{-1} M^* , 204 cm^{-1} M^{**} , 263 cm^{-1} M_1 , and 425 cm^{-1} M_4 modes with different cluster transitions. All these modes are Raman-active through the Elliot-Loudon scattering mechanism (\hat{S}^\pm terms). Whether the 273 cm^{-1} M_2 Raman-mode has a $\Delta S^z = 0$ or ± 1 cannot be unambiguously identified based on the Raman data set alone. However, this mode has been observed by electron spin resonance, which shows that the mode has a $\Delta S^z = -1$ field behaviour. The Raman-activity of this mode thus originates from the Elliot-Loudon mechanism. The 300 cm^{-1} M_3 Raman-mode may either be a transition to $|2, 0\rangle_{A_1}$ by a \hat{S}^- scattering process, or $|2, 1\rangle_{A_1}$ by a $\hat{S}^+ \hat{S}^-$ scattering process. This mode was not observed in the ESR study (indicated with an X). The scattering mechanism of the 300 cm^{-1} M_3 mode can thus not be unambiguously defined. Scattering to the $|15\rangle$ or $|16\rangle$ excited state (expected excitation energy $\approx 400 \text{ cm}^{-1}$) is Raman-allowed. This mode however could not be unambiguously resolved

due to the presence of a strong phonon mode. For completeness we've indicated the $0 \text{ cm}^{-1} \text{ M}_G$ in the table. This mode corresponds to the magnetic Goldstone mode. This mode was observed in the electron spin resonance study. All mentioned modes are indicated in Table [5.3](#).

Table 5.3: Magnetic Raman modes, spin cluster excitation energies, and Raman operators. For a detailed explanation of the table entries, see text.

$ n\rangle$	final state $ S, S^z\rangle$	ΔS^z	1-magnon (Elliott-Loudon)	2-magnon (exchange scattering)	$E_1 [cm^{-1}]$	$E_2 [cm^{-1}]$	$E_R [cm^{-1}]$	$E_{ESR} [cm^{-1}]$
$ 1\rangle$	$ 1, 1\rangle_{A_1}$	0	—	—	—	—	—	—
$ 2\rangle$	$ 1, 0\rangle_{A_1}$	-1	$\hat{S}_1^-, \hat{S}_2^-, \hat{S}_3^-, \hat{S}_4^-$	—	0(1)	96(β)	85(M _*)	0(M _G) 85(M _*)
$ 3\rangle$	$ 1, \bar{1}\rangle_{A_1}$	-2	—	—	159(4)	—	—	—
$ 4\rangle$	$ 0, 0\rangle_{E_1}$	-1	$\hat{S}_2^-, \hat{S}_3^-, \hat{S}_4^-$	—	236(β)	276(β)	273(M ₂)	270(M ₂)
$ 5\rangle$	$ 0, 0\rangle_{E_2}$	-1	\hat{S}_3^-, \hat{S}_4^-	—	—	—	—	—
$ 6\rangle$	$ 2, 2\rangle_{A_1}$	-3	—	—	338(4)	—	—	—
$ 7\rangle$	$ 2, \bar{1}\rangle_{A_1}$	-2	—	—	335(4)	—	—	—
$ 8\rangle$	$ 2, 0\rangle_{A_1}$	-1	$\hat{S}_1^-, \hat{S}_2^-, \hat{S}_3^-, \hat{S}_4^-$	—	310(1)	314(β)	300(M ₃ ?)	X
$ 9\rangle$	$ 2, 1\rangle_{A_1}$	0	—	$\hat{S}_1^+ \hat{S}_2^-, \hat{S}_1^+ \hat{S}_3^-, \hat{S}_1^+ \hat{S}_4^-, \hat{S}_2^+ \hat{S}_1^-, \hat{S}_2^+ \hat{S}_2^-, \hat{S}_2^+ \hat{S}_3^-, \hat{S}_2^+ \hat{S}_4^-, \hat{S}_3^+ \hat{S}_1^-, \hat{S}_3^+ \hat{S}_2^-, \hat{S}_3^+ \hat{S}_3^-, \hat{S}_3^+ \hat{S}_4^-, \hat{S}_4^+ \hat{S}_1^-, \hat{S}_4^+ \hat{S}_2^-, \hat{S}_4^+ \hat{S}_3^-, \hat{S}_4^+ \hat{S}_4^-$	272(1)	288(β)	300(M ₃ ?)	—
$ 10\rangle$	$ 2, 2\rangle_{A_1}$	+1	$\hat{S}_1^+, \hat{S}_2^+, \hat{S}_3^+, \hat{S}_4^+$	—	206(1)	260(β)	204(M ^{**}) 263(M ₁)	202(M ^{**}) 263(M ₁)
$ 11\rangle$	$ 1, \bar{1}\rangle_{E_1}$	-2	—	—	380(8)	—	—	—
$ 12\rangle$	$ 1, \bar{1}\rangle_{E_2}$	-2	—	—	—	—	—	—
$ 13\rangle$	$ 1, 0\rangle_{E_1}$	-1	$\hat{S}_2^-, \hat{S}_3^-, \hat{S}_4^-$	—	419(8)	—	425(M ₄)	420(M ₄)
$ 14\rangle$	$ 1, 0\rangle_{E_2}$	-1	\hat{S}_3^-, \hat{S}_4^-	—	—	—	—	—
$ 15\rangle$	$ 1, 1\rangle_{E_1}$	0	—	$\hat{S}_1^+ \hat{S}_2^-, \hat{S}_1^+ \hat{S}_3^-, \hat{S}_1^+ \hat{S}_4^-, \hat{S}_2^+ \hat{S}_1^-, \hat{S}_2^+ \hat{S}_2^-, \hat{S}_2^+ \hat{S}_3^-, \hat{S}_2^+ \hat{S}_4^-, \hat{S}_3^+ \hat{S}_1^-, \hat{S}_3^+ \hat{S}_2^-, \hat{S}_3^+ \hat{S}_3^-, \hat{S}_3^+ \hat{S}_4^-, \hat{S}_4^+ \hat{S}_1^-, \hat{S}_4^+ \hat{S}_2^-, \hat{S}_4^+ \hat{S}_3^-, \hat{S}_4^+ \hat{S}_4^-$	396(β)	401(β)	X	—
$ 16\rangle$	$ 1, 1\rangle_{E_2}$	0	—	—	—	—	—	—

Temperature dependence

We wish to discuss the temperature dependent scattering behaviour of the spin excitation modes M_1 (263 cm^{-1}) and M_4 (425 cm^{-1}), and the phonon modes P_1 (231 cm^{-1}) and P_2 (444 cm^{-1}). Two scattering regions are decomposed into Lorentzian-lineshape profiles. This is shown in Fig. 5.10 for P_1 and M_1 at $T = 15\text{ K}$, 50 K and 80 K . A weakly scattering phonon P^* becomes visible at 80 K . For P_2 and M_4 the Lorentzian decomposition is shown at $T = 15\text{ K}$ and 50 K . At 80 K the magnetic mode has significantly broadened. For this temperature region the Lorentzian decomposition around M_4 becomes unreliable.

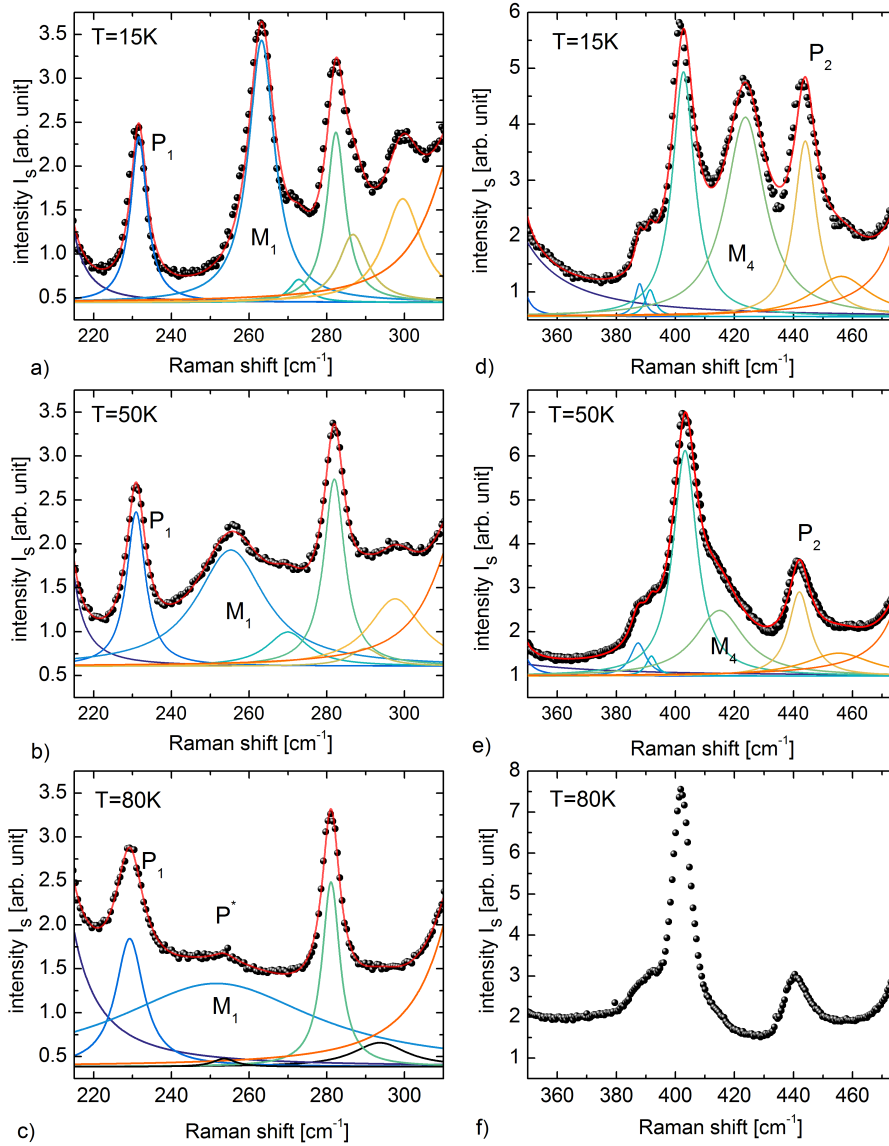


Figure 5.10: a) Lorentzian decomposition of the Raman spectrum around the P_1 phonon and M_1 spin excitation at $T = 15\text{ K}$ and b) $T = 50\text{ K}$, respectively. The spin excitation mode is well-defined. c) Above T_C the magnon mode M_1 has significantly broadened into a continuum type of magnetic scattering. Here it is assumed that the scattering response still can be fitted with a Lorentzian line shape. The phonon mode P_1 has also significantly broadened. A small phonon scattering contribution P^* is observed at higher temperatures. d) Lorentz-response decomposition of the Raman spectrum around the P_2 phonon and M_4 spin excitation at 15 K . e) The M_4 spin excitation has significantly softened at $T = 50\text{ K}$. f) Above T_C the magnetic mode has significantly broadened and the Lorentzian decomposition gets unreliable.

Spin cluster excitations For the spin cluster excitations a spectral weight transfer to lower Raman shift Ω is observed when the temperature increases towards T_C (also see the upper panel of Fig. 5.9). The magnetic spectral weight transfer is understood as a softening and broadening of the $\Delta S^z = \pm 1$ spin excitations. The energy of the M_1 excitation is plotted in Fig. 5.11a. Below T_C the temperature dependence of the excitation energy can be well-described by a scaling law of the form $\Omega(T) \propto (T_C - T)/T_C^m$, with $m \approx 0.02$ as exponent. Above $T_C \approx 58$ K magnetic scattering still persists, but the spin excitations have significantly broadened into a continuum type of magnetic scattering. This is most clearly seen in Fig. 5.10b for M_1 ($\Delta S^z = +1$). Above T_C the fitting of the peak position becomes unreliable. The temperature dependent spectral weight of M_1 is plotted in Fig. 5.11b. Up till T_C the spectral weight remains constant. Above T_C the determination of the spectral weight becomes unreliable, however, it stays finite. Figure 5.11c shows the temperature dependence of the line width at half maximum (inverse decay rate) of the M_1 excitation. The functional temperature dependence below T_C is well fitted by the second order polynomial $\frac{\Gamma}{2}(T) = \frac{\Gamma_0}{2}(T=0) + A \cdot T + B \cdot T^2$, with the largest contributions formed by $\frac{\Gamma_0}{2}(T=0)$ and $B \cdot T^2$. The latter process describes a four magnon interaction.²⁹ The large finite $\frac{\Gamma_0}{2}(T=0)$ term may result from inhomogeneous broadening from disorder. However, Laurita *et al.* (Ref. 29) argue that the spontaneous decay rate of spin cluster excitations in Cu_2OSeO_3 instead may originate from quantum fluctuations. For M_4 ($\Delta S^z = -1$) similar qualitative behaviour is observed, as most clearly seen in Fig. 5.9a.

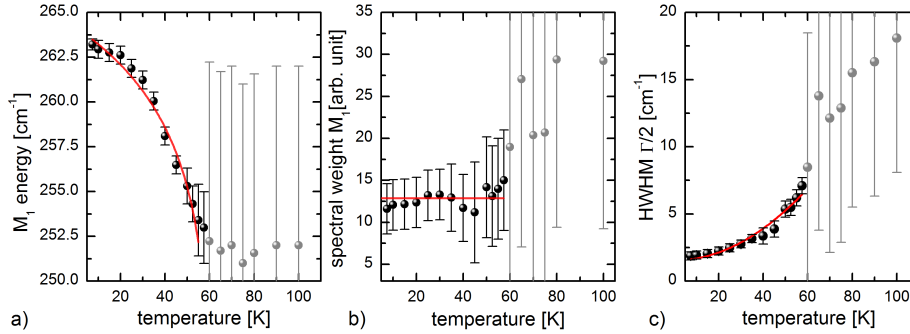


Figure 5.11: a) Temperature dependence of the M_1 spin excitation energy. Below T_C the temperature dependent position is well-fitted with a scaling function of the form $\Omega(T) \propto (T_C - T)/T_C^m$, with $m \approx 0.02$ as exponent (red curve). b) Temperature dependent spectral weight of the M_1 spin excitation. Below $T_C \approx 58$ K the spectral weight remains constant (red curve). Above $T_C \approx 58$ K the determination of the spectral weight becomes unreliable, however, it stays finite. c) Half width at half maximum (inverse decay rate) of the M_1 spin excitation. Below T_C a quadratic power law is observed, in addition to a strong spontaneous decay rate.

The temperature dependence of the magnetic scattering across the phase

transition of the high-energy spin excitations in Cu_2OSeO_3 is rather peculiar in light of the vast range of historic and contemporary magnetic Raman scattering literature.^[19,30] In the case of single spin (anti-)ferromagnets, such as NiF_2 presented above, the first order (Elliot-Loudon) scattering originates from low-energy zone-*center* magnons. The Γ -point one-magnon scattering vanishes above the (anti-)ferromagnetic critical temperature $T_{\text{N/C}}$, where the long-range spin correlation is strongly reduced. Second order exchange scattering from high-energy zone-*edge* magnon pairs, described by the pair-operators \hat{S}^+S^- and $\hat{S}^-\hat{S}^+$ ($\Delta S^z = 0$), is possible in antiferromagnets above T_{N} , since short-range correlations still exist.^[19,21]

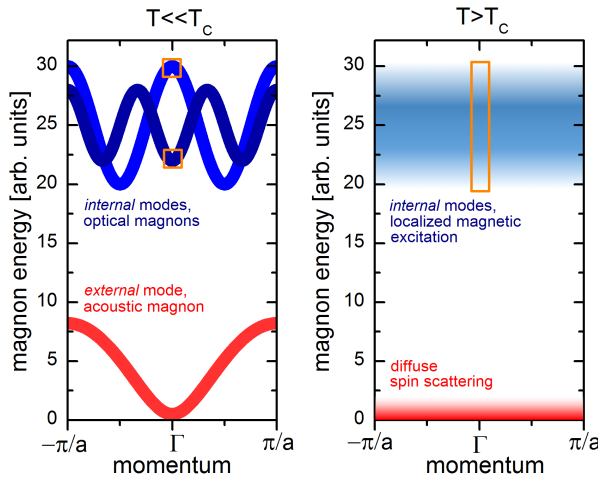


Figure 5.12: Cartoon picture of the magnon dispersion of a cluster magnet below and above the critical temperature T_C . A cluster magnet has well-defined low-energy *external* spin cluster excitation branches (red), and high energy *internal* spin cluster excitation branches (blue) below T_C . Above T_C the high-energy internal spin cluster excitation branches cross over into a broad dispersionless band of localized magnetic excitations (blue). The low energy external branches vanish above T_C due to the loss of inter-cluster correlations. Raman-scattering is possible at the Γ -point (indicated with orange squares).

The formation of Cu_4 spin clusters far above the long-range ordering temperature $T_C \approx 58$ K, and the resulting high-energy dispersive magnon branch below T_C results in the possibility to scatter from zone-center *internal spin cluster* excitations above and below T_C by the Elliot-Loudon mechanism.^[19,21] Below T_C high-energy *optical magnon* branches are well-defined and dispersive by the inter-cluster correlation. A cartoon is provided in the left panel of Fig. 5.12. Raman-scattering by the Elliot-Loudon mechanism is possible at the Γ -point (indicated with orange squares). However, above T_C inter-cluster correlations are lost, and the optical magnons cross over into a broad dispersionless band of localized cluster-internal spin excitations as depicted in the right panel of Fig. 5.12 (Refs. 31). This finite localized spin

cluster excitation density-of states at the Γ -point above T_C still allows for first-order scattering, but however will appear as broad continuum of magnetic scattering, as indicated with the orange rectangle.³¹

Phonons Figure 5.13a shows the phonon energy and half width at half maximum (HWHM) for the phonon P_1 . Figure 5.13b shows the phonon energy and spectral weight (SW) for the phonon P_2 . All plotted parameters show strong sensitivity to magnetic ordering. This is especially the case for the P_2 phonon, as for instance seen from the spectral weight. Neither, the spin wave theory calculations, nor neutron experiments, evidence the presence of a spin cluster excitation around 444 cm^{-1} . Instead, the P_2 mode should represent a motion of oxygen atoms.²⁷ The similar energy scale, and likely overlapping dispersion, of optical phonons and high-energy spin cluster excitations may lead to a phonon-magnon hybridization by magneto-elastic coupling.^{32,33} This in turn will lead to a strong temperature dependence for the line-width, position, and spectral weight of the optical phonons.

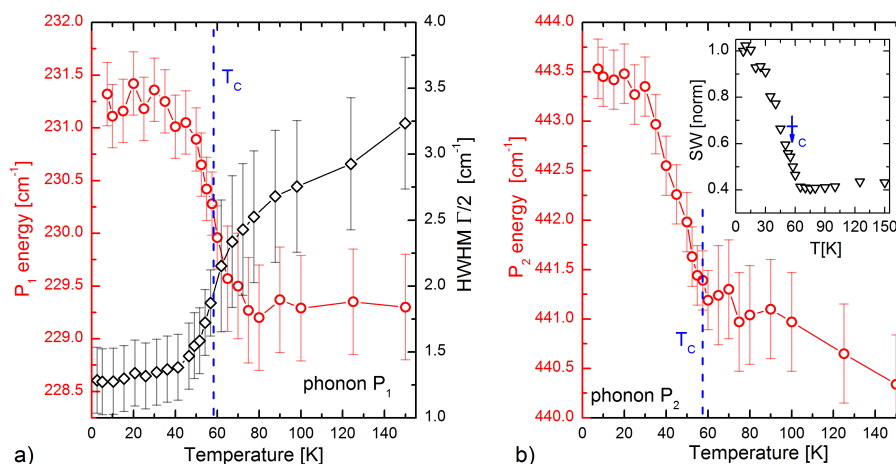


Figure 5.13: a) P_1 phonon energy and half width at full maximum (HWHM) and b) P_2 phonon energy with spectral weight (SW). Around the magnetic critical temperature $T_C \approx 58 \text{ K}$ an anomaly is observed in all phonon parameters.

5.5 Conclusions

Cu_4 triplet clusters form the relevant spin entity for the formation of long-range magnetic order in the cluster magnet Cu_2OSeO_3 . This leads to a characteristic spin excitation spectrum, which shows a clear division into weakly dispersing, high-energy *internal* cluster excitations and low-energy, strongly dispersing *external* cluster excitations. A Raman study of the high-energy spin excitations was performed. Four out of seven previously experimentally

observed cluster modes could be identified in the Raman spectra. The scattering mechanism of six out of seven experimentally observed cluster modes could be unambiguously identified as first-order Elliot Loudon scattering. The scattering mechanism of the 300 cm^{-1} excitation couldn't be unambiguously deduced based on the current data and previous reports in literature. The temperature dependent Raman scattering of the strong 265 cm^{-1} $\Delta S^z = \pm 1$ and 425 cm^{-1} high-energy cluster modes was studied in closer detail. These modes show to soften and broaden with increasing temperature, and persist above T_C as a broad magnetic scattering continuum. Above T_C , the Cu_4 clusters are decoupled, resulting in localized cluster-internal spin excitations. In the long-range ordered phase the internal cluster modes acquire dispersion by the inter-cluster exchange interactions, and form optical magnon branches, resulting in well-defined magnetic modes in the Raman spectrum. These observations support the picture that Cu_2OSeO_3 can be regarded as a generalized solid-state molecular crystal of spin nature. This chapter furthermore provides a solid foundation for the last chapter, where we will look at photoinduced long-range and cluster-internal order parameter dynamics.

5.6 Own contributions and acknowledgements

The section on the spin cluster eigenenergy spectrum and spin wave spectrum represents my understanding of the work described in References [1-3] and [11]. The wave functions calculated in Ref. [3] were used by myself to determine the Raman-activity of the spin cluster excitations, with the assistance of Christoph Boguschewski. The text of this chapter has been written by myself.

Prof. Petra Becker (University of Cologne) grew the Cu_2OSeO_3 single crystal. The Raman spectra presented in this chapter were collected and analyzed by myself. I would like to thank Rafael German for technical instructions on the Jobin Yvon machine.

I would like to thank Prof. D. Inosov (TU Dresden) for answering my questions about the inelastic neutron experiment. I would like to thank Dr. I. Rousochatzakis (Loughborough University, UK) and Dr. J. Romhányi (Okinawa, JP) for insightful discussions on their spin wave calculation papers. I furthermore would like to thank Christoph Boguschewski and Anuja Sahasrabudhe for fruitful discussions on the Raman data.

5.7 Bibliography

- [1] O. Janson, I. Rousochatzakis, A. A. Tsirlin, M. Belesi, A. A. Leonov, U. K. Rößler, J. Van den Brink, and H. Rosner, The quantum nature of skyrmions and half-skyrmions in Cu_2OSeO_3 , *Nat. Commun.* **5**, 5376 (2014).

- [2] M. Ozerov, J. Romhányi, M. Belesi, H. Berger, J.-Ph. Ansermet, Jeroen van den Brink, J. Wosnitzer, S. A. Zvyagin, and I. Rousochatzakis, Establishing the fundamental magnetic interactions in the chiral skyrmionic Mott insulator Cu_2OSeO_3 by terahertz electron spin resonance, *Phys. Rev. Lett.* **113**, 157205 (2014).
- [3] J. Romhányi, J. van den Brink, and I. Rousochatzakis, Entangled tetrahedron ground state and excitations of the magnetoelectric skyrmion material Cu_2OSeO_3 , *Phys. Rev. B* **90**, 140404 (2014).
- [4] J. M. Hopkinson, J. M. and H.-Y. Kee, Geometric frustration inherent to the trillium lattice, a sublattice of the B20 structure, *Phys. Rev. B* **74**, 224441 (2006).
- [5] J.-W. G. Bos, C. V. Colin, and T. T. M. Palstra, Magnetoelectric coupling in the cubic ferrimagnet Cu_2OSeO_3 , *Phys. Rev. B* **78**, 094416 (2008).
- [6] G. Venkataraman and V. C. Sanhi, External vibrations in complex crystals. *Rev. Mod. Phys.* **42**, 409 (1970).
- [7] P. N. Prasad and R. Kopelman, External, internal and semi-internal vibrations in molecular solids: spectroscopic criteria for identification, *Chem. Phys. Lett.* **21**, 505 (1973).
- [8] V. P. Gnezdilov, K. V. Lamonova, Y. G. Pashkevich, P. Lemmens, H. Berger, F. Bussy, and S. L. Gnatchenko, Magnetoelectricity in the ferrimagnetic Cu_2OSeO_3 : symmetry analysis and Raman scattering study, *Low Temp. Phys.* **36**, 550 (2010).
- [9] G. S. Tucker, J. S. White, J. Romhányi, D. Szaller, I. Kézsmárki, B. Roessli, U. Stuhr, A. Magrez, F. Groitl, P. Babkevich, P. Huang, I. Živković, and H. M. Rønnow, Spin excitations in the skyrmion host Cu_2OSeO_3 , *Phys. Rev. B* **93**, 054401 (2016).
- [10] L. Zhang, Y. A. Onykienko, P. M. Buhl, Y. V. Tymoshenko, P. Čermák, A. Schneidewind, A. Henschel, M. Schmidt, S. Blügel, D. S. Inosov, and Y. Mokrousov, Magnonic weyl states in Cu_2OSeO_3 , e-print arXiv:1901.06192 [cond-mat.mtrl-sci] (20189).
- [11] P. Y. Portnichenko, J. Romhányi, Y. A. Onykienko, A. Henschel, M. Schmidt, A. S. Cameron, M. A. Surmach, J. A. Lim, J. T. Park, A. Schneidewind, D. L. Abernathy, H. Rosner, J. van den Brink, and D. Inosov, Magnon spectrum of the helimagnetic insulator Cu_2OSeO_3 , *Nat. Commun.* **7**, 10725 (2016).
- [12] C. Kittel and P. McEuen, *Introduction to Solid State Physics*, 8th ed (John Wiley & Sons, New York, 2005).
- [13] S. V. Streltsov and D. I. Khomskii, Orbital physics in transition metal compounds: new trends, *Phys. Usp.* **60**, 1121-1146 (2017).
- [14] M. I. Kobets, K. G. Dergachev, E. N. Khatsko, A. I. Rykova, P. Lemmens, D. Wulferding, and H. Berger, Microwave absorption in the frustrated ferrimagnet Cu_2OSeO_3 , *Low Temp. Phys.* **36**, 176 (2010).
- [15] M. Garst, J. Waizner, and D. Grundler, Collective spin excitations of helices and magnetic skyrmions: review and perspectives of magnonics in non-centrosymmetric magnets, *J. Phys. D: Appl. Phys.* **50**, 293002 (2017).
- [16] M. Janoschek, F. Bernlochner, S. Dunsiger, C. Pfeleiderer, P. Böni, B. Roessli, P. Link, and A. Rosch, Helimagnon bands as universal excitations of chiral magnets, *Phys. Rev. B* **81**, 214436 (2010).
- [17] M. Kugler, G. Brandl, J. Waizner, M. Janoschek, R. Georgii, A. Bauer, K. Seemann, A. Rosch, C. Pfeleiderer, P. Böni, and M. Garst, Band structure of helimagnons in MnSi resolved by inelastic neutron scattering, *Phys. Rev. Lett.* **115**, 097203 (2015).

- [18] M. Weiler, A. Aqeel, M. Mostovoy, A. Leonov, S. Geprägs, R. Gross, H. Huebl, T. T. M. Palstra, and S. T. B. Goennenwein, Helimagnon resonances in an intrinsic chiral magnonic crystal, *Phys. Rev. Lett.* **119**, 237204 (2017).
- [19] M. G. Cottam and D. J. Lockwood, *Light scattering in magnetic solids*, (Wiley New York, NY, 1986).
- [20] F. G. Bass and M. I. Kaganov, Raman scattering of electromagnetic waves in ferromagnetic dielectrics, *Sov. Phys. JETP* **10**, 986 (1960).
- [21] P. A. Fleury and R. Loudon, Scattering of light by one- and two-magnon excitations, *Phys. Rev.* **166**, 514 (1968).
- [22] H. Kuzmany, *Solid-state spectroscopy: an introduction*, (Springer Verlag, 2009).
- [23] P. A. Fleury, S. P. S. Porto, and R. Loudon, Two-magnon light scattering in anti-ferromagnetic MnF_2 , *Phys. Rev. Lett.* **18**, 658 (1967).
- [24] P. A. Fleury, Paramagnetic spin waves and correlation functions in NiF_2 , *Phys. Rev.* **180**, 591 (1969).
- [25] D. J. Lockwood, in *Light scattering from electronic and magnetic excitations in transition-metal halides of Light scattering in solids III*, edited by M. Cardona and G. Güntherodt, (Springer, Berlin, Heidelberg, 1982)
- [26] M. I. Aroyo, A. Kirov, C. Capillas, J. M. Perez-Mato, and H. Wondratschek, *Bilbao Crystallographic Server. II. Representations of crystallographic point groups and space groups*, *Acta Crystallogr. Sect. A* **62**, 115 (2006).
- [27] K. H. Miller, X. S. Xu, H. Berger, E. S. Knowles, D. J. Arenas, M. W. Meisel, and D. B. Tanner, Magnetodielectric coupling of infrared phonons in single-crystal Cu_2OSeO_3 , *Phys. Rev. B* **82**, 144107 (2010).
- [28] T. Adams, A. Chacon, M. Wagner, A. Bauer, G. Brandl, B. Pedersen, H. Berger, P. Lemmens, and C. Pfleiderer, Long-wavelength helimagnetic order and skyrmion lattice phase in Cu_2OSeO_3 , *Phys. Rev. Lett.* **108**, 237204 (2012).
- [29] N. J. Laurita, G. G. Marcus, B. A. Trump, J. Kindervater, M. B. Stone, T. M. McQueen, C. L. Broholm, and N. P. Armitage, Low-energy magnon dynamics and magneto-optics of the skyrmionic Mott insulator Cu_2OSeO_3 , *Phys. Rev. B* **95**, (2017).
- [30] T. P. Devereaux and R. Hackl, Inelastic light scattering from correlated electrons, *Rev. Mod. Phys.* **79**, 175 (2007).
- [31] S. H. Liu, Magnetic excitations above the critical temperature. *Phys. Rev. B* **13**, 2979 (1976).
- [32] C. Kittel. Interaction of spin waves and ultrasonic waves in ferromagnetic crystals, *Phys. Rev.* **110**, 836 (1958).
- [33] Y. R. Shen and N. Bloembergen, Interaction between light waves and spin waves, *Phys. Rev.* **143**, 372 (1966).

Chapter 6

A tunable time-resolved spontaneous Raman spectroscopy setup for probing ultrafast collective excitation and quasiparticle dynamics in quantum materials

6.1 Introduction

The last decade has seen a surge of experiments where light is exploited as a strong external stimulus to manipulate quantum materials.^[1-3] The light-matter interaction can be a fully coherent process as in the case of the Floquet state in photon-dressed materials,^[4] or drive quantum materials into a strongly non-thermodynamic state by disturbance of the balance between electronic, orbital, spin, and lattice degrees of freedom. Seminal cases of the latter phenomenon include the photoinduced insulator-metal transition in VO₂,^[5] optical control of colossal magnetoresistivity in manganites,^[6] and transient signatures of photoinduced superconductivity in a stripe-ordered cuprate.^[7]

Integral in the description of the emanating dynamics in the optically driven non-equilibrium state is the creation and annihilation of electronic quasiparticles, collective excitations associated with the various degrees of freedom, and their interaction. Their transient annihilation and creation may, for instance, induce symmetry changes across photoinduced phase tran-

sitions,⁸ and dictates nonequilibrium temperatures,⁹ while their interaction underlies the coupling, and therefore the equilibration between the various degrees of freedom.¹⁰ A scala of partially complimentary pump-probe techniques have been developed to study quasiparticle and collective excitation dynamics, and their interaction. For instance, the coupling between low-energy collective excitations, and high-energy electronic excitations may be mapped into the time-domain, and quantified, through all-optical coherent fluctuation spectroscopy.^{11,12} A direct view on momentum-dependent electron and hole quasiparticle population dynamics is provided by means of the matured technique of time-resolved angle-resolved photoemission spectroscopy.^{8,13} The situation for direct probing of collective excitation populations is perhaps more ominous.¹⁴ Rather novel photon-probes of dynamics of collective excitations such as phonons, magnons, and orbital excitations are time-resolved diffuse x-ray scattering,¹⁵ and time-resolved resonant inelastic x-ray scattering.¹⁶ Plasmon dynamics in quantum materials has for instance successfully been probed with femtosecond electron energy loss spectroscopy.^{17,18} However, a quantification of occupation numbers and corresponding effective temperatures with these techniques still seems a stretch.

Time-resolved Raman scattering is a reasonably well-established probe for vibrational dynamics in organic materials,¹⁹⁻²³ and phonon population dynamics in semiconductor materials^{24,25} and carbon allotropes.²⁶⁻²⁹ With this technique the transient evolution of the spontaneous Raman spectrum after photo-excitation is studied.³⁰ The pump excitation mechanism only needs to induce incoherent dynamics. There are thus no special prerequisites to the pulse duration, as is the case with coherent pump-probe techniques.^{11,12} In the time-domain spectra transient changes in excitation energies, line-widths, and scattering intensities of Raman-active excitations can be obtained. This has the advantage over coherent excitation techniques that one can follow the true time evolution of the system through its incoherent response, rather than the time evolution of coherent excitations. Through detailed balance of the anti-Stokes to Stokes scattering intensity ratio the temporal evolution of selected effective mode temperatures can be directly determined,^{30,31} as in contrast to techniques relying on a comparison of the dynamical response with the thermodynamic temperature evolution. This makes time-resolved spontaneous Raman spectroscopy a truly unique technique in the study of ultrafast processes, and for instance allows testing of the validity, and limitations of widely applied multiple effective temperature models.^{9,32} An interesting situation is expected on the shortest time-scales, where truly non-thermal dynamics is present and the fluctuation dissipation theorem may not hold anymore. Phase transitions can be optically induced when a quantum material is driven far out-of-equilibrium. The associated symmetry changes across the phase transition can be deduced from the changes in selection rules of the transient Raman spectrum.³⁴ Since the transient excitation dynamics is directly measured in the frequency domain,

the renormalization of excitation energies and linewidths across the phase transition (or partial melting of a phase) may be measured with large accuracy. This should be compared and contrasted with time-domain techniques which rely on the detection of a frequency chirp in the coherent excitation dynamics.³³

Major factors to the limited use of time-resolved spontaneous Raman spectroscopy in the study of ultrafast dynamics in quantum materials are energy-time resolution limitations, the relevant excitation energy scales,³⁶ and low inelastic light scattering cross sections. In time-resolved Raman spectroscopy the time resolution and spectral resolving power are Fourier transform related. This asks for a proper choice of design parameters as we recapitulate in this article. The Fourier transform limit can in principle be overcome with the femtosecond stimulated variant of the technique.³⁷ A recent success with time-resolved femtosecond stimulated Raman spectroscopy (tr-FSRS) is the observation of a modification of the Heisenberg exchange in an antiferromagnet on the femtosecond timescale.³⁸ In FSRS the stimulated gain and loss intensities both have contributions from anti-Stokes and Stokes processes. The gain and loss ratio therefore cannot be easily interpreted in terms of an occupation number or equivalent temperature.³⁹ Time-resolved spontaneous Raman therefore stays an appealing technique to study quasiparticle and collective excitation population dynamics, and optimization of signal detection remains a central issue. Recent advances in high repetition rate amplified laser systems, tunable light sources, and detection techniques can nowadays bring the sensitivity of time-resolved spontaneous Raman spectroscopy close to that encountered in a continuous wave laser based steady-state spontaneous Raman scattering experiment, even without relying on resonances. A resurgence of the technique as a tool to probe quasiparticle population dynamics, photoinduced symmetry changes, and energy and momentum-transfer in quantum materials is thus foreseen.

In this chapter we present our flexible and efficient ultrafast time-resolved spontaneous Raman spectroscopy setup to study collective excitation and quasiparticle dynamics in quantum materials. The setup has a broad energy tuning range extending from the visible to near infrared spectral regions for both the pump and probe pulse energies. It thereby allows to selectively excite materials, and to probe under off- and on-resonant Raman conditions. The balance between energy and time-resolution can be controlled, allowing few picosecond time-resolution studies with an energy resolution down to $\Delta\nu \sim 7 \text{ cm}^{-1}$ or femtosecond studies with $\Delta\nu \sim 50 \text{ cm}^{-1}$ energy resolution. A high light collecting efficiency is realized by high numerical aperture collection optics, and a high-throughput flexible spectrometer. The functionality of the setup is demonstrated with three different case studies. We first focus on the zone-center longitudinal optical phonon (LO-phonon), and hole continuum dynamics in photo-excited silicon, and discuss the role of the Raman tensor by simultaneously tracking the Stokes and anti-Stokes spec-

tra. Changes in the Raman tensor resulting from photoinduced symmetry changes have been discussed previously.³⁴ Here it is shown that changes in the Raman tensor can additionally appear due to resonance effects. This can be used as an alternative probe to track electronic population dynamics. Higher order Raman processes can serve as an all-optical momentum dependent probe. We show evidence for dissimilar electron-phonon scattering rates at different high symmetry points in the Brillouin zone of silicon by detecting pump-induced changes in the two-phonon overtone spectrum. This measurement underscores the unique resolving power of measuring transient changes in excitation energies in the frequency domain. Demagnetization dynamics of helimagnetic order in the chiral insulator Cu_2OSeO_3 is studied by observing softening and broadening of a magnon excitation after photoexcitation. This illustrates the technique's feasibility to probe photoinduced phenomena in quantum materials, such as melting of phases, and photoinducing phase transitions. With the high stability and sensitivity of the described setup new avenues in ultrafast dynamical studies of quantum materials are foreseen. These include the tracking of order parameter evolution and detection of symmetry changes across photoinduced phase transitions, the qualitative determination of energy and angular momentum transfer rates in the relaxation of non-equilibrium states, and time- and momentum-resolved scattering.

6.2 The time-resolved spontaneous Raman spectroscopy setup

6.2.1 Design considerations

Typical design parameters for a time-resolved spontaneous Raman setup include energy resolution, time-resolution, the laser linewidth, and laser repetition rate.³⁰ Other design factors include tunability of the pump excitation and Raman probe light, and suitable schemes to filter the Raman scattered light from the elastically scattered light. The energy- and time-resolution parameters are of special importance in time-resolved spontaneous Raman spectroscopy. For a transform-limited Gaussian pulse the bandwidth-time relation is $\Delta\nu\Delta\tau \approx 14.7 \text{ cm}^{-1}\text{ps}$, with $\Delta\nu$ the frequency (energy) bandwidth of a pulse, and $\Delta\tau$ the pulse duration. Here $\Delta\nu$ and $\Delta\tau$ refer to the full width at half maximum (FWHM). A trade-off in time and energy resolution is thus inherent to the technique, and ideally a setup should allow control of energy and temporal resolution. The experimentally accessible region, limited by the Fourier transform relation, is indicated in Fig. 6.1. In materials with only a few Raman-active modes, such as IV and III-V semiconductors,^{24,40} or well-separated high-energy modes in for instance graphite allotrope materials,^{26,28} a pulse bandwidth of $\Delta\nu \approx 100 \text{ cm}^{-1}$ (FWHM) suf-

ferences to resolve individual modes, and thus sub-ps time-resolution can be realized (see Fig. 6.1). This energy resolution however generally isn't sufficient to study dynamics of collective excitations in quantum materials such as magnons^[41] and phonons, or the more complex types such as electromagnons,^[42] Cooper-pair breaking,^[35] and charge-density wave modes,^[43] since these modes generally are low energy excitations with $\Delta E < 120$ meV. This energy scale corresponds to Raman shifts of ~ 1000 cm^{-1} and lower, and thus requires a higher spectral resolving power. This holds especially in the lowest energy region ($\Omega < 100$ cm^{-1}) where for instance soft modes in ferroelectrics are observed.^[44] In this region stray light from spectrally broad laser pulses can hinder the observation of the modes of interest. Another case where high resolving power is necessary are materials of low crystallographic symmetry where more interesting modes of electronic and magnetic origin might overlap with a multitude of phonon modes.

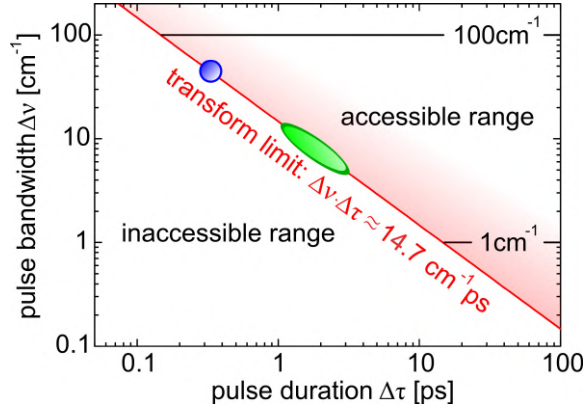


Figure 6.1: The Fourier transform relation $\Delta\nu\Delta\tau \approx 14.7$ cm^{-1}ps between pulse duration $\Delta\tau$ and pulse bandwidth $\Delta\nu$ puts a limit to the experimentally accessible energy and temporal dynamics range. The energy resolution region of interest for time-resolved spontaneous Raman studies of quantum materials is put between 1 cm^{-1} and 100 cm^{-1} . This leads to a few tens of picoseconds, to a few hundred of femtoseconds temporal resolution. The green ellipse indicates where the system operates in ps-mode. The time, and energy resolution can be controlled by detuning the SHBC, or by a pulse shaper. The blue dot is where the system operates when probe light is generated with the FS-OPA.

In spontaneous Raman spectroscopy the inelastically scattered light needs to be separated from the Raman excitation light. For higher energy modes such as vibrational excitations in carbon-based materials this can for instance be realized with notch filters. When tunability in probe wavelength is of importance a triple subtractive Raman spectrometer is still favored. In time-resolved spontaneous Raman spectroscopy an additional complication appears since the pump-excitation, and the pump-induced Raman spectrum need to be rejected. Different filtering schemes have been applied for this.^[30]

In a degenerate pump-probe experiment polarization optics are used to reject the pump-induced elastic, and inelastic scattered light. The downside is that only the parallel Raman polarization geometry can be studied.³⁴ In addition, unwanted polarization leakage also ends up in the Raman spectrum, and the lowest energy excitations are difficult to access. In a two-color setup however, the pump-induced elastic (and inelastic) scattering can be conveniently rejected by spectral filtering.^{21,30}

Amplified laser systems allow for tunable two-color experiments, as opposed to MHz-oscillator experiments which are limited to the fundamental and double wavelength for the pump and probe beams. In addition, with an amplifier the problem of average heating is avoided. For low repetition rate systems the average laser power can however bring challenges. The Raman intensity scales with average laser power. For detectable average laser powers with low repetition rate systems the pulse peak intensities can thus easily get too large, which may lead to nonlinear effects, and sample damage. The ideal situation between these laser system limits thus exists in the form of high repetition rate amplifiers.^{21,30}

6.2.2 System overview

The time-resolved Raman system consist of three main parts: I.) the amplified laser system and optical parametric amplifiers to generate pulses for selective pumping, and narrow-bandwidth pulses for Raman probing, II.) the table optics for pulse cleaning, polarization control and the delay line III.) the confocal Raman microscopy interface, the high efficiency spectrometer and charge-coupled device detector. A layout of the setup is shown in Fig. 6.2.

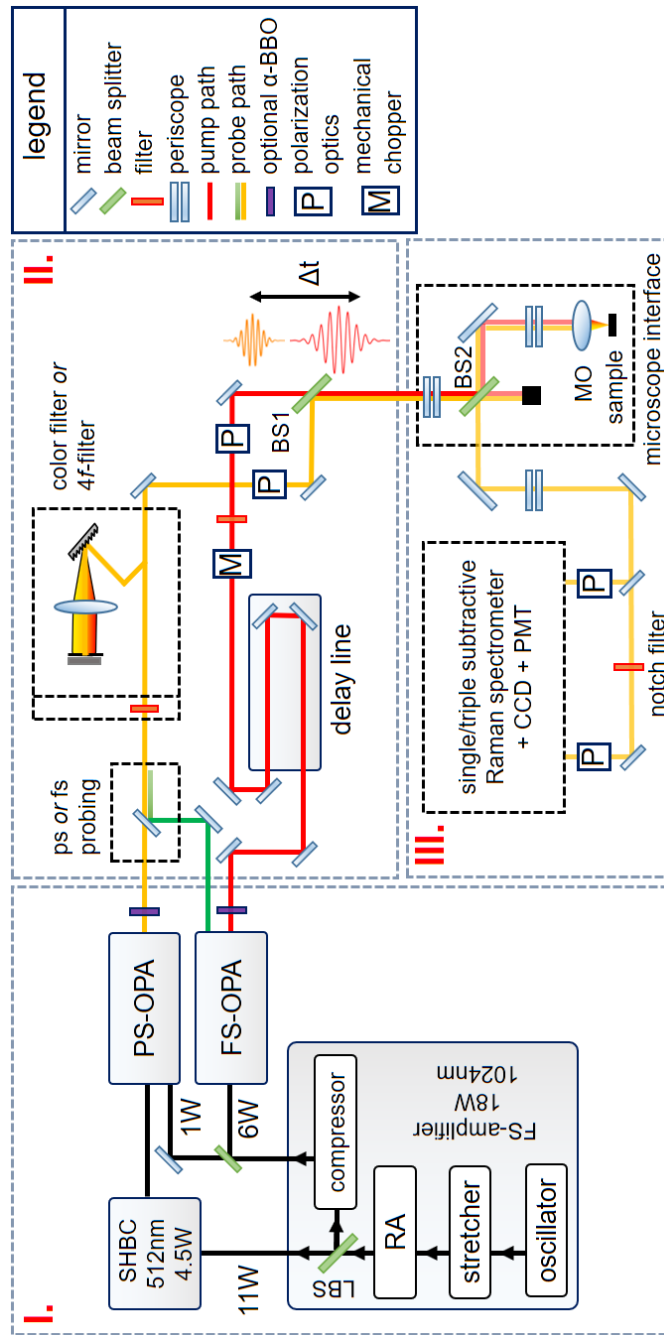


Figure 6.2: The femtosecond-picosecond time-resolved spontaneous Raman setup. Box 1.) Laser system and optical parametric amplifiers. Box 2.) Table optics and delay line. Box 3.) The confocal Raman microscope interface and detection system. See the text for details.

Amplified laser system & selective pump excitation and tunable Raman probe

A chirped pulse amplification based laser system (LIGHTCONVERSION PHAROS) was selected for the setup. The PHAROS laser system consists of a Kerr-lensing mode locked oscillator module, a regenerative amplifier (RA), and stretcher-compressor units which are all embedded in a compact module. The laser uses diode-pumped Yb:KGW (Ytterbium-doped potassium gadolinium tungstate) as the active medium. The emitted pulses have $\lambda_C = 1024$ nm central wavelength. An internal pulse picker allows to set the repetition rate up to $f_{\max} = 100$ kHz. After the regenerative amplification stage the 1024 nm stretched pulse beam is split into two beams. One beam is directly emitted as an 11 W output of non-compressed highly chirped 150 ps long pulses. The other beam is compressed, resulting in a 7 W average power beam of 0.3 ps duration pulses.

The uncompressed 11 W beam is routed to a second harmonic bandwidth compressor (LIGHTCONVERSION SHBC).⁴⁵ Inside the SHBC, a 1:1 beamsplitter divides the beam. A high-intensity grating gives the split beams an opposite chirp, after which the beams are overlapped on an β -BBO (barium borate) crystal. The SHBC converts the 1024 nm pulses of full-width at half maximum (FWHM) $\Delta\nu \approx 50$ cm^{-1} , into 512 nm transform limited pulses with $\Delta\nu \approx 10$ cm^{-1} FWHM and $\Delta\tau \approx 1.5$ ps temporal width. The SHBC output can directly be used as Raman probe light, or used to pump a three stage white-light seeded picosecond optical parametric amplifier (LIGHTCONVERSION PS-OPA). The white light seed is generated with 1 W of 0.3 ps 1024 nm compressed pulses. The PS-OPA can continuously tune the Raman probe wavelength from 630 nm to 950 nm. The signal and idler of the PS-OPA output can be externally doubled to tune the probe wavelength in the range 320 - 600 nm.

A total power of $P = 6$ W of the 0.3 ps 1024 nm compressed beam is routed to a double-pass white-light seeded optical parametric amplifier (LIGHTCONVERSION ORPHEUS FS-OPA) to generate pump pulses. The signal wavelength is continuously tunable from 620 nm to 1000 nm, where the idler runs from 1060 nm to 2500 nm. An external β -BBO crystal can be used to extend the pump wavelength range from 320 to 600 nm.

The time-resolved system operates in the green oval region in the $(\Delta\nu, \Delta\tau)$ -plane of Fig. 6.1 when probing is realized with the SHBC or PS-OPA output. High time-resolution, with lower energy resolving powers can be realized by only working with the FS-OPA. The FS-OPA's signal output is in this case still used for pumping. The residual output of the OPA's 0.3 ps, $\lambda_C = 512$ nm pump beam is used for probing. For the FS-OPA based operation mode the system works in the blue sphere in the $(\Delta\nu, \Delta\tau)$ -plane.

Table optics

Narrow-band laser line filters are placed in the pump beam to remove unwanted spectral components which may otherwise lead to spurious signals in the Raman spectra. The polarization state of the pump beam can be controlled by a Berek compensator. For the probe beam the unwanted spectral components are either removed by laser line filters or a folded grating-based pulse shaper,⁴⁶ where the latter results in the cleanest pulse, as required for probing small Raman shifts ($\Omega < 100 \text{ cm}^{-1}$). In addition, the pulse shaper allows to narrow down the spectral pulse bandwidth at least to about $\Delta\nu \approx 7 \text{ cm}^{-1}$ FWHM at the expense of time-resolution and average probing power. A Berek compensator is used to control the polarization state of the probe beam.

The temporal delay between the pump and probe pulse is controlled via a mechanical delay line of 30 cm length (PHYSIKALISCHE INSTRUMENTE M-531.EC) placed in the pump beam path. The step size resolution is $\sim 0.5 \mu\text{m}$, corresponding to a time-resolution of approximately $\sim 3 \text{ fs}$. The time-resolution is thus effectively determined by the pump-probe pulse cross-correlation. A silver-coated retro-reflector is mounted on the delay line. The pump and probe beams are made collinear before the Raman microscopy interface with beam combiner BS1. The mechanical chopper is only used when PMT-detection is used.

Raman interface, spectrometer, CCD-detector, and PMT-detector

The collinearly propagating pump and probe beams enter the Raman microscopy interface via a periscope. The collinear pump and probe beams are reflected from beam splitter BS2 (R/T = 0.2/0.8) into a high numerical aperture microscope objective MO (OLYMPUS LMPLFLN-series long working distance objectives are used, where the NA=0.4, 20 \times , working distance WD=12 mm is the standard choice). The backscattered light is collected by the microscope objective, transmitted through beam splitter BS2, and focused on the spectrometer entrance slit.

The maximum pump pulse energy lies around $\sim 150 \text{ nJ}$ at the sample position for 650 nm pump excitation. The maximum probe pulse energy lies around $\sim 20 \text{ nJ}$ at the sample position for 512 nm probe excitation when the grating-based pulse shaper is used. Since the Raman scattering efficiency scales with incident laser intensity, a large average incident probe power is preferred. For diffraction-limited pump-probe spot sizes this however results in a few challenges. Pulse fluences get too large, and samples damage easily. This can be solved by defocussing the microscope objective. The divergence of the scattered light in this case is corrected with a telescope system placed after BS2. This allows working with spot sizes of about $\sim 1 \mu\text{m}$ to $\sim 100 \mu\text{m}$ diameter. The samples can be placed in a JANIS ST500 coldfinger cryostat

with small working distance (about 2 mm).

A successful implementation of time-resolved Raman spectroscopy significantly hinges on the efficiency of the spectrometer. Raman-scattered light is an order $\mathcal{O} \sim 10^{-8}$ weaker compared to the incident excitation light. This necessitates a high stray light rejection. We use a cascade of three Czerny-Turner imaging spectrographs (TRIVISTA 555, S&I GMBH) which are operated in subtractive mode (high stray light rejection by the first two spectrometers).⁴⁷ Different sets of holographic, and ruled gratings allow to maximize the scattered light detection efficiency. Silver-coated optical elements ensure a high throughput. The last stage (spectrometer stage) has a second entrance port. This allows to bypass the subtractive stage of the spectrometer. In this case a notch filter is used to block the elastically scattered light. The use of a notch filter can provide up to a factor $2\times$ increase in throughput efficiency with respect to the subtractive filtering. A color filter may additionally be used to suppress the scattered pump light.

The used imaging spectrometer contains toroidal mirrors. This corrects for the astigmatism present in a spectrometer containing spherical mirrors.⁴⁸ In the toroidal case a smaller image size in the lateral direction is thus produced on the charge-coupled device (CCD) chip. This has the advantage that less CCD-rows need to be binned to integrate the scattered light spectrum. This significantly reduces the appearance of occasional spikes from cosmic events in the Raman spectrum, and reduces the CCD-readout noise with respect to an ordinary spectrometer. The low spherical aberration of the spectrometer makes that one can resort to the use of pseudo-confocal microscopy.⁴⁹ In this case the entrance slit rejects out-of-focus light in the horizontal direction, whereas the CCD-binning is used to digitally reject out-of-focus light in the vertical direction from the Raman spectrum. By resorting to pseudo-confocality the use of an opto-mechanical confocal system is avoided. In the latter case a secondary focus point through a mechanical pinhole before the spectrometer is used to obtain confocality. This would however lead to reflection losses for the scattered light from additional lenses. The CCD-detector is a low-etaloning PYLON-100:BR-EXCELON, 1340×100 pixels CCD, with a pixel size of $20 \times 20 \mu\text{m}^2$. The quantum-efficiency lies above $\text{QE} > 90\%$ for the wavelength range 450 - 900 nm.

Single channel detection with a photomultiplier (PMT) and lock-in detection was realized as a second detection possibility. The installed PMT is a HAMAMATSU R943-02 with a cadmium-doped GaAs photo-cathode, which is cooled with a HAMAMATSU C10372 thermoelectric cooler. The PMT signal is read out by a STANFORD RESEARCH SYSTEMS SR830 lock-in detector. The PMT-signal is amplified with a STANFORD RESEARCH SYSTEMS SR560 voltage preamplifier before lock-in read-out. A mechanical chopper is placed in the pump-beam path for time-resolved measurements, and in the probe-beam path for steady-state measurements.

6.2.3 Detection scheme of choice

In case of CCD-detection the intensity $I(t)$ of a broad Raman spectral range, generally tens of meV, is determined. The delay line is stepped, where after a Raman spectrum is acquired for multiple seconds for each time point. The scattering efficiency change is determined by comparing the after photoexcitation spectra with the before photoexcitation spectra. With PMT-detection the *change* $\Delta I_{int}(t)$ in integrated scattering intensity $I_{int}(t) = \int_{\Omega_1}^{\Omega_2} I(t) d\Omega$ of a spectral feature falling within a small spectral region $[\Omega_1:\Omega_2]$ dictated by the exit slit width is directly by the standard *differential* pump-probe spectroscopy scheme.^{30,50} In this case the pre-time-zero intensity I_0 needs to be separately determined.

A comparison in detection efficiency for both detection methods is made. Figure 6.3a shows a spectrum of the the silicon 520 cm^{-1} longitudinal optical (LO) phonon obtained with PMT-detection and 512 nm ps-pulses as Raman-excitation. The silicon sample was excited with 630 nm pulses under a photoexcitation density of about $n_0 \sim 1 \times 10^{19}\text{ cm}^{-3}$. Figure 6.3b shows the normalized change in scattering intensity for both the PMT and CCD detection mode. A reduction in scattering intensity is observed, which will be discussed in detail in the next paragraph. Each time-point corresponds to a total measurement time of 33 s (either integrated from the PMT or CCD signal). The relative change is fitted with an erfc-function (not shown). The fit amplitude and standard deviation are “signal” and “noise” respectively. This gives a signal-to-noise ratio $SNR_{CCD} \sim 16$, and $SNR_{PMT} \sim 4$. By CCD-detection a $4\times$ higher SNR is realized compared to PMT-detection. With CCD-detection a large spectral window is measured and peak shifts can be resolved. The CCD-mode therefore evidently is the preferred detection scheme.

6.3 Experimental results

6.3.1 Optical phonon population and hole continuum dynamics in silicon

Time-resolved Raman spectroscopy allows to address population dynamics of individual low-energy excitation modes after photo-excitation. Through detailed balance of the Stokes and anti-Stokes signals the population number of different modes can be determined, and calculated into effective mode temperatures.³¹ This direct way of measuring transient temperature evolution in the time-domain allows to test the validity and limitations of multiple effective temperature models,^{9,32} which on the shortest time-scales may not hold anymore due to the presence of truly non-thermal occupation statistics. Such effective temperature models are not only widely applied to describe ultrafast dynamics in simple materials,^{9,32} but also in quantum materials

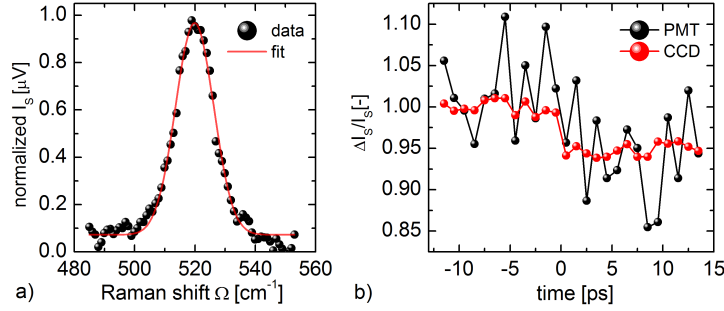


Figure 6.3: a) Steady-state spectrum of the silicon 520 cm^{-1} longitudinal optical (LO) phonon obtained with PMT-detection. The fit function is a Gaussian. b) Comparison of the normalized time-dependent scattering rate of the LO phonon after a photoexcitation of $n_0 \sim 1 \times 10^{19} \text{ cm}^{-3}$ as measured with the PMT and CCD. A stepwise reduction of the scattering amplitude of about 5% is observed. The integrated phonon response as measured with the CCD shows an about $4\times$ higher signal-to-noise.

where different spin, orbital, electronic and lattice degrees of freedom are present with their respective collective and quasiparticle excitations.^[51,52]

Raman tensor dynamics is a less treated aspect of time-resolved Raman scattering. It is however of crucial importance in the correct determination of effective mode temperatures.^[31] The anti-Stokes intensity scales as $I_{AS} \propto \chi^2 n$, where n is the mode occupation number, and χ^2 the squared Raman tensor. The Stokes-intensity scales as $I_S \propto \chi^2 [n + 1]$ and is thus less sensitive to transient population dynamics. This can be taken as a motivation to “neglect” dynamics of the Stokes-spectrum. However, from these relations it directly becomes clear that assigning transient anti-Stokes dynamics solely to transient population changes may not necessarily be true since the Raman tensor χ^2 may also show photoinduced changes. This is expected to be of special importance under resonant probing conditions. Below we demonstrate in intrinsic silicon that for a correct transient mode temperature determination indeed a dynamical modification of the Raman tensor χ^2 needs to be taken into account. Such a dynamical modification of the Raman tensor is expected to play a role in many other materials such as $3d/4d/5d$ transition metal oxides, carbon allotropes^[53] like graphene or Bucky-tubes, and transition metal dichalcogenides.^[54]

An intrinsic (100) oriented silicon wafer (resistivity $> 10000 \Omega\text{m}$), at room temperature, is excited above the indirect band-gap with 650 nm pulses of 0.3 ps duration. The Raman probe excitation is narrow-band ($\Delta\nu \approx 10 \text{ cm}^{-1}$ FWHM) pulsed light of 512 nm central wavelength, and 1.5 ps temporal duration. The pump and probe powers were set to $P_{\text{pump}} = 12 \text{ mW}$ and $P_{\text{probe}} = 1 \text{ mW}$ for the pump and probe beam respectively. With a pump spot size of $100 \mu\text{m}$ diameter, the photo-excitation density is about

$n_0 \sim 8 \times 10^{18} \text{ cm}^{-3}$. Both pump and probe beams are aligned with the [110] crystallographic directions. The backscattered light is collected with the single-stage spectrometer, where a notch-filter (KAISER OPTICAL SYSTEMS INC. SUPERNOTCH-PLUS 514.5 nm) is used to block the elastically scattered light.

Figure 6.4a and b show the anti-Stokes I_{AS} and Stokes I_S spectra of silicon (spectra at $t = -5$ ps). The spectra consist of the zone-center longitudinal optical (LO) phonon at $\pm 520 \text{ cm}^{-1}$, and an electronic continuum originating from hole scattering.^{55,56} The silicon peak has a (Gaussian) half width at half maximum of $\sim 8 \text{ cm}^{-1}$. This is larger than the intrinsic half-width of $\sim 3 \text{ cm}^{-1}$ at room temperature,⁵⁵ since Gaussian ps-pulses were used to collect the Raman spectrum. In Fig. 6.4c and d the differential anti-Stokes scattering intensity $\Delta I_{AS}(t) = I_{AS}(t) - I_{AS}(-5\text{ps})$, and Stokes scattering intensity $\Delta I_S(t) = I_S(t) - I_S(-5\text{ps})$ is shown for various representative delay-times. At 0 ps to 0.5 ps a scattering increase is observed on the anti-Stokes side. This corresponds to the creation of a transient optical phonon population. However, on the Stokes side a negative differential feature is observed, which evidently cannot originate from a transient phonon population. In addition a small positive shoulder in the $\Delta I_S(t)$ spectra is observed. The integrated phonon scattering intensities are shown in Fig. 6.5a. The phonon response is integrated over the spectral regions $\pm[460-580] \text{ cm}^{-1}$ (indicated with black bars) for the Stokes and anti-Stokes side respectively. A linear background was subtracted to take into account the increased hole continuum scattering over the integration region. The cross-correlation of the pump and probe pulse is plotted in faded blue for comparison.

The Stokes intensity I_S , and anti-Stokes intensity I_{AS} are given as:³¹

$$I_S(\omega_L - \Omega) \propto [\omega_L - \Omega]^3 \times C(\omega_L - \Omega, \omega_L) \times \chi^2(\omega_L - \Omega, \omega_L) \times [n(\Omega) + 1] \quad (6.1)$$

and

$$I_{AS}(\omega_L + \Omega) \propto [\omega_L + \Omega]^3 \times C(\omega_L + \Omega, \omega_L) \times \chi^2(\omega_L + \Omega, \omega_L) \times [n(\Omega)] \quad (6.2)$$

Here $\chi^2(\omega_L \pm \Omega, \omega_L)$ gives the Raman tensor square for the anti-Stokes and Stokes resonance, ω_L is the probe excitation frequency, and $n(\Omega)$ is the occupation number for the mode with energy $\hbar\Omega$. The factors $C(\omega_L \pm \Omega, \omega_L)$ contain the incident intensity, and optical constants (absorption, transmission and refractive index) at the incident and scattered frequencies.³¹ We however neglect the frequency dependence of C and χ^2 , which will lead to a small error of $< 5\%$ in the absolute phonon temperature determination.^{31,57} The anti-Stokes to Stokes scattering ratio can be used to calculate the phonon temperature, or equivalently the particle occupation number $n(\Omega)$, through the ratio:

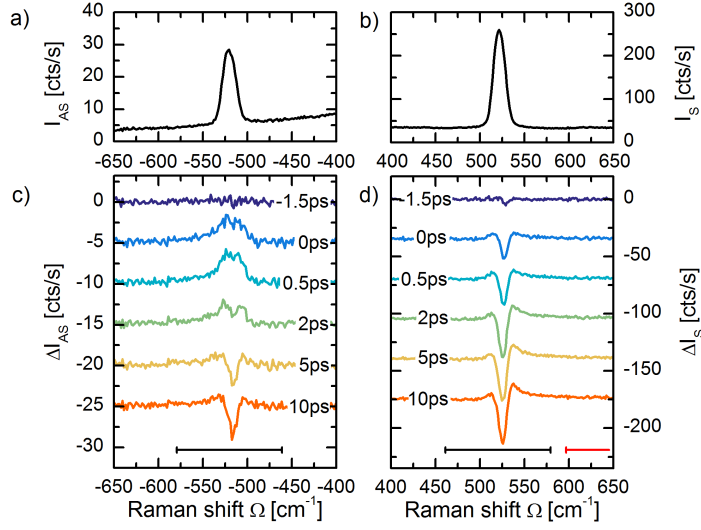


Figure 6.4: a) Anti-Stokes I_{AS} and b) Stokes I_S spectra of silicon. The main feature is the LO-phonon at $\pm 520 \text{ cm}^{-1}$. The background is attributed to hole continuum scattering. c) Differential anti-Stokes ΔI_{AS} and d) differential Stokes ΔI_S spectra for various representative time-delays. The anti-Stokes intensity shows a positive transient phonon intensity at 0.5 ps and 2 ps, corresponding to the creation, and decay, of an LO-phonon population. The Stokes side shows a transient reduction in phonon scattering efficiency due to a Raman tensor quench.

$$\begin{aligned}
 \frac{I_{AS}}{I_S}(\Omega) &= \frac{[\omega_L + \Omega]^3}{[\omega_L - \Omega]^3} \times \frac{C(\omega_L + \Omega, \omega_L)}{C(\omega_L - \Omega, \omega_L)} \times \frac{\chi^2(\omega_L + \Omega, \omega_L)}{\chi^2(\omega_L - \Omega, \omega_L)} \times \frac{n(\Omega)}{n(\Omega) + 1} \\
 &\approx \frac{[\omega_L + \Omega]^3}{[\omega_L - \Omega]^3} \times \exp\left(-\frac{\hbar\Omega}{k_B T}\right)
 \end{aligned} \tag{6.3}$$

In Fig. 6.5b the transient temperature, determined according to Eq. 6.3 is plotted. An average heating to 310 K is measured before time-zero. After photo-excitation the temperature rises by $\Delta T \approx 45 \text{ K}$ to 355 K within the time-resolution, followed by a decay with a time-scale of $\tau \approx 2.0 \pm 0.6 \text{ ps}$. The rapid rise, and consecutive decay is consistent with the transient creation of an optical phonon population through electron-phonon coupling, which thereafter decays into acoustic phonons through anharmonic coupling.⁵⁸ After 10 ps the temperature reaches quasi-equilibrium at an increased temperature of $\Delta T \approx 5 \text{ K}$, which does not recover within the measured time window.

Figure 6.5c shows the transient increase of hole continuum scattering in the region $+[600-650] \text{ cm}^{-1}$ (indicated with the red bar). The transient scattering signal is well-fitted with a step function convoluted with a cross-correlation function of the pump and probe pulse. The photoin-

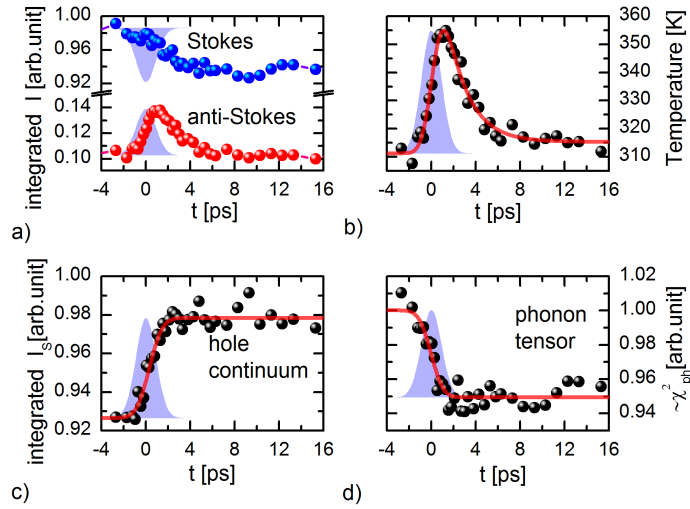


Figure 6.5: a) Transients of Stokes and anti-Stokes phonon intensity, as integrated over the blue highlighted regions in the Stokes and anti-Stokes spectra. On the anti-Stokes side a positive transient intensity is observed, which corresponds to a transient optical phonon population. The dynamics on the Stokes side is dominated by the tensor quench. b) Transient phonon temperature calculated through detailed balance. The temperature rises from 310 K to about 355 K, and recovers on a time-scale of $\tau \approx 2.0 \pm 0.6$ ps. c) Transient hole continuum scattering on the Stokes side in the green highlighted region. d) A transient phonon tensor quench is observed. In all graphs the cross-correlation of the pump and probe pulse is plotted in faded blue.

duced electron-hole-density has other effects on the Raman spectrum. Since the phonon Raman transition probability is proportional to the density of electrons in the valence band, and holes in the conduction band, the photoinduced electron-hole density is expected to alter χ^2 (Refs. [59, 60]). From the Stokes intensity I_S and the calculated population n , the time-evolution of χ^2 is calculated according to Eq. [6.1], and shown in Fig. [6.5]d. A step-wise tensor quench $\Delta\chi^2 \approx -5\%$ is observed, underlining the electronic origin of the transient decrease of the Stokes intensity I_S . The transient hole density in addition leads to an increase in the Fano-asymmetry, as evidenced by the ingrowing positive shoulder in the $\Delta I_S(t)$ spectra. The origin of the tensor quench and the transient Fano-asymmetry are discussed in more detail in chapter [7].

6.3.2 Time- and momentum resolved scattering in silicon

Electron-phonon, and phonon-phonon interaction strengths, or more generally the coupling between any type of quasiparticles, depends on the momentum of the interacting quasiparticles. [61] The characteristic timescales associated with optical phonon creation, and relaxation through anharmonic cou-

pling, are thus momentum-dependent.^{9,62} Pump-probe techniques spanning from x-ray to the optical range allow for time- and momentum-resolved probing. Whereas the momentum-dependence is implicit for pump-probe techniques in the x-ray range, such as diffuse scattering,¹⁵ diffraction,⁶³ or resonant inelastic x-ray scattering,¹⁶ this may not directly be obvious for optical pump-probe techniques as these are $\mathbf{k} \approx 0$ momentum transfer probes. Optical inelastic scattering techniques, notably femtosecond stimulated Raman spectroscopy,³⁸ and spontaneous Raman spectroscopy however can be utilized to disentangle momentum-dependent dynamics through higher-order scattering processes. In a two-particle process, two excitations of opposite momenta $+\mathbf{k}$ and $-\mathbf{k}$ are created (or annihilated).⁶⁴ Two-particle scattering processes appear in the inelastic light scattering spectrum as bands of the frequency dependence of the combined density of states of the excitation pair, weighted by a scattering efficiency distribution.⁶⁵ The multi-particle scattering response thus forms a mapping of momentum-space to the energy domain, and thereby allows for the study of momentum-resolved particle dynamics. After careful analysis of the line-shape even momentum-relaxation dynamics should be in principle feasible to detect.⁶⁶ With time-resolved spontaneous Raman spectroscopy we succeeded to detect photoinduced phonon softening of different high-symmetry Brillouin Zone-points (BZ-points) in the two-phonon spectrum of silicon. We find evidence that the softening at the different points occurs with dissimilar time-scales, which is indicative of dissimilar electron-phonon scattering rates.

Probing of the two-phonon spectrum on a (100) oriented silicon wafer was performed at room temperature. A 512 nm Raman probe excitation was used, with the probe polarization along the [110] axis. The two-phonon spectrum is observed between 920 cm^{-1} and 1040 cm^{-1} as seen in Fig. 5a (dark blue line). The two-phonon spectrum consists of a summation of TO-phonon overtones from four high-symmetry Brillouin Zone (BZ) points.⁶⁷ Previous reports have assigned the characteristic spectral features based on the analysis of critical points in the phonon density-of-states.^{65,67,68} The sharp increase at 920 cm^{-1} is related to scattering from the X-point, the shoulder at 940 cm^{-1} to the W-point, and the shoulder at 970 cm^{-1} to scattering from the L-point. The tail extending from 980 cm^{-1} to 1040 cm^{-1} is the overtone from the zone center, i.e. the Γ -point. The different regions are marked with bars.

The sample is excited above the indirect band-gap with 650 nm pulses of 0.3 ps duration, and pump polarization along the [110] axis. The photoinduced electron-hole density is $n_0 \sim 9 \times 10^{19} \text{ cm}^{-3}$. Figure 6.6a shows the transient Stokes spectra $I_S(t)$ of the two-phonon peak for various pump-probe delays. A photoinduced redshift of the two-phonon spectrum is observed, in addition to an increased hole continuum scattering background, as discussed above. Figure 6.6b shows the differential spectra $\Delta I_S(t) = I_S(t) - I_S(-2\text{ps})$ for the respective time-delays, where the hole con-

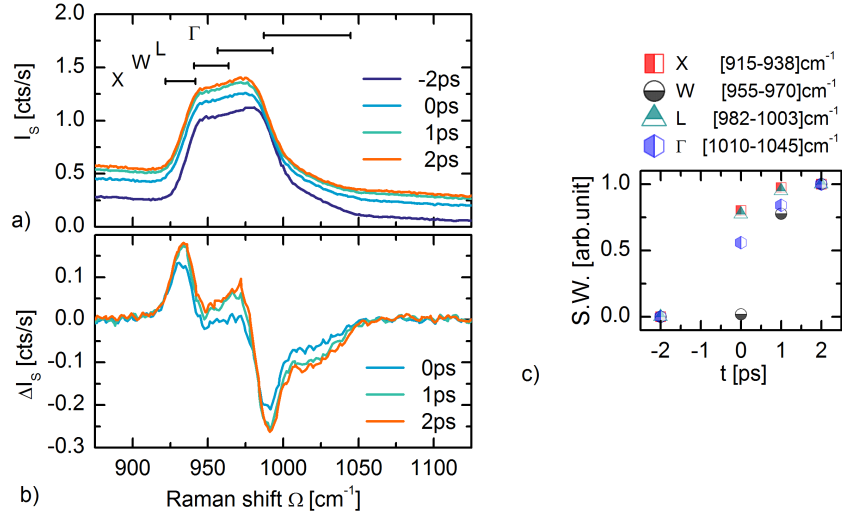


Figure 6.6: a) Two-phonon spectra $I_S(t)$ of photo-excited Silicon for various delay-times. Scattering regions originating from the different Brillouin Zone regions X, W, L, and Γ are indicated with bars. b) Corresponding differential spectra $\Delta I_S(t)$. The transient hole scattering response has been subtracted. The spectral shift at the W- and Γ -point appears to have a slower ingrowth than the X- and L-point. c) Spectral weight S.W. for representative regions in the two-phonon signal normalized on the S.W. at +2 ps.

tinuum scattering increase is subtracted (the tail of a Voigt profile is fitted to the increase in electronic scattering in the $\Delta I_S(t)$ spectra). The $\Delta I_S(t) / I_{-2\text{ps}}$ spectra are integrated over four different wavelength regions and plotted normalized to the $I_S / I_{-2\text{ps}}$ value at +2 ps. This gives the spectral weight S.W. as a function of time delay as shown in Fig. 6.6c.

The two-phonon Stokes signal has a $I_S(\omega) \propto \chi^2(\omega)[n^2(\Omega) + 1]$ dependence (cf. Eq. 6.1). Both the Raman tensor $\chi^2(\omega)$ and the population factor $[n^2(\Omega) + 1]$ transiently change upon photo-excitation as discussed above, where the population term can only increase. The tensor dynamics $\chi^2(\omega)$ thus appears to dominate the transient two-phonon response. This is also evidenced by the large redshift $\Delta\Omega \approx -2 \text{ cm}^{-1}$. The redshift is understood as a photoinduced phonon softening at the different high symmetry points in the Brillouin Zone. Extracting time-constants for the different BZ-points is not possible due the limited amount of time-delay points. However, from the $\Delta I_S(t)$ spectra in Fig. 6.6b, and the spectral weight S.W. in Fig. 6.6c, it appears that the phonon softening at the X- and L-point has a faster ingrowth than at the W- and Γ -point. This hints to dissimilar electron-phonon coupling constants for the different points. The quantitative determination of time-constants for the four BZ-points asks for a higher time-resolution. In spontaneous Raman spectroscopy this would however result in a loss of frequency resolving power, and thereby momentum-resolving power. This

would again lead to a complication in disentangling time- and momentum-resolved scattering, however now because of frequency resolution limitations. A qualitative disentanglement of momentum-dependent scattering in silicon thus forms an interesting study case for the time-resolved femtosecond stimulated Raman scattering variant.

6.3.3 Photoinduced melting of helimagnetic order in the chiral magnet Cu_2OSeO_3

The understanding of out-of-equilibrium phenomena in magnetic materials is a highly active part of condensed matter research.^[69] Recent scientific advances with a high potential towards applications include all-optical magnetization switching,^[70] and picosecond optical writing and read-out of magnetic bits.^[71] With increasingly complex magnetic phases and dynamical phenomena being studied, there is a high demand for novel all-optical probes. Magnetization dynamics in finite magnetization phases, such as ferromagnetic and ferrimagnetic order, or a more exotic phase such as the skyrmion lattice,^[72] can be probed by optical techniques which are sensitive to the order parameter \mathbf{M} which describes the (macroscopic) magnetization. Linear magneto-optical effects, for instance the Faraday or magneto-optical Kerr effect, measure a polarization rotation $\theta \propto \mathbf{M}$ proportional to the magnetization.^[73] The dynamical variant allows to detect photoinduced incoherent and coherent dynamics of the order parameter \mathbf{M} .^[52,72] All-optical detection of antiferromagnetic order dynamics already becomes more challenging. The antiferromagnetic order parameter \mathbf{L} is proportional to the difference in magnetic sublattice magnetizations; $\mathbf{L} \propto \mathbf{M}_\uparrow - \mathbf{M}_\downarrow$. Optical probing of \mathbf{L} is realized by second-order magneto-optical effects, such as magnetic linear birefringence and second harmonic generation. Ultrafast variants have been used to study photoinduced dynamics in antiferromagnets.^[74,75] For more complex net-zero magnetization order, such as cycloidal, helical, or spin wave order it is more challenging to probe the magnetic order parameter. One suggestion is tracking the thermalization of a magnon mode with THz-time-domain spectroscopy after photo-excitation, as was realized in the spin-cycloid material TbMnO_3 .^[76] The Raman-activity of a magnon mode would however permit all-optical detection, as opposed to detection through its dipole activity. Here we show that time-resolved Raman spectroscopy allows to all-optically probe melting of helimagnetic order after photo-excitation in the chiral magnet Cu_2OSeO_3 .^[77] This is realized by tracking the softening and broadening of a Raman-active magnon mode in the time-domain.

Cu_2OSeO_3 has a long-range magnetic ordering temperature of $T_N \approx 58 \text{ K}$.^[77] The magnetic ground state consists of helimagnetically aligned effective $S = 1$ spin clusters, which by itself consist of three-up-one-down $S = 1/2$ spins on the $\text{Cu}^{2+}(3d^9)$ sites.^[78,79] The spin cluster ordering results in high energy $\sim \text{meV}$ magnons, from which the magnons at the Γ -point

are observable by spontaneous Raman spectroscopy.^[80] A [111] oriented Cu_2OSeO_3 sample, at bias temperature 5 K in the helimagnetic phase was studied. The SHBC output at 512 nm, with $\Delta\nu \approx 10 \text{ cm}^{-1}$ FWHM was used as Raman probe (0.5 mW probe power at sample position). In Fig. 6.7a part of the Stokes spectrum is shown. The M-mode at $\Omega \approx 264 \text{ cm}^{-1}$ corresponds to a $\Delta S^z = +1$ magnon mode, which can be understood as a spin-flip excitation within the three-up-one-down spin cluster.^[81] The modes labeled “P” correspond to phonons, or regions of not fully resolved overlapping phonons.

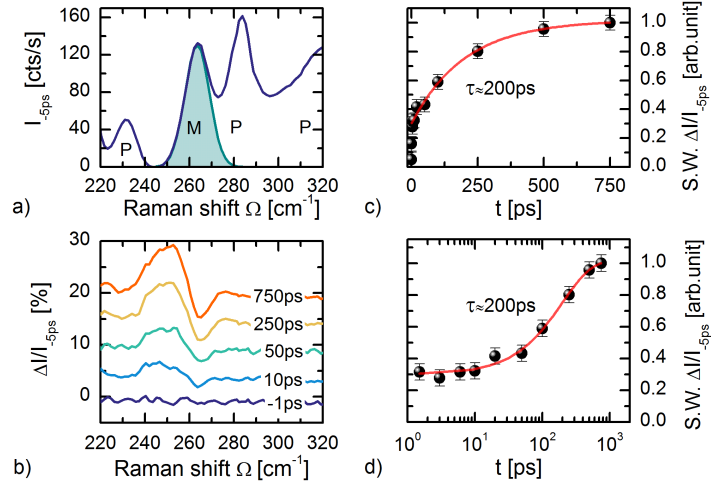


Figure 6.7: a) Part of the Raman spectrum of Cu_2OSeO_3 recorded with 512 nm pulsed probe light. The peak labeled “M” at $\Omega_M \approx 264 \text{ cm}^{-1}$ is a $\Delta S^z = +1$ spin cluster magnon. The peaks indicated by ”P” are phonons, or regions of not fully resolved phonons. b) Scaled differential Stokes spectra $\Delta I_S(t) / I_{-5ps}$ for representative delay-times. The derivative-like lineshape results from a dynamical softening and broadening of the magnon peak. c) linear and d) logarithmic scales of the spectral weight (S.W.) evolution of the ingrowing component in the $\Delta I_S(t) / I_{-5ps}$ spectra. The spectral weight transfer has a time-constant of $\tau \approx 200 \text{ ps}$.

Local crystal field excitations (see chapter 4) were excited with 0.3 ps, $\lambda = 570 \text{ nm}$ pump pulses (with 2 mW pump power, and fluence $F \approx 2 \text{ mJ/cm}^2$), after which the thermalization dynamics is measured in the transient Raman spectra. In Fig. 6.7b the scaled differential spectra $\Delta I_S(t) / I_{-5ps}$ are shown for representative time-delays, where $\Delta I_S(t) = I_S(t) - I_S(-5ps)$. A derivative-like lineshape is observed in the $\Delta I_S(t) / I_{-5ps}$ spectra, resulting from a spectral weight shift to lower Raman shift Ω for the magnon excitation. For the low temperatures, and Stokes range of interest ($\Omega = 220\text{--}320 \text{ cm}^{-1}$) the occupation number $n(\Omega, T) \ll 1$. The change in occupation thus also is $\Delta n(\Omega, T) \ll 1$. We thereby assign the spectral weight transfer to a change in the Raman tensor $\chi^2(\omega)$. This physically corresponds to a dynamic softening and broadening of the magnon excitation. From fitting of

the $\Delta S^z = +1$ peak position in the $I_S(t)$ spectra it is found that the dynamic shift $\Delta\Omega(750\text{ ps})$ at late delay times lies below 1 cm^{-1} . By comparison to the temperature dependent position we conclude that the transient magnetic temperature does not rise above 25 K. Under our pump excitation conditions the long-range magnetic order thus gets strongly perturbed, but not fully destroyed. The phonon peak shifts are too small to be resolvable in the $\Delta I_S(t) / I_{-5\text{ps}}$ spectra. The ingrowing spectral weight transfer (S.W.) of the $\Delta I_S(t) / I_{-5\text{ps}}$ signal, corresponding to the temporal evolution of the magnetic order parameter, is shown in Fig. 6.7c and d in linear and logarithmic timescales. A typical time-scale of $\tau \approx 200\text{ ps}$ for spin-lattice thermalization in insulators is observed.⁶⁹ This agrees well with the findings of Langner *et al.* where a spin-lattice thermalization time of $\tau \approx 300\text{ ps}$ was observed by means of time-resolved resonant x-ray diffraction.⁸² The slight discrepancy might originate from the different pump excitation conditions, and the different bias temperatures.

6.4 Conclusions and outlook

In this chapter a flexible and efficient ultrafast time-resolved spontaneous Raman spectroscopy setup was presented. Different conceptual time-resolved Raman studies of collective excitation and quasi-particle dynamics were discussed to illustrate the strength and capabilities of the setup. One of the strongest feats of time-resolved spontaneous Raman is the determination of transient population numbers, and effective modes temperatures through detailed balance of the anti-Stokes to Stokes intensity ratio. A less studied aspect of the dynamics is the resonance enhancement in the Raman process. This however plays a role, as we have demonstrated in the prototype test material silicon. We've shown that the photoinduced hole density leads to a quench of the Raman tensor, and in addition to an increase in electronic inelastic scattering. Dynamic changes in the electronic population and structure are of importance to photoinduced phenomena in many classes of quantum materials, such as $3d/4d/5d$ transition metal oxide materials, carbon allotropes, and transition metal dichalcogenides. Time-resolved resonant Raman can thereby provide a convenient tool to study both electronic population dynamics, as well as photoinduced changes in the electronic band structure such as band gap renormalization.

Although Raman spectroscopy is a zero-momentum transfer probe, momentum-dependent scattering can nevertheless be resolved in the higher-order Raman response. The overtone spectrum can thus serve as a momentum- and time-resolved scattering probe. As a proof of concept, we've studied photo-induced changes in the two-phonon response of silicon, and found evidence for dissimilar phonon softening rates at different high-symmetry points of the Brillouin Zone. Applying this concept to slower

phenomena, such as spin-lattice relaxation in $3d$ -antiferromagnetic materials, seems fortuitous to pursue, and possibly allows to detect momentum-dependent transient population dynamics and momentum relaxation.

Raman-active collective excitations such as magnons, charge-density wave modes, and the Cooper-pair breaking peak, can serve as a time-resolved probe for the order parameter of quantum phases. We illustrated this in the helimagnet Cu_2OSeO_3 , where the photoinduced melting of helimagnetic order can be tracked by the observation of a dynamic softening and broadening of a magnon peak. This principle can also be applied to probe dynamics of other net-zero magnetization order such as cycloidal, spin-density wave, and antiferromagnetic order. On a broader scope this can be applied to photoinduced phase transitions, where the associated change of symmetry can be derived from the transient Raman spectrum. The Raman spectrum of collective low energy excitations can additionally serve as a probe to study energy and angular momentum transfer between the lattice, electronic, orbital and magnetic degrees of freedom in quantum materials.

6.5 Own contributions and acknowledgements

The main part of this chapter is published under:

R. B. Versteeg, J. Zhu, P. Padmanabhan, C. Boguschewski, R. German, M. Goedecke, P. Becker, and P. H. M. van Loosdrecht,

A tunable time-resolved spontaneous Raman spectroscopy setup for probing ultrafast collective excitation and quasiparticle dynamics in quantum materials,

Struct. Dyn. **5**, 044301 (2018)

Reproduced from R.B. Versteeg *et al.*, Struct. Dyn. **5**, 044301 (2018), with the permission of AIP Publishing

The time-resolved Raman setup was designed by myself, Jingyi Zhu, and Paul van Loosdrecht. Me and Jingyi Zhu constructed the setup, with contributions made by Prashant Padmanabhan, Christoph Boguschewski, and Max Goedecke. The PMT/CCD comparison measurements were made by myself, with assistance from Jingyi Zhu and Max Goedecke. The one-phonon measurements were made and analysed by myself and Jingyi Zhu. The two-phonon measurements were made and analysed by myself. The Cu_2OSeO_3 spin excitation dynamics measurements were made and analysed by myself, with assistance from Jingyi Zhu. The Cu_2OSeO_3 single crystal was grown by Petra Becker. This chapter has been written by myself, with input from P. H. M. van Loosdrecht and Jingyi Zhu.

6.6 Bibliography

- [1] D. N. Basov, R. D. Averitt, and D. Hsieh, Towards properties on demand in quantum materials, *Nat. Mater.* **16**, 1077 (2017).
- [2] J. Zhang and R. D. Averitt, Dynamics and control in complex transition metal oxides, *Annu. Rev. Mater. Res.* **44**, 19 (2014).
- [3] M. Gandolfi, G. L. Celardo, F. Borgonovi, G. Ferrini, A. Avella, F. Banfi, and C. Giannetti, Emergent ultrafast phenomena in correlated oxides and heterostructures, *Phys. Scr.* **92**, 034004 (2017).
- [4] Y. H. Wang, H. Steinberg, P. Jarillo-Herrero, and N. Gedik, Observation of floquet-bloch states on the surface of a topological insulator, *Science*, **342**, 453 (2013).
- [5] A. Cavalleri, Cs. Tóth, C. W. Siders, J. A. Squier, F. Ráksi, P. Forget, and J. C. Kieffer, Femtosecond structural dynamics in VO₂ during an ultrafast solid-solid phase transition, *Phys. Rev. Lett.* **87**, 237401 (2001).
- [6] M. Rini, N. Dean, J. Itatani, Y. Tomioka, Y. Tokura, R. W. Schoenlein, and A. Cavalleri, Control of the electronic phase of a manganite by mode-selective vibrational excitation, *Nature* **449**, 72 (2007).
- [7] D. Fausti, R. I. Tobey, N. Dean, S. Kaiser, A. Dienst, M. C. Hoffmann, S. Pyon, T. Takayama, H. Takagi, and A. Cavalleri, Light-induced superconductivity in a stripe-ordered cuprate, *Science* **331**, 189 (2011).
- [8] F. Boschini, E. H. da Silva Neto, E. Razzoli, M. Zonno, S. Peli, R. P. Day, M. Michiardi, M. Schneider, B. Zwartsenberg, P. Nigge, R. D. Zhong, J. Schneeloch, G. D. Gu, S. Zhdanovich, A. K. Mills, G. Levy, D. J. Jones, C. Giannetti, and A. Damascelli, Collapse of superconductivity in cuprates via ultrafast quenching of phase coherence, *Nat. Mater.* **17**, 416 (2018).
- [9] P. Maldonado, K. Carva, M. Flammer, and P. M. Oppeneer, Theory of out-of-equilibrium ultrafast relaxation dynamics in metals, *Phys. Rev. B* **96**, 174439 (2017).
- [10] E. Turgut, D. Zusin, D. Legut, K. Carva, R. Knut, J. M. Shaw, C. Chen, Z. Tao, H. T. Nembach, T. J. Silva, S. Mathias, M. Aeschlimann, P. M. Oppeneer, H. C. Kapteyn, M. M. Murnane, and P. Grychtol, Stoner versus Heisenberg: Ultrafast exchange reduction and magnon generation during laser-induced demagnetization, *Phys. Rev. B* **94**, 220408 (2016).
- [11] B. Mansart, J. Lorenzana, A. Mann, A. Odeh, M. Scarongella, M. Chergui, and F. Carbone, Coupling of a high-energy excitation to superconducting quasiparticles in a cuprate from coherent charge fluctuation spectroscopy, *Proc. Natl. Acad. Sci. USA* **110**, 4539 (2013).
- [12] A. Mann, E. Baldini, A. Tramontana, E. Pomjakushina, K. Conder, C. Arrell, F. van Mourik, J. Lorenzana, and F. Carbone. Probing the electron-phonon interaction in correlated systems with coherent lattice fluctuation spectroscopy, *Phys. Rev. B* **92**, 035147 (2015).
- [13] J. A. Sobota, S. Yang, J. G. Analytis, Y. L. Chen, I. R. Fisher, P. S. Kirchmann, and Z.-X. Shen, Ultrafast optical excitation of a persistent surface-state population in the topological insulator Bi₂Se₃, *Phys. Rev. Lett.* **108**, 117403 (2012).
- [14] P. Abbamonte, Condensed-matter physics: Picking up fine vibrations, *Nat. Phys.* **9**, 759 (2013).
- [15] M. Trigo, M. Fuchs, J. Chen, M. P. Jiang, M. Cammarata, S. Fahy, D. M. Fritz, K. Gaffney, S. Ghimire, A. Higginbotham, S. L. Johnson, M. E. Kozina, J. Larsson, H. Lemke, A. M. Lindenberg, G. Ndabashimiye, F. Quirin, K. Sokolowski-Tinten,

- C. Uher, G. Wang, J. S. Wark, D. Zhu, and D. A. Reis, Fourier-transform inelastic x-ray scattering from time- and momentum-dependent phonon-phonon correlations, *Nat. Phys.* **9**, 790 (2013).
- [16] M. P. M. Dean, Y. Cao, X. Liu, S. Wall, D. Zhu, R. Mankowsky, V. Thampy, X. M. Chen, J. G. Vale, D. Casa, J. Kim, A. H. Said, P. Juhas, R. Alonso-Mori, J. M. Glowina, A. Robert, J. Robinson, M. Sikorski, S. Song, M. Kozina, H. Lemke, L. Patthey, S. Owada, T. Katayama, M. Yabashi, Y. Tanaka, T. Togashi, J. Liu, C. Rayan Serrao, B. J. Kim, L. Huber, C.-L. Chang, D. F. McMorrow, M. Först, and J. P. Hill, Ultrafast energy- and momentum-resolved dynamics of magnetic correlations in the photo-doped Mott insulator Sr_2IrO_4 , *Nat. Mater.* **15**, 601 (2016).
- [17] F. Carbone, B. Barwick, O.-H. Kwon, H. Soon Park, J. Spencer Baskin, and A. H. Zewail, EELS femtosecond resolved in 4D ultrafast electron microscopy, *Chem. Phys. Lett.* **468**, 107 (2009).
- [18] L. Piazza, C. Ma, H. X. Yang, A. Mann, Y. Zhu, J. Q. Li, and F. Carbone, Ultrafast structural and electronic dynamics of the metallic phase in a layered manganite, *Struct. Dyn.* **1**, 014501 (2014).
- [19] K. Iwata, S. Yamaguchi, and H. Hamaguchi, Construction of a transform-limited picosecond time-resolved Raman spectrometer, *Rev. Sci. Instrum.* **64**, 2140 (1993).
- [20] H. Hamaguchi and T. L. Gustafson, Ultrafast time-resolved spontaneous and coherent Raman spectroscopy: the structure and dynamics of photogenerated transient species, *Annu. Rev. Phys. Chem.* **45**, 593 (1994).
- [21] Y. Uesugi, Y. Mizutani, and T. Kitagawa, Developments of widely tunable light sources for picosecond time-resolved resonance Raman spectroscopy, *Rev. Sci. Instrum.* **68**, 4001 (1997).
- [22] S. K. Sahoo, S. Umaphathy, and A. W. Parker, Time-resolved resonance Raman spectroscopy: Exploring reactive intermediates, *Appl. Spectrosc.* **65**, 1087 (2011).
- [23] S. G. Kruglik, J.-C. Lambry, J.-L. Martin, M. H. Vos, and M. Negre, Subpicosecond Raman spectrometer for time-resolved studies of structural dynamics in heme proteins, *J. Raman Spectrosc.* **42**, 265 (2011).
- [24] J. A. Kash, J. C. Tsang, and J. M. Hvam, Subpicosecond time-resolved Raman spectroscopy of LO phonons in GaAs, *Phys. Rev. Lett.* **54**, 2151 (1985).
- [25] D. Y. Oberli, D. R. Wake, M. V. Klein, J. Klem, T. Henderson, and H. Morkoç, Time-resolved Raman scattering in GaAs quantum wells, *Phys. Rev. Lett.* **59**, 696 (1987).
- [26] D. Song, F. Wang, G. Dukovic, M. Zheng, E. D. Semke, L. E. Brus, and T. F. Heinz, Direct measurement of the lifetime of optical phonons in single-walled carbon nanotubes, *Phys. Rev. Lett.* **100**, 225503 (2008).
- [27] H. Yan, D. Song, K. F. Mak, I. Chatzakis, J. Maultzsch, and T. F. Heinz, Time-resolved Raman spectroscopy of optical phonons in graphite: Phonon anharmonic coupling and anomalous stiffening, *Phys. Rev. B* **80**, 121403 (2009).
- [28] K. Kang, D. Abdula, D. G. Cahill, and M. Shim, Lifetimes of optical phonons in graphene and graphite by time-resolved incoherent anti-Stokes Raman scattering, *Phys. Rev. B* **81**, 165405 (2010).
- [29] J.-A. Yang, S. Parham, D. Dessau, and D. Reznik, Novel electron-phonon relaxation pathway in graphite revealed by time-resolved Raman scattering and angle-resolved photoemission spectroscopy, *Sci. Rep.* **7**, 40876 (2017).
- [30] D. Fausti and P. H. M. van Loosdrecht, in Chapter 14: *Time-resolved Raman scattering of Optical Techniques for Solid-State Materials Characterization*, edited by

- R. P. Prasankumar and A. J. Taylor, (CRC Press, Boca Raton London New York, 2012).
- [31] A. Compaan and H. J. Trodahl, Resonance Raman scattering in Si at elevated temperatures, *Phys. Rev. B* **29**, 793 (1984).
- [32] L. Waldecker, R. Bertoni, R. Ernstorfer, and J. Vorberger, Electron-phonon coupling and energy flow in a simple metal beyond the two-temperature approximation, *Phys. Rev. X* **6**, 021003 (2016).
- [33] O. V. Misochko, M. Hase, K. Ishioka, and M. Kitajima, Observation of an amplitude collapse and revival of chirped coherent phonons in bismuth, *Phys. Rev. Lett.* **92**, 197401 (2004).
- [34] D. Fausti, O. V. Misochko, and P. H. M. van Loosdrecht, Ultrafast photoinduced structure phase transition in antimony single crystals, *Phys. Rev. B* **80**, 161207 (2009).
- [35] R. P. Saichu, I. Mahns, A. Goos, S. Binder, P. May, S. G. Singer, B. Schulz, A. Rusydi, J. Unterhinninghofen, D. Manske, P. Guptasarma, M. S. Williamsen, and M. Rübhausen, Two-component dynamics of the order parameter of high temperature $\text{Bi}_2\text{Sr}_2\text{CaCu}_2\text{O}_{8+\delta}$ superconductors revealed by time-resolved Raman scattering, *Phys. Rev. Lett.* **102**, 177004 (2009).
- [36] D. N. Basov, R. D. Averitt, D. van der Marel, M. Dressel, and K. Haule, Electrodynamics of correlated electron materials, *Rev. Mod. Phys.* **83**, 471 (2011).
- [37] P. Kukura, D. W. McCamant, and R. A. Mathies, Femtosecond stimulated Raman spectroscopy, *Annu. Rev. Phys. Chem.* **58**, 461 (2007).
- [38] G. Batignani, D. Bossini, N. Di Palo, C. Ferrante, E. Pontecorvo, G. Cerullo, A. Kimel, and T. Scopigno, Probing ultrafast photo-induced dynamics of the exchange energy in a Heisenberg antiferromagnet, *Nat. Photon.* **9**, 506 (2015).
- [39] U. Harbola, S. Umaphathy, and S. Mukamel, Loss and gain signals in broadband stimulated-Raman spectra: Theoretical analysis. *Phys. Rev. A* **88**, 011801 (2013).
- [40] K. T. Tsen, J. G. Kiang, D. K. Ferry, and H. Morkoç, Subpicosecond time-resolved Raman studies of LO phonons in GaN: Dependence on photoexcited carrier density, *Appl. Phys. Lett.* **89**, 112111 (2006).
- [41] P. A. Fleury and R. Loudon, Scattering of light by one- and two-magnon excitations, *Phys. Rev.* **166**, 514 (1968).
- [42] P. Rovillain, J. Liu, M. Cazayous, Y. Gallais, M-A. Measson, H. Sakata, and A. Sacuto, Electromagnon and phonon excitations in multiferroic TbMnO_3 , *Phys. Rev. B* **86**, 014437 (2012).
- [43] S. Sugai, Y. Takayanagi, and N. Hayamizu, Phason and amplitudon in the charge-density-wave phase of one-dimensional charge stripes in $\text{La}_{2-x}\text{Sr}_x\text{CuO}_4$, *Phys. Rev. Lett.* **96**, 137003 (2006).
- [44] T. Shigenari, *Raman spectra of soft modes in ferroelectric crystals in Ferroelectric Materials-Synthesis and Characterization*, edited by A. Peláiz-Barranco, (InTech, 2015)
- [45] F. Raoult, A. C. L. Boscheron, D. Husson, C. Sauteret, A. Modena, V. Malka, F. Dorchies, and A. Migus, Efficient generation of narrow-bandwidth picosecond pulses by frequency doubling of femtosecond chirped pulses, *Opt. Lett.* **23**, 1117 (1998).
- [46] H. Kawashima, M. M. Wefers, and K. A. Nelson, Femtosecond pulse shaping, multiple-pulse spectroscopy, and optical control, *Annu. Rev. Phys. Chem.* **46**, 627 (1995).

- [47] C. A. Palmer and E. G. Loewen, *Diffraction grating handbook*, 7th edition, (Newport Corporation, New York, 2014).
- [48] J. M. Lerner, Imaging spectrometer fundamentals for researchers in the biosciences: a tutorial, *Cytometry Part A* **69A**, 712 (2006).
- [49] K. P. J. Williams, G. D. Pitt, D. N. Batchelder, and B. J. Kip, Confocal Raman microspectroscopy using a stigmatic spectrograph and CCD detector, *Appl. Spectrosc.* **48**, 232 (1994).
- [50] D. J. Hilton, in Chapter 9: *Ultrafast pump-probe spectroscopy of Optical Techniques for Solid-State Materials Characterization*, edited by R. P. Prasankumar and A. J. Taylor, (CRC Press, Boca Raton London New York, 2012).
- [51] R. D. Averitt, A. I. Lobad, C. Kwon, S. A. Trugman, V. K. Thorsmølle, and A. J. Taylor, Ultrafast conductivity dynamics in colossal magnetoresistance manganites, *Phys. Rev. Lett.* **87**, 017401 (2001).
- [52] T. Ogasawara, K. Ohgushi, Y. Tomioka, K. S. Takahashi, H. Okamoto, M. Kawasaki, and Y. Tokura, General features of photoinduced spin dynamics in ferromagnetic and ferrimagnetic compounds, *Phys. Rev. Lett.* **94**, 087202 (2005).
- [53] A. C Ferrari and D. M. Basko, Raman spectroscopy as a versatile tool for studying the properties of graphene, *Nat. Nanotech* **8**, 235 (2013).
- [54] J.-U. Lee and H. Cheong, Resonance Raman effects in transition metal dichalcogenides, *J. Raman Spectrosc.* **49**, 66 (2018).
- [55] T. R. Hart, R. L. Aggarwal, and B. Lax, Temperature dependence of Raman scattering in silicon, *Phys. Rev. B* **1**, 638 (1970).
- [56] F. Cerdeira, T. A. Fjeldly, and M. Cardona, Effect of free carriers on zone-center vibrational modes in heavily doped *p*-type Si. II. optical modes, *Phys. Rev. B* **8**, 4734 (1973).
- [57] Pump-probe reflectivity measurements under similar conditions show that the optical properties change less than 0.2%.
- [58] P. G. Klemens, Anharmonic decay of optical phonons, *Phys. Rev.* **148**, 845 (1966).
- [59] Y. Gillet, M. Giantomassi, and X. Gonze, First-principles study of excitonic effects in Raman intensities, *Phys. Rev. B* **88**, 094305 (2013).
- [60] D. Sangalli, S. Dal Conte, C. Manzoni, G. Cerullo, and A. Marini, Nonequilibrium optical properties in semiconductors from first principles: A combined theoretical and experimental study of bulk silicon, *Phys. Rev. B* **93**, 195205 (2016).
- [61] J. L. Birman and V. M. Agranovich, *Theory of Light Scattering in Condensed Matter*, (Plenum Press, New York, 1975).
- [62] N. Tandon, J. D. Albrecht, and L. R. Ram-Mohan, Electron-phonon interaction and scattering in Si and Ge: Implications for phonon engineering, *J. Appl. Phys.* **118**, 045713 (2015).
- [63] S. L. Johnson, M. Savoini, P. Beaud, G. Ingold, U. Staub, F. Carbone, L. Castiglioni, M. Hengsberger, and J. Osterwalder, Watching ultrafast responses of structure and magnetism in condensed matter with momentum-resolved probes, *Struct. Dyn.* **4**, 061506 (2017).
- [64] M. Cardona, in Chapter 1 of *Light Scattering in Solids*, edited by M. Cardona, (Springer-Verlag, Berlin Heidelberg New York, 1975).
- [65] F. A. Johnson and R. Loudon, Critical-point analysis of the phonon spectra of diamond, silicon and germanium, *Proc. R. Soc. London, Ser. A* **281**, 274 (1964).

- [66] D. J. Lockwood and M. G. Cottam, Light scattering from magnons in MnF_2 , *Phys. Rev. B* **35**, 1973 (1987).
- [67] P. A. Temple and C. E. Hathaway, Multiphonon Raman spectrum of silicon, *Phys. Rev. B* **7**, 3685 (1973).
- [68] Y. Gillet, S. Kontur, M. Giantomassi, C. Draxl, and X. Gonze, Ab initio approach to second-order resonant Raman scattering including exciton-phonon interaction, *Sci. Rep.* **7**, 7344 (2017).
- [69] A. Kirilyuk, A. V. Kimel, and T. Rasing, Ultrafast optical manipulation of magnetic order, *Rev. Mod. Phys.* **82**, 2731 (2010).
- [70] M. Savoini, R. Medapalli, B. Koene, A. R. Khorsand, L. Le Guyader, L. Duò, M. Finazzi, A. Tsukamoto, A. Itoh, F. Nolting, A. Kirilyuk, A. V. Kimel, and T. Rasing, Highly efficient all-optical switching of magnetization in GdFeCo microstructures by interference-enhanced absorption of light, *Phys. Rev. B* **86**, 140404 (2012).
- [71] A. Stupakiewicz, K. Szerenos, D. Afanasiev, A. Kirilyuk, and A. V. Kimel, Ultrafast nonthermal photo-magnetic recording in a transparent medium, *Nature* **542**, 71 (2017).
- [72] N. Ogawa, S. Seki, and Y. Tokura, Ultrafast optical excitation of magnetic skyrmions, *Sci. Rep.* **5**, 9552 (2015).
- [73] P. S. Pershan, Magneto-Optical Effects, *J. Appl. Phys.* **38**, 1482 (1967).
- [74] D. Bossini, A. M. Kalashnikova, R. V. Pisarev, T. Rasing, and A. V. Kimel, Controlling coherent and incoherent spin dynamics by steering the photoinduced energy flow, *Phys. Rev. B* **89**, 060405 (2014).
- [75] M. Fiebig, N. P. Duong, T. Satoh, B. B. van Aken, K. Miyano, Y. Tomioka, and Y. Tokura, Ultrafast magnetization dynamics of antiferromagnetic compounds, *J. Phys. D* **41**, 164005 (2008).
- [76] P. Bowlan, S. A. Trugman, X. Wang, Y. M. Dai, S.-W. Cheong, E. D. Bauer, A. J. Taylor, D. A. Yarotski, and R. P. Prasankumar, Directly probing spin dynamics in insulating antiferromagnets using ultrashort terahertz pulses, *Phys. Rev. B* **94**, 184429 (2016).
- [77] S. Seki, X. Z. Yu, S. Ishiwata, and Y. Tokura, Observation of skyrmions in a multiferroic material, *Science* **336**, 198 (2012).
- [78] O. Janson, I. Rousochatzakis, A. A. Tsirlin, M. Belesi, A. A. Leonov, U. K. Rößler, J. Van den Brink, and H. Rosner, The quantum nature of skyrmions and half-skyrmions in Cu_2OSeO_3 , *Nat. Commun.* **5**, 5376 (2014).
- [79] M. Ozerov, J. Romhányi, M. Belesi, H. Berger, J.-Ph. Ansermet, Jeroen van den Brink, J. Wosnitza, S. A. Zvyagin, and I. Rousochatzakis, Establishing the fundamental magnetic interactions in the chiral skyrmionic Mott insulator Cu_2OSeO_3 by terahertz electron spin resonance, *Phys. Rev. Lett.* **113**, 157205 (2014).
- [80] V. P. Gnezdilov, K. V. Lamonova, Y. G. Pashkevich, P. Lemmens, H. Berger, F. Bussy, and S. L. Gnatchenko, Magnetoelectricity in the ferrimagnetic Cu_2OSeO_3 : symmetry analysis and Raman scattering study, *Low Temp. Phys.* **36**, 550 (2010).
- [81] J. Romhányi, J. van den Brink, and I. Rousochatzakis, Entangled tetrahedron ground state and excitations of the magnetoelectric skyrmion material Cu_2OSeO_3 , *Phys. Rev. B* **90**, 140404 (2014).
- [82] M. C. Langner, S. Roy, S. W. Huang, J. D. Koralek, Y.-D. Chuang, G. L. Dakovski, J. J. Turner, J. S. Robinson, R. N. Coffee, M. P. Minitti, S. Seki, Y. Tokura, and R. W. Schoenlein, Nonlinear ultrafast spin scattering in the skyrmion phase of Cu_2OSeO_3 , *Phys. Rev. Lett.* **119**, 107204 (2017).

Chapter 7

Dynamical resonance quench and Fano interference in spontaneous Raman scattering from quasiparticle and collective excitations

7.1 Introduction

A quantum-mechanical description of the nature and transport properties of the various quasiparticles and collective excitations in semiconductors is integral to characterizing the physical properties of a wide array of technologically relevant materials.^[1,2] Hot carrier and phonon relaxation dynamics in semiconductors,^[3,4] for example, plays a central role in our understanding of carrier transport and energy dissipation in electronic and optoelectronic devices. As such, an accurate interpretation of the quasiparticle and collective excitation interactions and dynamics is vital not only from a fundamental perspective, but also to enable new applications.

Over the past four decades, a range of ultrafast spectroscopic probes have provided us insight into carrier and phonon relaxation dynamics and their respective time-scales in semiconductors.^[4,5] These measurements often rely on the coherent excitation of phonons, of which the dynamics is consecutively probed in the modulation of the refractive index.^[6-8] A more direct view of phonon dynamics is provided by time-resolved inelastic scattering techniques.^[9-12] This has the advantage over coherent excitation techniques that one can follow the true time evolution of a photoexcited material through its incoherent response, rather than the time evolution of coherent excitations.

Time-resolved spontaneous Raman scattering is a reasonably well-established probe for incoherent phonon population dynamics in semiconductors,^[11,13,18] and vibrational dynamics in molecules.^[11,19-25] More recently the technique has been applied to study phonon dynamics in a range of carbon allotropes.^[11,26-32] Through detailed balance of the anti-Stokes I_{AS} to Stokes I_S scattering intensity ratio the (phonon) population number n can be directly quantified by $I_{AS}/I_S \propto n/(n+1)$. This relation stems from the fluctuation dissipation theorem,^[33] which on ultrafast timescales (\ll ps) may lose its validity due to the presence of truly non-thermal occupation statistics. The inelastic light scattering selection rules $|\hat{E}_S \cdot \chi_A'' \cdot \hat{E}_I|^2$ for incoming electric field \hat{E}_I and scattered field \hat{E}_S entail the symmetry A of the Raman-scattering channel χ_A'' .^[34] This may be used to probe symmetry changes across a photoinduced phase transition, as was demonstrated for a high-to-low structural symmetry transition in antimony,^[35] and melting of the superconducting condensate in a high-temperature cuprate superconductor.^[36] Two largely unexplored aspects to time-resolved spontaneous Raman are the role of the Raman resonance enhancement in the time-domain,^[32] and the dynamic interaction between quasiparticle and collective excitation scattering, with the latter interaction leading to a Fano interference. Here we demonstrate a photo-induced resonance quench, and Fano-interference in the transient phononic and electronic spontaneous Raman response of an intrinsic indirect band gap semiconductor.

7.2 Experimental details

An intrinsic (100) oriented silicon sample (resistivity $>10000 \Omega \cdot \text{cm}$) was used for the experiments. Time-resolved Raman scattering experiments were performed using a 740 nm optical pump pulse with a temporal width of 0.3 ps. The transient Raman spectra are recorded in a backscattering geometry using a 512 nm, 1.5 ps probe pulse.^[12] The polarization of both the pump and probe beams were aligned with the [110] crystallographic direction of the sample and the cross polarized scattered light was measured.

7.3 Results and discussion

The steady-state Raman spectrum of silicon is well-known, the main features being the optical phonon peak centered at $\pm 520 \text{ cm}^{-1}$, and, in p -doped silicon, a broad and relatively weak electronic continuum extending to several hundred cm^{-1} . This feature is attributed to inter-valence band Raman scattering between the uppermost heavy- and light-hole valence bands.^[37-39] Coupling of the optical phonon to this continuum leads to a pronounced Fano asymmetry of the optical phonon Raman response.^[40]

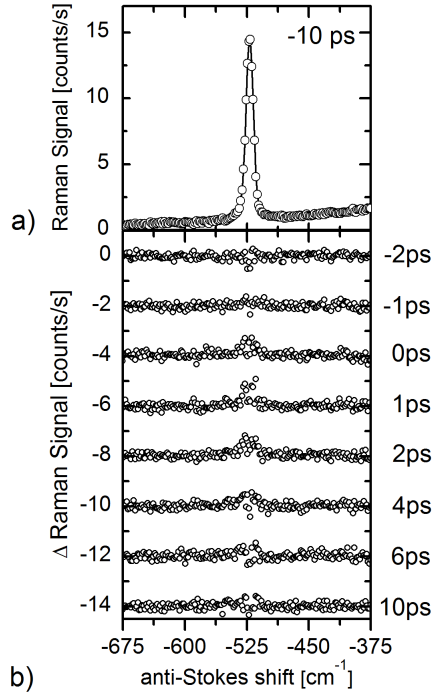


Figure 7.1: Time-resolved spontaneous silicon anti-Stokes Raman spectra recorded at a carrier density of $\sim 1.8 \times 10^{18} \text{ cm}^{-3}$. a) Anti-Stokes spectrum before optical excitation. b) Difference spectra obtained by subtracting the -10 ps spectrum from the spectra at indicated delays.

Figure 7.1 shows the transient (differential) anti-Stokes Raman spectra of silicon with a photoexcited carrier density of around $\sim 1.8 \times 10^{18} \text{ cm}^{-3}$ measured at various pump-probe delay times.⁴¹ For this relatively low transient carrier density, one observes a fast increase of the intensity near the optical phonon response at -520 cm^{-1} which subsequently decreases with time until it vanishes after 6-10 ps. This corresponds to the expected creation of an optical phonon population through the electron-phonon interaction, which subsequently decays on a ps timescale through anharmonic coupling with acoustic phonons.^{26,27,29,30,42}

However, this simple picture is incomplete, as demonstrated in Fig. 7.2 at higher excited carrier density ($\sim 1.8 \times 10^{19} \text{ cm}^{-3}$) from both anti-Stokes (left panels) and Stokes (right panel) difference Raman spectra. Particularly striking is the non-trivial substructure and the notable asymmetry between the Stokes and anti-Stokes spectra. At early delay times (1-2 ps) the anti-Stokes difference spectra show a positive response near the phonon frequency, with slight negative difference signal in the middle, while a negative difference signal dominates on the Stokes side. For longer time delays, the negative signal on both sides gains strength until the Stokes and anti-Stokes

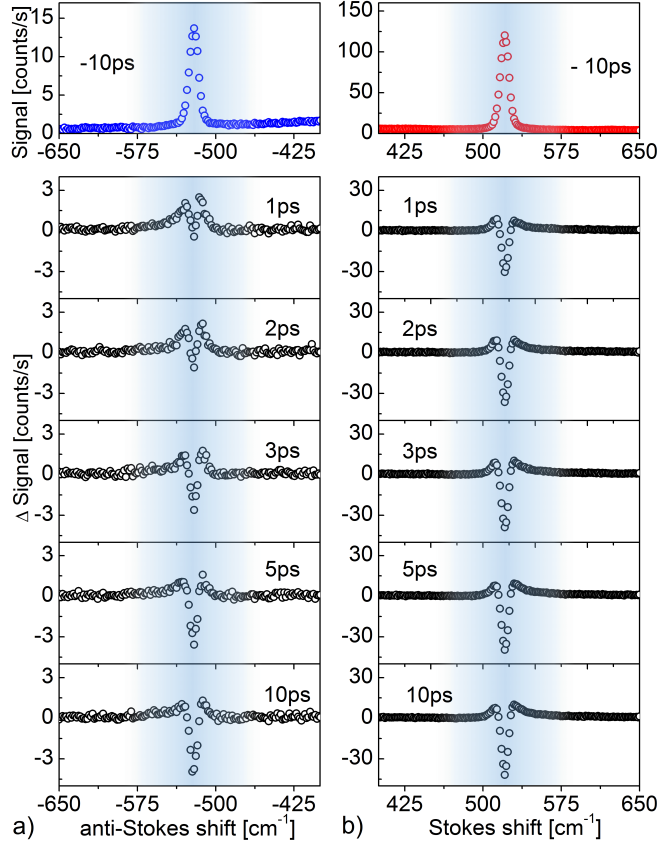


Figure 7.2: Lower panels: Time-resolved spontaneous silicon Raman difference spectra recorded at a carrier density of $\sim 1.8 \times 10^{19} \text{ cm}^{-3}$ for anti-Stokes (a) and Stokes (b) scattering. These spectra are obtained by subtracting the spectra recorded for -10 ps delay (top panels) from the spectra recorded at positive pump-probe delays.

signals become symmetric with a negative component in the middle and positive shoulders on the sides at $\sim 10 \text{ ps}$. The negative phonon difference signal persists for several nanoseconds, which is on the order of the carrier population lifetime. These spectral features originate from mixed effects of the optically induced phonon and hole populations, spectral broadening, and a Fano interference with the hole continuum.⁴⁰ We first focus on the observed changes in the overall signal intensity.

The spectra from Fig. 2 were integrated over the optical phonon contribution (460 cm^{-1} to 580 cm^{-1}) and corrected by subtracting the increasing electronic background.⁴³ The resulting relaxation dynamics are shown in Fig. 7.3a. The Stokes signal shows an immediate decrease in the scattering intensity after optical excitation. In contrast, the anti-Stokes signal first shows a rapid increase of scattering intensity which decreases only at later

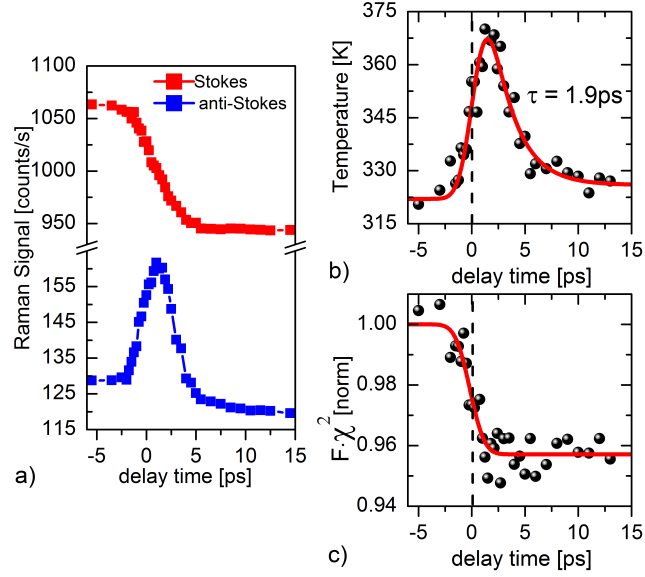


Figure 7.3: Relaxation dynamics of phonon equivalent temperature and Raman scattering strength at a carrier density of $\sim 1.8 \times 10^{19} \text{ cm}^{-3}$. (a) Decay of the optical phonon intensity for Stokes scattering (red squares) and anti-Stokes scattering (blue squares). (b) Extracted phonon temperature evolution. (c) Time-evolution of the Raman scattering strength $F \cdot \chi^2$.

time delays. To understand this behavior, we note that the Raman signal for a specific phonon mode is determined by the population n_p , the Raman tensor square χ^2 , and the related optical coefficient function F . It can be expressed³²⁴ as

$$I_S = C \cdot F_S \cdot \omega_S^3 \cdot \chi_S^2 \cdot (1 + n_p) \quad (7.1)$$

and

$$I_{AS} = C \cdot F_{AS} \cdot \omega_{AS}^3 \cdot \chi_{AS}^2 \cdot n_p \quad (7.2)$$

for the Stokes and anti-Stokes response, respectively. The factor C includes the factors which are equal for both sides, such as the excitation laser energy dependence and the excitation being scattered from (*i.e.* the phonon frequency). The optical coefficient function F can be written as

$$F_S = \frac{\mathcal{T}_S}{(\alpha_L + \alpha_S) \cdot \eta_S} \quad (7.3)$$

and

$$F_{AS} = \frac{\mathcal{T}_{AS}}{(\alpha_L + \alpha_{AS}) \cdot \eta_{AS}} \quad (7.4)$$

for Stokes and anti-Stokes scattering, respectively. Here \mathcal{T} , α and η are the transmission coefficient, absorption coefficient and refractive index at the corresponding photon energies. These optical constants and the Raman tensor are strongly resonance dependent, and usually depend on temperature, which complicates the determination of phonon population based on the above formula. However, as demonstrated in Ref. [34](#), these correction factors are close to unity well below the resonance energy (3.45 eV). As such, the following relation holds:

$$F_S \cdot \chi_S^2 \approx F_{AS} \cdot \chi_{AS}^2 \equiv F \cdot \chi^2 \quad (7.5)$$

Using this relation and formula (1) and (2), one can now determine the phonon population and the phonon temperature from the experimental data. The resulting phonon temperature and the scattering strength $F \cdot \chi^2$ are plotted in Fig. [7.3b](#) and [7.3c](#). Before time zero, the phonon temperature is ~ 320 K, showing an average heating above room temperature. Upon excitation, the phonon temperature rapidly increases to ~ 370 K after which it decays close to the average value within a few picoseconds. An exponential fit gives a lifetime of approximately 1.9 ps (solid line in Fig. [7.3b](#)), consistent with the expected decay dynamics of optical phonons into acoustic phonons.[13,17,29,42](#)

More surprising is the rapid decrease of about 5% in the scattering strength $F \cdot \chi^2$ upon excitation. A convolution of a step function and a Gaussian with half width of our setup resolution fits well (solid line in Fig. [7.3e](#)) to the curve. Apparently, the reduction of the scattering strength can either originate from changes in the optical coefficient function F (which is dictated by the optical constants), or from the Raman tensor square χ^2 immediately after photoexcitation. Generally, the change of optical constants upon excitation are small. To confirm this, we performed a reflectivity measurement with identical excitation conditions, which shows that the changes of reflectivity upon excitation is less than 0.2%, (Fig. [7.7](#) in the appendix). This small change in reflectivity, indicating a negligible change of the refractive index and thus the other derived optical constants, is not sufficient to explain the observed large change in scattering strength $F \cdot \chi^2$.

A more likely scenario for the observed decrease in scattering strength $F \cdot \chi^2$ arises from the resonant nature of the Raman scattering in silicon at the Raman probe excitation energies used in this study. The scattering is resonant to vertical transitions from the topmost valence band to the lowest conduction band in the $\Gamma - L$ direction in the Brillouin zone, and is thereby proportional to charge population.[44](#) In addition to this, excitonic effects are thought to play a role as well.[45](#) The pump laser pulse optically induces a hole density in the valence band, as evidenced by the observed changes in the hole continuum scattering (Fig. [7.4d](#)).[43](#) The optically induced charge density could lead to changes in the excitonic effects on the Raman resonance

discussed in Ref. [45], which would lead to a strongly probe pulse energy dependent change in χ^2 . However, our experiments show that the optically induced changes in the Raman spectra do not depend on probe energy within our experimental accuracy (see appendix). Excitonic effects therefore do not appear to play a large role in the tensor quench. Obviously the resonant enhancement also strongly depends on the number of available initial and final states. Here, in particular the hole population in the vicinity of the Γ -point is of interest. [44] Recent quantum theoretical work on silicon has shown that a few percent of the valence band states will be unoccupied at a photoexcitation density of $\sim 10^{19} \text{ cm}^{-3}$, (Ref. [46]) which would lead to a reduction of χ^2 of about 5-10% (Ref. [32]). This is in good agreement with our observations, and we hence attribute the transient reduction of the Raman resonance to the photoinduced hole density.

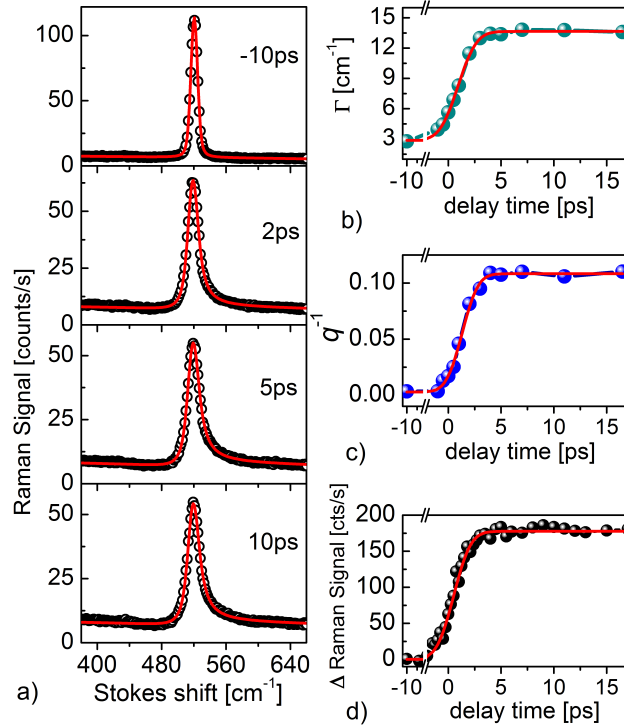


Figure 7.4: Transient Fano interference and hole population dynamics at a photoinduced density of $\sim 4.3 \times 10^{19} \text{ cm}^{-3}$. (a) Time dependent Raman spectra (circles) and Fano-fits (red lines). (b) Fitted line-width parameter Γ . (c) Fitted inverse Fano parameter q^{-1} . (d) Hole scattering dynamics integrated in the spectral range from 650 cm^{-1} to 750 cm^{-1} .

We now turn to the line shape of the phonon response, and hole dynamics. Fano interference between the optical phonon and the electronic hole continuum in *p*-doped silicon is expected to be weak for the 512 nm probe wavelength.³⁷⁻³⁹ However, at higher excitation densities, the changes in the Fano interference induced by the optical excitation are observable,⁴⁰ as can be seen in Fig. 7.4a, which shows the transient Raman Stokes spectra (circles) at an excitation density of $\sim 4.3 \times 10^{19} \text{ cm}^{-3}$ for various time delays. Generally the Fano line-shape can be described by

$$I \propto \frac{(q + \epsilon)^2}{1 + \epsilon^2} \quad (7.6)$$

where q is the so-called Fano parameter which is inversely proportional to the spectral density of the electronic continuum, and $\epsilon = 2(\omega - \omega_0)/\Gamma$ with ω_0 the bare phonon frequency, and Γ the line width parameter, which apart from the bare phonon part, has a contribution due to the Fano interference proportional to the spectral density of the electronic continuum.⁴⁷ The transient behavior of the inverse Fano parameter q^{-1} and the line-width Γ obtained from fits (solid lines in Fig. 7.4a) are depicted in Fig. 7.4b and 7.4c. Before time zero, the Raman peak resembles a Lorentzian line shape ($q^{-1} \approx 0.003$), whereas after photoexcitation the line-shape shows a pronounced Fano asymmetry ($q^{-1} \approx 0.11$). As expected, a nearly stepwise time scale of the initial response of both Γ and q^{-1} were observed, which are identical to the electronic continuum dynamics (Fig. 7.4d). Since these parameters are all governed by the dynamics of the optically induced long-lived holes, no decay of these induced effects is observed within the measured time window. Finally, we note the values of the Fano parameters in our pump-probe experiments of pure silicon are consistent with results obtained from steady-state Raman scattering silicon for similar hole-doping levels (see appendix).

7.4 Conclusions

In summary, time-resolved spontaneous Raman scattering experiments on an intrinsic semiconductor show a prominent dynamic asymmetry between both the intensity and line-shape of the phononic Stokes and anti-Stokes responses. These asymmetries originate from the interplay between the transient phonon population dynamics, a quench of the phonon Raman resonance due to a photoinduced hole population, and an enhanced Fano interference due to the same hole population, in line with simple expectations. The present results provide a deeper understanding of the spontaneous Raman-scattering response of semiconductors to strong optical excitation, and expand the use of time-resolved spontaneous Raman scattering in the study of collective excitation and quasiparticle dynamics in solid state

materials.

7.5 Appendix

7.5.1 Carrier density calibration by laser parameters and Fano interference

The carrier density Δn created by the laser excitation can be estimated by:

$$\Delta n = \frac{(1 - R)E_{\text{pulse}}}{\pi r^2 \delta h \nu} \quad (7.7)$$

where R is the reflectivity of silicon ($R \sim 0.35$ at 740 nm), E_{pulse} is the pulse energy, δ is the optical penetration depth ($\delta \sim 6.7 \cdot 10^{-4} \text{ cm}^{-1}$ at $\lambda = 740 \text{ nm}$). r is the pump spot radius, which is measured to be $\approx 20 \mu\text{m}$. h is the Planck constant and ν is the pump photon frequency. With these parameters the excited carrier density is estimated to be $1.2 \times 10^{19} \text{ cm}^{-3}$ for an excitation pulse energy of 40 nJ at $\lambda = 740 \text{ nm}$. We use this value to linearly calibrate carrier densities generated at different excitation laser energies.

Fano interference on absorption line shapes was discussed in Fano's earlier publications.^[48,49] Similar discrete and continuum states interference was also observed in steady-state Raman scattering of heavily doped silicon,^[37-39] and was interpreted as interference between electronic and phonon transitions. The observed Fano interference in the phonon scattering is strongly influenced by the Raman probe wavelength and chemically doped carrier densities. In our study we observed a photoinduced Fano effect.

Figure 7.5 shows the Fano parameter q after photoexcitation ($t = 10 \text{ ps}$) versus the photoinduced carrier density estimated by using Eq. 7.7. The values are compared to Fano parameters of chemically doped silicon.^[38,50] As shown in Fig. 7.5a, the q parameters fall within the same carrier density region as those observed from steady-state Raman measurements on chemically doped silicon. This indicates that the photoinduced carrier density in pure silicon has a similar effect as in the case of chemical doping. The optically induced Fano interference can thus also be used as a calibration of carrier density generated by laser pulses. In addition, as indicated in Fig. 7.5b, the value of q^{-1} is linearly proportional to the photoinduced hole density.

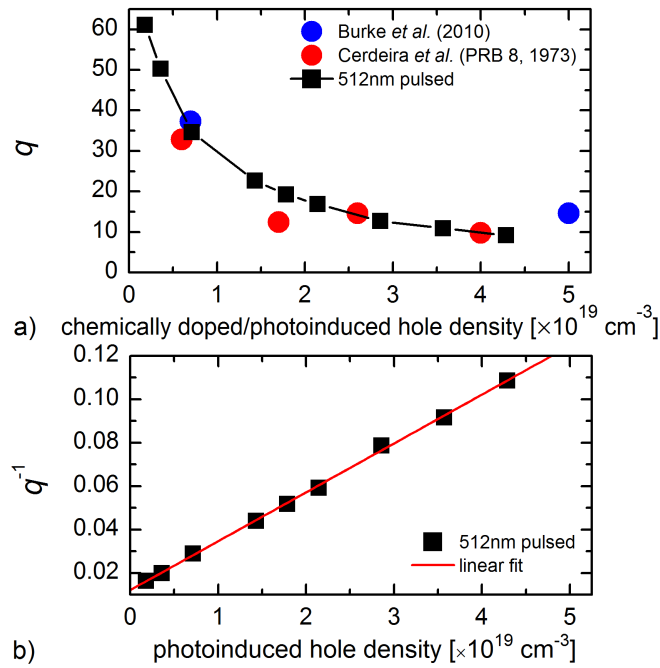


Figure 7.5: a) Carrier density dependence of Fano parameter q in chemically p -doped silicon and in laser excited intrinsic silicon. The red dots are from Ref. [38] with Raman excitation wavelength of 488 nm. The blue dots are from Ref. [39] using 532 nm as a Raman excitation. The black squares are from our experimental data with probe pulses with a 512 nm wavelength. b) q^{-1} versus photoinduced carrier density.

7.5.2 Transient reflectivity

Figure [7.7] shows the photoinduced reflectivity change at 512 nm probe wavelength for an $\sim 2 \times 10^{19} \text{ cm}^{-3}$ excitation density. The change is less than 0.2% at late delay times.

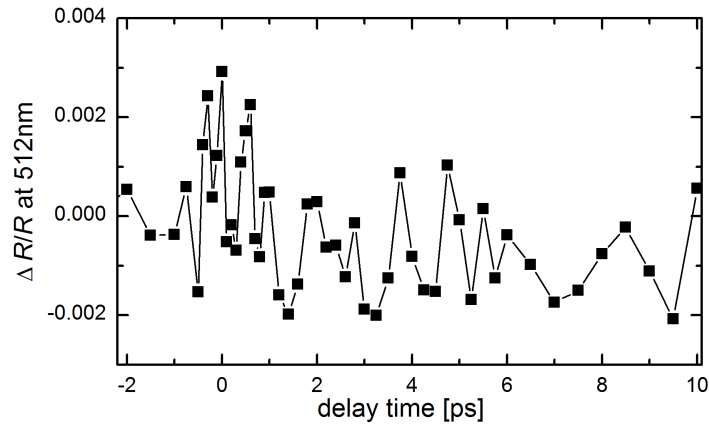


Figure 7.6: Time-resolved reflectivity changes of silicon upon 740 nm excitation and probe at 512 nm. The excited carrier density is around $\sim 2 \times 10^{19} \text{ cm}^{-3}$. The change is less than 0.2% at long delay times.

7.5.3 Dynamics at 410 nm probe wavelength

The experiment was repeated for 410 nm Raman probe wavelength. A scattering efficiency drop of about 6% is observed.

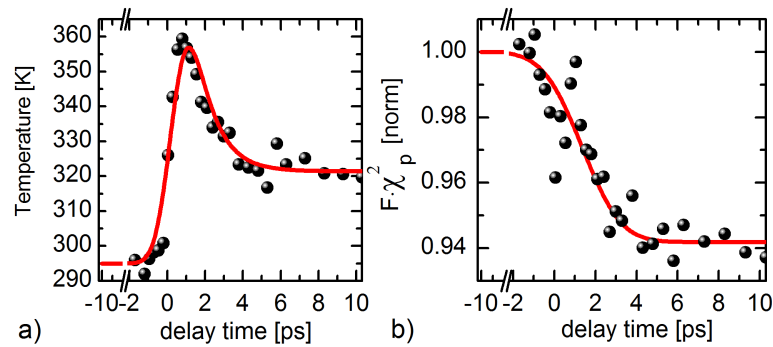


Figure 7.7: a) Extracted phonon temperature evolution. b) Extracted Raman scattering strength behavior with time.

7.6 Own contributions

The main part of this chapter is published in:

J. Zhu, R. B. Versteeg, P. Padmanabhan, and P. H. M. van Loosdrecht,
 Dynamical resonance quench and Fano interference in spontaneous
 Raman scattering from quasiparticle and collective excitations,
 Phys. Rev. B **99**, 094305 (2019)
 © 2016 “American Physical Society”

Me and Jingyi Zhu constructed the time-resolved Raman spectroscopy setup. Jingyi Zhu carried out the experiments described in this chapter. Jingyi Zhu and myself analysed the data. The text of this chapter has been written by Jingyi Zhu, myself, and P. H. M. van Loosdrecht.

7.7 Bibliography

- [1] P. Bhattacharya, R. Fornari, and H. Kamimura, *Comprehensive semiconductor science and technology*, (Elsevier, Boston, 2011).
- [2] M. Hase, M. Kitajima, A. M. Constantinescu, and H. Petek, The birth of a quasiparticle in silicon observed in time-frequency space, *Nature* **426**, 51 (2003).
- [3] M. Hase and M. Kitajima, Interaction of coherent phonons with defects and elementary excitations, *J. Phys. Condens. Matter* **22**, (2010).
- [4] A. Othonos, Probing ultrafast carrier and phonon dynamics in semiconductors, *J. Appl. Phys.* **83**, 1789 (1998).
- [5] A. J. Sabbah and D. M. Riffe. Measurement of silicon surface recombination velocity using ultrafast pump-probe reflectivity in the near infrared, *J. Appl. Phys.* **88**, 6954 (2000).
- [6] A. J. Sabbah and D. M. Riffe. Femtosecond pump-probe reflectivity study of silicon carrier dynamics, *Phys. Rev. B* **66**, 165217 (2002).
- [7] D. M. Riffe and A. J. Sabbah, Coherent excitation of the optic phonon in Si: Transiently stimulated Raman scattering with a finite-lifetime electronic excitation, *Phys. Rev. B* **76**, 085207 (2007).
- [8] K. Kato, K. Oguri, A. Ishizawa, K. Tateno, T. Tawara, H. Gotoh, M. Kitajima, H. Nakano, and T. Sogawa, Doping-type dependence of phonon dephasing dynamics in Si, *Appl. Phys. Lett.* **98**, 141904 (2011).
- [9] M. Trigo, M. Fuchs, J. Chen, M. P. Jiang, M. Cammarata, S. Fahy, D. M. Fritz, K. Gaffney, S. Ghimire, A. Higginbotham, S. L. Johnson, M. E. Kozina, J. Larsson, H. Lemke, A. M. Lindenberg, G. Ndabashimiye, F. Quirin, K. Sokolowski-Tinten, C. Uher, G. Wang, J. S. Wark, D. Zhu, and D. A. Reis, Fourier-transform inelastic x-ray scattering from time-and momentum-dependent phonon-phonon correlations, *Nat. Phys.* **9**, 790 (2013).
- [10] D. C. Hannah, K. E. Brown, R. M. Young, M. R. Wasielewski, G. C. Schatz, D. T. Co, and R. D. Schaller, Direct measurement of lattice dynamics and optical phonon excitation in semiconductor nanocrystals using femtosecond stimulated Raman spectroscopy, *Phys. Rev. Lett.* **111**, 107401 (2013).

- [11] D. Fausti and P. H. M. van Loosdrecht, in Chapter 14 of *Optical Techniques for Solid-State Materials Characterization*, edited by R. P. Prasankumar and A. J. Taylor, (CRC Press, Boca Raton London New York, 2012).
- [12] R. B. Versteeg, J. Zhu, P. Padmanabhan, C. Boguschewski, R. German, M. Goedecke, P. Becker, and P. H. M. van Loosdrecht, A tunable time-resolved spontaneous Raman spectroscopy setup for probing ultrafast collective excitation and quasiparticle dynamics in quantum materials, *Struct. Dyn.* **5**, 044301 (2018).
- [13] J. A. Kash, J. C. Tsang, and J. M. Hvam. Subpicosecond time-resolved Raman spectroscopy of LO phonons in GaAs, *Phys. Rev. Lett.* **54**, 2151 (1985).
- [14] D. Y. Oberli, D. R. Wake, M. V. Klein, J. Klem, T. Henderson, and H. Morkoç, Time-resolved Raman scattering in GaAs quantum wells, *Phys. Rev. Lett.* **59**, 696 (1987).
- [15] K. T. Tsen and H. Morkoç, Population relaxation time of nonequilibrium lo phonons and electron-phonon interactions in GaAs – Al_xGa_{1-x}As multiple-quantum-well structures, *Phys. Rev. B* **34**, 4412 (1986).
- [16] K. T. Tsen and H. Morkoç, Subpicosecond time-resolved Raman spectroscopy of LO phonons in GaAs – Al_xGa_{1-x}As multiple-quantum-well structures, *Phys. Rev. B* **38**, 5615 (1988).
- [17] J. J. Letcher, K. Kang, D. G. Cahill, and D. D. Dlott, Effects of high carrier densities on phonon and carrier lifetimes in Si by time-resolved anti-stokes Raman scattering, *Appl. Phys. Lett.* **90**, 252104 (2007).
- [18] K. T. Tsen, J. G. Kiang, D. K. Ferry, and H. Morkoç, Subpicosecond time-resolved Raman studies of LO phonons in GaN: Dependence on photoexcited carrier density, *Appl. Phys. Lett.* **89**, 112111 (2006).
- [19] A. L. Malinovsky, A. A. Makarov, and E. A. Ryabov, Slow intramolecular vibrational redistribution: the latest results for trifluoropropyne, a comparison with the other terminal acetylenes and the mechanism, *Phys. Scripta* **85**, 058102 (2012).
- [20] K. Iwata, H. Okajima, S. Saha, and H. O. Hamaguchi, Local structure formation in alkyl-imidazolium-based ionic liquids as revealed by linear and nonlinear Raman spectroscopy, *Acc. Chem. Res.* **40**, 1174 (2007).
- [21] S. K. Sahoo, S. Umopathy, and A. W. Parker, Time-resolved resonance Raman spectroscopy: Exploring reactive intermediates, *Appl. Spectrosc.* **65**, 1087 (2011).
- [22] A. Matsuda, H. Nagao, K. G. Nakamura, and K. Kondo, Time-resolved Raman spectra of ring-stretching modes of benzene derivatives under laser-driven shock compression at 1 GPa, *Chem. Phys. Lett.* **372**, 911 (2003).
- [23] I. E. I. Petterson, F. W. L. Esmonde-White, W. de Wilde, M. D. Morris, and F. Ariese, Tissue phantoms to compare spatial and temporal offset modes of deep Raman spectroscopy, *Analyst* **140**, 2504 (2015).
- [24] H. Hamaguchi and T. L. Gustafson, Ultrafast time-resolved spontaneous and coherent Raman spectroscopy: the structure and dynamics of photogenerated transient species, *Annu. Rev. Phys. Chem.* **45**, 593 (1994).
- [25] S. G. Kruglik, J.-C. Lambry, J.-L. Martin, M. H. Vos, and M. Negrerie, Subpicosecond raman spectrometer for time-resolved studies of structural dynamics in heme proteins, *J. Raman Spectrosc.* **42**, 265 (2011).
- [26] K. Kang, T. Ozel, D. G. Cahill, and M. Shim, Optical phonon lifetimes in single-walled carbon nanotubes by time-resolved Raman scattering, *Nano Lett.*, **8**, 4642 (2008).

- [27] D. Song, F. Wang, G. Dukovic, M. Zheng, E. D. Semke, L. E. Brus, and T. F. Heinz, Direct measurement of the lifetime of optical phonons in single-walled carbon nanotubes, *Phys. Rev. Lett.* **100**, 225503 (2008).
- [28] H. Yan, D. Song, K. F. Mak, I. Chatzakis, J. Maultzsch, and T. F. Heinz, Time-resolved Raman spectroscopy of optical phonons in graphite: Phonon anharmonic coupling and anomalous stiffening, *Phys. Rev. B* **80**, 121403 (2009).
- [29] K. Kang, D. Abdula, D. G. Cahill, and M. Shim, Lifetimes of optical phonons in graphene and graphite by time-resolved incoherent anti-Stokes Raman scattering, *Phys. Rev. B* **81**, 165405 (2010).
- [30] I. Chatzakis, H. Yan, D. Song, S. Berciaud, and T. F. Heinz, Temperature dependence of the anharmonic decay of optical phonons in carbon nanotubes and graphite, *Phys. Rev. B* **83**, 205411 (2011).
- [31] J.-A. Yang, S. Parham, D. Dessau, and D. Reznik, Novel electron-phonon relaxation pathway in graphite revealed by time-resolved Raman scattering and angle-resolved photoemission spectroscopy, *Sci. Rep.* **7**, 40876 (2017).
- [32] J. Zhu, R. German, B. Senkovskiy, D. Haberer, F. Fischer, A. Grüneis, and P. H. M. van Loosdrecht, Exciton and phonon dynamics in highly aligned 7-atom wide armchair graphene nanoribbons as seen by time-resolved spontaneous Raman scattering, *Nanoscale* **10**, 17975 (2018).
- [33] R. Loudon, Time-reversal symmetry in light-scattering theory, *J. Raman Spectrosc.* **7**, 10 (1978).
- [34] A. Compaan and H. J. Trodahl, Resonance Raman scattering in Si at elevated temperatures, *Phys. Rev. B* **29**, 793 (1984).
- [35] D. Fausti, O. V. Misochko, and P. H. M. van Loosdrecht, Ultrafast photoinduced structure phase transition in antimony single crystals, *Phys. Rev. B* **80**, 161207 (2009).
- [36] R. P. Saichu, I. Mahns, A. Goos, S. Binder, P. May, S. G. Singer, B. Schulz, A. Rusydi, J. Unterhinninghofen, D. Manske, P. Guptasarma, M. S. Williamsen, and M. Rübhausen, Two-component dynamics of the order parameter of high temperature $\text{Bi}_2\text{Sr}_2\text{CaCu}_2\text{O}_{8+\delta}$ superconductors revealed by time-resolved Raman scattering, *Phys. Rev. Lett.* **102**, 177004 (2009).
- [37] F. Cerdeira, T. A. Fjeldly, and M. Cardona, Interaction between electronic and vibronic Raman scattering in heavily doped silicon, *Solid State Commun.* **13**, 325 (1973).
- [38] F. Cerdeira, T. A. Fjeldly, and M. Cardona, Effect of free carriers on zone-center vibrational modes in heavily doped p -type Si. II. optical modes, *Phys. Rev. B* **8**, 4734 (1973).
- [39] B. G. Burke, J. Chan, K. A. Williams, Z. L. Wu, A. A. Puretzky, and D. B. Geohegan, Raman study of Fano interference in p -type doped silicon, *J. Raman Spectrosc.* **41**, 1759 (2010).
- [40] K. Kato, Y. Hasegawa, K. Oguri, T. Tawara, T. Nishikawa, and H. Gotoh, Relationship between the Fano asymmetry parameter and time-domain spectra studied by time-resolved measurement of carriers and phonons in p -type Si, *Phys. Rev. B* **97**, 104301 (2018).
- [41] The carrier density has been determined from the incident photon density and the optical properties of silicon, see *Suppl. Mat.*
- [42] P. G. Klemens, Anharmonic decay of optical phonons, *Phys. Rev.* **148** (1966).

-
- [43] K. Tanaka, H. Ohtake, and T. Suemoto, Determination of intervalley scattering time in germanium by subpicosecond time-resolved Raman spectroscopy, *Phys. Rev. Lett.* **71**, 1935 (1993).
 - [44] J. B. Renucci, R. N. Tyte, and M. Cardona, Resonant Raman scattering in silicon, *Phys. Rev. B* **11**, 3885 (1975)
 - [45] Y. Gillet and M. Giantomassi, and X. Gonze, First-principles study of excitonic effects in Raman intensities, *Phys. Rev. B* **88**, 094305 (2013).
 - [46] D. Sangalli, S. D. Conte, C. Manzoni, G. Cerullo, and A. Marini, Nonequilibrium optical properties in semiconductors from first principles: A combined theoretical and experimental study of bulk silicon, *Phys. Rev. B* **93**, 195205 (2016).
 - [47] M. Cardona and G. Güntherodt, *Light Scattering in Solids IV*, in page 128 (Springer-Verlag, Berlin, Heidelberg, New York, Tokyo, 1984).
 - [48] U. Fano, Effects of configuration interaction on intensities and phase shifts, *Phys. Rev.* **124**, 1866 (1961).
 - [49] U. Fano, G. Pupillo, A. Zannoni, C. W. Clark, On the absorption spectrum of noble gases at the arc spectrum limit, *J. Res. Natl. Inst. Stan.* **110**, 583 (2005).
 - [50] M. Chandrasekhar, J. B. Renucci, and M. Cardona, Effects of interband excitations on Raman phonons in heavily doped *n*-Si, *Phys. Rev. B* **17**, 1623 (1978).

Chapter 8

Coupled dynamics of long-range and internal spin cluster order in Cu_2OSeO_3

8.1 Introduction

Quantum materials with at least two length scales for electronic interactions lead to the self-formation of generalized molecular crystals of charge, spin, and orbital nature.^[1,2] From strong, shorter length scale electronic interactions solid-state “molecules” or clusters form, which “crystallize” through weaker, longer length scale electronic interactions. Such emergent solid-state molecular ground states have been identified in, for instance, the mineral Fe_3O_4 where trimeron orbital molecules form,^[3,4] molybdenates with triangular orbital plaquette molecules,^[5,6] and the chiral magnet Cu_2OSeO_3 where tetrahedral spin triplets form.^[7] The order-to-disorder phase transition pathways in such quantum materials comprises disordering of both the order inside the individual cluster actors, as well as the emerging long-range cluster order. An understanding of such dynamic double order parameter behaviour is important for the fundamental understanding of electronic correlations in solid-state molecular ground states and from the perspective of potential switching applications based on spin, charge and orbital degrees of freedom.^[4,8,9]

In this context we investigate the nonequilibrium dynamics of spin cluster and long-range order in the cluster Mott insulator Cu_2OSeO_3 . Nonequilibrium dynamic studies of Cu_2OSeO_3 have predominantly focused on the chiral magnetism, in particular the manipulation and excitation of the metamagnetic Skyrmion phase.^[10-13] An equally intriguing aspect of the nonequilibrium dynamics concerns the disordering pathways of long-range and spin triplet cluster order. The nonequilibrium dynamics is governed by lattice and spin excitations of long-range and internal cluster character and their

coupling. This is expected to lead to rather rich and interesting dynamic behaviour, which can be mapped in the time-domain by ultrafast spectroscopy techniques.

The spin cluster formation in Cu_2OSeO_3 results from the geometric distortion away from a perfect magnetic pyrochlore lattice.^{7,14} The magnetic unit cell is shown in Fig. 8.1a, and consists of 16 Cu^{2+} $S = \frac{1}{2}$ spins on a distorted pyrochlore lattice.¹⁵ Long and short Cu^{2+} - Cu^{2+} path ways are identified with correspondingly weak (dashed lines) and strong (full lines) exchange interactions. The $S = 1$ spin clusters form through the strong intra-cluster exchange interactions far above the long-range ordering temperature $T_C \approx 58$ K, below which the weak inter-cluster exchange interactions order the Cu_4 spin clusters into a spin cluster helix with a chiral pitch of approximately 62 nm.^{7,16,17} The cluster magnetic order leads to distinctly different types of low- and high-energy spin excitations with long-range and internal Cu_4 cluster character. The high-energy cluster modes can be understood as spin flip excitations of the triplet tetrahedron, as illustrated in Fig. 8.1b. The collective motion of the ordered triplet clusters gives rise to spin excitations at low energy, including the Goldstone mode of the magnetically long-range ordered state.¹⁸⁻²⁰

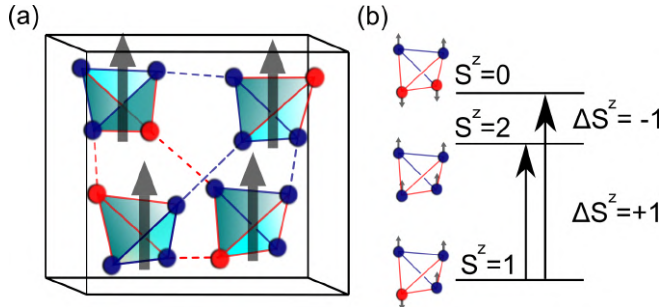


Figure 8.1: The magnetic unit cell of Cu_2OSeO_3 . The red (spin-down) and blue (spin-up) Cu^{2+} $S = \frac{1}{2}$ spins reside on a distorted pyrochlore lattice. The exchange paths can be classified into strong (full lines) and weak (dashed line) exchange couplings. The blue lines represent a predominantly ferromagnetic exchange, whereas the red lines correspond to a predominantly antiferromagnetic exchange. The three-up-one-down spin triplet ($S = 1$) clusters are indicated in light blue, with spin in grey. b) Spin flip excitations of a triplet tetrahedron. The spin flip leads to a raise or lowering of the cluster’s total magnetic quantum number S^z .

Time-resolved spontaneous Raman spectroscopy²¹ allowed us to synchronously probe photoinduced spin and lattice dynamics in Cu_2OSeO_3 . Our results reveal an efficient coupling of the high-energy spin cluster excitations to optical phonons, and more importantly, that the photoinduced magnetization dynamics is governed by a double order parameter behaviour reflecting both the disordering of long-range and internal spin cluster order.

8.2 High-energy spin cluster excitations

Before turning to the the non-equilibrium optical spectroscopy results, we discuss the equilibrium inelastic light scattering response of Cu_2OSeO_3 . Single crystals of a few mm^3 size were synthesized by chemical transport reaction growth.^[22] A (111) oriented plate-shaped sample with a flat as-grown face was used. The Raman probing is realized with 2.42 eV pulses of $\Delta\nu \approx 1.2 \text{ meV}$ ($\approx 10 \text{ cm}^{-1}$) bandwidth (full-width at half-maximum, FWHM) and $\Delta\tau \approx 1.5 \text{ ps}$ (FWHM) duration. The probe beam polarization is parallel to the crystallographic $[1\bar{1}0]$ axis. The probing is carried out in an unpolarized Raman geometry in order to optimize the scattered light detection efficiency. The energy resolution typically lies around 10 cm^{-1} and is largely dictated by the probe pulse bandwidth.

Figure 8.2 shows the steady-state Raman spectra at temperatures ranging from 5 K to 75 K. The large amount of atoms in the structural unit cell results in a rich set of phonon modes, as indicated with an asterisk in the figure.^[23-25] Two strongly temperature dependent modes are observed, which were previously assigned to $\Delta S^z = +1$ ($\hbar\Omega \sim 32 \text{ meV}$) and $\Delta S^z = -1$ ($\hbar\Omega \sim 53 \text{ meV}$) high-energy spin cluster excitations at the center of the Brillouin zone.^[18-20] For these modes, which are Raman-active through the Elliot-Loudon scattering mechanism,^[26,27] a spectral weight transfer to lower Stokes shift Ω is observed when the temperature increases towards T_C , as indicated with the grey arrows. The magnetic spectral weight transfer is understood as a softening and broadening of the $\Delta S^z = \pm 1$ spin excitations. Above $T_C \approx 58 \text{ K}$ magnetic scattering still persists, however as a broad scattering continuum.^[25] Similar critical behaviour was observed for a spin cluster transition in the THz-range of the absorption spectrum.^[28]

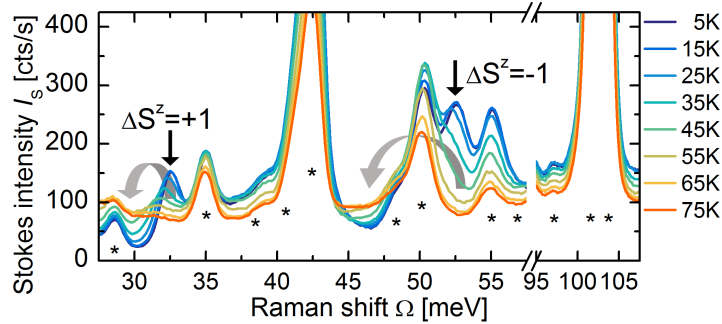


Figure 8.2: Temperature-dependent steady-state Raman spectra. The modes indicated with an asterisk (*) are phonons, or not fully resolved phonon regions. High-energy spin cluster excitations are observed at $\hbar\Omega \sim 32 \text{ meV}$ ($\Delta S^z = +1$) and $\hbar\Omega \sim 53 \text{ meV}$ ($\Delta S^z = -1$).

The conceptual picture of spin cluster excitations indicated in Fig. 8.1b applies well above T_C where no long-range order exists between the clusters. In this limit the high-energy spin excitations can be regarded as localized cluster-internal excitations with a resultingly broad continuum light scattering spectrum.²⁹ In the long-range ordered phase these internal cluster modes acquire dispersion by the inter-cluster exchange interactions, and form optical magnon branches, resulting in well-defined magnetic modes in the Raman spectrum.^{20,30} The Raman-active high-energy $\Delta S^z = \pm 1$ spin excitations thus form an optical probe for both the long-range and internal spin cluster order.

8.3 Photoinduced long-range and internal cluster order dynamics

We now turn to the optically induced spin and lattice dynamics. The Cu_2OSeO_3 sample, cooled to 5 K, is excited in the crystal-field excitation region (see chapter 4) with 2.18 eV pump pulses of $\Delta\tau \approx 0.3$ ps (FWHM) duration at a fluence of $F \approx 2$ mJ/cm². The fraction of photoexcited Cu^{2+} -sites per pulse lies around $\sim 5 \cdot 10^{-6}$ (see appendix Par. 8.5.3 for the calculation). The weak pump-excitation conditions ensure that we probe the near-equilibrium dynamics of the helimagnetic phase. The thermalization of the system is measured by the time-evolution of the Stokes spectrum. The Raman-probe pulse falls in the low energy tail of the charge transfer excitation region (see chapter 4). The Stokes Raman scattering intensity $I_S(\Omega)$ is proportional to $I_S(\Omega) \propto V_{\text{probe}}[\alpha(\omega)] \cdot \chi_R^2(\Omega) \cdot [n(\Omega) + 1]$ (Ref. 31). Here $V_{\text{probe}}[\alpha(\omega)]$ describes the probe volume term, which depends on the absorption coefficient $\alpha(\omega)$ at the scattered photon frequency ω . $\chi_R^2(\Omega)$ gives the squared Raman tensor and $[n(\Omega) + 1]$ the population factor. Under the weak pump excitation conditions the (transient) occupation number $n(\Omega) \ll 1$ and can thus be neglected, i. e. $I_S(\Omega) \propto V_{\text{probe}}[\alpha(\omega)] \cdot \chi_R^2(\Omega)$.

In Fig. 8.3 we show our main result: the transient evolution of the Stokes spectrum $I_S(\Omega, t)$, where t refers to the pulse delay time and Ω to the Stokes shift. For clarity the pre-time-zero Stokes spectrum $I_S(\Omega, -5$ ps) is plotted in Fig. 8.3a. Figures 8.3b and 8.3c show the differential Stokes spectra $\Delta I_S(\Omega, t) = I_S(\Omega, t) - I_S(\Omega, -5$ ps), and scaled differential Stokes spectra $\Delta I_S(\Omega, t)/I_S(\Omega, -5$ ps) for the time-delays indicated in the figure. The two main observations are a decrease with subsequent recovery of the phonon-scattering intensity, and a transient broadening and spectral weight transfer to lower Ω of the $\Delta S^z = \pm 1$ spin excitations. Similar behaviour is observed at higher bias temperatures, as shown in the appendix in Par. 8.5.1.

The scattering intensity of selected phonon (ph) modes is integrated over a range $\sim 3 \times \text{FWHM}$ centered at the phonon energy to give $I_{\text{ph}}(t)$. Figure 8.4a shows the relative transient phonon scattering intensity

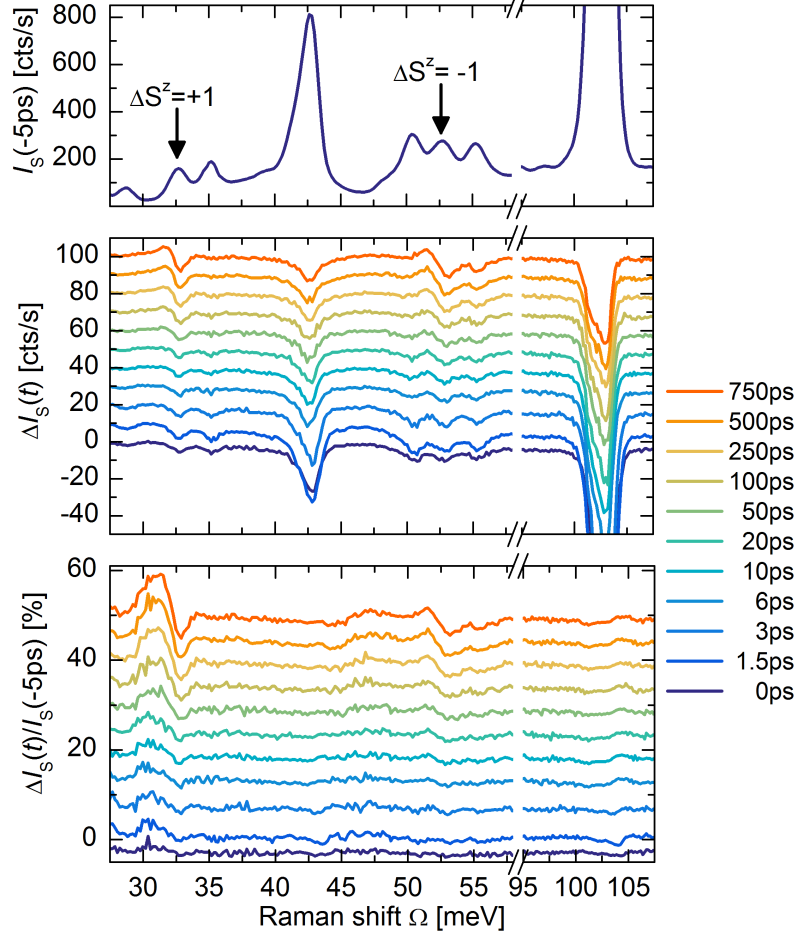


Figure 8.3: a) Stokes spectrum at 5 K. The spin cluster excitations are indicated with arrows. The other peaks are phonons. b) Differential Stokes spectra for indicated time-delays. The phonon modes show a reduction in scattering efficiency, which does not fully recover within the measured time window. The $\Delta S^z = \pm 1$ spin excitations show a dynamic softening and broadening. c) Scaled differential spectra. From these spectra it becomes clear that the phonons only show a negligible frequency shift, in sharp contrast with the $\Delta S^z = \pm 1$ spin excitations. After $t > 100$ ps the spin excitation spectral weight transfer keeps on increasing.

$\Delta I_{\text{ph}}(t)/I_{\text{ph}}(-5 \text{ ps})$ for the 103 meV phonon. For all phonons an initial Stokes scattering efficiency decrease of $\sim 5\%$ after excitation is observed, with a partial recovery within the temporal pump-probe pulse overlap (see appendix Par. 8.5.4). A slower recovery time-scale of $\tau_{\text{ph}} \sim 45$ ps is observed to $\Delta I_{\text{ph}}(t)/I_{\text{ph}}(-5 \text{ ps}) \approx -1.5\%$ at late delay times. The phonon spectral shape hardly changes, as most clearly seen in the scaled differential Stokes spectra (Fig. 8.3c). From these observations it becomes apparent that the Raman spectra show an overall reduction and recovery in scattering effi-

ciency due to a transient change in absorption, with a concomitant change in $V_{\text{probe}}[\alpha(\omega)]$. The transient change in absorption is verified by a transient absorption spectroscopy measurement under similar excitation conditions, as discussed in Par. [8.5.8](#).

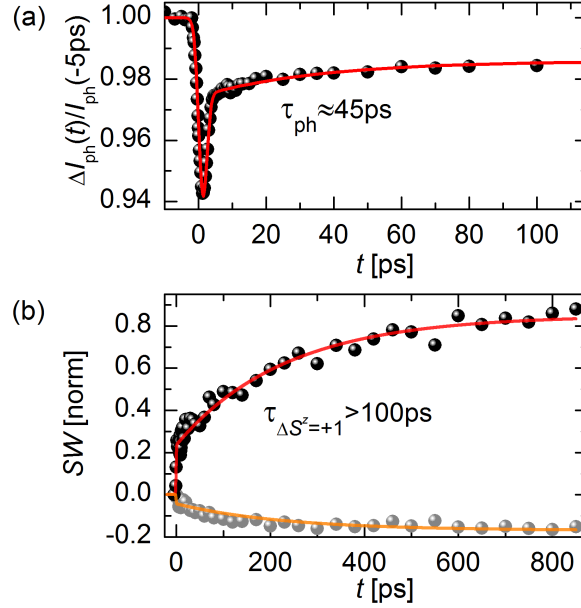


Figure 8.4: a) $\Delta I_{\text{ph}}(t)/I_{\text{ph}}(-5 \text{ ps})$ transient for the 103 meV phonon region. An initial scattering reduction and partial recovery within the time-resolution is observed, in addition to a longer time-scale recovery. Global fitting approximately gives the same long recovery time-constant of $\tau_{\text{ph}} \sim 45 \text{ ps}$ for all phonons. b) The softening of the $\Delta S^z = +1$ spin excitation occurs on a significantly slower timescale of $\tau_{\Delta S^z = \pm 1} > 100 \text{ ps}$. Plotted is the increasing (black dots) and decreasing (grey dots) component of the spectral weight transfer.

A transient softening and broadening of the $\Delta S^z = \pm 1$ spin excitation scattering is observed due to excitation of the magnetic system. Note that the asymmetric line shape in the (scaled) differential spectra originates from a line shape change in χ_{R}^2 , and not from the population term $n(\Omega)$. The time dependent dynamics of the spin excitation scattering is convoluted with the change in the probing volume. This effect is deconvoluted by scaling the spectrum with the scattering intensity of the phonon response, giving the intensity ratio:

$$\frac{I_{\Delta S^z = \pm 1}}{I_{\text{ph}}} \propto \frac{\chi_{\Delta S^z = \pm 1}^2}{\chi_{\text{ph}}^2} \quad (8.1)$$

The intensity ratio is integrated over the increasing and decreasing scat-

tering spectral component (integration range 28.5-32.3 meV and 32.7-33.5 meV respectively), to give a spectral weight function (SW) of the high-energy spin-excitation scattering, as plotted for $\Delta S^z = +1$ in Fig. 8.4b. A stepwise ($\tau < 1.5$ ps) SW transfer is observed, followed by a $\tau_{\Delta S^z = \pm 1} > 100$ ps spin-lattice relaxation component. A zoom-in on the early time-scale spectral dynamics of the $\Delta S^z = +1$ excitation is plotted in Fig. 8.5. The SW transfer at $t = 0$ ps and $t = 1.5$ ps amounts to about 15% to 30% respectively of the SW transfer at late time-delays t . This evidences an efficient ultrafast spin disordering mechanism, in agreement with the observations described in Ref. 12. Similar dynamics is observed for the $\Delta S^z = -1$ excitation. Comparison of the $\Delta S^z = +1$ spin excitation peak shift at late delay times with steady-state data allows to calculate a heating of $\Delta T \approx 7$ K when quasi-equilibrium is established, in good agreement with the temperature increase estimated from the pulse power, absorption coefficient, and low temperature heat capacity 17,32 of Cu_2OSeO_3 (see appendix Par. 8.5.2 and 8.5.3).

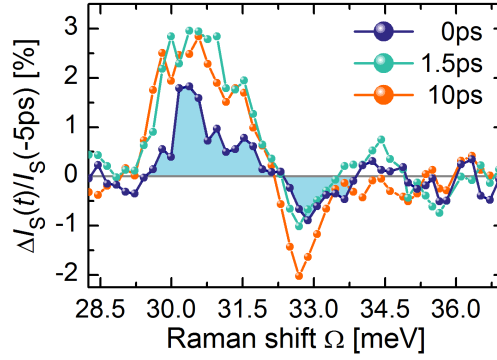


Figure 8.5: Differential Stokes spectra $\Delta I_S(\Omega, t)/I_S(\Omega, -5 \text{ ps})$ of the $\Delta S^z = +1$ excitation at early delay times. At pump-probe overlap ($t = 0$ ps) a spectral weight shift is established, revealing an efficient energy relaxation channel on the shortest time-scale (< 1.5 ps).

The disordering of long-range and internal spin cluster order occurs through different spin-lattice relaxation channels. 9,33,34 After the optical excitation the electronically excited system dissipates energy by emission of optical phonons, which subsequently decay into acoustic phonons. 35-37 The rapid magnetic spectral weight transfer on the shortest timescale is evidence of an additional decay mechanism for the optical phonons into high-energy spin cluster excitations, which leads to an ultrafast reduction of long-range and internal spin cluster order. Such efficient phonon-magnon decay is enabled by the energy-momentum-dispersion overlap of the optical phonons and the high-energy spin cluster excitations. 20,33

The separation between long-range and internal spin cluster order dynamics becomes apparent over longer timescales. The long timescale spin-

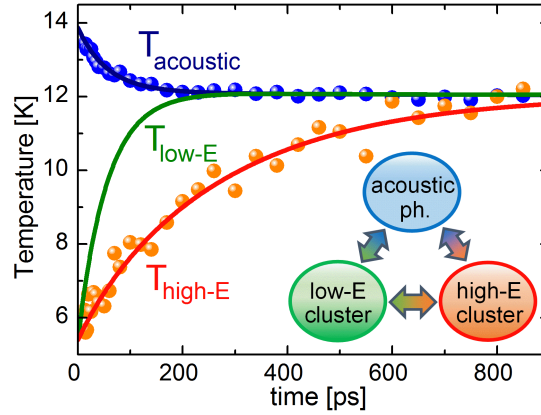


Figure 8.6: Acoustic phonon (ph.), low-energy (low-E), and high-energy (high-E) spin excitation equilibration dynamics after $t > 6$ ps. Effective temperatures are indicated with T_{acoustic} for the acoustic phonons, and $T_{\text{low-E}}$ and $T_{\text{high-E}}$ for the low-energy and high-energy spin cluster excitations.

lattice equilibration is microscopically dictated by the coupling between acoustic phonons, and low- and high-energy spin cluster excitations.³⁴ The low-energy cluster excitation thermalization dynamics can be obtained by fitting a phenomenological three-temperature model⁹ to the phonon and high-energy spin excitation transients, as shown in Fig. 8.6. The change in the acoustic phonon temperature is proportional to the change in the phonon Raman scattering intensity. The change in the high-energy spin excitation temperature is proportional to the observed spin excitation spectral weight transfer. The solid lines are the solution to the three-temperature model.³² See appendix Par. 8.5.6 for more details on the effective temperature modeling. A long-range disordering time of $\tau_{\text{LRO}} \sim 55$ ps is found from the low-energy spin excitation thermalization. The high-energy spin excitations form a dual probe of long-range and internal spin cluster order. From the high-energy spin excitation thermalization we infer an internal cluster disordering time of $\tau_{\text{cluster}} \sim 400$ ps. Similar demagnetization timescales were reported in Ref. 12.

The separation into double magnetic order parameter dynamics is understood from vastly different phonon-magnon interactions. Acoustic phonons couple strongly to the low-energy spin cluster excitations,³⁸ but only weakly to the high-energy spin cluster excitations.³³ Phonon decay into low-energy spin excitations of the long-range ordered state describes the conventional demagnetization pathway of insulating magnetic materials.^{9,34} The disordering of internal spin cluster order however has to occur through upconversion of acoustic phonons and/or low-energy spin excitations into high-energy spin cluster excitations, forming a scattering bottleneck in the equilibration dynamics.

8.4 Conclusions and outlook

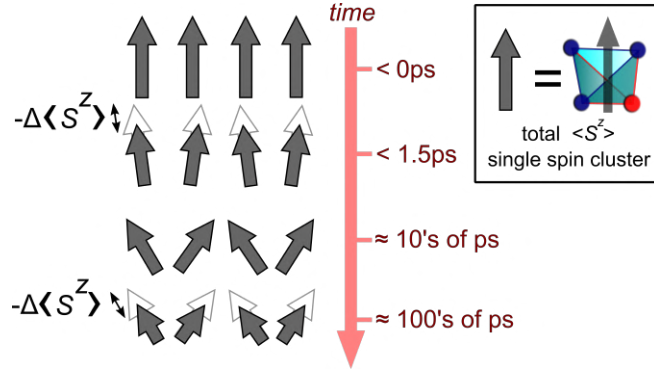


Figure 8.7: Summary of the photoinduced multiple ps-decade spin disordering dynamics. The total spin length $\langle S^z \rangle$ of a single spin cluster is indicated with a grey arrow. The disordering of internal spin cluster order is depicted as a $-\Delta\langle S^z \rangle$ spin length reduction. Long-range disordering is depicted by a reorientation of the cluster spins.

The multiple ps-decade long-range and internal spin cluster order parameter dynamics is summarized in Fig. 8.7. An initial ultrafast ($\tau < 1.5$ ps) reduction of long-range and internal spin cluster order results from the decay of optical phonons into high-energy spin cluster excitations. This is depicted by a disordering of the cluster spin alignment and a $-\Delta\langle S^z \rangle$ decrease in spin length for the clusters. On the 10's of ps timescale the long-range ordering of spin clusters decreases by decay of acoustic phonons into low-energy spin excitations. On the 100's of ps timescale the internal spin cluster order decreases through upconversion of acoustic phonons and/or low-energy spin excitations into high-energy spin cluster excitations.

The present results provide a new viewpoint on the photoinduced nonequilibrium dynamics in the cluster Mott insulator Cu_2OSeO_3 , and highlight the double magnetic order parameter dynamics of cluster magnets. Addressing nonequilibrium multiple order parameter dynamics is not only important in cluster magnets like Cu_2OSeO_3 , but also in contemporary problems in the study of quantum materials consisting of long-range ordered “molecules”, such as unraveling the nature and speed limit of phase transitions in orbital cluster Mott insulators,⁴⁸ and destabilization of spin-dimer competing phases in spin liquid candidate materials.³⁹

8.5 Appendix

8.5.1 Transient spectra at 15 K, 38 K, and 60 K

The time-resolved Raman spectroscopy experiments have been carried out at $T = 5$ K, 15 K, 38 K and 60 K sample bias temperature. Similar graphs, as presented in Fig. 3a,b, and c in the main article are shown here for $T = 15$ K, 38 K, and 60 K sample bias temperature. The spin excitations are indicated with arrows. The other excitations are phonons or not fully resolved multiple phonons. For 15 K and 38 K bias temperature it is still possible to resolve spin excitation dynamics. At 60 K the spin excitations have significantly broadened. No photoinduced change in the spin excitations could be resolved at 60 K sample bias temperature.

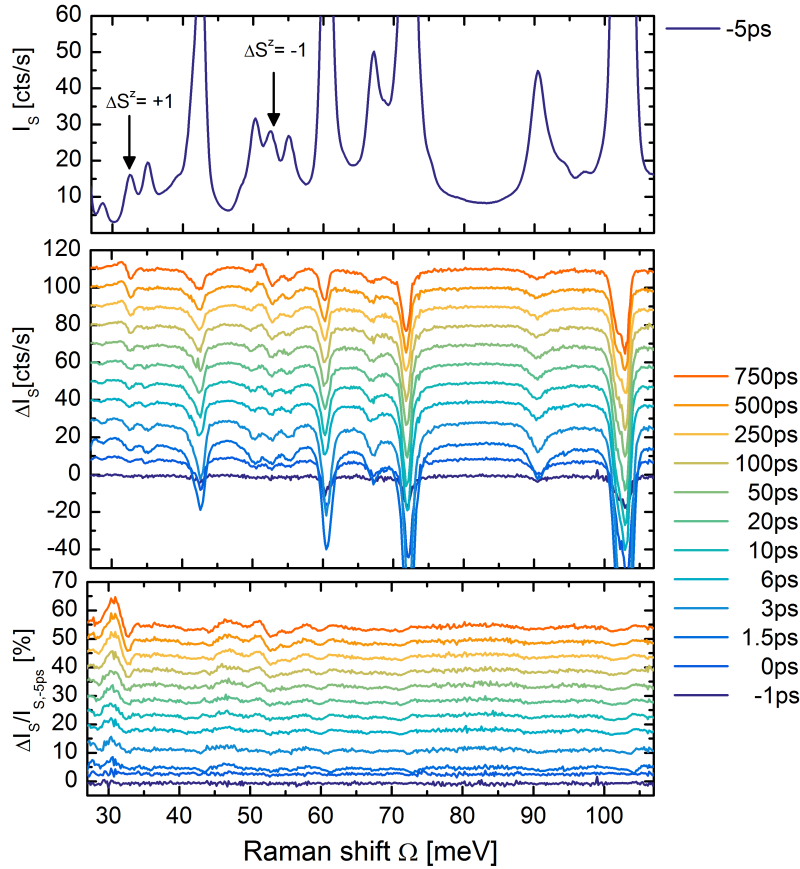


Figure 8.8: Transient Raman data at $T = 15$ K sample bias temperature. a) Pre-time-zero spectrum for comparison. The spin excitations $\Delta S^z = \pm 1$ are indicated. b) Differential Raman spectra for indicated time-delays. c) Scaled differential spectra for indicated time-delays.

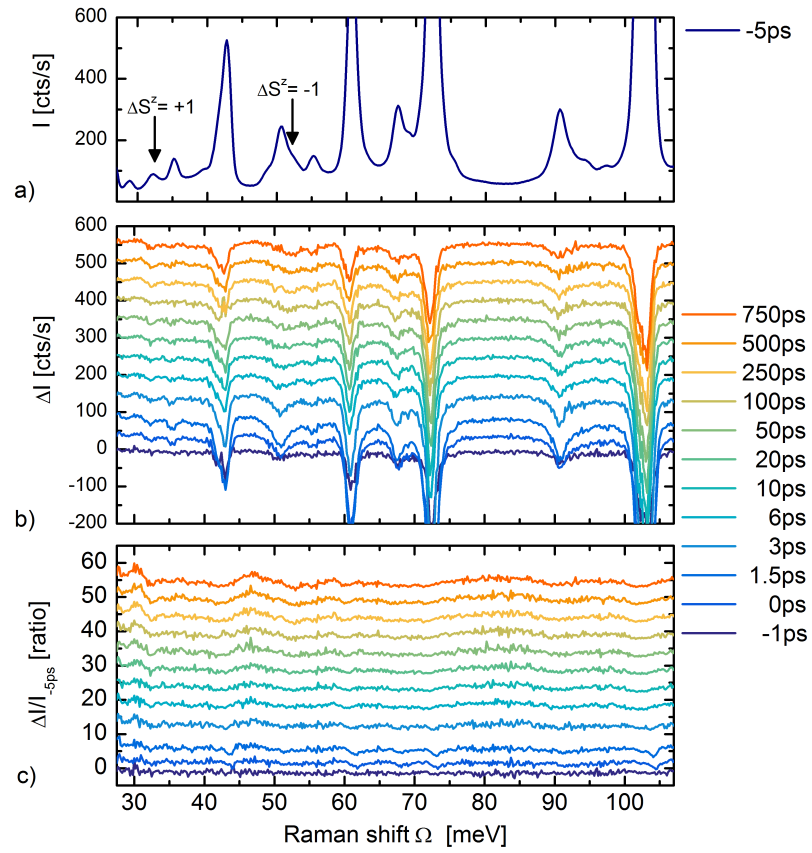


Figure 8.9: Transient Raman data at $T = 38$ K sample bias temperature. a) Pre-time-zero spectrum for comparison. The spin excitations $\Delta S^z = \pm 1$ are indicated. b) Differential Raman spectra for indicated time-delays. c) Scaled differential spectra for indicated time-delays.

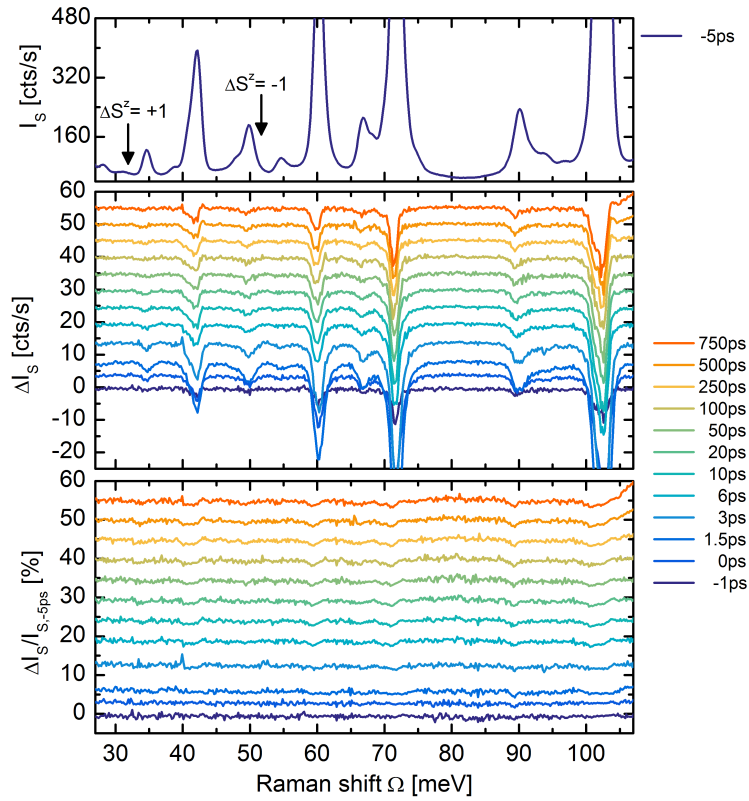


Figure 8.10: Transient Raman data at $T = 60$ K sample bias temperature. a) Pre-time-zero spectrum for comparison. The $\Delta S^z = \pm 1$ spin excitations have significantly softened with respect to low temperatures. The low temperature position is indicated. b) Differential Raman spectra for indicated time-delays. No clear change in magnetic scattering is observed. c) Scaled differential spectra for indicated time-delays. No clear change in magnetic scattering could be resolved.

8.5.2 Supporting data of transient magnetic scattering at $T=5\text{ K}$

$\Delta S^z = -1$ transient scattering

The normalized integrated transient magnetic scattering spectral weight for the 425 cm^{-1} ($\Delta S^z = -1$) spin excitation is shown below. The magnetization dynamics has a typical timescale of $\tau > 100\text{ ps}$. The case for the 265 cm^{-1} ($\Delta S^z = +1$) spin excitation, which shows similar dynamics, is shown in the main text. The scattering intensity of the 103 meV phonon is plotted for comparison. A global fit with a single exponential increase and decrease respectively, gives a time constant of $\tau \approx 208 \pm 50\text{ ps}$ for the $\Delta S^z = -1$ spin excitation scattering. This is in good agreement with the $\tau \approx 230 \pm 40\text{ ps}$ time constant observed for the $\Delta S^z = +1$ excitation (assuming single exponential).

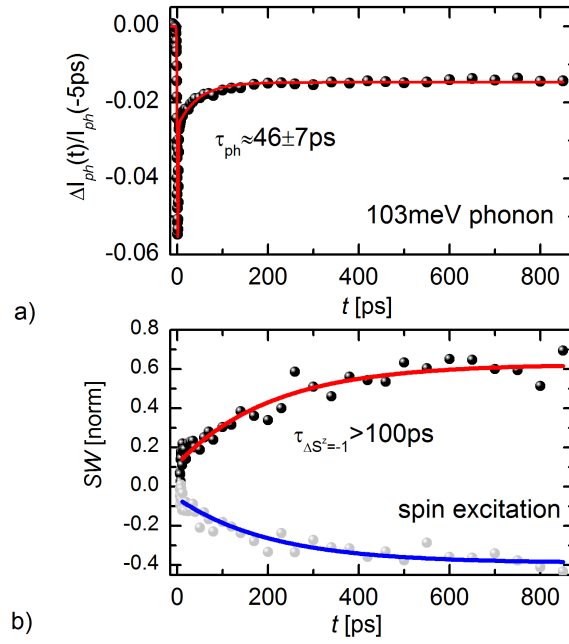


Figure 8.11: Transient scattering intensity for the 103 meV phononic region. b) Intensity ratio of increasing/decreasing magnetic scattering intensity to phononic scattering ratio for the $\Delta S^z = -1$ magnon. The magnetization dynamics has a typical timescale of $\tau > 100\text{ ps}$.

Peak shift of $\Delta S^z = +1$ spin excitation

A small photoinduced peak shift is observed for both spin excitations. Shown in Fig. 8.12a is the Raman spectrum $I_S(t)$ around the $\Delta S^z = +1$ excitation for $t = -5$ ps, and $t = 750$ ps. The peak position of the 265 cm^{-1} ($\Delta S^z = +1$) spin excitation is determined for both times. The fit function is a sum of 5 Gaussian peak position (4 phonons and 1 spin excitation). A photoinduced peak shift of $\Delta\Omega \approx -0.2 \text{ cm}^{-1} \approx -0.025 \text{ meV}$ is observed at 750 ps. Comparison with the steady-state temperature dependent peak position allows to deduce an effective heating of about $\Delta T[\text{K}] \approx 7 \text{ K}$.

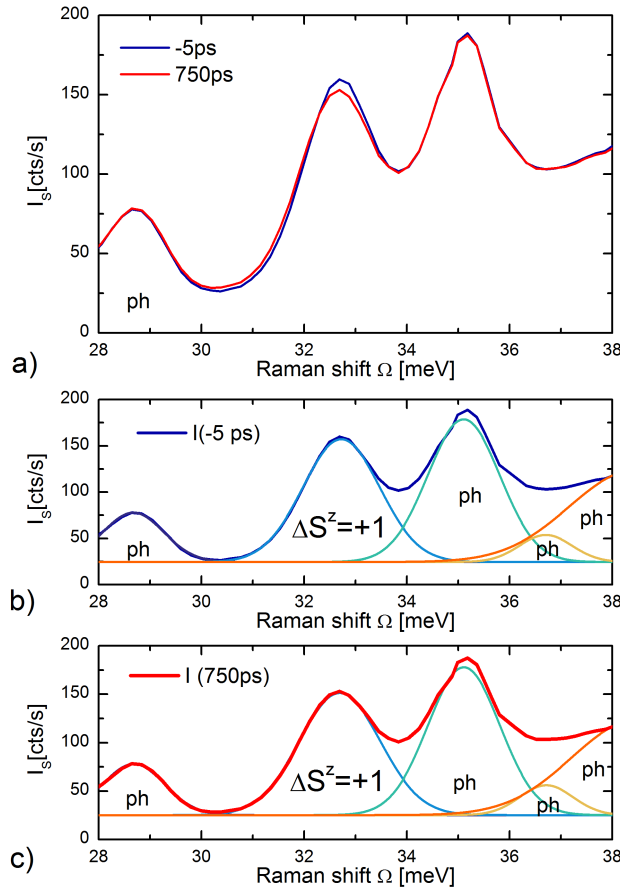


Figure 8.12: a) Raman spectrum $I_S(t)$ around the $\Delta S^z = +1$ excitation before time-zero and 750 ps at quasi-equilibrium. b) 5 Gaussian decomposition of the spectral region containing the $\Delta S^z = +1$ spin excitation at -5 ps. b) 5 Gaussian decomposition of the spectral region containing the $\Delta S^z = +1$ spin excitation at 750 ps time-delay.

8.5.3 Temperature increase estimated from heat capacity

A power $P = 1.9 \text{ mW}$ is measured at the sample position in the data set of the main part of this chapter. With photon energy 2.18 eV and laser repetition rate $f = 100 \text{ kHz}$ this corresponds to a pulse energy of $E_{\text{pulse}} \approx 19 \text{ nJ}$. The amount of photons per pulse is given by $n_{\gamma} \approx 5.44 \cdot 10^{10}$ photons/pulse. With a spot radius $r \approx 18 \pm 5 \mu\text{m}$ a fluence $F \approx 2.0 \text{ mJ/cm}^2$ is obtained for this pump power. The penetration depth at 5 K at $\lambda = 570 \text{ nm}$ light is $\delta = 1/\alpha \approx 200 \mu\text{m}$. Approximating the pump volume as a cylinder, $V_{\text{pump}} \approx 0.195 \cdot 10^{-6} \text{ cm}^{-3}$ is calculated. At low temperatures the unit cell has a volume $V_{\text{u.c.}} \approx 705 \cdot 10^{-24} \text{ cm}^{-3}$ (Ref. [15]). The pump volume contains an amount of $V_{\text{pump}}/V_{\text{u.c.}} \approx 2.77 \cdot 10^{14}$ unit cells. Each unit cell contains 16 Cu_2OSeO_3 formula units, [20] and with 2 Cu's in the formula unit this means that there is a total of $n \approx 8.9 \cdot 10^{15}$ Cu sites within the pump volume. The fraction of photoexcited Cu-sites per pulse thus equals $\eta^* \approx (1 - R) \cdot n_{\gamma}/n \approx 4.9 \cdot 10^{-6} \approx 5 \text{ ppm}$ for a fluence $F \approx 2.0 \text{ mJ/cm}^2$. Here $R \approx 0.12$ is the reflection coefficient which is nearly temperature independent at $\lambda = 570 \text{ nm}$.

The temperature increase $\Delta T = T^* - T_0$ due to the pump pulse can be estimated as:

$$\Delta Q = \rho V_{\text{pump}} \int_{T_0}^{T^*} C_p dT \quad (8.2)$$

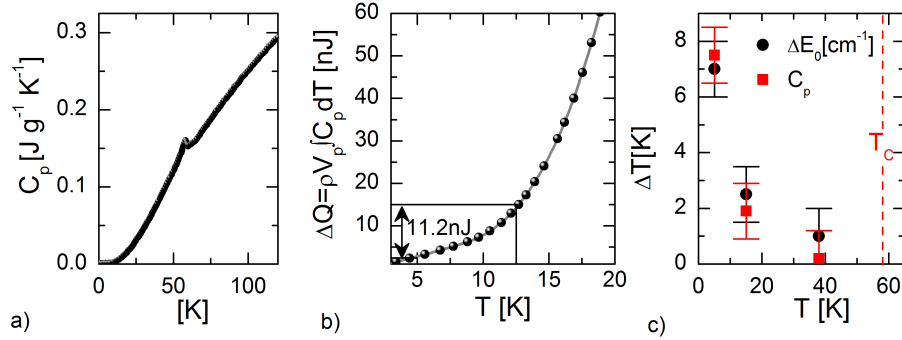


Figure 8.13: a) Heat capacity taken from Ref. [17] b) The overall energy absorbed per laser pulse at a fluence $F \approx 2.0 \text{ mJ/cm}^2$ equals $\Delta Q \approx 11.2 \text{ nJ}$. This leads to a temperature increase of about $\Delta T \approx 6 - 7 \text{ K}$ at $T_{\text{bias}} = 5 \text{ K}$. c) The transient peak excitation shift at quasi-equilibrium is calculated into an effective heating $\Delta T [\text{K}]$ (black dots). The heating shows overall agreement with the heat capacity trend (red squares).

In analogy to above-band gap optical transitions in semiconductors, each pump pulse releases an energy $\Delta Q \approx (2.2 - 0.9)/2.2 \approx 11.2 \text{ nJ}$. Here the onset of crystal-field excitations is $E_{\text{gap}} \approx 0.9 \text{ eV}$. The specific mass of Cu_2OSeO_3

is $\rho \sim 5.0893 \text{ g cm}^{-3}$.^[15] The heat capacity data (Fig. 8.13a) has been taken from Ref. [17]. This allows to calculate an average temperature increase of $\Delta T \approx 6 - 7 \text{ K}$ for $T_{\text{bias}} = 5 \text{ K}$, as shown in Fig. 8.13b.

The peak shifts at 750 ps with respect to pre- t_0 are calculated for the different temperature sets into an effective temperature raise $\Delta T[\text{K}]$ by comparison with the temperature-dependent peak position of the $\Delta S^z = +1$ excitation. In Fig. 8.13c the red squares indicate the temperature increase based on the heat capacity calculation and the black dots indicate the temperature rise based on the peak shift. A good overall agreement is observed.

8.5.4 Different phonons at $T = 5 \text{ K}$ and $F \approx 2 \text{ mJ/cm}^2$

Five phonons/not fully resolved phonon region transients were globally fitted for the 5 K transient Stokes data set with $F \approx 2 \text{ mJ/cm}^2$ excitation. The analyzed phonons are indicated in Fig. 8.14. A description of the corresponding atomic vibrations is given along the lines of Ref. [24]. The analyzed phonons have a vastly different vibrational character. The phonon transients are integrated over the green shaded areas to give $I_{\text{ph}}(t) = \int I_{\text{S}}(\Omega, t) d\Omega$ and shown in Fig. 8.15 as relative transient phonon scattering intensity $\Delta I_{\text{ph}}(t)/I_{\text{ph}}(-5 \text{ ps})$.

The phonon transients $I_{\text{ph}}(t)$ are globally fitted with the following fit formula:

$$I_{\text{ph}}(t) = \mathcal{G}(t, \sigma) \otimes [a_1 \cdot \exp(-(t - t_0)/\tau_{\text{ph}}) + a_2 \cdot \theta(t - t_0)] + a_3 \cdot \mathcal{G}(t, \sigma) + I_{\text{ph}}(-5 \text{ ps}) \quad (8.3)$$

The term between brackets is a single exponential decay function with amplitude a_1 and Heaviside step function $\theta(t - t_0)$ with amplitude a_2 . This describes the exponential recovery τ_{ph} and the “infinite τ_{∞} ” plateau at quasi-equilibrium in the phonon intensity $I_{\text{ph}}(t)$. These terms are convoluted with a Gaussian $\mathcal{G}(t, \sigma)$ with width σ determined by the pump-probe pulse cross-correlation. Time-zero is indicated with t_0 . The Gaussian captures the fast scattering efficiency reduction and increase which cannot be resolved with our time-resolution. $I_{\text{ph}}(-5 \text{ ps})$ is the pre- t_0 phonon scattering intensity. t_0 and σ are global fit parameters while the other parameters are free parameters for each phonon transient.

For all phonons an initial Stokes scattering efficiency decrease of $\sim 5\%$ after excitation is observed with a partial recovery within the temporal pump-probe pulse overlap. A slower recovery time-scale of $\tau_{\text{ph}} \sim 45 \text{ ps}$ is observed to $\Delta I_{\text{ph}}(t)/I_{\text{ph}}(-5 \text{ ps}) \approx -0.015$ at late delay times. Global fitting of the indicated phonons with a varying τ_{ph} and amplitudes, but fixed t_0 and σ , gives the time-constants indicated in Fig. 8.15. Within the fit accuracy the phonon recovery time τ_{ph} is equal for each phonon. This evidences that the scattering efficiency decrease originates in the non-resonant prefactor

$V_{\text{probe}}[\alpha(\omega)]$ as discussed in the main text. A global fit of the 5 phonons with a shared τ_{ph} and σ , with only the amplitudes as free parameters gives $\tau_{\text{ph}} \sim 45 \pm 5$ ps.

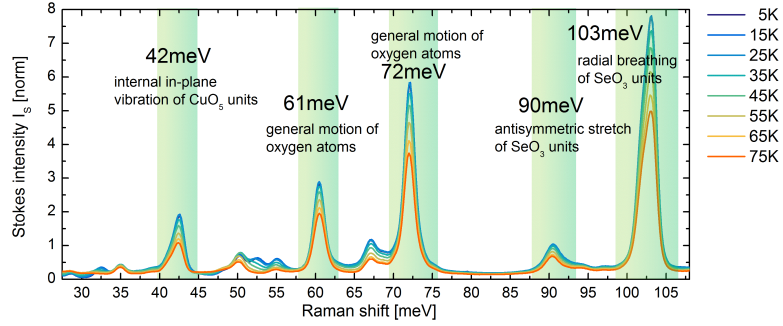


Figure 8.14: Different phonons/not fully resolved phonon regions are analyzed. A description of the corresponding atomic vibrations is indicated according to Miller *et al.* (Ref. 24).

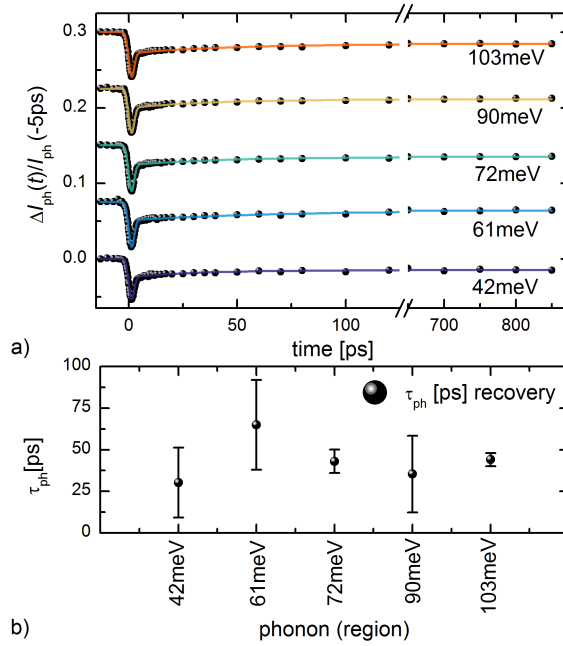


Figure 8.15: a) Scaled phonon transients $\Delta I_{\text{ph}}(t)/I_{\text{ph}}(-5\text{ps})$. The transients correspond to the phonon modes indicated in Fig. 8.14. Similar behavior is observed for each phonon mode: a scattering efficiency drop is followed by a partial recovery on a time-scale of $\tau_{\text{ph}} \sim 45$ ps. b) Fit results τ_{ph} for the indicated phonons. Within error bars all the phonons show similar recovery time-constants.

8.5.5 Fluence dependence at $T = 5$ K

A fluence dependence has been carried out at $T = 5$ K. The fit formula for the transient phonon scattering response is given in Eq. 8.3. In Fig. 8.16a the $\Delta I_{\text{ph}}(t)/I_{\text{ph}}(-5 \text{ ps})$ transients of the 103 meV phonon are plotted. The fluence F is indicated in mJ/cm^2 . In Fig. 8.16b the differential scattering amplitude at 1.5 ps (maximum reduction) and at quasi-equilibrium (750 ps) for the 103 meV phonon region are shown. Both differential amplitudes grow linearly with increasing fluence. The phonon recovery time τ_{ph} (single exponential fit) does not depend on fluence F , as seen in Fig. 8.16c. These observations argue for that we work in the linear excitation regime. This may also be expected, since the excitation density is on the order of $\mathcal{O} \sim 10^{-6} - 10^{-5}$ photons/Cu-atom (see Par. 8.5.3).

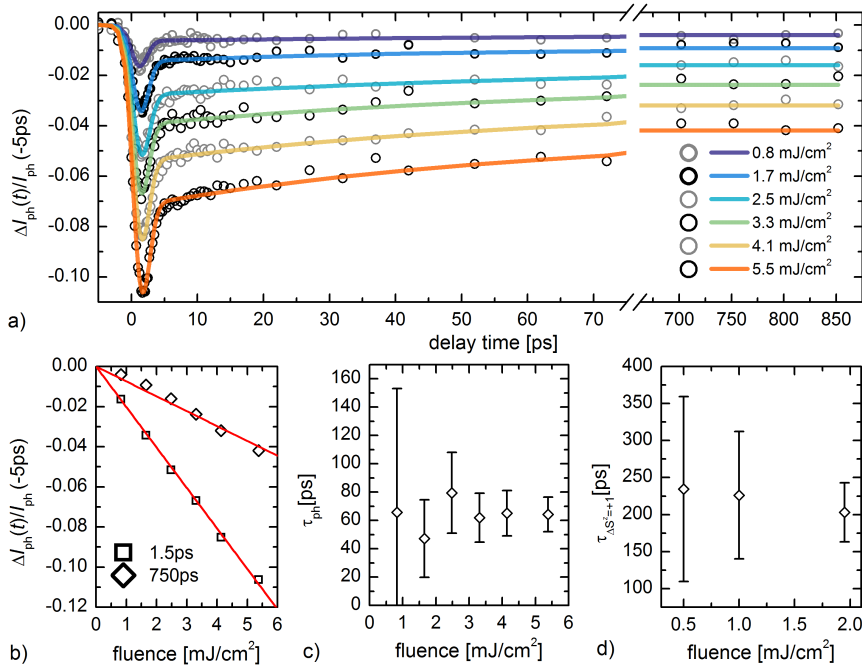


Figure 8.16: a) Fluence dependent $\Delta I_{\text{ph}}(t)/I_{\text{ph}}(-5 \text{ ps})$ transients of the 103 meV phonon. b) Amplitudes of $\Delta I_{\text{ph}}(t)/I_{\text{ph}}(-5 \text{ ps})$ for the 103 meV phonon transient as a function of fluence. The squares are at $t = 1.5 \text{ ps}$ where the scattering reduction is maximum. The diamonds are the scattering efficiency at $t = 750 \text{ ps}$, corresponding to quasi-equilibrium. c) The recovery time τ_{ph} remains constant in fluence F . d) Fluence dependence of transient magnetic spectral weight transfer time $\tau_{\Delta S^z=+1}$ (single exponential fit function) for the $\Delta S^z = +1$ spin excitation.

Data sets for longer integration times are made for less fluence points to measure the fluence dependence of the transient magnetic spectral weight transfer of the $\Delta S^z = +1$ spin excitation, as plotted in Fig. 8.16d. The

$\tau_{\Delta S^z=+1}$ (single exponential fit function) appears to be not fluence dependent in the studied fluence range, which again argues that we work in a linear photoexcitation regime.

8.5.6 Three-temperature model

The long timescale spin-lattice equilibration dynamics is microscopically dictated by the coupling between acoustic phonons, and low- and high-energy spin cluster excitations. We fitted a phenomenological three temperature model^[9] (3TM) to the 10's to 100's ps-decade dynamics transients in order to obtain the disordering time for the long-range and internal spin cluster order. We consider a closed system after $t > 6$ ps, with effective temperatures $T_{\text{acoustic}} = T_{\text{ac.}}$ for the acoustic phonon bath, $T_{\text{low-E}}$ for the low-energy spin cluster excitation bath, and $T_{\text{high-E}}$ for the high-energy spin cluster excitation bath.

From the high-energy spin excitation peak shift at $t = 850$ ps we deduce a quasi-equilibrium temperature $\Delta T \approx 7$ K above $T_{\text{bias}} = 5$ K, i.e. $T(850 \text{ ps}) \approx 12$ K. The acoustic phonon temperature, indicated with blue spheres in Fig. 4 of the main article, is linearly proportional to the recovery of the 103 meV phonon scattering intensity, with $T_{\text{acoustic}}(850 \text{ ps}) \approx 12$ K and $T_{\text{acoustic}}(6 \text{ ps}) \approx 14$ K. The high-energy spin excitation temperature, indicated with orange spheres, is linearly proportional to the increasing component of the transient spin excitation spectral weight transfer SW . The quasi-equilibrium temperature is set to $T_{\text{high-E}} \approx 12$ K. The temperature at $t = 6$ ps is set to about $T_{\text{low-E}} \approx 5.5$ K, i.e. slightly above $T_{\text{bias}} = 5$ K.

The three-temperature model is given as follows:

$$\begin{aligned} C_{\text{ac.}} \frac{\partial T_{\text{ac.}}}{\partial t} &= -g_1(T_{\text{ac.}} - T_{\text{low-E}}) - g_2(T_{\text{ac.}} - T_{\text{high-E}}) \\ C_{\text{low-E}} \frac{\partial T_{\text{low-E}}}{\partial t} &= -g_1(T_{\text{low-E}} - T_{\text{ac.}}) - g_3(T_{\text{low-E}} - T_{\text{high-E}}) \\ C_{\text{high-E}} \frac{\partial T_{\text{high-E}}}{\partial t} &= -g_2(T_{\text{high-E}} - T_{\text{ac.}}) - g_3(T_{\text{high-E}} - T_{\text{low-E}}) \end{aligned} \quad (8.4)$$

where the C_i 's indicate the heat capacities of the respective quasiparticle baths, and the g_i 's their couplings. To be more specific: $g_1 \equiv g_{\text{ac.-low-E}}$, $g_2 \equiv g_{\text{ac.-high-E}}$, and $g_3 \equiv g_{\text{low-E-high-E}}$. The (relative) heat capacities for the acoustic phonon, low-energy spin excitation and high-energy spin excitation baths are set to fulfill $C_{\text{acoustic}} > C_{\text{low-E}} \gg C_{\text{high-E}}$ ($1 > 0.25 > 5 \cdot 10^{-8}$) (Ref. [32]). The difference between the temperature transients T_{acoustic} and $T_{\text{high-E}}$ and their respective 3TM functions are minimized by varying the coupling parameters g_i . The resulting temperature functions are plotted with solid lines in Fig. 4 of the main manuscript.

$T_{\text{low-E}}$ approximately exponentially increases with $\tau_{\text{LRO}} \sim 55$ ps, giving the long-range disordering time. The high-energy spin excitations form a

dual probe of long-range and internal spin cluster order. Assuming a bi-exponential decay for the high-energy spin excitation transient, we find a $\tau_{\text{cluster}} \sim 400$ ps for the disordering of internal spin cluster order.

8.5.7 Temperature dependent time constants

The temperature dependence of the transient magnetic scattering time for the $\Delta S^z = +1$ excitation, and the phonon recovery time τ_{ph} , is shown in Fig. 8.17. No temperature dependence is apparent between 5 K and $T_C \approx 58$ K within the experimental accuracy.

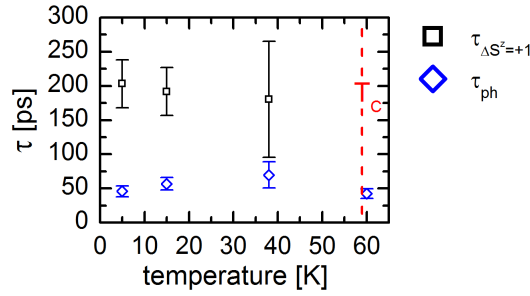


Figure 8.17: Temperature dependence of the transient spin excitation scattering for the $\Delta S^z = +1$ excitation $\tau_{\Delta S^z=+1}$ and the phonon recovery time τ_{ph} .

A qualitative temperature functional can be set up for the transient magnetic scattering time by assuming that the long-term equilibration dynamics is solely composed of upconversion of acoustic phonons into spin cluster excitations. This reduces the problem to a two-temperature model, of which the equilibration time can be related to the respective heat capacities of the two baths.^[40] The lattice heat capacity has a standard $C_{\text{lattice}}(T) \propto T^3$ dependence. The cluster excitations are gapped and only make a small contribution to the total heat capacity. This temperature functional is proportional to:

$$C_{\text{cluster}}(T) \propto \exp(-\Delta/k_B T) \cdot T^{3/2} \quad (8.5)$$

The $\propto T^{3/2}$ is the standard low-temperature magnetic heat capacity functional.^[32] The heat capacity for gapped excitations decreases exponentially.^[41] Here k_B is the Boltzmann-factor and Δ the energy gap, which is $\Delta > 25$ meV in the case of Cu_2OSeO_3 .

For the heat capacities we know that $C_{\text{lattice}} \gg C_{\text{cluster}}$. The equilibration time therefore can be estimated as:

$$\tau = \frac{1}{g} \frac{C_{\text{lat.}} C_{\text{cl.}}}{(C_{\text{lat.}} + C_{\text{cl.}})} \approx \frac{C_{\text{cl.}}}{g} \propto \frac{\exp(-\Delta/k_B T) \cdot T^{3/2}}{g} \quad (8.6)$$

Here g is the coupling constant between the cluster order bath and the lattice bath. The lattice and cluster bath heat capacities are indicated with $C_{\text{lat.}}$ and $C_{\text{cl.}}$. We thus see that under the most simple approximation of a 2TM the transient magnetic spectral weight transfer time thus has to increase with temperature. This behaviour does not capture the temperature independent time constant plotted in Fig. 8.17. Effective temperature modelling of magnetization in Cu_2OSeO_3 thus only works to a certain extent.

8.5.8 Transient absorption spectroscopy measurement

A transient absorption spectroscopy measurement was performed at $T = 10$ K on a double-polished sample with [111] orientation and a thickness of $221 \mu\text{m}$. The sample was photoexcited with 2.0 eV pump pulses at a fluence of $F \approx 0.2 \text{ mJ/cm}^2$. This results in a similar order of magnitude of photoexcitation density as the time-resolved Raman study. A broadband white light probe pulse measures the change in absorption within the green transparency window of Cu_2OSeO_3 .

Figure 8.18 shows the static absorption α measured in units of cm^{-1} (right y-axis) at $T = 10$ K (also see chapter 4). The left y-axis gives the photo-induced absorption $\Delta\alpha$ at different indicated time-delays. The change in absorption is positive. Figure 8.19a shows the time-transient of the integrated $\Delta\alpha$ signal around 2.35 eV probe energy on long time-scales. A $\tau_2 \sim 50$ ps is observed. On the fastest time-scale, as shown in Fig. 8.19b a $\tau_1 \sim 0.5$ ps decay is observed.

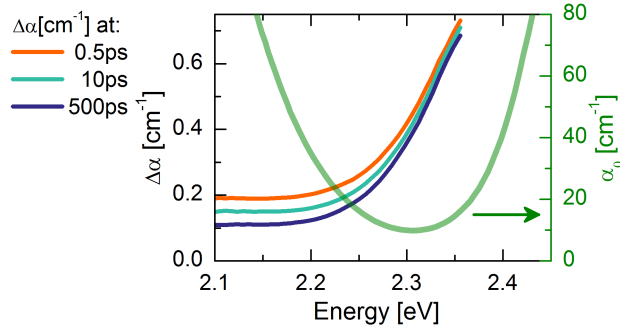


Figure 8.18: The green curve gives the static absorption α measured in units of cm^{-1} . The left y-axis gives the photoinduced absorption $\Delta\alpha$ at different indicated time-delays. In both the crystal-field and charge transfer excitation region an increase in absorption is observed.

The observation of a photoinduced increase in absorption supports the assignment of the decrease in Raman scattering efficiency to a decrease of the probe volume term $V_{\text{probe}}[\alpha(\omega)]$. The long timescale of $\tau_2 \sim 50$ ps corresponds to the lattice thermalization. The short timescale of $\tau_1 \sim 0.5$ ps is

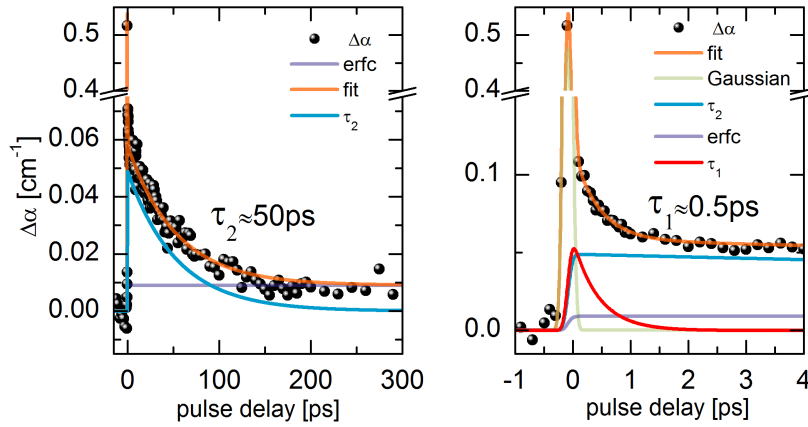


Figure 8.19: a) Time-transient of the integrated $\Delta\alpha$ signal around 2.35 eV probe energy on long time-scales. A $\tau_2 \sim 50$ ps is observed. b) A faster decay of $\tau_1 \sim 0.5$ ps decay is observed, which is tentatively assigned to optical phonon to acoustic phonon decay.

tentatively assigned to optical phonon to acoustic phonon decay.

8.6 Own contributions and acknowledgements

The main part of this chapter is based on the manuscript:

R. B. Versteeg, J. Zhu, C. Boguschewski, F. Sekiguchi, A. Sahasrabudhe, K. Budzinauskas, P. Padmanabhan, P. Becker, D. I. Khomskii, and P. H. M. van Loosdrecht,
Coupled dynamics of long-range and internal spin cluster order in Cu_2OSeO_3
e-print arXiv:1902.05329 [cond-mat.mtrl-sci] (2019).

I performed the steady-state and time-resolved Raman spectroscopy experiments, with assistance from Jingyi Zhu, Christoph Boguschewski and Anuja Sahasrabudhe. Fumiya Sekiguchi and Kestutis Budzinauskas performed the transient absorption measurement. The data analysis was performed by myself. The single crystal used in this study has been grown by Petra Becker. The text of the main part of this chapter has been written by myself, with contributions from P. H. M. van Loosdrecht and D. I. Khomskii. The appendix part has been written by myself.

I would like to thank D. Inosov (Dresden, DE), S. Diehl (Cologne, DE), C. Kollath (Bonn, DE) and F. Parmigiani (Trieste, IT) for fruitful discussion.

8.7 Bibliography

- [1] J. P. Attfield, Orbital molecules in electronic materials. *APL Mater.* **3**, 17 (2015).
- [2] S. V. Streltsov and D. I. Khomskii, Orbital physics in transition metal compounds: new trends, *Phys. Usp.* **60**, 1121 (2017).
- [3] M. S. Senn, J. P. Wright, and J. P. Attfield, Charge order and three-site distortions in the Verwey structure of magnetite, *Nature* **481**, 173 (2012).
- [4] S. de Jong, R. Kukreja, C. Trabant, N. Pontius, C. F. Chang, T. Kachel, M. Beye, F. Sorgenfrei, C. H. Back, B. Bräuer, W. F. Schlotter, J. J. Turner, O. Krupin, M. Doehler, D. Zhu, M. A. Hossain, A. O. Scherz, D. Fausti, F. Novelli, M. Esposito, W. S. Lee, Y.-D. Chuang, D. H. Lu, R. G. Moore, M. Yi, M. Trigo, P. Kirchmann, L. Pathey, M. S. Golden, M. Buchholz, P. Metcalf, F. Parmigiani, W. Wurth, A. Föhlich, C. Schüßler-Langeheine, and H. A. Dürr, Speed limit of the insulator-metal transition in magnetite, *Nat. Mater.* **12**, 882 (2013).
- [5] J. P. Sheckelton, J. R. Neilson, D. G. Soltan, and T. M. McQueen, Possible valence-bond condensation in the frustrated cluster magnet $\text{LiZn}_2\text{Mo}_3\text{O}_8$, *Nat. Mater.* **11**, 493 (2012).
- [6] W. H. McCarroll, L. Katz, and R. Ward, Some ternary oxides of tetravalent molybdenum, *J. Am. Chem. Soc.* **79**, 5410 (1957)
- [7] O. Janson, I. Rousochatzakis, A. A. Tsirlin, M. Belesi, A. A. Leonov, U. K. Rößler, J. Van den Brink, and H. Rosner, The quantum nature of skyrmions and half-skyrmions in Cu_2OSeO_3 , *Nat. Commun.* **5**, 5376 (2014).
- [8] S. Wall, S. Yang, L. Vidas, M. Chollet, J. M. Glowina, M. Kozina, T. Katayama, T. Henighan, M. Jiang, T. A. Miller, D. A. Reis, L. A. Boatner, O. Delaire, M. Trigo, Ultrafast disordering of vanadium dimers in photoexcited VO_2 , *Science* **362**, 572 (2018).
- [9] A. Kirilyuk, A. V. Kimel, and T. Rasing, Ultrafast optical manipulation of magnetic order, *Rev. Mod. Phys.* **82**, 2731 (2010).
- [10] S. Seki, X. Z. Yu, S. Ishiwata, and Y. Tokura, Observation of skyrmions in a multiferroic material, *Science* **336**, 198 (2012).
- [11] N. Ogawa, S. Seki, and Y. Tokura, Ultrafast optical excitation of magnetic skyrmions, *Sci. Rep.* **5**, 9552 (2015).
- [12] M. C. Langner, S. Roy, S. W. Huang, J. D. Koralek, Y.-D. Chuang, G. L. Dakovski, J. J. Turner, J. S. Robinson, R. N. Coffee, M. P. Minitti, S. Seki, Y. Tokura, and R. W. Schoenlein, Nonlinear ultrafast spin scattering in the skyrmion phase of Cu_2OSeO_3 , *Phys. Rev. Lett.* **119**, 107204 (2017).
- [13] J. S. White, I. Živković, A. J. Kruchkov, M. Bartkowiak, A. Magrez, and H. M. Rønnow, Electric-field-driven topological phase switching and Skyrmion-lattice metastability in magnetoelectric Cu_2OSeO_3 , *Phys. Rev. Applied* **10**, 014021 (2018).
- [14] J. M. Hopkinson and H.-Y. Kee, Geometric frustration inherent to the trillium lattice, a sublattice of the B20 structure, *Phys. Rev. B* **74**, 224441 (2006).
- [15] J.-W. G. Bos, C. V. Colin, and T. T. M. Palstra, Magnetoelectric coupling in the cubic ferrimagnet Cu_2OSeO_3 , *Phys. Rev. B* **78**, 094416 (2008).
- [16] G. S. Tucker, J. S. White, J. Romhányi, D. Szaller, I. Kézsmárki, B. Roessli, U. Stuhr, A. Magrez, F. Groitl, P. Babkevich, P. Huang, I. Živković, and H. M. Rønnow. Spin excitations in the skyrmion host Cu_2OSeO_3 , *Phys. Rev. B* **93**, 054401 (2016).

- [17] T. Adams, A. Chacon, M. Wagner, A. Bauer, G. Brandl, B. Pedersen, H. Berger, P. Lemmens, and C. Pfleiderer, Long-wavelength helimagnetic order and skyrmion lattice phase in Cu_2OSeO_3 , *Phys. Rev. Lett.* **108**, 237204 (2012).
- [18] J. Romhanyi, J. van den Brink, and I. Rousochatzakis, Entangled tetrahedron ground state and excitations of the magnetoelectric skyrmion material Cu_2OSeO_3 , *Phys. Rev. B* **90**, 140404 (2014).
- [19] M. Ozerov, J. Romhanyi, M. Belesi, H. Berger, J.-Ph. Ansermet, Jeroen van den Brink, J. Wosnitzer, S. A. Zvyagin, and I. Rousochatzakis, Establishing the fundamental magnetic interactions in the chiral skyrmionic Mott insulator Cu_2OSeO_3 by terahertz electron spin resonance, *Phys. Rev. Lett.* **113**, 157205 (2014).
- [20] P. Y. Portnichenko, J. Romhanyi, Y. A. Onykienko, A. Henschel, M. Schmidt, A. S. Cameron, M. A. Surmach, J. A. Lim, J. T. Park, A. Schneidewind, D. L. Abernathy, H. Rosner, J. van den Brink, and D. Inosov, Magnon spectrum of the helimagnetic insulator Cu_2OSeO_3 , *Nat. Commun.* **7**, 10725 (2016).
- [21] D. Fausti and P. H. M. van Loosdrecht, in *Optical Techniques for Solid-State Materials Characterization*, edited by R. P. Prasankumar and A. J. Taylor, (CRC Press, Boca Raton London New York, 2012).
- [22] M. Belesi, I. Rousochatzakis, H. C. Wu, H. Berger, I. V. Shvets, F. Mila, and J-Ph. Ansermet, Ferrimagnetism of the magnetoelectric compound Cu_2OSeO_3 probed by ^{77}Se NMR, *Phys. Rev. B* **82**, 094422 (2010).
- [23] V. P. Gnezdilov, K. V. Lamonova, Y. G. Pashkevich, P. Lemmens, H. Berger, F. Bussy, and S. L. Gnatchenko, Magnetoelectricity in the ferrimagnetic Cu_2OSeO_3 : symmetry analysis and Raman scattering study, *Low Temp. Phys.* **36**, 550 (2010).
- [24] K. H. Miller, X. S. Xu, H. Berger, E. S. Knowles, D. J. Arenas, M. W. Meisel, and D. B. Tanner, Magnetodielectric coupling of infrared phonons in single-crystal Cu_2OSeO_3 , *Phys. Rev. B* **82**, 144107 (2010).
- [25] V. S. Kurnosov, V. P. Gnezdilov, V. V. Tsapenko, P. Lemmens, and H. Berger, Analysis of the low-frequency spectrum of the cubic noncentrosymmetric ferrimagnet Cu_2OSeO_3 , *Low Temp. Phys.* **38**, 489 (2012).
- [26] M. G. Cottam and D. J. Lockwood, *Light scattering in magnetic solids*, (Wiley New York, NY, 1986).
- [27] P. A. Fleury and R. Loudon, Scattering of light by one- and two-magnon excitations, *Phys. Rev.* **166**, 514 (1968).
- [28] N. J. Laurita, G. G. Marcus, B. A. Trump, J. Kindervater, M. B. Stone, T. M. McQueen, C. L. Broholm, and N. P. Armitage, Low-energy magnon dynamics and magneto-optics of the skyrmionic Mott insulator Cu_2OSeO_3 , *Phys. Rev. B* **95**, 235155 (2017).
- [29] S. H. Liu, Magnetic excitations above the critical temperature, *Phys. Rev. B* **13**, 2979 (1976).
- [30] E. J. Samuelsen and M. Melamud, Spin waves in antiferromagnets with alternating strong and weak coupling, *J. Phys. C: Solid State Physics* **7**, 4314 (1974).
- [31] A. Compaan and H. J. Trodahl, Resonance Raman scattering in Si at elevated temperatures, *Phys. Rev. B* **29**, 793 (1984).
- [32] N. Prasai, B. A. Trump, G. G. Marcus, A. Akopyan, S. X. Huang, T. M. McQueen, and J. L. Cohn, Ballistic magnon heat conduction and possible Poiseuille flow in the helimagnetic insulator Cu_2OSeO_3 , *Phys. Rev. B* **95**, 224407 (2017).
- [33] C. Kittel, Interaction of spin waves and ultrasonic waves in ferromagnetic crystals, *Phys. Rev.* **110**, 836 (1958).

-
- [34] A. V. Kimel, R. V. Pisarev, J. Hohlfeld, and T. Rasing, Ultrafast quenching of the antiferromagnetic order in FeBO₃: Direct optical probing of the phonon-magnon coupling, *Phys. Rev. Lett.* **89**, 287401 (2002).
- [35] P. G. Klemens, Anharmonic decay of optical phonons, *Phys. Rev.* **148**, 845 (1966).
- [36] T. Ogasawara, K. Ohgushi, Y. Tomioka, K. S. Takahashi, H. Okamoto, M. Kawasaki, and Y. Tokura, General features of photoinduced spin dynamics in ferromagnetic and ferrimagnetic compounds, *Phys. Rev. Lett.* **94**, 087202 (2005).
- [37] L. Perfetti, P. A. Loukakos, M. Lisowski, U. Bovensiepen, H. Eisaki, and M. Wolf, Ultrafast electron relaxation in superconducting Bi₂Sr₂CaCu₂O_{8+δ} by time-resolved photoelectron spectroscopy, *Phys. Rev. Lett.* **99**, 197001 (2007).
- [38] T. Nomura, X.-X. Zhang, S. Zherlitsyn, J. Wosnitza, Y. Tokura, N. Nagaosa, and S. Seki, Phonon magnetochiral effect, e-print arXiv:1809.08775 [cond-mat.mtrl-sci] (2018).
- [39] Z. Alpichshev, F. Mahmood, G. Cao, and N. Gedik, Confinement-deconfinement transition as an indication of spin-liquid-type behavior in Na₂IrO₃, *Phys. Rev. Lett.* **114**, 017203 (2015).
- [40] A. Caretta, M. C. Donker, D. W. Perdok, D. Abbaszadeh, A. O. Polyakov, R. W. A. Havenith, T. T. M. Palstra, and P. H. M. van Loosdrecht, Measurement of the acoustic-to-optical phonon coupling in multicomponent systems, *Phys. Rev. B* **91**, 054111 (2015).
- [41] A. Tari, *The specific heat of matter at low temperatures* (Imperial College, London, 2003)

Summary

This thesis addresses optically probed order and dynamics in the chiral cluster magnet Cu_2OSeO_3 . Cu_4 triplet clusters form the relevant spin entity for the formation of long-range magnetic order in this Mott insulator. As such, we can envision the magnetic ground state of this material as being a helix of spin clusters. Under an applied magnetic field different metamagnetic phases form, among others and most intriguingly, a topologically protected skyrmion lattice phase. The broken spatial inversion and time-reversal symmetry leads to a variety of optical phenomena in Cu_2OSeO_3 , which are studied with a newly constructed polarization spectroscopy setup. It is shown that the broken spatial inversion symmetry leads to strong dipole active crystal field excitations below the charge transfer gap, and in addition, to natural optical activity. The natural optical activity may be used as a probe for structural chirality, and shows sensitivity to magnetic ordering, evidencing a finite magneto-electric coupling. Under external magnetic fields a strong magneto-optical response is observed, which is discussed to originate from spin cluster formation and the relative ease of magnetic domain reorientation. The strong Faraday-rotation is used to probe the metamagnetic phase transitions and to all-optically map the metamagnetic phase diagram of Cu_2OSeO_3 , including the topologically protected skyrmion lattice phase. Previous work has shown that the long-range spin cluster ordering results in a characteristic spin wave spectrum which can be divided into low-energy external and high-energy internal spin cluster excitations. Here, spontaneous Raman spectroscopy was used to observe multiple spin cluster transitions at the Brillouin zone center, of which the Raman-activity is discussed to originate in the Elliot-Loudon light scattering mechanism. The temperature dependent scattering response of the high-energy internal cluster modes shows a crossover from broad continuum scattering above the critical temperature T_C into well-defined magnetic modes below T_C , which is discussed to originate from a change of the character of the internal cluster modes. Above T_C the internal spin cluster excitations have a localized magnetic excitation character, while in the long-range ordered phase the modes acquire dispersion, and correspond to optical magnons. Finally, using a home built novel time-resolved Raman spectroscopy setup, the photoinduced near-equilibrium spin and lattice dynamics of the helimagnetic phase was probed.

Multiple ps-decade spin-lattice relaxation dynamics is observed, evidencing a separation of the order parameter dynamics into disordering of long-range and internal spin cluster order. The observations of the steady-state and time-resolved Raman study exemplify that Cu_2OSeO_3 can be regarded as a solid-state molecular crystal of spin nature.

Zusammenfassung

Die vorliegende Doktorarbeit befasst sich mit optische Studien der Ordnung und Dynamik in dem chiralen Clustermagnet Cu_2OSeO_3 . Cu_4 triplet Cluster bilden die relevante Spineinheiten für die langreichweitige magnetische Ordnung in diesem Mott-Isolator. Im Grundzustand richten die Spinclustern sich Helimagnetisch aus. Verschiedene metamagnetische Phasen formen sich in einem magnetischen Feld, einschließlich eines topologisch geschützten Skymionengitters. Es wird besprochen wie der Bruch der Räumlicher- und Zeitumkehrsymmetrien in Cu_2OSeO_3 zu einer Vielzahl von optische Effekten führt, welche mittels eines zu diesem Zweck aufgebauten Polarizationspektroskopieaufbaus untersucht werden. Die gebrochene räumliche Inversionssymmetrie führt zu starken, dipolaktiven Kristalfeldanregungen unterhalb der Ladungstransferbandlücke, und darüber hinaus zur optischen Aktivität, welches benutzt werden kann um die kristallographische Chiralität eines Cu_2OSeO_3 Kristalls zu bestimmen. Die (kristallographische) optische Aktivität zeigt eine Kopplung an die helimagnetischen Ordnung, in Übereinstimmung mit der Tatsache dass Cu_2OSeO_3 ein magnetoelektrisches Material ist. Ein starker magneto-optischer Effekt ist messbar wenn ein magnetisches Feld angelegt wird. Die Stärke des magneto-optischen Effektes lässt sich mittels der Clusterformierung und der weichen magnetokristallinen Anisotropie erklären. Die Faraday-Rotation lässt sich nutzen um die feld- und temperaturabhängigen metamagnetischen Phasenübergänge zu messen und um das metamagnetische Phasendiagramm, - inklusive Skymionengitterphase -, rein optisch zu kartieren. Die aus spin Clustern bestehende langreichweitige magnetische Ordnung führt zu einem charakteristischen Spinwellenspektrum, welches in niedrigenergetische externe und hochenergetische interne Clusteranregungen unterteilt werden kann. In dieser Arbeit werden Clusteranregungen im Zentrum der Brillouinzone mittels Ramanspektroskopie gemessen. Die Clusteranregungen sind durch den Elliot-Loudon Lichtstreuungsmechanismus Ramanaktiv. Oberhalb der langreichweitigen Ordnungstemperatur T_C wird ein breites kontinuierliches magnetisches Lichtstreuungsspektrum gemessen, im Gegenteil zu Temperaturen unterhalb vom T_C , wo scharfe magnetische Anregungen gemessen werden. Dieser Übergang im Lichtstreuungsspektrum lässt sich durch eine Änderung der Natur der Clusteranregungen erklären. Die Clusteranregungen sind lokalisierte magnetis-

che Anregungen oberhalb T_C . In der langreichweitigen geordneten Phase zeigen die Clusteranregungen eine Dispersion. Photoinduzierte Spin- und Kristalgitterdynamik wurde gemessen mittels eines zu diesem Zweck aufgebauten zeitaufgelösten Ramanspektroskopieaufbaus. Die Ergebnisse zeigen Spin-Gitterdynamik über mehrere ps-Dekaden. Dies lässt sich wie folgt interpretieren: zuerst löst sich die langreichweitige magnetische Ordnung auf, und signifikant später erst die interne Clusterordnung. Die Ergebnisse der Ramanstudien bestätigen die Beschreibung von Cu_2OSeO_3 als magnetischer Molekulkristall vom Spin Freiheitsgrad.

Samenvatting

Dit proefschrift behandelt optisch gemeten orde en dynamica in de chirale clustermagneet Cu_2OSeO_3 . Cu_4 tripletclusters vormen de relevante spin-eenheden voor de magnetische langeafstandsordering in deze Mott-isolator. Zodoende kunnen we de magnetische grondtoestand voorstellen als een helix gevormd uit spinclusters. Verschillende metamagnetische fases vormen onder een extern magnetisch veld, waaronder een topologisch beschermde skyrmionroosterfase. Gebroken geometrische inversiesymmetrie en tijdsomkerings-symmetrie leiden tot een variëteit aan optische fenomenen in Cu_2OSeO_3 , die bestudeerd worden met een speciaal voor deze studie gebouwde polarisatiespectroscopieopstelling. We laten zien dat de gebroken geometrische inversiesymmetrie leidt tot sterke dipoolactieve kristalveldexcitatie beneden de ladingstransferbandkloof en tot optische activiteit. De optische activiteit kan gebruikt worden als meetmethode voor de chiraliteit van de kristalstructuur. Daarnaast is de (kristallografische) optische activiteit gekoppeld aan de helimagnetische ordening. Dit laat zien dat Cu_2OSeO_3 een magneto-elektrisch materiaal is. Een sterk magneto-optisch effect is meetbaar wanneer een extern magnetisch veld wordt aangelegd. De sterkte van het magneto-optische effect komt voort uit de spinclusterordering en de zwakke magnetokristallijne anisotropie. De Faraday-rotatie wordt gebruikt om de veld- en temperatuurafhankelijke metamagnetische faseovergangen te meten en om het metamagnetische fase-diagram, inclusief de skyrmionroosterfase, volledig optisch in kaart te brengen. In eerder werk is aangetoond dat de langeafstandsordering van spinclusters leidt tot een karakteristiek spinexcitatie-spectrum, dat kan worden verdeeld in laagenergetische externe en hoogenergetische interne spinclusterexcitatie. In het hier beschreven onderzoek wordt Ramanspectroscopie gebruikt om Brillouinzone Γ -punt spinclusterexcitatie te meten. Deze spinclusterexcitatie zijn Raman-actief door het Elliot-Loudon lichtstrooiingsmechanisme. Boven de langeafstandsorderingstemperatuur T_C wordt een breed continue magnetisch lichtstrooiingspectrum gemeten, terwijl beneden T_C scherpe excitatie worden gemeten. Deze verandering in het lichtstrooiingspectrum komt voort uit het veranderen van het karakter van de interne spinclusterexcitatie. De spinclusterexcitatie zijn lokale dispersieloze magnetische excitatie boven T_C , terwijl in de langeafstandsgeordende fase de spinclusterexcitatie disper-

sie vertonen. De foto-geïnduceerde spin- en kristalroosterdynamica van Cu_2OSeO_3 wordt bestudeerd met behulp van een speciaal voor dit experiment opgebouwde tijdsopgeloste Ramanspectroscopieopstelling. De resultaten laten spin-roosterrelaxatiedynamica over meerdere ps-decaden zien. Dit laat zich als volgt verklaren: eerst wanordent de langeafstandsclusterordering en significant later de interne spinclusterordering. De resultaten van de Ramanstudie onder thermodynamisch evenwicht en de tijdsopgeloste Ramanstudie laten zien dat Cu_2OSeO_3 kan worden beschouwd als een moleculair kristal van spinvrijheidsgraad.

Acknowledgements

During my time in Cologne I had the pleasure to meet a lot of new people, work with many scientists and other university staff, got inspired by many, and from time to time got necessary support.

I would first like to thank my promotor Prof. Paul van Loosdrecht for giving me the opportunity to work in his new group in Cologne. Paul, we know each other already from my third study year (2010), the year when my interest in condensed matter physics got awakened. At that time I blindly chose the elective course “Photons and Matter”, and years later I find myself in Germany, finishing a PhD thesis on photons and matter. This says a great deal about you, and that’s why I want to thank you for sharing with me your enthusiasm for condensed matter physics and optical spectroscopy! Very early on you gave me (and other students) the opportunity to work at a high level of independence, and work on topics which in the first place should interest us students. This allowed me to work out studies of the research proposal on skyrmions which I wrote during the Nanoscience master. Of course I did not do this alone. I want to thank you for your guidance during the PhD project, your suggestions on how to improve myself as a scientist, the scientific discussions, and of course also the good times outside the scientific context. You always try to make your students reach for the best of what they can. In my case that lead to a thesis of around 200 pages. I want to wish you all the best with all the nice science to come from the CRC, and we surely keep in touch.

I would like to thank Prof. Markus Grüninger for being referent, but above all for the input to the Optically Probed project. I feel like that this project became a success thanks to your enthusiasm, knowledge, and drive to deliver “a good scientific product” (students and papers). I learned a great deal from you!

I would like to thank Prof. Christian Back from the Technische Universität München for being a thesis referent. I would like to thank Prof. Achim Rosch for being the Vorsitzender der Prüfungskommission, and for the discussions we had over the years on my PhD project.

I would like to thank Prof. Petra Becker and Prof. Ladislav Bohatý for providing our group with the highest quality samples one could possibly wish for. The Cu_2OSeO_3 Raman project became a success, and I hope that

some of the many trial and error studies on other samples I started will eventually be picked up by a successor. I also want to thank you for sharing with me your enthusiasm for mineralogy and crystallography over the years in Cologne!

I would like to thank Prof. Daniel Khomskii for all his help and suggestions with the cluster manuscript. This has made the work an order of magnitude better, but above all, the discussions were a source of renewed inspiration for me. I'm sure you will inspire many more physicists at the University of The World, and stay the number one trendsetter in transition metal oxide physics for many more years to come!

I also want to thank Prof. Fulvio Parmigiani. Fulvio, by chance we met in my first week when I was in Berkeley in 2012. Back then you were so kind to show me, a lost Dutch student, around in Berkeley, one of the many home towns you have. During your many visits to Cologne I have come to know you as a source for physics inspiration and a walking encyclopedia of electromagnetism. More importantly, you know how to inspire students and to make sure that the "the physics flame" keeps burning, something which I believe many students before me have already written about you, and I also want to acknowledge this as being true! Furthermore, I always enjoyed the dinners with you and Caesarina, and our chats on culture, history, and food of the most beautiful country on earth, Italy!

Jingyi, working with you was from time to time a pleasure, and also from time to time tough. I think we can both be very proud of the results we booked together over the last 4 years: a successful setup, which resulted in many time-resolved Raman publications and surely more to come for the group! I will never forget your "just do" and "no shitty bla bla" philosophy, and will apply this again whenever the situation is appropriate!

Simon, you were one of the first master students to join the group, and that during a wild west time which by now I can categorize as "the early years". This time knew many highlights, such as placing optical tables in labs, making working in the lab more comfortable with Lautsprecher, the shared passion for music ranging from "swag" to classical music, getting the first MOKE spectra, and the first observation of Skyrmi's through the "Kerraday"-effect! I think we together formed a very good team of "2 PhD students" during your master project and my PhD project. Without your lab skills and talents the magneto-optics project would not have run as smoothly as it did!

Britta, du bist schon von Anfang an in der Gruppe. Ich möchte mich für die sehr schöne Zeit, die wir zusammen im Institut (und im Bergischen Land) verbracht haben, bedanken. Du warst immer für ein gutes Gespräch und Unterstützung mit Bürokratie oder Buchungen da. Ich wünsche dir das allerbeste im Norden!

Thomas, I want to also thank you for helping out with Bürokratie in the early years, the nice time in the group, and above all an unforgettable

Carnaval experience.

Ich möchte auch Jens Koch und Michael Kuß für die technische Unterstützung im Labor danken. Dabei möchte ich auch Lucie Hamdan, Norbert Henn und Ralf Müller danken. Die mechanische- und e- Werkstatt hat vor allem in den ersten Jahren unserer Arbeitsgruppe viel geholfen. Meinen größten dank dafür!

Ignacio, I want to thank you for your work on the magneto-optics project and for introducing me to the art of preparing samples for optical studies (already back in 2013, time flies!). I wish you and your family all the best in Cologne!

Christoph, you joined the group in the wild west time where the time-resolved Raman setup had to be constructed, and of course used for science. After trying out a few other magnetic materials we decided to work on Cu_2OSeO_3 . The results of our work together turned out to become the major part of my PhD thesis! I want to thank you for all the effort you have put into this project, and I'm happy that I could work this into 2 publications with you as a co-author! Also I should thank you for showing me that Star Wars is not that bad after all (I'm a fan now). I wish you all the best with your new job!

Dario, you are a bright student and it was a pleasure to work with you. The time you spent in the lab paid off and helped to successfully finish the magneto-optical project. I want to wish you all the best with the rest of your physics study!

Max, when you came by for a bachelor project, I tried to steer you into choosing a magneto-optics project because that would work, and NOT the time-resolved Raman with photomultiplier project, because I felt that would be asking for disaster. How have you proven me wrong! With your inexhaustible enthusiasm and perseverance you just got the job done! I've learned a lot of working with you together. Your mindset is fantastic, where you even showed to be enthusiastic about measuring noise. You furthermore made me change my opinion on singer-song guitar music, a second time you proved me wrong. I wish you all the best chasing your dreams, and that you do this demonstrates what a great person you are!

Anuja, you were the last student I worked with. Your project was again wild west, because science just maybe is wild west. During your master project you were not thrown off balance when hardship arose. I see that you have true passion for science, and that's why I'm absolutely sure you'll be again successful in your PhD with topic "magnetism". I'm gonna miss the coffee breaks together!

Ionela, we only worked together on the SrRuO_3 project, but I wish we could have worked together more intensively. I always enjoyed our science discussions and lunch breaks together, and we will see each other again!

Ramil, you worked on the SrRuO_3 project, which was really your project, and I could sort of be the "Static MOKE consultant". You have shown to

work independently, quickly figured out that you can solve lab challenges, and you produced a lot of data! I always enjoyed our chats about “the future”. I wish you success with your PhD project in Moscow!

Prashant, we started off as acquaintances, and by now are best friends! GaV₄S₈ was the magic material to make this happen. You are the most gifted experimental (lab and numerical simulation) physicist I met. Our teamwork delivered a beautiful Padmanabhan *et al.* on GaV₄S₈. More importantly than the time in the lab and the numerous science discussions, were the coffees, the 4th of July grill, Thanksgiving parties, and movie nights with the group, where you were always the driving force to organize this. When somebody leaves the group, this is always felt, especially after you left. However, even from January 2018 onward you still live on in the group, for instance through by now commonly used American sayings like “put it on the back burner”. The most beautiful memories were made after you left Cologne, and when we met in your homeland. The bar crawl by car with you and Sandhya in Galveston, where we maybe have only walked a 100 feet in total and drove the rest, was an unforgettable experience. Just recently we met in the city of Frank Underwood. This weekend was again unforgettable, and we can call ourselves “shutdown survivors”. See you in Detroit!

Matteo, I know you already from when I did a bachelor project in the OCMP group in Groningen. Back then you were already the “go to” person to discuss the most complex science questions, and you’ve stayed this person in Cologne. I’m very happy to see that you’ve found your place in Geneva, and we will surely meet again.

Yajun, we already met each other in Groningen, but only really started to know each other in Cologne. I think that everybody we know will agree with me that you are one of the kindest persons on planet earth. We always had a good time in office 315 (even in the weekends). Two very special days were back in our old town Groningen, where you had your defense and I had the honour to be paranimf. I wish you and your family all the best, and I’m sure that one day our paths will cross again!

Kestutis Kestinauskas, we know each other from day 1 (1st of September 2013) and if I recollect well, we went for lunch together on that day to get a kebab(as). Over the years I still did not learn to appreciate this highly nutritious product as much as you do, but we nevertheless found a shared passion in coffee (since 2017 known as “cofveve”). We always had a good time in the lab(as) and office 315 (ordering stuff at Thorlabas and working with Matlabas). Also I enjoyed the good times at the WG and Bickendorf. I still hope that one day I can come and visit you, Vaiva, and Jonas in Lithuania, where I’m sure it won’t be as cold as you always pretend it to be.

Henning, you are my reliable partner to enjoy the “Gastronomie” at the Mensa, a chat during a smoke break (where I would smoke an imaginary cigarette) or a walk around the physics building. As it turned out, we

have a shared passion for the most mental sports there is, darts! The darts tournament you, Rafael, and me visited in the Lanxess Arena I will always remember!

Rafael, you are one of the kindest and helpful persons I met in Cologne. You are the go to person when it comes down to (advice on) dealing with Deutsche und Kölsche Situationen. Over the years I've realized that you are a modern Goethe. You can do science, play violin and bass guitar, direct music videos, screenwriting, and I'm absolutely sure that one day the world can expect literature and poetry from your hand.

Evgenia, Bernhard, Elina, Kiran, Fumiya, Yu, Sebastian, Fatima, Hamed, Lin, Chris, Lena, Alessandro, Jörg, Manpreet, the SFB staff members Benita and Clara, the colleagues from the SFB student council Henry, Finn Lasse, Daniel, and all the other colleagues from the II. Physikalisches Institut, I also want to thank you for the good times together over the last years!

Andrea Severing, we really only got to know each other around the magnetism conference in Barcelona in 2015. You were there with your team, and I was the only delegate from our group. I recollect this as a fantastic week. I want to thank you for being such a kind person, and for all the support and advice you gave me over the years!

I would like to thank Petra Neubauer for the good chats we had from time to time, for survival help when the occasion asked for it during my years at the faculty, and the financial support through the Bonn-Cologne Graduate School.

Ron Tobey, I realized that the acknowledgments of my PhD thesis are an appropriate place to thank you again. Back in Groningen, when I received my Master's degree, you told me that I would take with me a "optics toolbox" from the time in your group. This lab skills toolbox showed to be an invaluable asset, and formed a rock solid foundation which helped me to succeed during during my PhD career.

I would like to thank Aisha Aqeel and Prof. Thomas Palstra from the University of Groningen for the big Cu_2OSeO_3 crystals. The size of these crystals were instrumental for the success of the magneto-optical project!

There is of course also still a world outside the physics bubble.

Alberto, we know each other for more than five years now. In this time a special friendship has built up between us. The visits and the welcoming ambiance in Via Fossamana, and the trips to Mantova and other cities in north Italy I reminisce as beautiful days, like a daydream. I hope we soon see each other again.

Felix, our paths in life could have already crossed in The Netherlands, but we eventually met in Cologne. A special friendship for me has grown between us, two Mr. Know It All's.

Robin, we kennen elkaar vanaf week 1, waar het bleek dat we in hetzelfde schuitje zaten van "nieuw en Nederlander in Keulen". Als we elkaar weer zien is het altijd gezellig, en ik hoop dat dat ook zo blijft. De dag dat jij

en André “De Boompjes” zijn geworden herinner ik me als een van mijn mooiste dagen in Keulen!

Ich möchte mich auch bei alle Freunden von SC. Aqua Köln, insbesondere den Freunde des SC. Aqua Spezial Teams, bedanken für die (geistig) entspannende Trainingsstunden im Schwimmbecken, welche ich von Zeit zu Zeit gut brauchen konnte.

Ich möchte auch allen meinen Freunden an der Bachemer Straße, insbesondere Imge und Lorraine, für die schöne Zeit danken, die wir zusammen verbracht haben. Wir werden uns sicherlich in der Zukunft wieder treffen!

Mart en Geert, we spreken elkaar bijna elke dag. Geert, jij was “die irritante Geert met die grote tas” ten tijde van dat ik ook nog een carrière buiten het laserschieten had. Mart, we hebben elkaar leren kennen in Groningen tijdens een heel kort tijdsbestek tussen Berkeley en Keulen (2013). Jij was toen die veels te aardige jongen, en dat ben je nog steeds. Dat er een vriendschap is gegroeid tussen ons drieën waarin we alles kunnen delen met elkaar, vind ik heel bijzonder, ook gezien het feit dat we de afgelopen jaren verspreid hebben gewoond. Als we weer bij elkaar zijn in een van de drie wereldsteden Keulen, Maastricht of Barcelona, dan is dat een garantie voor mooie tijden. En nu is deze vriendschap schriftelijk vereeuwigd in het dankwoord van mijn proefschrift over lasers schieten, pieuw pieuw!

Kjell, Joris en Tamme (en Mart die hier al boven genoemd is), we zien elkaar de laatste jaren minder, maar als we weer samen zijn, danwel in Keulen, Amsterdam of op vakantie, dan is het weer net zo gezellig als vroeger. Ik zal nooit jullie hulp in de begindagen van Keulen vergeten. Dank daarvoor!

Eric en Hans, we zijn al vrienden sinds het werkcollege van week 1. Ik wil jullie bedanken voor de (moral) support die jullie me hebben gegeven. Helaas zien we elkaar veel minder dan tijdens onze studietijd in Groningen, een tijd die ik soms nog wel mis. Gelukkig hebben we elkaar toch elk jaar weer meerdere keren gezien, en dan is het altijd weer zo gezellig als vroeger. Ik weet zeker dat dat zo blijft!

Tenslotte wil ik nog de allerbelangrijkste personen in mijn leven bedanken. Bob en Hettie, mijn dank aan jullie zal altijd veel verder reiken dan wat ik in een paar zinnen opschrijven kan. De start in Keulen was complex, maar jullie waren er voor mij, net zoals jullie dat al een heel leven voor mij zijn. Ik ben jullie dankbaar voor alle mogelijkheden die jullie mij hebben gegeven om mij te ontwikkelen, te zijn wie ik ben, mij de vrijheid geven keuzes te maken die goed en kwaad uitpakken, en ik ben dankbaar voor dat we een hechte familie zijn, al een leven lang. Walter, hoe verder ik weg woon, des te meer groeit onze band. Ik zie meer en meer in dat we helemaal niet zo verschillend zijn. Als we weer met zijn vieren (of zessen) compleet zijn aan de Wismarstraat, dan zijn dat gelukkige dagen. Het is fijn om te weten dat Zwolle altijd een thuis blijft. Iason, we hebben elkaar in Keulen ontmoet. Sinds een paar jaartjes ben jij mijn grote alles. We hebben

enorm veel mooie momenten samen beleefd, en de tijd met jou samen is de mooiste tijd hier in Keulen voor mij geweest. Jij bent er voor mij in tijden van noodweer. Ik hoop dat ik dat ook voor jou kan zijn. Samen gaan wij de toekomst tegemoet!

List of publications

Peer reviewed

6. P. Padmanabhan, F. Sekiguchi, **R. B. Versteeg**, E. Slivina, S. Bordács, V. Tsurkan, I. Kézsmárki, P. H. M. van Loosdrecht, Optically driven collective spin excitations and magnetization dynamics in the Néel-type-skyrmion host GaV₄S₈, *Phys. Rev. Lett.* **122**, 107203 (2019)
5. J. Zhu, **R. B. Versteeg**, P. Padmanabhan, and P. H. M. van Loosdrecht, Dynamical resonance quench and Fano interference in spontaneous Raman scattering from quasiparticle and collective excitations, *Phys. Rev. B* **99**, 094305 (2019)
4. L. Wysocki, R. Mirzaaghayev, M. Ziese, L. Yang, J. Schöpf, **R. B. Versteeg**, A. Bliesener, J. Engelmayer, A. Kovács, L. Jin, F. Gunkel, R. Dittmann, Paul H. M. van Loosdrecht and I. Lindfors-Vrejoiu, Magnetic coupling of ferromagnetic SrRuO₃ epitaxial layers separated by ultrathin non-magnetic SrZrO₃/SrIrO₃, *Appl. Phys. Lett.* **113**, 192402 (2018)
3. **R. B. Versteeg**, J. Zhu, P. Padmanabhan, C. Boguschewski, R. German, M. Goedecke, P. Becker, and P. H. M. van Loosdrecht, A tunable time-resolved spontaneous Raman spectroscopy setup for probing ultrafast collective excitation and quasiparticle dynamics in quantum materials, *Struct. Dyn.* **5**, 044301 (2018)
2. **R. B. Versteeg**, I. Vergara, S. D. Schäfer, D. Bischoff, A. Aqeel, T. T. M. Palstra, M. Grüninger, and P. H. M. van Loosdrecht, Optically probed symmetry breaking in the chiral magnet Cu₂OSeO₃, *Phys. Rev. B* **94**, 094409 (2016)
1. M. C. Langner, S. Roy, A. F. Kemper, Y.-D. Chuang, S. K. Mishra, **R. B. Versteeg**, Y. Zhu, M. P. Hertlein, T. E. Glover, K. Dumesnil, R. W. Schoenlein, Scattering bottleneck for spin dynamics in metallic helical antiferromagnetic dysprosium, *Phys. Rev. B* **92**, 184423 (2015)

Preprints

- **R. B. Versteeg**, J. Zhu, F. Sekiguchi, C. Boguschewski, A. Saharabudhe, K. Budzinauskas, P. Padmanabhan, P. Becker, D. I. Khomskii, and P. H. M. van Loosdrecht, Coupled dynamics of long-range and internal spin cluster order in Cu₂OSeO₃, e-print arXiv:1902.05329 [cond-mat.mtrl-sci] (2019).

Offizielle Erklärung

Ich versichere, dass ich die von mir vorgelegte Dissertation selbständig angefertigt, die benutzten Quellen und Hilfsmittel vollständig angegeben und die Stellen der Arbeit – einschließlich Tabellen, Karten und Abbildungen –, die anderen Werken im Wortlaut oder dem Sinn nach entnommen sind, in jedem Einzelfall als Entlehnung kenntlich gemacht habe; dass diese Dissertation noch keiner anderen Fakultät oder Universität zur Prüfung vorgelegen hat; dass sie – abgesehen von unten angegebenen Teilpublikationen – noch nicht veröffentlicht worden ist sowie, dass ich eine solche Veröffentlichung vor Abschluss des Promotionsverfahrens nicht vornehmen werde. Die Bestimmungen der Promotionsordnung sind mir bekannt. Die von mir vorgelegte Dissertation ist von Prof. Dr. Ir. P.H.M. van Loosdrecht betreut worden.

Teilpublikationen:

- **R. B. Versteeg**, J. Zhu, F. Sekiguchi, C. Boguschewski, A. Saharabudhe, K. Budzinauskas, P. Padmanabhan, P. Becker, D. I. Khomskii, and P. H. M. van Loosdrecht, Coupled dynamics of long-range and internal spin cluster order in Cu_2OSeO_3 , e-print arXiv:1902.05329 [cond-mat.mtrl-sci] (2019).
- J. Zhu, **R. B. Versteeg**, P. Padmanabhan, and P. H. M. van Loosdrecht, Dynamical resonance quench and Fano interference in spontaneous Raman scattering from quasiparticle and collective excitations, accepted for publication in Phys. Rev. B
- **R. B. Versteeg**, J. Zhu, P. Padmanabhan, C. Boguschewski, R. German, M. Goedecke, P. Becker, and P. H. M. van Loosdrecht, A tunable time-resolved spontaneous Raman spectroscopy setup for probing ultrafast collective excitation and quasiparticle dynamics in quantum materials, Struct. Dyn. **5**, 044301 (2018)
- **R. B. Versteeg**, I. Vergara, S. D. Schäfer, D. Bischoff, A. Aqeel, T. T. M. Palstra, M. Grüninger, and P. H. M. van Loosdrecht, Optically probed symmetry breaking in the chiral magnet Cu_2OSeO_3 , Phys. Rev. B **94**, 094409 (2016)

Köln, den 11. März 2019

Rolf Baldwin Versteeg

Rolf Baldwin Versteeg

Lebenslauf

✉ rolfbversteeg@gmail.com

— Persönliche Daten

Geburtsdatum 22.07.1990
Geburtsort Zwolle, Niederlande
Staats-
angehörigkeit Niederländisch

— Akademischer Werdegang und Ausbildung

2013–Aktuell **Promotionsstudium in Experimentalphysik**, Universität zu Köln, Köln, Deutschland.
2011–2013 **Masterstudium Nanoscience**, Rijksuniversiteit Groningen, Groningen, Niederlande (*cum laude*).
2008–2011 **Bachelorstudium Physics**, Rijksuniversiteit Groningen, Groningen, Niederlande (*cum laude*).
2002–2008 **Vorbereidend wetenschappelijk onderwijs**, Thorbecke Scholengemeenschap, Zwolle, Niederlande.

— Sonstige wissenschaftliche Erfahrung

09-12/2012 Forschungsaufenthalt am Lawrence Berkeley National Laboratory, Kalifornien, USA

— Stipendien

2014 Bonn-Cologne Graduate School of Physics and Astronomy Honours Stipendium
2012 Groninger Universiteitsfonds Excellent Student Stipendium
2012 Stichting Dr. Hendrik Muller's Vaderlandsch Fonds Stipendium

— Internationale Konferenzbeiträge

Jan. 2019 Joint MMM-Intermag Conference, Washington, District of Columbia, USA, (*contributed talk*)
Nov. 2018 Workshop "Correlated Electrons in Transition-Metal Compounds: New Challenges", Dresden, Germany (*poster presentation*)
Sept. 2018 CRC1238 International Conference "Control and Dynamics of Quantum Materials", Bensberg, Germany (*invited talk*)
Feb. 2018 Ultrafast Phenomena in Cooperative Systems Gordon Research Conference, Galveston, Texas, USA (*young investigator presentation*)
Feb. 2018 Ultrafast Phenomena in Cooperative Systems Gordon Research Conference, Galveston, Texas, USA (*poster presentation*)
July 2015 20th International Conference on Magnetism, Barcelona, Spain (*contributed talk*)

